Impedance Model of the CERN SPS and Aspects of LHC Single-Bunch Stability

THÈSE N^{O} 4585 (2010)

PRÉSENTÉE LE 4 MARS 2010

À LA FACULTÉ SCIENCES DE BASE
LABORATOIRE DE PHYSIQUE DES ACCÉLÉRATEURS DE PARTICULES
PROGRAMME DOCTORAL EN PHYSIQUE

ÉCOLE POLYTECHNIQUE FÉDÉRALE DE LAUSANNE

POUR L'OBTENTION DU GRADE DE DOCTEUR ÈS SCIENCES

PAR

Benoît SALVANT

acceptée sur proposition du jury:

Prof. O. Schneider, président du jury
Prof. L. Rivkin, Dr E. Métral, directeurs de thèse
Prof. O. Boine-Frankenheim, rapporteur
Dr E. Shaposhnikova, rapporteur
Prof. T. Nakada, rapporteur

ÉCOLE POLYTECHNIQUE
FÉDÉRALE DE LAUSANNE
Suisse
2010

Abstract

Upgrades of the CERN particle accelerators complex are planned to increase the potential of physics discovery in the LHC. In this respect, the beam coupling impedances of the SPS and LHC are expected to be among the limitations to the intensity upgrade scheme.

In this thesis work, we present a general framework to better understand the impedance of a particle accelerator. In a first step, the impedance of single components are gathered into an impedance model accounting for the whole machine. In order to assess the relevance of this impedance model, its impact on beam dynamics is simulated and can be compared to impedance observables measured with beam.

This general framework was applied to compute a more accurate transverse impedance model of the SPS from theoretical models for the 20 kickers and the 6.9 km long beam pipe, as well as time domain electromagnetic simulations of the 106 horizontal and 96 vertical SPS beam position monitors. Comparing *HEADTAIL* macroparticle simulations to beam-based measurements in the SPS, this transverse impedance model turned out to account for 65% of the vertical impedance measured in the machine and showed in addition that the large negative quadrupolar horizontal impedance of the kickers can be held responsible for the measured positive coherent horizontal tune shift with increasing beam intensity.

In the course of implementing this framework, new contributions were brought to the understanding of impedances and wake fields. A more general formula was derived for the longitudinal impedance of a multilayer cylindrical beam pipe. New formulae for the transverse quadrupolar impedances of simple models of kickers were also derived and successfully benchmarked to electromagnetic simulations. In addition, *MOSES* mode coupling analytical calculations were successfully benchmarked against *HEADTAIL* macroparticle simulations in predicting a Transverse Mode Coupling Instability at injection in the SPS between azimuthal modes -2 and -3. Finally, new RF bench measurements validated the theory proposed by B. Zotter and E. Métral, thereby confirming that the low frequency transverse impedance of the LHC collimators –, which largely dominates the LHC transverse impedance – is less critical than initially expected.

Keywords: BPM, collimator, *CST Particle Studio*, collective effects, dipolar and quadrupolar impedance contributions, *HEADTAIL* macroparticle simulations, high intensity beams, single-bunch instabilities, impedance, kicker, LHC, mode coupling, *MOSES*, plug in modules, SPS, TMCI, wake field.

Résumé

Dans le cadre d'un plan d'amélioration du complexe d'accélérateurs de particules du CERN, les impédances du SPS et du LHC figurent parmi les limitations qui pourraient empêcher d'augmenter les performances du LHC pour les utilisateurs des expériences de physique des particules. L'objectif de ce travail de thèse est de fournir un cadre général pour obtenir le modèle d'impédance d'une machine à partir de l'impédance de ses éléments constitutifs et d'estimer la validité de ce modèle en comparant ses effets simulés sur la dynamique du faisceau de particules aux observables caractéristiques de l'impédance qui peuvent être mesurées avec le faisceau dans la machine.

Ce cadre général a été appliqué au cas du SPS, pour lequel un modèle d'impédance transversale plus fiable a été obtenu à partir de calculs théoriques de l'impédance des 20 kickers du SPS et de sa chambre à vide, ainsi que de simulations électromagnétiques des moniteurs de position du faisceau (106 BPM horizontaux et 96 BPM verticaux). La comparaison entre des simulations effectuée avec le code *HEADTAIL* et des mesures avec le faisceau du SPS a permis de conclure que ce modèle d'impédance transversale du SPS explique d'une part 65% de l'impédance verticale mesurée dans la machine et montre d'autre part que l'impédance horizontale quadripôlaire négative des kickers pourrait être responsable de la pente positive mesurée de la fréquence bétatronique cohérente horizontale en fonction de l'intensité du faisceau dans le SPS.

Au cours de l'implémentation de ce cadre général, ce travail de thèse a également apporté des contributions nouvelles à la compréhension des impédances et des champs de sillage. Une formule plus générale permettant de calculer l'impédance longitudinale d'un cylindre multicouches a été obtenue. Par ailleurs, de nouvelles formules de l'impédance transversale quadripôlaire de modèle simples de kickers ont été obtenues et comparées avec succès à des simulations électromagnétiques. En outre, des calculs analytiques de couplage de modes avec le code *MOSES* ont été comparés avec succès à des simulations *HEADTAIL*, et les deux codes prédisent une Instabilité de Couplage de Modes Transversaux à l'injection dans le SPS entre les modes -2 et -3. Enfin, de nouvelles mesures sur banc ont permis de valider la théorie proposée par B. Zotter et E. Métral, et ont confirmé que l'impédance transversale à basse fréquence des collimateurs du LHC – qui domine largement l'impédance transversale du LHC – représente une limitation moins critique qu'initialement prévue.

Mots-clés: BPM, champs de sillage, collimateur, contributions d'impédance dipolaires et quadripôlaires, couplage entre modes, *CST Particle Studio*, effets collectifs, faisceaux de particules de haute intensité, impédance, interconnexion, instabilités de paquet unique, kicker, LHC, *MOSES*, simulations *HEADTAIL*, SPS.

Acknowledgments

I am very proud to have worked under the supervision of Elias Métral. During these three years at CERN, he has shown fascinating knowledge and skill, yet never vaunting it. His door and cellphone have never been shut, and he has always been available to patiently explain, motivate, advise and help. He guided me to challenging subjects, and was always open to my initiatives. On every occasion, Elias puts his students and colleagues first, and he has set a great example for me. Words cannot fully express my gratitude to Elias for all he did for me during these three exceptional years.

I am indebted to Lenny Rivkin for having directed my thesis within the Laboratoire de Physique des Accélérateurs de Particules at EPFL. Despite the distance and time constraints, Lenny always made himself available when I needed advice, and he provided me with help and support on numerous occasions.

My appreciation goes to Oliver Schneider (EPFL, President of the jury) as well as Oliver Boine-Frankenheim (GSI Darmstadt, Germany), Tatsuya Nakada (EPFL) and Elena Shaposhnikova (CERN) for having taken the time to be members of my PhD jury, and for their very useful comments on the manuscript and the thesis work.

I would like to thank Alain Hilaire, Malika Meddahi, David Robin (Berkeley Lab) and Oliver Brüning for introducing me to the fascinating field of accelerator physics. I am grateful to Oliver, Francesco Ruggiero and Gianluigi Arduini for their warm welcome back into their teams a few years later regardless of my atypical profile.

I am thankful to Chiara Bracco, Tatiana Pieloni, and Guido Sterbini, fellow EPFL PhD students, as well as Gianluigi Arduini, Giulia Bellodi, Rama Calaga, Christian Carli, Nicolas Mounet, Bernhard Holzer and Elena Shaposhnikova for their very useful advice and help during the PhD examination process.

I am also very grateful to the colleagues who have helped me throughout my PhD. I would like to acknowledge the following persons for their significant contributions to various levels of my thesis work:

- The *"impedance team"*:

  Gianluigi Arduini, Helmut Burkhardt, Elena Benedetto, Rama Calaga (BNL, Upton, NY), Fritz Caspers, Yong Ho Chin (KEK, Japan), Alexej Grudiev, Elias Métral, Nicolas Mounet, Diego Quatraro, Federico Roncarolo, Giovanni Rumolo, Elena Shaposhnikova, Bruno Spataro (INFN, Frascati, Italy), Carlo Zannini and Bruno Zotter.

- The *"3D simulation team"*:

  Lukas Hänichen, Wolfgang Müller (TU Darmstadt, Germany), Christian Boccard, Rama Calaga, Alessandro d'Elia, Erk Jensen, Tom Kroyer, Rolf Wegner, Carlo Zannini and colleagues from EN/MME and EN/MEF.

- The *"control room team"*:

  Gianluigi Arduini, Thomas Bohl, Rama Calaga, Heiko Damerau, Marek Gasior, Wolfgang Höfle, Riccardo de Maria (BNL, Upton, NY), Elias Métral, Yannis Papaphilippou, Giulia Papotti, Stefano Redaelli, Giovanni Rumolo, Elena Shaposhnikova, Ralph Steinhagen, Rogelio Tomás, Jorg Wenninger, Simon White, as well as all PSB, PS and SPS supervisors and operators.

- The *"software, hardware and support team"*:

  Oliver Aberle and Ralph Assmann for the Collimation Project, Mike Barnes, Enrico Bravin, John Evans, John Jowett, Anh Eymann-Nguyen (EPFL), Delphine Rivoiron, Olivier Sebastia, colleagues from BTE desktop as well as BE/RF, TE/ABT and EN/STI workshops.

Without their competence and generosity, significant bits would be missing from this thesis work. In view of my personal experience, the CERN management teams should be praised for having succeeded to create such a nice and sound teamwork atmosphere.

In particular, a very special thanks goes to Giovanni Rumolo for having patiently introduced me to the wonderful world of beam dynamics simulations. Our day-to-day collaboration on many topics has been invaluable to me. Together with Carlo, Elias, Federico, Giulia, Nicolas, Rama, Rogelio, Madeleine, Simon, Tatiana, Yngve Levinsen and many others, Giovanni creates a friendly atmosphere that turns our building into much more than a simple workplace.

Next door to Giovanni, Rogelio Tomás also proved to be an inexhaustible source of knowledge and good mood.

Rama Calaga, Nicolas Mounet and Carlo Zannini have not been at CERN for a long time yet I would already like to thank them a lot for our many nice and fruitful collaborations.

I am very grateful to Fritz Caspers for his expertise, determination and creative ideas. Our efficient RF measurement teamwork together with him and Federico Roncarolo has been a particularly exciting experience.

Finally, I feel very lucky to have had the opportunity to work together with a worldwide impedance expert such as Bruno Zotter. His dedication to the field of beam impedances forces my admiration.

Last but not least, I am thankful to Christine for her encouragement and patience during these countless working nights. On another level, I do not expect anything good would have occurred to me without the ever-present love and care of my parents and grandparents. My dearest wish is that Christine and I will follow their admirable example.

Contents

Chapter 1

Introduction

The beam coupling impedance is one of the limitations to the performance of particle accelerators. As the number of particles circulating in the accelerator is increased to enhance the probability of interesting particle physics results, electromagnetic fields generated by these accelerated particles in their surrounding become significant. The resulting forces perturb the designed motion of the beam and affects its quality for the end users. This perturbing effect is usually expressed in terms of the beam coupling impedance.

This work focuses on the beam impedance and its consequences in the CERN Super Proton Synchrotron (SPS) as an injector into the Large Hadron Collider (LHC). The current performance of the SPS machine is satisfactory for the initial phase of LHC operation with nominal parameters. However, an upgrade of the LHC injector complex is foreseen to improve the potential for physics discovery. The implementation of this upgrade requires a five-fold increase of the number of particles accelerated in the SPS, which is far beyond the current capabilities of the SPS due to the beam impedance in particular. In order to be able to reduce this impedance when it will be needed for the upgrade, the accelerator equipments that contribute significantly to the beam SPS impedance should be identified so that they can be modified, removed or replaced. Another prerequisite to an efficient impedance reduction campaign is to gain sufficient understanding of the factors that enable to increase or decrease the beam impedance. For these reasons, the main aim of this work is to improve our current understanding of the impedance of the SPS and lay the framework to obtain a more accurate impedance model.

In Chapter 2, the scientific and technical contexts of the CERN LHC complex are briefly mentioned. We then move to the needed theoretical description of single and collective particle motions in an accelerator in Chapter 3. We briefly give the motivations and implementation strategy for the CERN impedance database *ZBASE* in Chapter 4, before presenting new theoretical tools, new simulations and new measurements to better assess the impedance of accelerator elements to provide input impedance data for *ZBASE* in Chapter 5. In particular, theoretical results include a formula for the longitudinal impedance of an infinitely long cylindrical beam pipe made of an arbitrary number of layers of given materials in all ranges of frequencies (Section 5.1), together with an expression for the vertical and horizontal quadrupolar impedances of simple models of kickers, which represent a major contributor to the SPS impedance (Section 5.2.4). These theoretical predictions for kickers are then benchmarked with 3D ElectroMagnetic (EM) impedance simulations in Section 5.3. In the same section, we present 3D EM impedance simulations of Beam Position Monitors (BPMs), whose complex geometry can not be solved with analytical formulae, and benchmark these EM simulations to Radio Frequency (RF) measurements of these BPMs on a bench. The end of Chapter 5 is dedicated to addressing the urging question of the transverse impedance of the LHC collimators, which constitutes the dominating source of transverse impedance in the LHC ring. RF measurements of the transverse dipolar impedance of LHC collimators are reported and compared to the available theoretical predictions in order to conclude on their validity. The consequences of the beam impedance on the beam dynamics are then dealt with in Chapter 6. We first briefly recall the theoretical mode coupling formalism at the root of the code *MOSES* in Section 6.1, before comparing its theoretical predictions with macroparticle simulations performed with the *HEADTAIL* code for simple impedance models in Section 6.2. The SPS impedance contributions obtained in Chapter 5 are then gathered in an improved SPS impedance model. Macroparticle simulations of the interaction of this SPS impedance with a single bunch provides beam dynamics observables, which can be compared to measurements with beam in the SPS in Chapter 6.3 in order to assess (1) the validity of the current SPS impedance model and (2) the fundamental nature of a fast vertical instability that limits the single bunch intensity at injection in the SPS.

Chapter 2

The CERN Large Hadron Collider and its Injector Chain

2.1 The Large Hadron Collider (LHC)

2.1.1 Brief General Overview

Founded in 1954, the European Organization for Nuclear Research (CERN) is a multinational laboratory for particle physics located at the French-Swiss border near Geneva. As of September 2009, CERN has 20 European member states and more than 40 other states from all over the world are involved in CERN programmes. With around 2500 employees and 8000 visiting scientists representing 580 universities, 85 nationalities and half of the world's particle physicists, CERN is the largest particle physics laboratory in the world [1].

Motivations for building the LHC

The CERN Large Hadron Collider (LHC) is a particle accelerator designed to push the energy frontier in particle physics [2]. The goal of the LHC is to create the conditions to observe the immediate aftermath of hadron collisions at energies that have never been reached before in particle accelerators [3]. Analyzing the interaction of hadron constituents at such high energies is a key to improve our fundamental understanding of matter. In particular, particle physicists expect to encounter new phenomena that would take place beyond the current energy frontier set by the operating Tevatron at Fermi National Laboratory (Batavia, IL, USA). Physicists hope that these potential new phenomena could validate or invalidate particle physics theories. In fact, even though the current theory that describes the fundamental particles and their interactions – the Standard Model [4]– has proven very successful in explaining a vast majority of the physical phenomena that have been observed until now, fundamental questions remain [5], which include:

- The Standard Model does not explain how a particle gets to have a mass. Physicists have elaborated theories in which a boson could be the vector of the gravitational field. This so-called Higgs boson has been sought for many years in the Large Electron Positron collider (LEP) at CERN, and now in the Tevatron at Fermilab.

One of the most advertised goals of building LHC is to conclude on the existence of this Higgs boson.

- Are the leptons and quarks the fundamental building blocks of the matter we know or are they themselves made of other smaller building blocks?
- If the Standard Model predicts a matter/antimatter symmetry, why does there seem to be so much matter and so little antimatter in our universe?
- Current theories use extra dimensions, and supersymmetric particles to explain experimental observations we do not yet understand. However, evidence of these concepts have never been unveiled.

With the LHC, physicists are looking forward to be surprised and observe phenomena they did not predict, in order to improve our understanding of what we are made of, and how it all works together.

Selected milestones of the LHC project

The LHC project is a unique experiment both by its physical size and by the number of worldwide collaborating institutes and personnel (see the LHC footprint in the Geneva area in Fig. 2.1). It is therefore not a surprise that the time scale of this project is also large. The first workshop on LHC feasibility was held in 1984. Research and development effort on high field superconducting magnets – the most challenging components of the LHC – was started in 1990. The LHC design study report was published in 1991, and the CERN council decided to build the LHC in 1994 and to install it in the 27 km circumference tunnel built for the Large Electron Positron Collider (LEP), which operated between 1989 and 2000. The LHC installation started after LEP was shut down and decommissioned. Four massive particle detectors were built to observe the phenomena induced by the hadron collisions as precisely as possible (ALICE, ATLAS, CMS and LHCb, see Fig. 2.2). A comprehensive Design Report was written in 2004, which contains all relevant information on the design of the LHC complex [6]. Following the installation and hardware commissioning phase, the first beam circulated in the LHC during a few days in 2008, and LHC commissioning is planned to restart by the end of 2009.

2.1.2 Brief Technical Overview

Performance of the LHC

As already mentioned in Section 2.1.1, the goal of the LHC is to collide particles and generate new interesting events that could be observed with particle detectors. These detectors need to accumulate a sufficient amount of these interesting events to be in the position to announce a discovery. Similarly a sufficient amount of collisions without the occurrence of this interesting event have to be recorded to exclude an energy range for that event to occur. The critical parameter of a particle collider is then its ability to produce enough events of interest in a given amount of machine time. This ability is measured by a quantity called luminosity ($\mathcal{L}$), defined by the number of detected events

Figure 2.1: Aerial view of the CERN site in Geneva, together with the Jura, Geneva lake and the Alps. The thin superimposed red line indicates the position of the underground LHC tunnel. ©CERN.

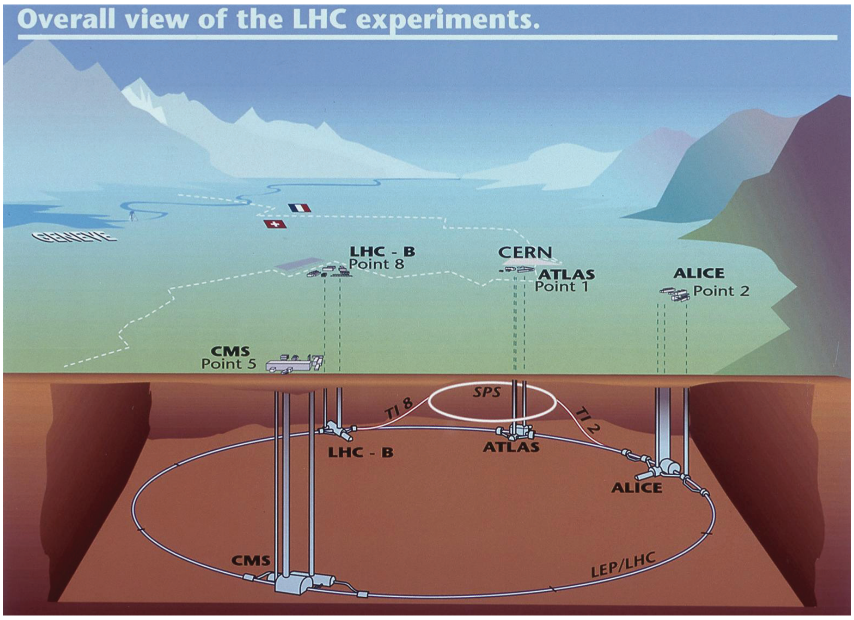

Figure 2.2: Artist's view of the CERN site on surface and underground, highlighting the LHC tunnel and the four particle detectors ALICE, ATLAS, CMS and LHCb. ©CERN.

of interest per second in the machine ($d\mathcal{N}/dt$) divided by the likelihood of occurrence of that event (referred to as the event production cross section σ_p) [7]

$$\mathcal{L} = \frac{d\mathcal{N}}{dt}\frac{1}{\sigma_p}. \tag{2.1}$$

The value of the production cross section of a given nuclear physics event is a function of the center of mass energy of the colliding particles, and is independent of the other accelerator parameters. On the other hand, the luminosity is independent of the event of interest but strongly depends on the parameters of the particle beams at the moment of observation. To increase the total number of events of interest observed over a given period of time,

- one can probe an energy range over which the production cross section of that event is larger. In the case of hadron collisions (as in Fermilab's Tevatron and CERN's LHC), the total center of mass energy available can be unevenly distributed between the quarks and gluons constituting the hadrons. Then, even if the energy spread of the colliding hadrons is well defined, the energy spread of the colliding quarks is much larger, resulting in a large range of energies available for nuclear physics events. A hadron collider is therefore a machine primarily used to discover new physics events, and its beam energy should be as high as possible. This is why the LHC was designed to produce the maximum energy available with the financial and technological constraints (head-on collision of two beams was chosen instead of one beam colliding into a fixed target [7]; circular machine was chosen to reach high energies by providing the beam with a fraction of the needed energy increase at every turn; the design nominal energy was the largest energy reachable with the maximum magnetic field available over the length of the existing LEP tunnel). On the contrary, colliding leptons (as in CERN's LEP, and linear collider projects) allow to focus on a precise energy and study physics events unveiled by hadron colliders.

- one can reduce the background noise produced by other events occurring in or around the detector. This background noise in a hadron collider is much larger than in a lepton collider, due to the numerous interactions happening between the constituents of the colliding nucleons.

- one has to find an optimized trade off between the highest nominal luminosity possible and the machine time over which this luminosity can be maintained. In the theoretical case of two bunched beams colliding head-on with identical Gaussian profiles (see the example for two LHC beams in Fig. 2.3), the luminosity can be calculated as [7]

  $$\mathcal{L} = \frac{N_b^{(1)} N_b^{(2)} f_{rev} N}{4\pi\sigma_x\sigma_y}, \tag{2.2}$$

  where $N_b^{(1)}$, and $N_b^{(2)}$ are the number of particles per bunch in beam 1 and beam 2, f_{rev} is the revolution frequency of the particles around the circular accelerator, N is the number of bunches per beam, σ_x and σ_y are the horizontal and vertical r.m.s. beam size. In a real accelerator, this luminosity is reduced due the practical

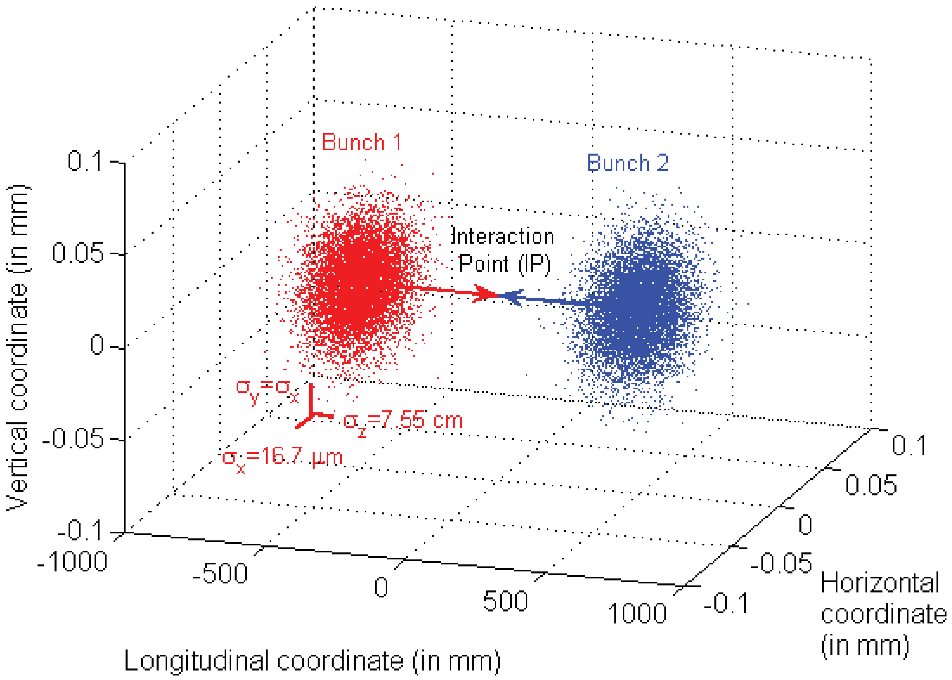

Figure 2.3: Schematic view of two LHC proton bunches (bunch 1 from beam 1 in red and bunch 2 from beam 2 in blue) colliding at an IP with the nominal r.m.s. sizes ($\sigma_x = 16.7$ μm, $\sigma_y = 16.7$ μm, $\sigma_z = 7.55$ cm). Please note that the longitudinal z axis is squeezed by 4 orders of magnitude compared to the transverse axes (horizontal x and vertical y) to show the normal distribution in all planes. In reality, the bunch distribution is contained within the dimensions of a 10 cm long human hair. The dots used to represent the protons are not to scale.

need to collide the beams with a small angle, also called crossing angle. One can see in Eq. (2.2) that the maximum luminosity is produced by the most intense beam squeezed in the smallest transverse beam dimensions. Unfortunately, the parameters of stored beams in all circular machines deteriorate over time due to many processes. These processes draw particles off their design trajectory, leading to an increase of the transverse beam sizes $\sigma_{x,y}$, and/or losses against the chamber of the accelerator, i.e. a decrease of the number of particles per bunch $N_b^{(1,2)}$. Besides, the accelerator operation needs to be regularly stopped for maintenance. Finally, unexpected incidents occur and may reduce the performance of the accelerator, in particular the number of protons per bunch or the number of bunches. Therefore, luminosity is a function of physical time. At the end of the run, the performance of the LHC will be assessed by the total number of detected events of interest, and the real figure of merit is therefore the luminosity integrated over the lifetime of the LHC.

Short Description of the LHC layout

The LHC momentum goal set in the design report is a collision center of mass momentum of 14 TeV/c. To reach this beam momentum, it was chosen to simultaneously accelerate two proton beams circulating in opposite directions with a momentum of 7 TeV/c [6]. The 27 km long 3.8 m wide LHC tunnel ring is buried 50 to 175 m underground between the Jura and Lake Geneva. The LHC proton beam circulates in a continuous beam pipe – also called vacuum chamber –, surrounded by a large number and variety of accelerator equipments:

- magnets to bend, focus the proton beam transversally and correct its trajectory,
- radio frequency (RF) cavities to accelerate and focus longitudinally the proton beam,
- diagnostics to assess all kinds of machine and beam parameters,
- feedback systems to damp injection oscillations and beam instabilities,
- vacuum pumps to minimize interaction of protons with residual gaz,
- collimators to intercept protons on unwanted trajectories,
- and of course the huge detectors placed at four out of 8 locations where the counter-rotating beams cross path and can collide. These locations are also called Interaction Points (IPs).

The goal beam momentum of 7 TeV/c was set to take maximum profit of the dimensions of the existing LEP tunnel. The main limitation lies in the magnet capability to bend the proton beam with the maximum magnetic field strength available and keep it on the 27 km long circular trajectory. As it will be seen in Eq. (3.11a), increasing the energy of a beam of given particles in a synchrotron can only be obtained by increasing the magnetic field strength, the physical length over which this magnetic strength is applied, or both. Since the LHC tunnel physical circumference is fixed, maximizing the LHC beam energy means applying the highest magnetic field strength in the magnets ($\left|\vec{B}\right| = 8.3$ T for the LHC main magnets), and filling the LHC circumference with as many magnets as possible (1232 main magnets are installed in the LHC). Reaching such a high magnetic field strength requires very large current densities in the coil, which was made possible by using Niobium-Titanium (NbTi) alloys cooled to a temperature of 1.9 K (-271 °C) for the coils' cables. At this temperature, the NbTi alloy is superconducting and its resistivity is low enough to allow a critical current density of 1000 to 2000 A/mm^2 through the cable. However, the need to cool these coils to 1.9 K requires one of the largest and most complex superfluid Helium cooling system in the world. Besides, to produce the highest magnetic field strength at the location of the accelerated particle beam, these extremely "cold" coils have to be placed as close as possible to an extremely "warm" beam. Indeed, the stored energy of the full LHC proton beam at top energy (2808 bunches of 1.15 10^{11} protons each at 7 TeV/c means a total energy $E_t = 360$ MJ). This energy stored in the full LHC beam is then equivalent to the energy of a 38-ton-truck driving at 500 km/h. Two important remarks have to be made on this huge energy stored in the LHC beam:

- Erroneous steering of the full LHC beam to the vacuum chamber would result in punching a hole through the beam pipe and the many expensive elements behind it. Such erroneous steering unfortunately happen in particle accelerators and can be caused for instance by an equipment malfunction or a wrong command sent by the operator or the control system. To prevent such incidents from destroying equipments, a complex redundant Machine Protection System has been put in place to detect failures or unexpected events, and quickly direct the LHC beam to a dedicated Beam Dumping System that has been designed to absorb the enormous destructive power stored in the LHC beam [2].

- Even if on average the full beam is on its design trajectory along the accelerator, some protons are bound to be diverted from their design trajectories due to several processes (see Fig. 2.4). Scattering processes affect the trajectory of single protons (scattering with residual gas in the beam pipe, scattering with protons within the bunch, head-on collisions). Resonance processes linked with magnet imperfections and/or misalignments will drive single protons within bunches on oscillating trajectories with larger and larger amplitudes. Electromagnetic interactions with the beam environment will selectively push certain proton bunches to coherently oscillate around the design trajectory. Whichever the process, these bunches can hit the beam pipe, and these collisions will produce heat. Depending on the location and the intensity of these losses, this heat deposition may warm the NbTi alloy of the coil above the critical temperature, leading to a quench, and the need to stop the operation of the machine. A dedicated collimation system has been designed to intercept the protons that are bound to be lost in order to concentrate the losses in regions where the heat deposition does not affect the operation of the machine.

As a consequence, a safe and reliable operation of the LHC demands higher performance and tighter control of all machine systems (vacuum, cryogenics, diagnostics, machine protection, collimation, hardware) than of any other accelerator in the world.

2.2 The LHC Injectors

As mentioned in the previous section, the LHC has been designed to simultaneously accelerate two proton beams circulating in opposite directions from an injection momentum of 450 GeV/c to a collision momentum of 7 TeV/c. A chain of smaller proton machines and transfer lines is used to accelerate the beam from the proton source and provide the 450 GeV/c proton beam to the LHC. The whole CERN accelerator complex is shown in Fig 2.5. The protons path from the source to the LHC ring is:

(a) LINAC2 (source and linear accelerator)

The protons for the LHC beam are produced from hydrogen by a duoplasmatron with a kinetic energy of 100 keV, focused and preaccelerated to 750 keV in an RF Quadrupole, and finally accelerated in the 30 m drift tube linear accelerator (LINAC) to reach a kinetic energy of 50 MeV at the exit of LINAC2.

(b) Booster (four superimposed synchrotron rings)

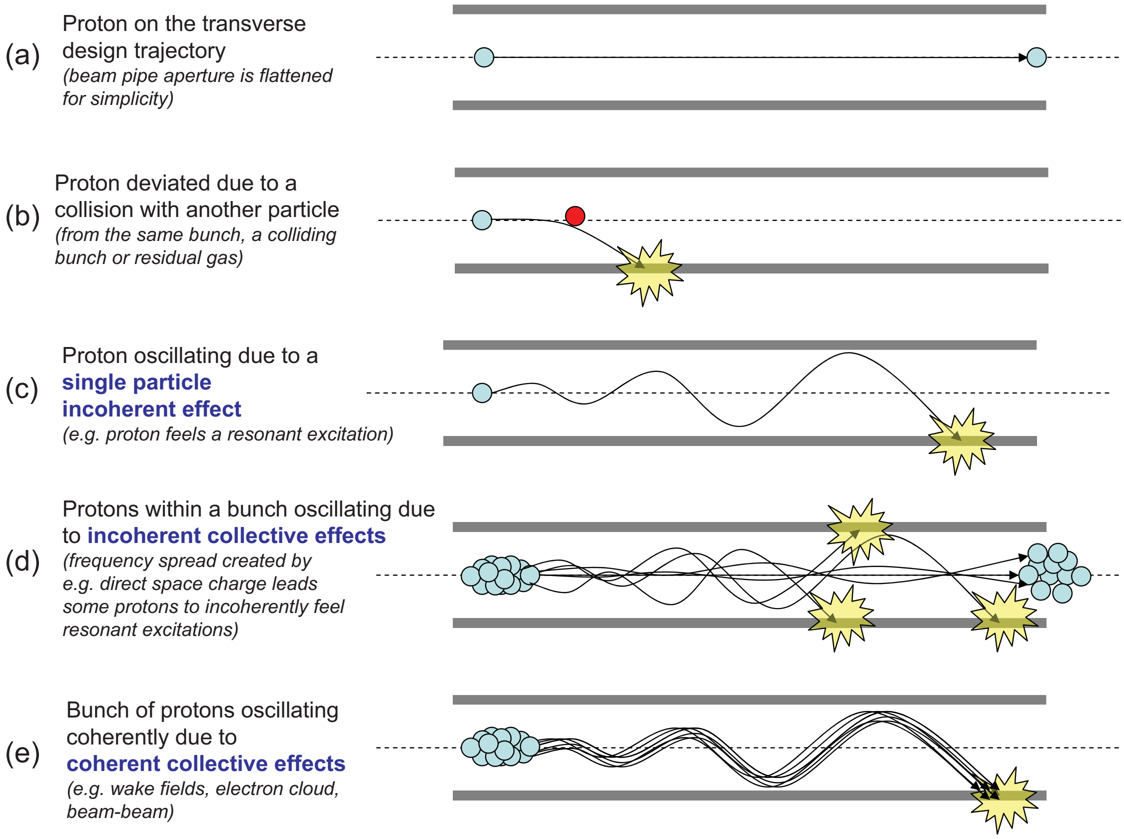

Figure 2.4: Schematic view of different types of proton losses in an accelerator. (a) Proton (blue circle) on the design transverse orbit within the vacuum chamber. The transverse aperture is in general not flat. (b) A proton encounters a collision with another particle (red) and is lost against the vacuum chamber. (c) Example of single particle loss: a proton feels a resonant excitation, oscillates around the design orbit and is lost. (d) Example of collective incoherent loss: each proton in the bunch feels the direct electromagnetic fields created by the other protons (direct space charge field, described in more details in Chapter 3). The tune spread of the protons in the intense bunch is large. As in (c), some protons feel resonant excitations and are individually lost while the transverse beam size increases. (e) Example of collective coherent loss (instability): protons in a bunch feel the perturbating electromagnetic field due to the interaction of the beam with its environment (impedance, electron cloud or the counter-rotating beam in the IP, refer to chapter 3 for more details). Contrary to (c) and (d), the protons in the bunch are oscillating coherently, and a large fraction of the protons is quickly lost [8].

The 50 MeV protons are then injected into the Proton Synchrotron Booster (PSB or PS Booster), and accelerated to a kinetic energy of 1.4 GeV. The PSB consists of 4 rings on top of each other of 25 m radius.

(c) PS (synchrotron ring)

The 1.4 GeV protons extracted from the PS Booster are injected into the 100 m radius Proton Synchrotron (PS, built in 1959), where they are accelerated to a momentum of 26 GeV/c. In addition, significant radio frequency manipulations take place in the PS to obtain the nominal bunch parameters for the LHC beam (bunch splitting and bunch rotation).

(d) SPS (synchrotron ring)

The 26 GeV/c protons are extracted from the PS to the TT2 transfer line that leads them into the 6.91 km circumference Super Proton Synchrotron (SPS). There, the protons get accelerated to a momentum of 450 GeV/c, ready to be injected into the LHC through two separate transfer lines. TT60/TI2 injects beam 1 circulating clockwise in the LHC, and TT40/TI8 injects beam 2 circulating anticlockwise in the LHC.

It is important to state that the objectives in terms of beam parameters set for the injector complex have been fulfilled, and that the expected nominal beam is available for the LHC [9]. Injector upgrades needed to obtain the ultimate beam parameters and beyond will be mentioned in Section 2.3. Besides this proton accelerator chain, CERN hosts a number of machines non related to proton collisions in LHC, and they will not be discussed in this document:

- CERN Neutrinos to Gran Sasso (CNGS),
- CLIC Test Facility (CTF3),
- the heavy ions injector chain into LHC (LINAC 3 and Low Energy Ion Ring (LEIR))
- fixed target experiments in the East Area of the PS and North Area of the SPS,
- the Isotope Mass Separator (ISOLDE),
- the Antiproton Decelerator (AD),
- the Neutrons Time Of Flight experiment (n-TOF).

In adition to providing beam to the LHC, the LHC injectors are strongly involved in delivering beam to most of these experiments.

2.3 Plans for an Upgrade of the LHC Complex

In order to maximize the performance of the LHC for the experiments, an upgrade of the LHC complex is currently under study.

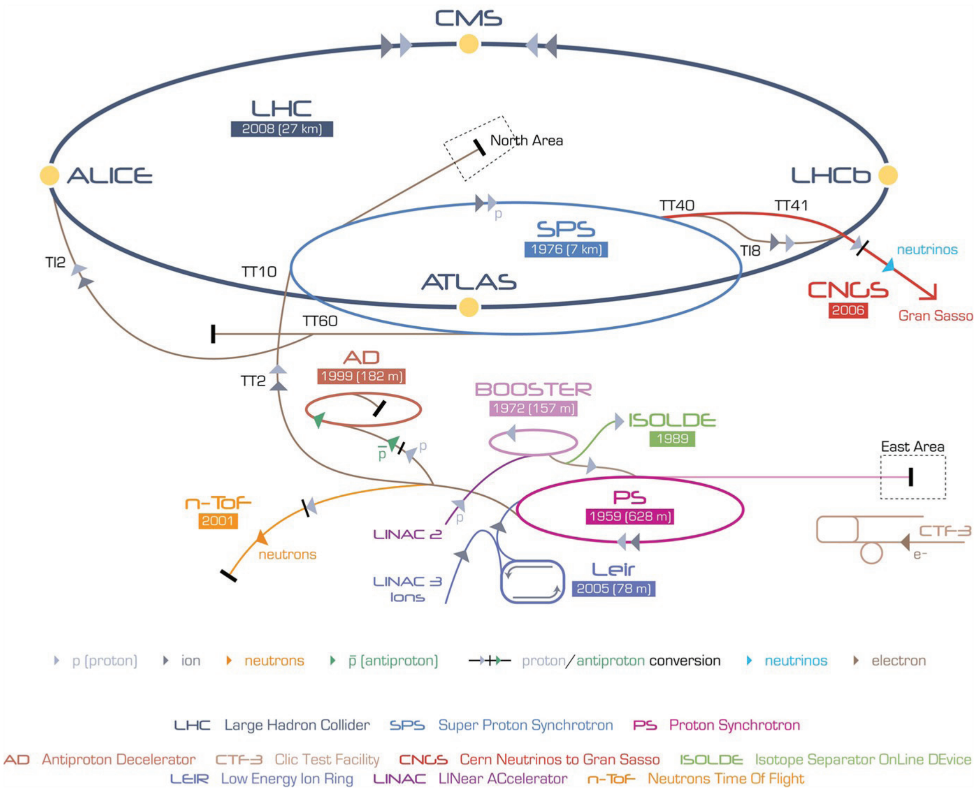

Figure 2.5: Schematics of the CERN accelerator complex. The proton accelerator chain starts with LINAC2 and follows the BOOSTER, the PS, the TT2 transfer line, the SPS, the TT60/TI2 (for beam 1) and TT40/TI8 transfer lines (for beam 2) to finally reach the LHC. ©CERN.

2.3.1 Motivations for the LHC Upgrade

Due to the major technical and financial challenges involved, the LHC might be the only energy frontier collider available to particle physicists for the next decades [10, 11, 12]. Despite recent promising studies in other methods of particle acceleration such as plasma wake field acceleration [13, 14], no other solution will be available in the short term to reach high energies and high luminosities. As a consequence, the performance of the LHC needs to be pushed as far as technically and financially possible. After the first physics results have been obtained with current hardware, an upgrade of the LHC complex is planned in order to fully exploit its capabilities and provide with the opportunity to discover new physics [15]. It is important to stress that the first physics results as well as the experience of operating the detectors and the accelerator chain will be major inputs to decide how to upgrade LHC. However, as mentioned in section 2.1.2, the final performance of the LHC will be measured by its beam energy and its luminosity integrated over its years of operation. Possible upgrade options to increase both energy and integrated luminosity are therefore already under study [16].

2.3.2 Possible Implementations of the LHC Upgrade

Energy Upgrade

An increase of the beam energy would require higher field magnets, as mentioned in section 2.1.2, and research effort has started to build magnets generating fields up to 20 T [17].

Luminosity Upgrade

As of September 2009 (i.e. before the first collisions in the LHC), potential areas for increasing the LHC integrated luminosity have been identified [18]:

- The aging injection chain is a major threat to the reliable operation of the LHC [9]. In fact, a large number of equipments are running well beyond their design performance and their repair/replacement becomes more difficult as time passes. As a consequence, a project has been launched to replace the current injectors (Linac 2, PS Booster and PS) by a new chain of injectors (Linac 4, SPL, PS2). In the current schemes, the SPS and LHC would not be replaced, but upgraded [19].
- New beam separation schemes are studied to reduce the beam crossing angle at the IP, which could lead to a gain in integrated luminosity.
- A small transverse beam size at the IP is limited both by the transverse size of the beam injected into the LHC, but also by the capability to focus the beam at the IP. That is why (1) the design of the new injector chain focuses on being able to produce intense bunches with smaller beam sizes and (2) a detailed "Phase 1" upgrade is already planned for 2013 to enable a better focusing of the beam at the IP.
- As of today, the LHC beam intensity is predicted to be limited by the quench limit of the LHC magnets [20]. All current upgrade schemes are however aiming at increasing the intensity per bunch from the nominal 1.15 10^{11} protons per bunch to

the "ultimate" value of 1.7 10^{11} or even 4.9 10^{11} protons per bunch (p/b) [21]. Due to unwanted losses and emittance increase along the LHC injection synchrotrons, today's intensity for the nominal LHC type beam is 1.5 10^{11} (PSB), 1.3 10^{11} (PS), and 1.15 10^{11} (SPS) protons per bunch with nominal longitudinal and transverse emittances [22]. This is therefore another argument to design a new injection chain capable of producing the beam intensity that may be needed for the upgrade.

Besides the beam brightness increase and the reliability improvement, the design of this new injector chain includes requirements for more availability and flexibility from the injectors. Since the SPS is planned to be kept in place in the upgrade schemes, it is particularly important to understand its limitations and find solutions to reach the required higher beam intensities. This thesis work is one contribution to this framework.

Chapter 3

Collective Effects in Synchrotrons

In Chapter 2, the need to generate dense particle beams for physics experiments was stressed. As already mentioned in Fig. 2.4, multi-particle phenomena perturb the motion of single particles and may affect the beam quality. This chapter defines general notions of single particle transverse and longitudinal motion in a circular accelerator and then focuses on the study of a specific type of collective effects generated by wake fields or impedances. Let us first consider a circular accelerator and define the coordinates that will be used in this manuscript.

3.1 Definition of the Coordinate System

When an accelerator is designed, one of the first steps is to choose the ideal trajectory on which all the accelerated particles should circulate. This ideal trajectory is called the design orbit. The design orbit can be a straight line (linac), a spiral (cyclotrons), or a succession of arcs and straight lines (synchrotron). The coordinates of a reference proton on an ideal circular design orbit of radius ρ is sketched in Fig. 3.1. The reference proton velocity is $v = \beta c$. An arbitrary reference is chosen as origin for angle θ and curvilinear position $s = vt$.

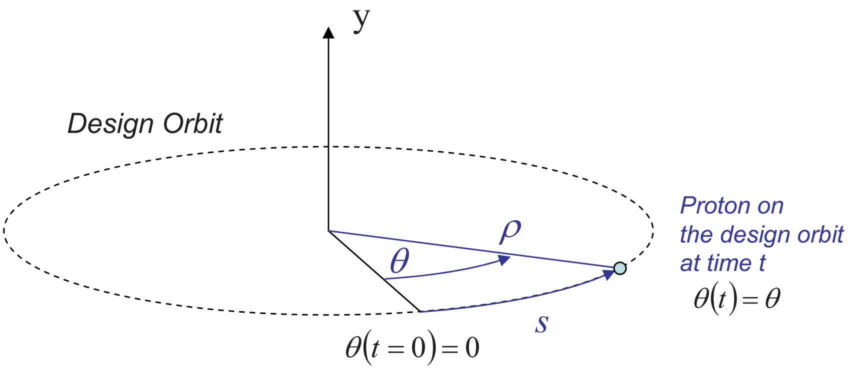

Figure 3.1: Sketch of a proton on the ideal design orbit of a circular accelerator.

The coordinates of any other proton on a given trajectory are displayed on Fig. 3.2.

The horizontal, vertical and longitudinal positions (x, y and z) at time t are defined with respect to the position of the reference proton at time t. In Section 3.2.2, the longitudinal deviation z from the reference particle position will also be expressed as a time delay $\tau = z/v$ with respect to the reference particle.

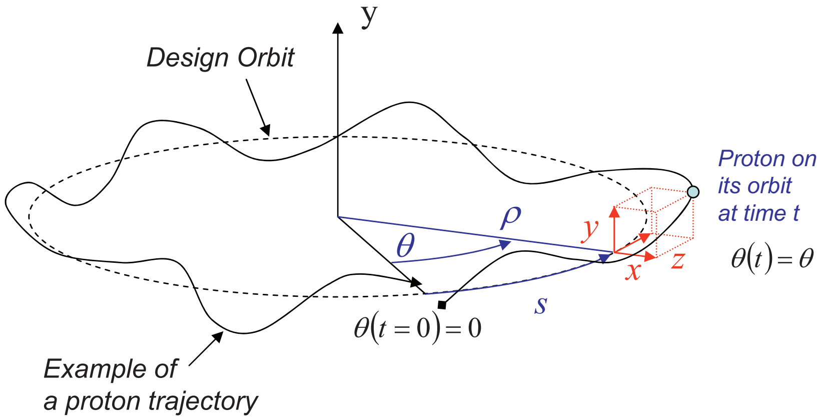

Figure 3.2: Sketch of a proton on a trajectory different from the design orbit. In this case of a beam circulating counterclockwise, the reader is advised that the referential (x, z, y) is orthonormal direct.

The cylindrical coordinate system ($r = \rho + x$, θ, y), based on the orthonormal frame ($\vec{u}_x = \vec{u}_\rho$,$\vec{u}_s = \vec{u}_\theta$,$\vec{u}_y$) will be used. It is important to notice that the conventions classically used in accelerators impose that the horizontal position x is positive if the particle travels outward from the design orbit, the vertical position y is positive if the particle is above the design orbit, and the longitudinal position z is in the same direction as the velocity of the design particle. As a consequence, depending on the direction of rotation, the referential (x, y, z) may not be orthonormal direct. This is for instance the case in Fig. 3.2. A notable exception to this convention is the accelerator design program *MAD* [23], where the (x, y, z) referential is kept orthonormal direct by having the vertical coordinate point downwards in the case of Fig. 3.2. Finally, the derivative of a given function f with respect to t will be noted $\dot{f}$ and the derivative of this function f with respect to s will be noted f'. Since $s = vt$ we have

$$\dot{f} = \frac{df}{dt} = \frac{df}{ds}\frac{ds}{dt} = v\frac{df}{ds} = vf'. \tag{3.1}$$

Similarly,

$$\ddot{f} = \frac{d}{dt}\left(\frac{df}{ds}\frac{ds}{dt}\right) = \frac{d}{ds}\left(\frac{df}{ds}\frac{ds}{dt}\right)\frac{ds}{dt} = v^2 f'' + f'v\frac{dv}{ds}. \tag{3.2}$$

3.2 Single Particle Motion in a Synchrotron

The study of collective effects requires a prior understanding of the motion of single particles in a circular accelerator. References [24], [25], [26], [27] were very useful in preparing this section. The motion of a single particle in a circular accelerator is driven by the Lorentz force $\vec{F}$

$$\vec{F} = q(\vec{E} + \vec{v} \times \vec{B}), \tag{3.3}$$

where q is the charge of the particle ($q = e$ for the proton), $\vec{E}$ and $\vec{B}$ are the electric and magnetic fields at the location of the particle. The longitudinal and transverse motions of a single particle are classically studied separately. This separation can be justified as the particle acceleration and longitudinal focusing in the bucket is most efficiently performed with RF cavities, whereas the different types of magnets are responsible for steering, focusing and stabilizing the particle transverse orbit. The longitudinal and transverse motions are however coupled in the case of non zero chromaticity and in studying transverse collective effects, as will be seen in Chapters 5 and 6. In the case of the CERN synchrotrons (PSB, PS, SPS and LHC), the protons have already been accelerated longitudinally before injection, and we can assume that their transverse velocity $v_\perp$ can be neglected compared to their longitudinal velocity v_s. As a consequence the total velocity can be expressed as $v = \sqrt{v_x^2 + v_y^2 + v_s^2} \approx v_s$. Besides, we assume that the longitudinal magnetic field B_s can be neglected. In this case, the Lorentz Force $\vec{F}$ on a proton is decomposed in its longitudinal component F_s and its transverse components F_x and F_y as

$$F_x = e(E_x + v_s B_y), \tag{3.4a}$$

$$F_s = eE_s, \tag{3.4b}$$

$$F_y = e(E_y - v_s B_x). \tag{3.4c}$$

It is important to note that this set of equations only holds in the frame defined in Fig. 3.2. Besides, in this section, since we only consider the dynamics of a single particle. Intensity effects will be taken into account in Section .

3.2.1 Transverse Betatron Motion

From Eq. (3.4a) and (3.4c), steering and focusing the particles in the horizontal (resp. vertical) plane requires generating horizontal (resp. vertical) electric fields or vertical (resp. horizontal) magnetic fields. If a magnetic field strength of the order of 8 T can be obtained over large lengths in the LHC, the technology to obtain electric field strengths that would reliably produce the same bending force on the protons is not available. This is why magnetic fields are classically used to act on the transverse trajectories. The transverse components of the Lorentz force then become

$$F_x = ev_s B_y, \tag{3.5a}$$

$$F_y = -ev_s B_x. \tag{3.5b}$$

The following paragraphs aim at defining the fundamental parameters of transverse motion (tune, transverse emittance, beta function, phase advance, chromaticity, dispersion, momentum compaction factor), showing the form of unperturbed transverse motion in a synchrotron and finally mentioning the perturbations that can result in resonant losses.

Deriving the Transverse Equations of Motion

We now write the relativistic equation of motion for a proton in a constant magnetic field, assuming there is no electric field [28]:

$$\frac{d}{dt}\left(m_0 \gamma \vec{v}\right) = \vec{F} = q\left(\vec{E} + \vec{v} \times \vec{B}\right) = e\vec{v} \times \vec{B}, \tag{3.6}$$

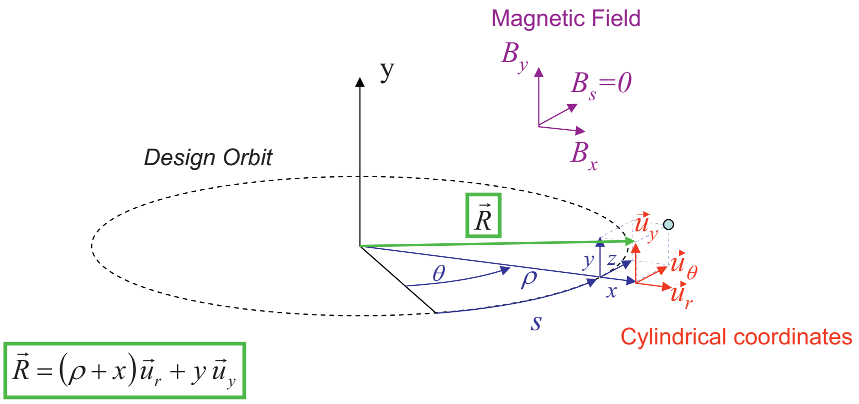

Figure 3.3: Sketch of a proton on a trajectory different from the design orbit with cylindrical coordinates (r, θ, y).

where m_0 is the rest mass of the proton, γ is the Lorentz factor defined by $\gamma = 1/\sqrt{1-\beta^2}$, and β is defined as $\beta = v/c$, i.e. the particle velocity relative to the speed of light c. The energy $\mathcal{E} = m_0\gamma c^2$ of a particle in a constant magnetic field is a constant of motion since the external force is always perpendicular to the proton velocity. The relativistic mass $m_0\gamma$ is therefore also a constant of motion and we can write:

$$\frac{dv_x}{dt} = \frac{ev_sB_y}{m_0\gamma}, \tag{3.7a}$$

$$\frac{dv_y}{dt} = \frac{-ev_sB_x}{m_0\gamma}. \tag{3.7b}$$

Switching to cylindrical coordinates (r, θ, y) as displayed in Fig. 3.3, the transverse position $\vec{R}$, velocity $\vec{V} = d\vec{R}/dt$, and acceleration $\vec{A} = d\vec{V}/dt$ in the transverse plane can be written:

$$\vec{R} = r\vec{u}_r + y\vec{u}_y, \tag{3.8a}$$

$$\vec{V} = \dot{r}\vec{u}_r + r\dot{\theta}\vec{u}_\theta + \dot{y}\vec{u}_y, \tag{3.8b}$$

$$\vec{A} = \left(\ddot{r} - r\dot{\theta}^2\right)\vec{u}_r + \left(2\dot{r}\dot{\theta} + r\ddot{\theta}\right)\vec{u}_\theta + \ddot{y}\vec{u}_y. \tag{3.8c}$$

Identifying the transverse acceleration components Eq. (3.7) and (3.8), we have

$$m_0\gamma\left(\ddot{r} - r\dot{\theta}^2\right) = ev_sB_y, \tag{3.9a}$$

$$m_0\gamma\ddot{y} = -ev_sB_x. \tag{3.9b}$$

Using $v_s = r\dot{\theta}$, we get

$$m_0\gamma\ddot{r} - \frac{m_0\gamma v_s^2}{r} = ev_sB_y, \tag{3.10a}$$

$$m_0\gamma\ddot{y} = -ev_sB_x. \tag{3.10b}$$

To order 0, keeping a proton on the design orbit $r = \rho$ requires $\ddot{r} = 0$, i.e.

$$p_0 = -eB_y^0\rho, \tag{3.11a}$$
$$B_x^0 = 0, \tag{3.11b}$$

where $p_0 = m_0\gamma^0 v_s^0$ is the design momentum and B_y^0 (resp. B_x^0) is the constant vertical (resp. horizontal) magnetic field strength felt by the proton. Since this constant magnetic field is generated in practice by dipole magnets, it is also called dipolar field. The dipolar vertical magnetic field B_y^0 is needed to compensate the centrifugal force. As announced in Section 2.1.2 when justifying the need for huge machines and high magnetic field strength to reach high energies, the proton momentum $p_0 = m_0\gamma v_s$ can only be increased if the dipole magnetic field strength B_y^0 and/or the bending radius ρ are increased. In general, there is no constant horizontal magnetic field since no vertical bending radius is needed on average. Coming back to Eq. (3.10a), we use now $r = x + \rho$

$$m_0\gamma\ddot{x} - \frac{m_0\gamma v_s^2}{x+\rho} = ev_sB_y, \tag{3.12a}$$
$$m_0\gamma\ddot{y} = -ev_sB_x. \tag{3.12b}$$

Since we assumed that the horizontal deviation x is much smaller than the machine radius ρ, we can develop $1/(x+\rho)$ to first order in x/ρ:

$$\frac{1}{x+\rho} = \frac{1}{\rho}\left(1 - \frac{x}{\rho}\right) + o\left(\frac{x}{\rho}\right),$$

and use the first order Taylor expansion in x of the vertical magnetic field into a dipolar and quadrupolar field strength,

$$B_y = B_y^0 + x\frac{dB_y}{dx} + o(x).$$

Similarly,

$$B_x = y\frac{dB_x}{dy} + o(x),$$

since $B_x^0 = 0$ (Eq. (3.11b)). The following equations are then obtained:

$$\ddot{x} + x\left(\frac{v_s^2}{\rho^2} - \frac{ev_s}{m_0\gamma}\frac{dB_y}{dx}\right) = \frac{ev_sB_y^0}{m_0\gamma} + \frac{v_s^2}{\rho}, \tag{3.13a}$$
$$\ddot{y} + y\frac{ev_s}{m_0\gamma}\frac{dB_x}{dy} = 0. \tag{3.13b}$$

It is now convenient to replace the time variable t by the curvilinear variable $s = vt$. Using $\ddot{x} = v_s^2x''$ as there is no longitudinal acceleration ($dv/ds = 0$) (Eq. 3.2) we have

$$x'' + x\left(\frac{1}{\rho^2} - \frac{e}{m_0\gamma v_s}\frac{dB_y}{dx}\right) = \frac{eB_y^0}{m_0\gamma v_s} + \frac{1}{\rho}, \tag{3.14a}$$
$$y'' + y\frac{e}{m_0\gamma v_s}\frac{dB_x}{dy} = 0. \tag{3.14b}$$

One of the Maxwell equations [29] - which will be extensively used to calculate the wakes and impedances (see Eq. (5.15d)) - can be applied to the vacuum region inside the magnet in the absence of electrical currents and fields to yield $\vec{\nabla} \times \vec{B} = 0$. As a consequence, remembering that we assumed that $B_s = 0$, we have in particular $dB_x/dy = dB_y/dx$. The transverse magnetic field strength gradients are equal. If we call g this gradient and use the fact that the momentum of the particle is $p \approx p_s = m_0\gamma v_s$, we obtain

$$x'' + x\left(\frac{1}{\rho^2} - \frac{eg}{p}\right) = \frac{eB_y^0}{p} + \frac{1}{\rho}, \tag{3.15a}$$

$$y'' + y\frac{eg}{p} = 0. \tag{3.15b}$$

Finally, assuming the proton may not move with the design momentum p_0 but with a slightly different momentum $p = p_0 + \Delta p$ with $\Delta p << p_0$, we can write

$$\frac{1}{p} = \frac{1}{p_0} - \frac{\Delta p}{p_0^2} + o\left(\frac{\Delta p}{p_0^2}\right),$$

and obtain the transverse equations of motion for a proton in a circular accelerator in the linear approximation

$$x'' + x\left(\frac{1}{\rho^2} - k\right) = \frac{1}{\rho}\frac{\Delta p}{p_0}, \tag{3.16a}$$

$$y'' + ky = 0, \tag{3.16b}$$

where we defined the quadrupole strength $k = eg/p_0$, neglected the second order terms in $x\Delta p$, and used $eB_y^0/p_0 = -1/\rho$ found in (Eq. 3.11). Equation (3.16) also holds if we only consider a local portion of an accelerator with a local radius of curvature $\rho(s)$ and a local focusing strength $k(s)$. In this more general case, the equations of motion in both planes can be written as Hill's equations

$$x'' + K_h(s)x = \frac{1}{\rho(s)}\frac{\Delta p}{p_0}, \tag{3.17a}$$

$$y'' + K_v(s)y = 0, \tag{3.17b}$$

with $K_h(s) = 1/\rho(s)^2 - k(s)$ in the horizontal plane and $K_v(s) = k(s)$ in the vertical plane. The compilation of the local radii of curvature and the focusing strengths along the design orbit constitutes the machine linear lattice. In a real accelerator, momentum error is not the only perturbation to the motion of a single proton. Magnetic field strength errors and alignment errors in the magnets create errors both in the horizontal and vertical plane, adding terms to the right hand side of Eq. (3.17). It is also important to note that we have not considered linear coupling between the vertical and horizontal planes. Let us first solve the Hill's equations of motion in the case of an unperturbed proton with design momentum ($\Delta p = 0$).

Solution of the Homogeneous Equations of Motion

In this paragraph, we deal with the vertical plane only, but all definitions and formulae apply also for the horizontal plane. The general solution of the homogeneous Hill's equation of motion (Eq. (3.17b)) is

$$y(s) = \sqrt{\tilde{\varepsilon}_y}\sqrt{\beta_y(s)}\cos\left(\psi_y(s) + \phi_y^0\right), \tag{3.18a}$$

$$y'(s) = -\frac{\sqrt{\tilde{\varepsilon}_y}}{\sqrt{\beta_y(s)}}\left[\alpha_y \cos\left(\psi_y(s) + \phi_y^0\right) + \sin\left(\psi_y(s) + \phi_y^0\right)\right], \tag{3.18b}$$

where $\beta_y(s)$ is the vertical beta function and

$$\psi_y(s) = \int_{\hat{s}=0}^{s} \frac{1}{\beta_y(\hat{s})} d\hat{s}$$

is the vertical phase advance. We also defined

$$\alpha_y(s) = -\frac{\beta_y'(s)}{2}.$$

Both $\tilde{\varepsilon}_y$ and ϕ_y^0 are constants defined by the initial conditions. The steps to obtain this solution using the Floquet theorem can be found in Ref. [24]. The unperturbed uncoupled motion of a proton in the vertical plane is therefore a pseudo cosine curve (called betatron oscillation) for which both amplitude and frequency vary along the longitudinal coordinate s. The amplitude $\sqrt{\tilde{\varepsilon}_y \beta_y(s)}$ of these betatron oscillations follows the variation of the local β-function, whereas the frequency of the oscillations varies with the phase advance $\psi_y(s)$. One betatron oscillation is performed when the phase advance amounts to 2 π. The number of betatron oscillations performed by the proton in one turn - defined as the proton vertical tune Q_y - can therefore be calculated from the total phase advance accumulated over one turn:

$$Q_y = \frac{\psi(s+L) - \psi(s)}{2\pi} = \frac{1}{2\pi}\int_{s}^{s+L} \frac{1}{\beta_y(s)} ds, \tag{3.19}$$

where Q_y is the vertical tune, and L is the length of the design orbit. As an illustration, the vertical tune of the proton's orbit sketched in Fig. 3.2 happens to be $5 < Q_y < 6$. Besides, using equations 3.18a and 3.18b, it can be checked that the following equation

$$\frac{1}{\beta_y(s)}\left[y^2(s) + \beta_y(s)y'(s) + \alpha_y(s)y(s)\right] = \tilde{\varepsilon}_y$$

holds. Defining the parameter $\gamma_y(s)$

$$\gamma_y(s) = \frac{1 + \alpha_y^2(s)}{\beta_y(s)}$$

we can write:

$$\gamma_y(s)y^2(s) + 2\alpha_y(s)y(s)y'(s) + \beta_y(s)y'^2(s) = \tilde{\varepsilon}_y. \tag{3.20}$$

Equation (3.20) is the implicit equation of an ellipse of constant area $\pi\tilde{\varepsilon}_y$ in the phase space plane (y, y'). Along the design orbit, this phase space ellipse may vary in shape and orientation, but its area remains $\tilde{\varepsilon}_y$. An ensemble of protons injected in a machine has a distribution of initial amplitudes y and angles y'. This initial phase space distribution can be characterized by its beam size $\sigma_y(0)$, and its beam divergence $\sigma_y'(0)$. Along the accelerator, each proton therefore traces an ellipse of different area $\tilde{\varepsilon}_y$ in the (y, y') phase space. The 95% transverse emittance $\varepsilon_y^{95\%}$ is defined by the phase space ellipse that contains 95% of the ellipse trajectories of all protons. In addition, in the present case of an unperturbed uncoupled unaccelerated proton in a linear lattice assuming zero dispersion (see next paragraph for the description of dispersion), the r.m.s. vertical emittance ε_y (related to 95% emittance by $\varepsilon_y^{95\%} \approx 6\,\varepsilon_y$ for a Gaussian beam) is a constant of motion and depends only on the initial vertical beam size $\sigma_y(0) = \sqrt{\varepsilon_y \beta_y(0)}$ and divergence $\sigma'_y(0) = \sqrt{\varepsilon_y \gamma_y(0)}$. The vertical r.m.s. beam size $\sigma_y(s)$ and beam divergence $\sigma_{y'}(s)$ along the accelerator are then given by

$$\sigma_y(s) = \sqrt{\varepsilon_y \beta_y(s)} \quad \text{and} \quad \sigma_{y'}(s) = \sqrt{\varepsilon_y \gamma_y(s)}. \tag{3.21}$$

It is interesting to note at this point that the transverse emittance of an accelerated proton is not a constant of motion. In this case, the Liouville theorem can be used to prove that the normalized emittance $\varepsilon_N = \varepsilon\beta\gamma$ is conserved. As a consequence, in a chain of accelerators such as the LHC complex, the beam emittance shrinks with energy, requiring larger aperture and/or different optics at lower energy than higher energy. Now that many fundamental parameters of the motion of an unperturbed uncoupled unaccelerated proton in a linear lattice have been defined, let us now consider the case of an off-momentum proton.

Solution of Hill's Equation with Momentum Error

With Eq. (3.17a), considering a proton with a given momentum error Δp leads to solve the inhomogeneous Hill equation in the horizontal plane. The general solution for the trajectory $x(s)$ is then the sum of the homogeneous solution found in the previous paragraph and a particular solution that can be a complicated function of s, depending on the lattice of the machine. This particular solution normalized by the momentum spread $\Delta p/p_0$ is defined as the dispersion $D(s)$. Therefore an off-momentum proton will perform betatron oscillations around the closed orbit determined by the dispersion multiplied by its momentum spread. Coming back further to Eq. (3.15), if we do not neglect the second order term in $x\Delta p$ and write

$$k(s) = \frac{eg(s)}{p} = \frac{eg(s)}{p_0}\left(1 - \frac{\Delta p}{p_0}\right) = k_0(s) + \Delta k(s),$$

we can conclude that a proton with a momentum deviation feels a different transverse focusing strength. This different focusing strength causes a change in the number of oscillations per turn for the off momentum proton, i.e. a tune shift ΔQ with respect to the tune Q_0 of the design proton. This tune shift due to momentum spread is a crucial parameter in the study of transverse instabilities and it can be characterized by the chromaticity ξ

$$\frac{\Delta Q}{Q_0} = \xi \frac{\Delta p}{p_0}. \tag{3.22}$$

Solution of Hill's Equation with Magnetic Errors

Magnet powering and magnet alignment imperfections also perturb the proton motion. Dipole errors change the closed orbit and quadrupole errors cause a tune shift and modify the design β-function. These inevitable imperfections also lead to resonant losses, a major concern for all operating synchrotrons. To give an idea of how these single particle losses occur, let us assume for simplicity that the focusing term in Hill equations is constant (smooth approximation). In the vertical plane for instance, we have Eq. (3.17b), which is the equation of a linear undamped oscillator with resonant wavenumber $\kappa_0 = \sqrt{K_v}$. In this simpler case, the phase advance is $\psi(s) = \kappa_0 s$ and the tune is

$$Q_y = \sqrt{K_v} R = \sqrt{K_v} \frac{L}{2\pi} = \sqrt{K_v} \frac{\beta c}{\omega_0},$$

where we recall that R is the radius of the machine, L is the length of the machine, and ω_0 is the angular revolution frequency of the particle. We can therefore write the unperturbed single particle equation of motion as

$$y''(s) + \left(\frac{2\pi Q_y}{L}\right)^2 y(s) = 0 \qquad \text{with solution} \qquad y_0(s) = A\cos\left(\frac{2\pi Q_y}{L} s + \phi_A\right), \tag{3.23}$$

where A and ϕ_A are constants. A magnet error can then be treated as a perturbation force F driving the oscillator [27]:

$$y''(s) + \left(\frac{2\pi Q_y}{L}\right)^2 y(s) = \frac{F}{m_0 \gamma \beta^2 c^2}. \tag{3.24}$$

For instance, a localized horizontal dipole error ΔB_x over length l gives the same vertical angle kick $\Delta y'$

$$\Delta y' = -\frac{e \Delta B_x l}{m_0 \gamma v_s}$$

to the proton at each turn. The force generated by this dipole error at location s_0 can be represented by a periodic Dirac delta function $\delta(s - s_0)$. Using the Fourier series of this Dirac comb, we get

$$\begin{aligned} y''(s) + \left(\frac{2\pi Q_y}{L}\right)^2 y(s) &= -\delta(s - s_0) \frac{e l \Delta B_x}{m_0 \gamma v_s} \\ &= -\frac{e l \Delta B_x}{L m_0 \gamma v_s} \sum_{r=-\infty}^{+\infty} \cos\left(\frac{2\pi r s}{L}\right). \end{aligned} \tag{3.25}$$

The driving term in the r.h.s. contains wavenumber components that are multiples of $\kappa = 2\pi/L$. As a consequence, choosing a lattice so that the tune Q_y is an integer puts the resonator wavenumber κ_0 exactly at one of the frequencies of the driving perturbation. In the absence of damping, the motion is unstable and the proton is eventually lost. Similarly, a localized vertical quadrupole focusing strength error ΔK_v over length l gives at each turn the vertical angle kick $\Delta y' = l \Delta K_v y(s)$ to the proton

$$\begin{aligned} y''(s) + \left(\frac{2\pi Q_y}{L}\right)^2 y(s) &= \delta(s - s_0) l \Delta K_v y(s) \\ &= \frac{l \Delta K_v}{L} \sum_{r=-\infty}^{+\infty} \cos\left(\frac{2\pi r s}{L}\right) y(s). \end{aligned} \tag{3.26}$$

But assuming the error is a perturbation of the motion, we can write

$$y(s) \approx y_0(s) = A \cos\left(\frac{2\pi Q_y}{L} s + \phi_A\right)$$

in the right hand side of Eq. (3.26) and use trigonometric identities to obtain

$$y''(s) + \left(\frac{2\pi Q_y}{L}\right)^2 y(s) = \frac{l \Delta K_v A}{2L} \sum_{r=-\infty}^{+\infty} \left[\cos\left(\frac{2\pi(r+Q_y)s}{L}\right) + \cos\left(\frac{2\pi(r-Q_y)s}{L}\right)\right], \tag{3.27}$$

where we discarded the constant phase ϕ_A that only adds other terms and changes constant A. The resonance condition now becomes $Q_y = r \pm Q_y$, leading to $Q_y = r/2$. As a consequence, choosing a lattice so that the tune Q_y is an half integer puts the resonator frequency κ_0 exactly at one of the frequencies of the driving perturbation, which would again be very detrimental to the beam. A thorough treatment of resonances [30] shows that resonances occur as soon as the following equation is satisfied:

$$mQ_x + nQ_y = l. \tag{3.28}$$

where m, n and l are integers. Since the rationals are dense in the reals, it is not possible to stay away from all resonances. However, the larger the resonance order, the smaller the effect on the beam. Resonances up to the 11th order are taken into account in a proton machine such as the LHC. Besides, mechanisms such as chromaticity, non linear effects and collective effects create a tune spread in both transverse planes. The working point of a machine (operating values of Q_x and Q_y) is chosen so that the transverse tunes footprint avoids as much as possible crossing low order resonances. Resonance crossing due to large transverse tune spread is a major concern for low energy machines such as the PS Booster.

Many fundamental notions of transverse linear beam dynamics have been introduced. Let us now study the motion in the longitudinal plane, that we only introduced until now through the proton design momentum and momentum error.

3.2.2 Longitudinal Synchrotron Motion

From Eq. (3.4b), the acceleration of protons can be performed with a longitudinal electric field E_s. Larger fields can be reached with radio frequency (RF) fields than electrostatic fields and this is why electric fields in synchrotrons are generally obtained with a system of RF cavities. As will be seen in section 6, understanding the longitudinal motion (also called synchrotron motion) is important to the study of transverse instabilities of bunched beams. This section aims at deriving the equations of motion of protons in the longitudinal plane. Refs. [26] and [31] were very useful in understanding the longitudinal single particle dynamics. First we need to define the longitudinal electric field that will accelerate the protons, assuming for simplicity that there is only one RF cavity in the ring.

Longitudinal Electric Field in an RF Cavity

In the gap of an ideal RF cavity, the oscillating longitudinal electric field $E_s(t)$ felt by a proton with a phase ϕ with respect to the phase of the RF cavity voltage $\phi_{\text{rf}}(t) = \omega_{\text{rf}} t$ can be written

$$E_s(t) = \frac{V}{g} \sin\left(\phi_{\text{rf}}(t) + \phi\right), \tag{3.29}$$

where ω_{rf} is the RF voltage angular frequency, V is the cavity voltage amplitude assumed to be constant over the cavity gap g. Since the electric field in the cavity oscillates with time, the proton feels a varying electric field between its time of entrance in the gap and its time of exit of the gap. In a synchrotron, the RF cavity is designed to accelerate the reference proton each time it passes through the gap. Therefore the RF phase has to be tuned to give a positive longitudinal kick to the reference proton at each turn (i.e. with a proton revolution period $L/(\beta c)$). The reference proton is also called the synchronous particle as it is designed to always come back to the RF cavity with the same phase $\phi = \phi_0$ with respect to the RF phase[1]. The RF voltage angular frequency ω_{rf} is then chosen as an integer multiple h of the design angular revolution frequency ω_0

$$\omega_{\text{rf}} = h\omega_0. \tag{3.30}$$

This harmonic number h indicates the maximum number of bunches that can be accelerated in the machine. In the SPS, $h = 4620$ and the current scheme for the LHC beam is composed of 4 batches of 72 bunches. In the LHC $h = 35640$ and 2808 bunches per ring are scheduled to be accelerated. It is now interesting to calculate the boost a proton gets as it passes through this cavity.

Energy Gain in an RF Cavity

The energy gain per turn $\Delta\mathcal{E}$ of a particle of charge e passing through an RF cavity is equal to the work of the Lorentz force Eq. (3.4b) felt by the proton over the gap g of the RF cavity:

$$\Delta\mathcal{E} = e\int_{s=-g/2}^{g/2} E_s(s)ds = e\int_{t=t_{\text{entrance}}}^{t_{\text{exit}}} E_s(t)\beta c dt. \tag{3.31}$$

The velocity increase per turn is assumed small compared to the longitudinal proton velocity $v = \beta c$ (i.e. the acceleration is slow compared to the revolution period). If the studied proton is in the middle of the RF cavity gap at time $t = 0$, we have

$$\Delta\mathcal{E} = e\beta c\frac{V}{g}\int_{t=-g/(2\beta c)}^{g/(2\beta c)} \sin\left(h\omega_0 t + \phi\right) dt, \tag{3.32}$$

which gives

$$\Delta\mathcal{E} = e\hat{V}\sin\phi, \tag{3.33}$$

when expanding the sine, integrating over time t, and defining the effective voltage as $\hat{V} = TV$ and the transit time factor as

$$T = \frac{\sin\left(\frac{h\omega_0 g}{2\beta c}\right)}{\frac{h\omega_0 g}{2\beta c}}.$$

---

[1] The synchronous phase ϕ_0 is also often referred to as ϕ_s in the literature.

In the absence of other sources of energy change, the energy rate $d\mathcal{E}/dt$ is related to the energy gained per turn

$$\frac{d\mathcal{E}}{dt} = \frac{\omega}{2\pi}\Delta\mathcal{E},$$

where ω is the angular revolution frequency of the proton. The energy rate is therefore given by

$$\frac{d\mathcal{E}}{dt} = \frac{\omega}{2\pi}e\hat{V}\sin\phi. \tag{3.34}$$

Equation (3.34) contains the revolution frequency ω and before we carry on, we need to link a change in momentum to a change in revolution frequency in order to obtain the equations of longitudinal motion. To this end, the momentum compaction and the phase slip factors are introduced.

Closed Orbit Length Change with Momentum (Momentum Compaction)

We have already mentioned in Section 3.2.1 (p. 22) that a momentum deviation changes the shape of the closed orbit and therefore its length L. This closed orbit length change $\Delta L = L - L_0$ due to momentum is characterized by the momentum compaction factor α_{cp}

$$\alpha_{\mathrm{cp}} = \frac{\Delta L/L_0}{\Delta p/p_0}. \tag{3.35}$$

The closed orbit circumference L_0 of the trajectory for an on-momentum proton is

$$L_0 = \oint ds = \oint \rho(s)d\theta.$$

From the definition of the dispersion $D(s)$ (p. 22), a proton with a small momentum deviation Δp is characterized by the trajectory $x_D(s) = D(s)\Delta p/p_0$ with bending radius $R(s) = \rho(s) + x_D(s)$. The dispersion orbit length L_D is then expressed along its own curvilinear coordinate s_D by

$$L_D = \oint ds_D = \oint (\rho(s) + x_D(s))d\theta = \oint \left(1 + \frac{x_D(s)}{\rho(s)}\right) ds = L_0 + \Delta L.$$

We can then find an expression for the momentum compaction factor:

$$\frac{\Delta L}{L} = \alpha_{\mathrm{cp}}\frac{\Delta p}{p_0}\ \text{, with } \alpha_{\mathrm{cp}} = \frac{1}{L}\oint \frac{D(s)}{\rho(s)}ds. \tag{3.36}$$

In most accelerators, a positive momentum deviation increases the length of the closed orbit trajectory, which means α_{cp} is in general positive. However, negative momentum compaction lattices can be obtained and studies are in fact underway to use a negative momentum compaction factor in the future PS2 in order to avoid crossing transition. Now that the momentum compaction factor α_{cp} has been obtained, we can define the phase slip factor η, a fundamental parameter of longitudinal motion.

Revolution Frequency Change with Momentum and Transition Energy

The phase slip factor η is here defined as (it is important to note that different conventions for the sign of η are commonly used)

$$\eta = -\left(\frac{\Delta\omega/\omega_0}{\Delta p/p_0}\right). \tag{3.37}$$

We will now express η as a function of the momentum compaction factor α_{cp} and the proton energy. Differentiating the logarithm of the expression of the angular revolution frequency $\omega = \beta c/R$ gives

$$\frac{d\omega}{\omega} = \frac{d\beta}{\beta} - \frac{dR}{R} = \frac{1}{\gamma^2}\frac{dp}{p} - \frac{dR}{R},$$

where we used

$$d\beta/\beta = (1-\beta^2)dp/p = (1/\gamma^2)dp/p.$$

Using $dR/R = dL/L$, as well as Eq. (3.35) and assuming small deviations from synchronous parameters, we can write

$$\eta = \alpha_{\mathrm{cp}} - \frac{1}{\gamma^2}. \tag{3.38}$$

In the case of today's LHC complex synchrotrons, a momentum increase leads to both a velocity increase and a bending radius increase: the proton moves faster but its orbit length increases. These two contributions to the angular frequency are acting against each other. In fact, η switches sign at

$$\gamma_t = \sqrt{1/\alpha_{\mathrm{cp}}}$$

in Eq. (3.38). That special energy $m_0\gamma_t c^2$ for which $\eta = 0$ is called the transition energy.

- $\gamma < \gamma_t$ leads to $\eta < 0$ and a momentum increase leads to a revolution frequency increase.
- $\gamma > \gamma_t$ leads to $\eta > 0$ and a momentum increase leads to a revolution frequency decrease.
- $\gamma = \gamma_t$ leads to $\eta = 0$ and a momentum change does not affect the revolution frequency (to first order).

Crossing transition in an accelerator requires a lot of care in order to avoid deterring the quality of the beam. The LHC beam crosses transition neither in the SPS nor in the LHC, but it does in the PS. Constant operating issues during transition crossing forces the PS2 project team to consider using a negative momentum compaction factor to avoid crossing transition, but at the expense of a more complicated lattice [32]. The relative change of closed orbit length and revolution frequency due to momentum change have been defined and the longitudinal equations of motion can now be obtained.

1st Longitudinal Equation of Motion

The parameters of a non synchronous proton (momentum p, orbital angle θ, phase ϕ, angular frequency ω, closed orbit radius R and energy $\mathcal{E}$) are assumed to be a small deviation from the parameters of the synchronous proton (p_0, θ_0, ϕ_0, ω_0, closed orbit radius $R_0 = \rho$ and energy $\mathcal{E}_0$):

$$\begin{aligned} p &= p_0 + \Delta p, \\ \theta &= \theta_0 + \Delta\theta, \\ \phi &= \phi_0 + \Delta\phi, \\ \omega &= \omega_0 + \Delta\omega, \\ R &= R_0 + \Delta R, \\ \mathcal{E} &= \mathcal{E}_0 + \Delta\mathcal{E}. \end{aligned}$$

For a proton lagging behind the synchronous proton by a time $\Delta t = t - t_0$, we can write that the orbital angle difference is $\Delta\theta = -\omega_0 \Delta t$ (to first order). This proton comes at a later time to the center of the RF cavity and therefore its phase ϕ with respect to the RF phase is larger than for the synchronous proton $\Delta\phi = h\omega_0\Delta t$. Then, we have $\Delta\phi = -h\Delta\theta$, and we can write

$$\Delta\omega = \frac{d(\Delta\theta)}{dt} = -\frac{1}{h}\frac{d(\Delta\phi)}{dt} = -\frac{1}{h}\frac{d\phi}{dt}, \tag{3.39}$$

since the phase of the synchronous proton ϕ_0 is assumed to change slowly with time compared to the phase ϕ. Using the phase slip factor η (Eq.(3.37)) one obtains

$$\Delta p = -\frac{p_0}{\eta\omega_0}\Delta\omega = \frac{p_0}{\eta h \omega_0}\frac{d\phi}{dt}. \tag{3.40}$$

Differentiating $\mathcal{E}^2 = \mathcal{E}_0^2 + p^2c^2$ gives $d\mathcal{E} = vdp$, and from small deviations we have $\Delta\mathcal{E} = v\Delta p = \beta_0 c\Delta p = \omega_0 R_0 \Delta p$. We can then rewrite Eq.(3.40):

$$\frac{\Delta\mathcal{E}}{\omega_0} = \frac{R_0 p_0}{\eta h \omega_0}\frac{d\phi}{dt}. \tag{3.41}$$

This is the first longitudinal equation of motion with variables $\Delta\mathcal{E}/\omega_0$ and ϕ.

2nd Longitudinal Equation of Motion

The second equation of motion can be obtained starting from Eq. (3.33) and using $\Delta\mathcal{E} = v\Delta p$:

$$\Delta p = \frac{e\hat{V}}{\omega R}\sin\phi. \tag{3.42}$$

Assuming again that the momentum increase per turn is small compared to the momentum, we can write

$$\frac{dp}{dt} = \frac{\Delta p}{T} = \frac{e\hat{V}}{2\pi R}\sin\phi, \tag{3.43}$$

which, for the particular case of the synchronous particle, gives

$$2\pi R_0 \frac{dp_0}{dt} = e\hat{V}\sin\phi_0, \tag{3.44}$$

so that we can write the difference of Eq. (3.43) and 3.44 as

$$2\pi\left(R\frac{dp}{dt}-R_0\frac{dp_0}{dt}\right)=e\hat{V}\left(\sin\phi-\sin\phi_0\right). \tag{3.45}$$

The bending radius R and momentum p of the non synchronous proton can be expressed as deviations from the synchronous proton and only first order terms are kept so that the left hand side factor can be worked out as:

$$R\frac{dp}{dt}-R_0\frac{dp_0}{dt}=(R_0+\Delta R)\left(\frac{dp_0}{dt}+\frac{d\Delta p}{dt}\right)-R_0\frac{dp_0}{dt}=\Delta R\frac{dp_0}{dt}+R_0\frac{d\Delta p}{dt}.$$

Using the momentum compaction factor definition for any particle and for the specific case of the synchronous particle, we have to first order

$$\alpha_{\mathrm{cp}}R_0/p_0=\Delta R/\Delta p\approx dR/dp\approx dR_0/dp_0.$$

Therefore we can use $\Delta R=(dR_0/dp_0)\,\Delta p$ and finally

$$R\frac{dp}{dt}-R_0\frac{dp_0}{dt}=\frac{dR_0}{dp_0}\frac{dp_0}{dt}\Delta p+R_0\frac{d\Delta p}{dt}=\frac{dR_0}{dt}\Delta p+R_0\frac{d\Delta p}{dt}=\frac{dR_0\Delta p}{dt}=\frac{d\frac{\Delta\mathcal{E}}{\omega_0}}{dt}.$$

Coming back to Eq. (3.45), we can write the second longitudinal equation of motion

$$2\pi\frac{d\frac{\Delta\mathcal{E}}{\omega_0}}{dt}=e\hat{V}\left(\sin\phi-\sin\phi_0\right). \tag{3.46}$$

The longitudinal equations of motion are therefore

$$\frac{\Delta\mathcal{E}}{\omega_0}=\frac{R_0p_0}{\eta h\omega_0}\frac{d\phi}{dt}, \tag{3.47a}$$

$$2\pi\frac{d\frac{\Delta\mathcal{E}}{\omega_0}}{dt}=e\hat{V}\left(\sin\phi-\sin\phi_0\right). \tag{3.47b}$$

Substituting $\frac{\Delta\mathcal{E}}{\omega_0}$ from Eq. (3.47a) into Eq. (3.47b), we obtain a second order nonlinear equation of motion for the phase.

$$\frac{d}{dt}\left(\frac{R_0p_0}{\eta h\omega_0}\frac{d\phi}{dt}\right)-\frac{e\hat{V}}{2\pi}\left(\sin\phi-\sin\phi_0\right)=0. \tag{3.48}$$

The equation of adiabatic longitudinal motion can be obtained if one considers that the parameters of the synchronous trajectory (R_0, p_0, ω_0 and η) are changing slowly with time

$$\ddot{\phi}-\frac{e\hat{V}\eta h\omega_0}{2\pi R_0p_0}\left(\sin\phi-\sin\phi_0\right)=0. \tag{3.49}$$

An analytic solution of Eq. (3.49) can be found for small amplitude oscillations. This analytical solution will be compared to the numerical solution of Eq (3.48) for the case of the PS.

Small Amplitude Synchrotron Oscillations in the Adiabatic Regime

For small phase oscillations we can afford to keep only first order terms in $\Delta\phi = \phi - \phi_0$, and we can write

$$\begin{aligned}\sin\phi - \sin\phi_0 &= \sin(\phi_0 + \Delta\phi) - \sin\phi_0 = \sin\phi_0\cos\Delta\phi + \sin\Delta\phi\cos\phi_0 - \sin\phi_0 \\ &= \Delta\phi\cos\phi_0 + o(\Delta\phi).\end{aligned}$$

Using the adiabatic assumption that accounts for ϕ_0 changing very slowly with time, the linearized equation of longitudinal motion is

$$\frac{d^2\Delta\phi}{dt^2} - \frac{e\hat{V}\cos\phi_0\eta h\omega_0}{2\pi R_0 p_0}\Delta\phi = 0, \tag{3.50}$$

and the synchrotron motion is stable only if $\eta\cos\phi_0 < 0$ as all other parameters are positive if we consider proton acceleration. In this stable case, we can define the synchrotron angular frequency ω_s

$$\omega_s = \sqrt{\frac{e\hat{V}h\omega_0\left|\eta\cos\phi_0\right|}{2\pi R_0 p_0}}, \tag{3.51}$$

and the synchrotron tune $Q_s = \omega_s/\omega_0$

$$Q_s = \sqrt{\frac{e\hat{V}h\left|\eta\cos\phi_0\right|}{2\pi v_0 p_0}}. \tag{3.52}$$

Multiplying Eq. (3.50) by $\frac{d(\Delta\phi)}{dt}$, and integrating over time t gives a constant of synchrotron motion:

$$\left(\frac{d\left(\Delta\phi\right)}{dt}\right)^2 + \omega_s^2\left(\Delta\phi\right)^2 = \text{constant}. \tag{3.53}$$

The acceleration is assumed adiabatic and we can write $\frac{d(\Delta\phi)}{dt} = \dot{\phi}$. Substituting $\dot{\phi}$ into Eq. (3.53) thanks to Eq. (3.47a), we obtain

$$\left(\frac{\Delta\mathcal{E}}{\omega_0}\right)^2 + \left(\frac{Q_s R_0 p_0}{\eta h}\right)^2\left(\Delta\phi\right)^2 = \text{constant}. \tag{3.54}$$

As for the transverse betatron motion, the linearized synchrotron motion is an ellipse in the phase space $(\phi, \Delta\mathcal{E}/\omega_0)$ centered on $(\phi_0, 0)$ with maximum phase and energy excursions related by

$$\left(\Delta\phi\right)_{max} = \frac{\left|\eta\right| h}{Q_s R_0 p_0}\left(\Delta\mathcal{E}/\omega_0\right)_{max}. \tag{3.55}$$

The longitudinal emittance ε_l of a Gaussian bunch distribution with r.m.s. bunch length $\sigma_{\Delta\phi}$ and energy spread $\sigma_{\Delta\mathcal{E}/\omega_0}$ is defined as the ellipse area in the phase space $\left(\frac{\phi}{h}, \frac{\Delta E}{\omega_0}\right)$:

$$\varepsilon_l = \frac{4\pi}{h}\sigma_{\Delta\mathcal{E}/\omega_0}\sigma_{\Delta\phi}. \tag{3.56}$$

An injected proton distribution with r.m.s. bunch length

$$\sigma_{\Delta\phi} = \frac{\left(\Delta\phi\right)_{max}}{2},$$

and energy spread

$$\sigma_{\Delta\mathcal{E}/\omega_0} = \frac{(\Delta\mathcal{E}/\omega_0)_{max}}{2},$$

that satisfies linear matching equation Eq. (3.55) remains within the initial ellipse and its longitudinal emittance is conserved. We say that the bunch is matched to the longitudinal bucket. If the bunch is not matched to the bucket, it will oscillate and could filament, which would lead to a longitudinal emittance blow-up. It is important to notice that the longitudinal emittance is defined as the area covered by the proton distribution in the longitudinal phase space, whereas the transverse emittance is defined as the area covered by the proton distribution in the transverse phase space divided by π in Eq. 3.20. The solution of the linearized adiabatic synchrotron motion for an LHC-type bunch of longitudinal emittance $\varepsilon_l = 2$ eVs at energies around transition energy ($\gamma_t = 6.09$) in the PS is presented in green in Fig. 3.4. The other relevant PS parameters to obtain the synchrotron motion are:

- the momentum compaction factor $\alpha_{cp} = 0.027$,
- the voltage $V = 0.2$ MV,
- the harmonic number $h = 8$,
- the design orbit radius $R_0 = 100$ m,
- the linear rate of change of momentum $\dot{p} = 46$ GeV/c/sec during acceleration.

Remembering that $\sin\phi_0 > 0$ is needed to give a positive acceleration the synchronous proton (see Eq.(3.44)), and $\eta\cos\phi_0 < 0$ is needed for stable synchrotron motion, we can write

- below transition, $\eta < 0$ so we need $\cos\phi_0 > 0$ for stable motion, i.e. $\phi_0 \in \left]0; \frac{\pi}{2}\right[$,
- above transition, $\eta > 0$ so we need $\cos\phi_0 < 0$ for stable motion, i.e. $\phi_0 \in \left[\frac{\pi}{2}; \pi\right[$.

As a consequence, the RF phase must be quickly flipped from ϕ_0 to $\pi - \phi_0$ when crossing transition to avoid unstable longitudinal motion. When the amplitude of the synchrotron motion is large, the linear assumption does not hold anymore, and the elliptical linear motion in synchrotron phase space is distorted by the non linear terms.

Large Amplitude Synchrotron Oscillations in the Adiabatic Regime

Coming back to Eq. (3.49), and using the definition of the synchrotron tune in Eq. (3.52), we can write

$$\ddot{\phi} + \frac{\omega_s^2}{\cos\phi_0}(\sin\phi - \sin\phi_0) = 0. \tag{3.57}$$

This non linear equation was solved numerically using Mathematica and is compared to the linear small amplitude approximation in Fig. 3.4. Finally, another important parameter is the phase space area available for stable longitudinal motion. This available area is called the RF acceptance (bucket), and corresponds to the maximum possible longitudinal emittance.

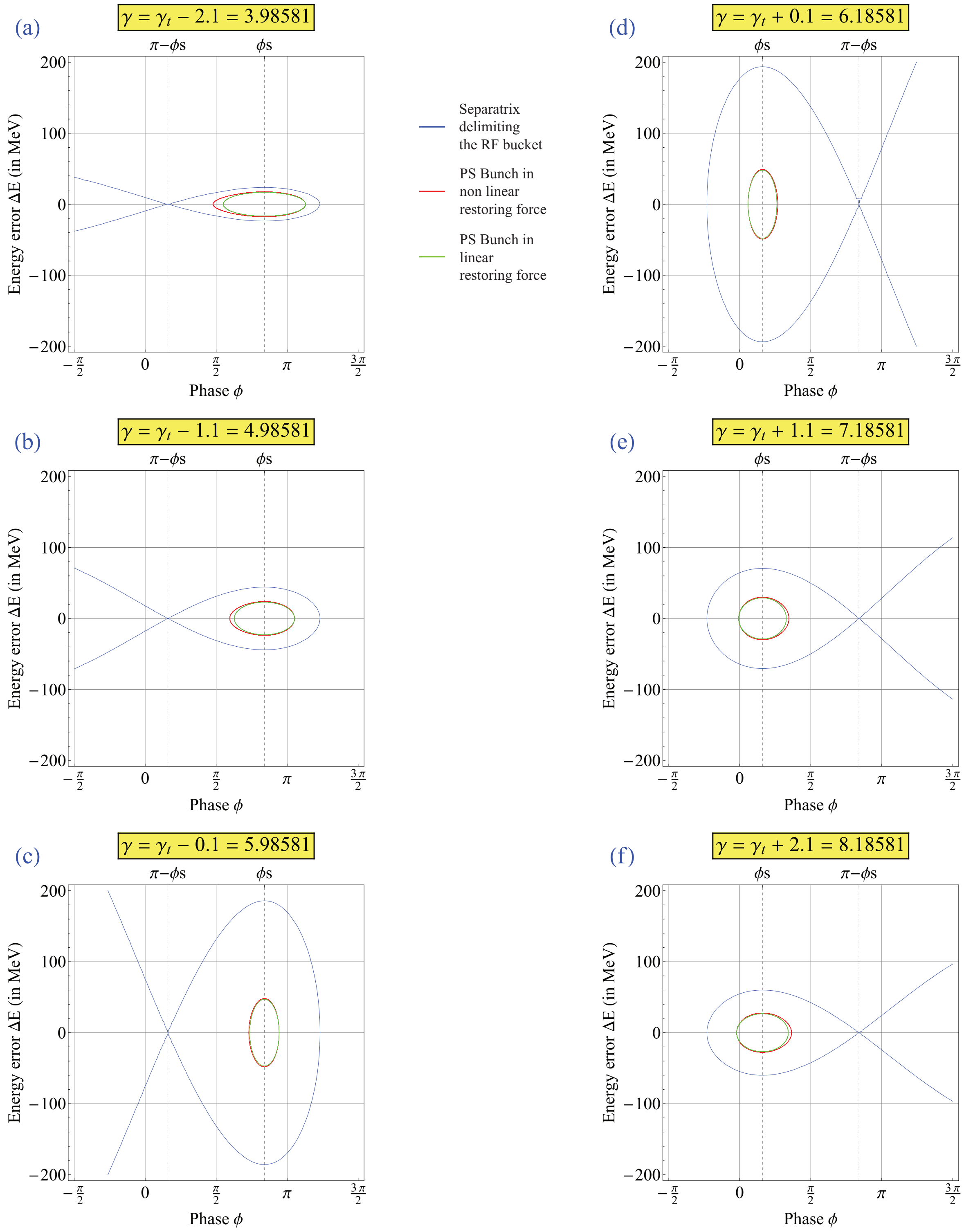

Figure 3.4: Representations of the areas in longitudinal phase space covered by the PS bunch and PS bucket with increasing beam energy from (a) to (f), crossing transition between (c) and (d): bunch area for a linear restoring force (green line), for a non linear restoring force (red line) of a proton corresponding to an emittance of 2 eV.s – calculated in the linear assumption –, and separatrix delimiting the RF bucket (blue line). Relevant PS parameters: $\alpha_{cp} = 0.027$, $V = 0.2$ MV, $h = 8$, $R_0 = 100$ m, and $\dot{p} = 46$ GeV/c/sec.

RF Bucket and Longitudinal Emittance

Let us find the equation of the separatrix, the curve that bounds the stable area of phase space and defines the bucket. Multiplying Eq. (3.57) by $\dot{\phi}$, and integrating over time t gives the following constant of synchrotron motion

$$\frac{\dot{\phi}^2}{2} - \frac{\omega_s^2}{\cos\phi_0}\left(\cos\phi + \phi\sin\phi_0\right) = \text{Constant.} \tag{3.58}$$

To find that constant of motion for the separatrix, we just need to find the phase space coordinates of one point that belongs to the separatrix. Assuming stable motion of the synchronous proton ($\eta\cos\phi_0 < 0$), and positive acceleration ($\sin\phi_0 > 0$), we observe that the second term in Eq. (3.57) corresponds to an attractive force only if $\sin\phi - \sin\phi_0$ is of the same sign as $\phi - \phi_0$, i.e. only if $\phi < \pi - \phi_0$. If $\phi > \pi - \phi_0$ the force is repulsive and the synchrotron motion is unstable. In addition, from the equations of synchrotron motion Eq. (3.47b), the phase space point $(\phi = \pi - \phi_0, \Delta\mathcal{E}/\omega_0 = 0)$ is a fixed point and therefore belongs to the separatrix. Its coordinates can then be used to define the separatrix from Eq. (3.58).

$$\frac{\dot{\phi}^2}{2} - \frac{\omega_s^2}{\cos\phi_0}\left(\cos\phi + \phi\sin\phi_0\right) = -\frac{\omega_s^2}{\cos\phi_0}\left(\cos\left(\pi - \phi_0\right) + \left(\pi - \phi_0\right)\sin\phi_0\right). \tag{3.59}$$

This separatrix equation can be solved numerically and is shown in blue for typical SPS parameters at injection in Fig. 3.5, and for PS parameters for the LHC bunch around transition in Fig. 3.4. Besides the fact that the synchrotron motion with linear forces is

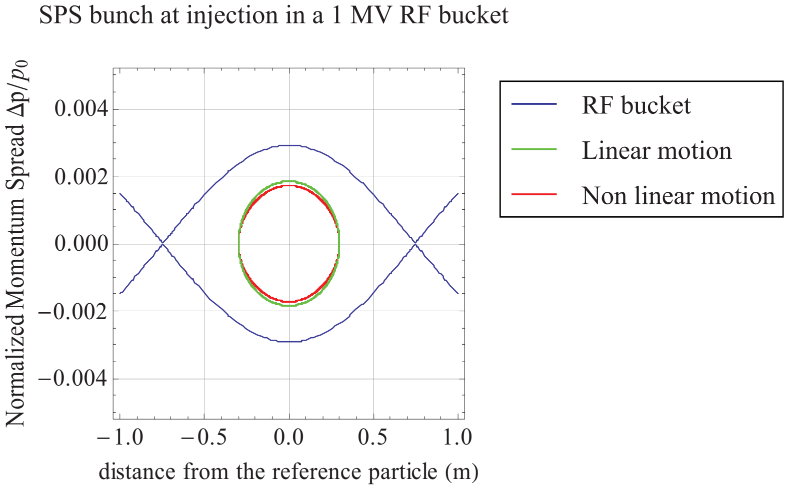

Figure 3.5: SPS longitudinal synchrotron motion at injection : bunch area for a linear restoring force (green line), for a non linear restoring force (red line) of a proton corresponding to an emittance of 0.15 eV.s - calculated in the linear assumption -, and separatrix delimiting the stationary RF bucket (blue line). Relevant SPS parameters are presented in Tab. B.5 in the appendix of this manuscript.

close to the synchrotron motion with non linear forces in the case of a matched bunch that is small compared to the RF bucket area, Fig. 3.4 enables to realise interesting aspects of transition crossing. The synchronous phase brutal switch at transition requires a simultaneous quick change in RF phase of $\pi - 2\phi_0$. In addition, the height of the bucket increases significantly at transition, causing strong distortions to the bunch shape. For these reasons, transition crossing has to be carefully managed. The transverse and longitudinal motions have been described and their fundamental parameters have been defined. We can now study a perturbation to this motion caused by the interaction of the protons with themselves and their environment.

3.3 Wake Fields and Beam Coupling Impedances

As mentioned in the introductory chapter, the external electromagnetic fields needed to guide a proton beam in an accelerator are perturbed by the electromagnetic fields generated by the protons themselves. This field perturbation acts back on the proton beam and may affect its quality. The more protons the larger the perturbation of the fields and the larger the proton motion perturbation. This perturbation does not appear if a single particle is considered: it is a collective effect. Similarly to the study of single particle motion, the longitudinal and transverse collective effects are classically studied separately. Longitudinal collective effects perturb the longitudinal distribution, while transverse collective effects affect the transverse distribution. This discussion will focus in Chapter 6 on a specific type of collective effects, the Transverse Mode Coupling Instability (TMCI). In the literature, this collective effect is also called fast head-tail effect, strong head-tail instability, transverse turbulent instability, or transverse microwave instability, and is similar to the beam break up observed in linacs. TMCI is known to be one of the major limitations in electron storage rings. The mechanism of this instability can be intuitively understood as follows:

(a) Every ultrarelativistic particle in the bunch generates transverse electromagnetic fields proportional to its transverse displacement.

(b) These so-called transverse wakefields create a transverse force on the trailing particles.

(c) Turn after turn, this transverse force can resonantly excite the motion of the trailing particles and lead to coherent oscillations of growing amplitude, a coherent instability. Simplified models where the beam is represented by only two macroparticles which interact through a constant wake field (for instance in [33]) enable to realize that unstable motion can be achieved if the charge of the macroparticles is set beyond a given threshold.

(d) The bunched longitudinal motion leads particles in the tail of the bunch to be periodically exchanged with particles in the head of the bunch, thereby providing a damping mechanism for the instability. But this exchange can take much more time than the revolution period, so that particles are repeatedly excited by the wake fields. In the SPS for instance, it takes around $1/Q_s = 250$ turns to perform a full synchrotron oscillation, therefore half this number of turns to exchange the head and tail particles.

In view of this TMCI example, it becomes clear that these wake fields are the cause of collective effects, and their nature needs to be defined more precisely. In this task, the books by K.Y. Ng [34], A. Chao [33], B. Zotter and S.A. Kheifets [35], as well as the courses by T. Weiland and R. Wanzenberg [36] and by E. Métral and G. Rumolo [8] have been very useful. The reader is advised that the longitudinal coordinate notations s and z used in this chapter do not correspond to the notations used for single particle dynamics.

3.3.1 Wake Fields

The electromagnetic fields generated in the wake of a collection of moving charged particles are referred to as wake fields. These wake fields are a function of both observation location (x, y, s) and observation time t. They include the direct interaction of the beam particles with themselves (direct space charge field), but also the fields created by the interaction of these particles with their surrounding (indirect field). The direct space charge field leads to an internal force and does not affect the coherent motion of the bunch of particles. The indirect wake field generate an external force on the bunch, and may generate a coherent motion, as in the case of the TMCI. As an illustration of the wake fields, results of 3D CST Particle Studio [37] simulations of the electromagnetic fields generated by the passage of an ultrarelativistic positively charged bunch through a coarse model of a CLIC copper collimator (Fig. 3.6) are shown in Fig. 3.7 for the transverse electric field and Fig. 3.8 for the longitudinal electric field. *CST Particle Studio* is a commercial software tool used to

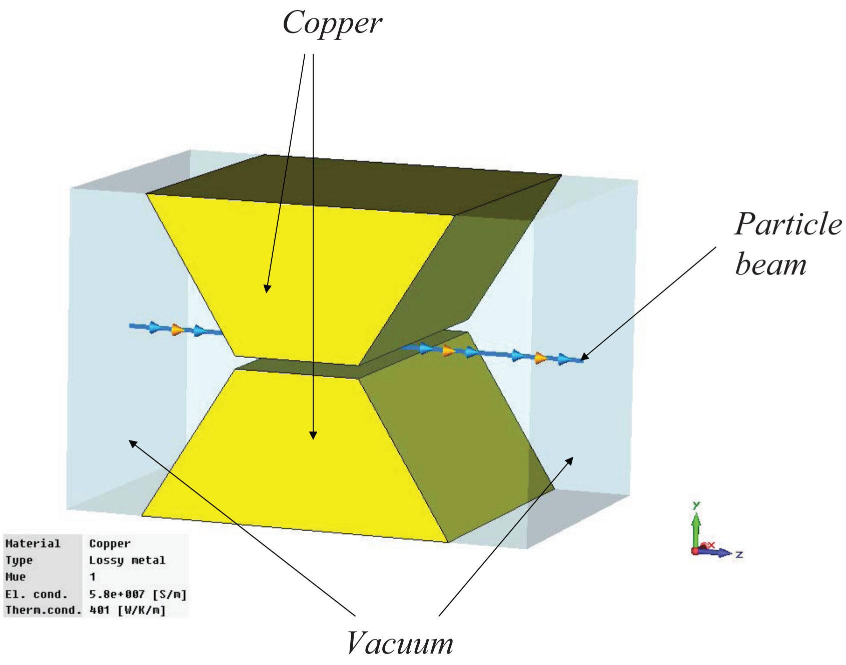

Material	Copper
Type	Lossy metal
Mue	1
El. cond.	5.8e+007 [S/m]
Therm.cond.	401 [W/K/m]

Figure 3.6: Model for a CLIC copper collimator for *CST Particle Studio* simulations. The bunch is along the z-axis, displaced vertically by 10 μm. Bunch length (r.m.s) $\sigma_z = 0.1$ mm; collimator dimensions: gap 0.1 mm, length 2 mm, length including taper 5 mm; Perfect conductor at the boundaries at (x,y)=±2.5 mm; Perfect matching layer at the boundaries z= ±3.75 mm.

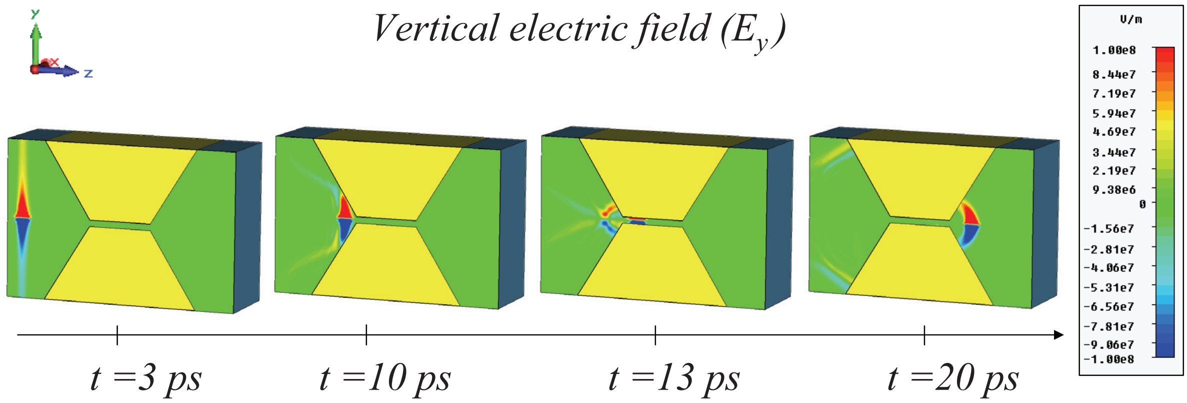

Figure 3.7: Simulated vertical electric wake field observed at various times t in the $x = 0$ plane. At $t = 3$ ps, the direct repulsive vertical electric fields created by the bunch can be clearly seen radiating from the bunch location. At $t = 10$ ps, the electric fields around the bunch get distorted by the collimator taper, and reflexions can be observed. At $t = 13$ ps, the bunch passes in the gap and the electric fields get squeezed in it while strong reflections waves gather and travel back upstream. At $t = 20$ ps, the bunch leaves the gap and the vertical electric fields pattern bends toward the copper taper surface while reflections waves upstream start to die out. After some time, the vertical electric field will resume its initial pattern.

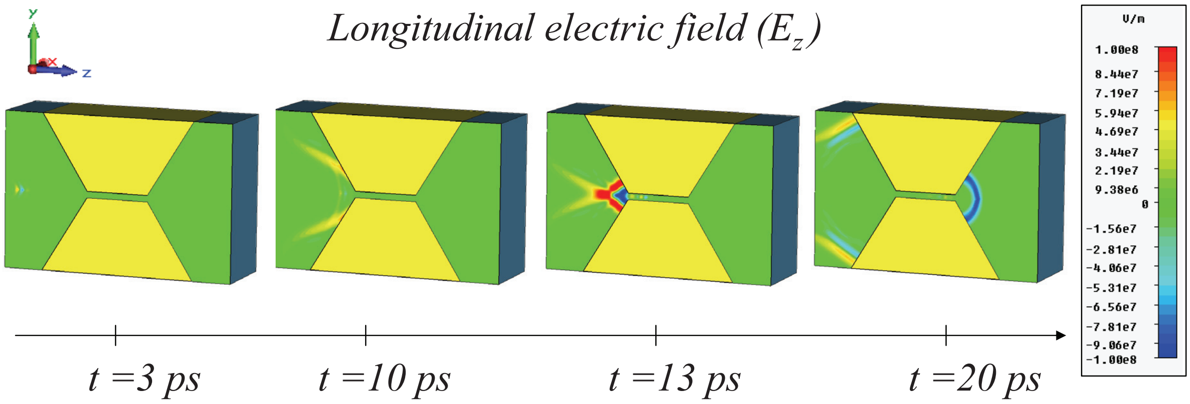

Figure 3.8: Simulated longitudinal electric wake field observed at various times t in the $x = 0$ plane. The position of the bunch is not obvious from the longitudinal electric field map alone, but is given away at the same time steps in Fig. 3.7. Since the particles are ultrarelativistic, the longitudinal wake fields are negligible before the bunch reaches the collimator ($t = 3$ ps). As the bunch passes through the collimator, strong reflections can be observed. Immediately behind the bunch, the wake electric fields are negative, therefore decelerating the positively charged particles.

compute electromagnetic fields in the surrounding of a modeled bunch of moving particles. Since the geometry of the bunch surrounding is in general complicated, it simplifies the problem by subdividing the volume into small homogeneous mesh cells in which Maxwell's equation can be solved analytically. The global simulated result is then obtained by summing up the contributions of all the mesh cells and solving the resulting large system of equations numerically. The obvious limitation of such volume discretization methods is that the total number of mesh cells is limited by the CPU memory, thereby restricting the volume which can be handled and limiting the high frequency resolution of the results. The parameters of the simulation therefore have to be set carefully, and the simulation results should be checked with thorough relevance and convergence studies. Coming back to Fig. 3.7 and Fig. 3.8, the incoming bunch of ultrarelativistic particles creates a large vertical electric field but negligible longitudinal electric field [33] in the rectangular perfect conductor beam pipe at time $t = 3$ ps. As can be seen at later times, the traversal of the collimator causes reflexions and strong distortions of the electromagnetic fields in the surrounding of the bunch. These distortions constitute wake fields of the collimator created by the Gaussian bunch. Even for such a simple structure, we can see that the wake fields show rather complicated features in time and space. In practice, it is assumed that a given accelerator element (RF cavity, bellow, magnets, etc. - see Fig. 3.9) creating the indirect wake is infinitely small in length, so that neither longitudinal nor transverse motions of the particles are affected during their passage through the element. This is also the case of the *CST* simulations: the source charge distribution itself is not affected by the electromagnetic fields it generates. In addition, since the particle velocity is assumed not to change during the traversal of the equipment, the wake force effect on a trailing particle (also called test particle) can be represented as an abrupt momentum change $\Delta\vec{p}$, also called a "kick" (see Fig. 3.10). In this case, we are not interested in the wake fields

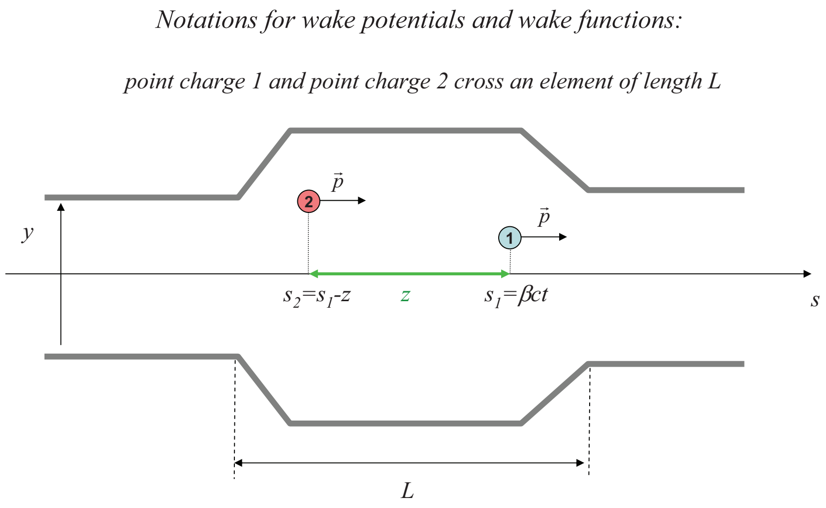

Figure 3.9: Notations used in the expressions of the wake potential $W(z)$ and the wake function $G(z)$: two point charges - charges q_1 and q_2, same longitudinal momentum $\vec{p}$ with q_2 following behind q_1 at a distance z - cross an accelerator element of length L.

everywhere at any time, but we focus on the integrated wake fields seen by a trailing particle following the source distribution with a given delay.

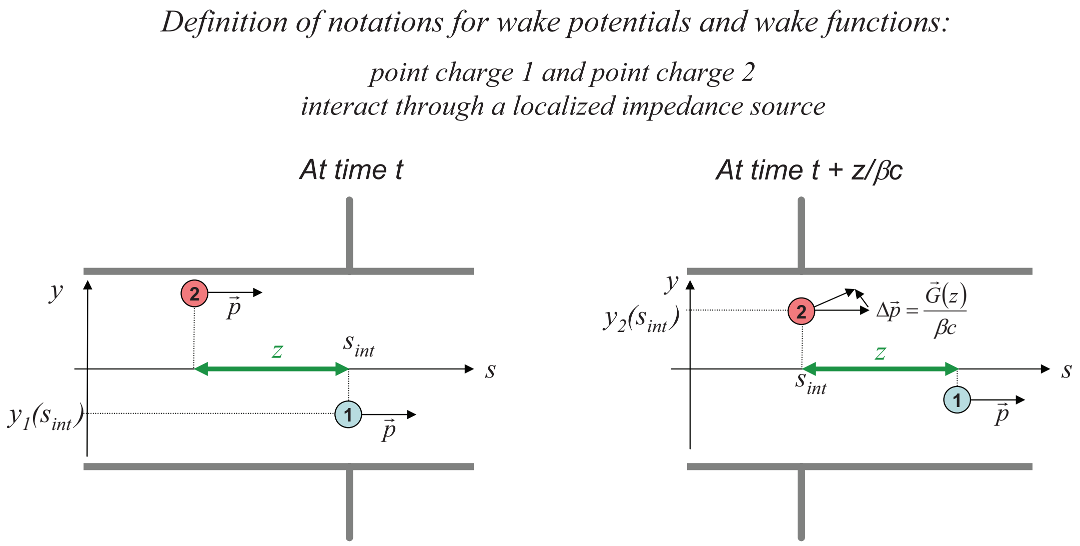

Definition of notations for wake potentials and wake functions:

point charge 1 and point charge 2
interact through a localized impedance source

Figure 3.10: Assumption used for the definition of the wake potentials and wake function: the interaction of the point charges with the accelerator element is localized at longitudinal coordinate s_{int}. The kick generated by source point charge 1 is generated at s_{int} at time t (left drawing) and felt by trailing particle 2 at s_{int} at time $t + z/\beta c$ (right drawing). In this approximation, the only relevant vertical coordinates to assess the beam dynamics are $y_1(s_{int})$ and $y_2(s_{int})$.

3.3.2 Wake Potentials

The wake potential $\vec{W}(x_1, y_1, x_2, y_2, z)$ of an accelerator element of length L is defined as the kick $\beta c \Delta p$ corresponding to the integrated Lorentz force $\vec{F}(x_1, y_1, x_2, y_2, s_2, t)$ generated by a source distribution – total charge q_1, velocity $\beta_1 c$, location $(x_1, y_1, s_1 = \beta ct)$ –, and felt by a particle trailing behind the source by a distance z – total charge q_2, velocity $\beta_2 c$, location $(x_2, y_2, s_2 = s_1 - z)$:

$$\vec{W}(x_1, y_1, x_2, y_2, z) = -\frac{1}{q_1 q_2} \int_{s_2=0}^{L} \left[\vec{F}\left(x_1, y_1, x_2, y_2, s_2, t\right)\right]_{t=(s_2+z)/\beta_2 c} ds_2. \tag{3.60}$$

An illustration for a point charge distribution is presented in Fig. 3.10. The wake potential is normalized to both source and test charges. Different sign conventions may be used for the definition of the wake potential. Here, a positive longitudinal wake potential means that a charge of the same sign as the source distribution gets slowed down by the wake force. Using the expression of the Lorentz force for a momentum aligned with the axis s in Eq. (3.4), the longitudinal wake potential $W_{//}$ and the transverse wake potentials W_x and W_y can then be written:

$$\begin{aligned}
W_{//}(x_1, y_1, x_2, y_2, z) &= -\frac{1}{q_1} \int_{s_2=0}^{L} \left[E_s\left(x_1, y_1, x_2, y_2, s_2, t\right)\right]_{t=\frac{z+s_2}{c}} dz_2, \\
W_x(x_1, y_1, x_2, y_2, z) &= -\frac{1}{q_1} \int_{s_2=0}^{L} \left[\left\{E_x - \beta c B_y\right\}\left(x_1, y_1, x_2, y_2, s_2, t\right)\right]_{t=\frac{z+s_2}{c}} ds_2, \qquad (3.61) \\
W_y(x_1, y_1, x_2, y_2, z) &= -\frac{1}{q_1} \int_{s_2=0}^{L} \left[\left\{E_y + \beta c B_x\right\}\left(x_1, y_1, x_2, y_2, s_2, t\right)\right]_{t=\frac{z+s_2}{c}} ds_2,
\end{aligned}$$

where we chose this time (x, y, z) as a direct orthonormal frame. As an example, the wake potentials simulated from *CST Particle Studio* using the model defined in Fig. 3.6 are presented in Fig. 3.11. This example of a CLIC copper collimator shows that changes of the geometrical surroundings of the beam create significant wake potential. In fact, a non zero resistivity of the vacuum chamber also creates wake potentials as can be seen in the example of an ultrarelativistic beam traveling in a beam pipe of rectangular section (see Fig. 3.12). The wake potentials, which can be obtained from simulation codes like CST Particle Studio or GdfidL [38] are characteristics of an accelerator element but also of the particle distribution that was used to generate them. Since the longitudinal particle distribution may change from one set of beam parameters to another, it would be interesting to obtain a function with which the wake potential for any distribution could be computed: the wake function.

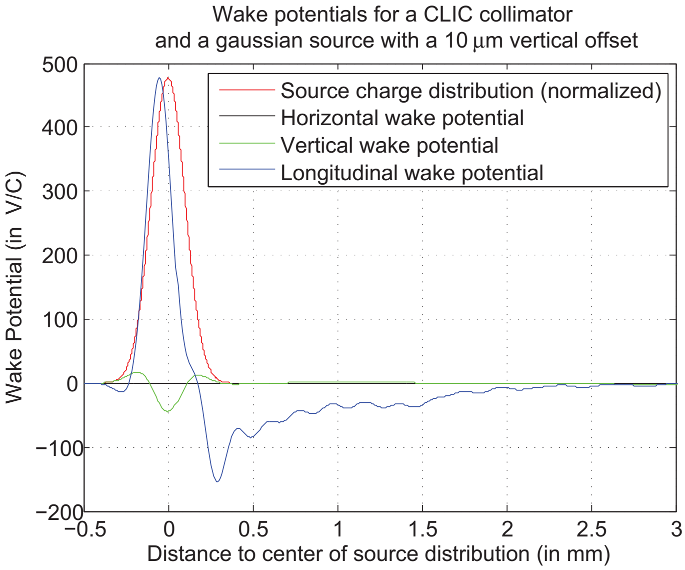

Figure 3.11: Wake potentials simulated with *CST Particle Studio*: longitudinal wake potential (in blue) and transverse wake potentials (horizontal in black and vertical in green). The source bunch longitudinal Gaussian distribution is also plotted in red (normalized to the maximum of the wakes for display purposes). The integration of all wake fields is performed along the s axis. The source bunch is displaced vertically by 10 μm, and the wake potentials were not normalized with respect to this displacement. The plane $x = 0$ is a symmetry plane and the source distribution was not displaced horizontally, then the horizontal wake potential is negligible.

3.3.3 Wake Functions

The wake function $\vec{G}(x_1, y_1, x_2, y_2, z) = \left\{G_x, G_y, G_{//}\right\}$ is that special wake potential generated by a moving point charge $\delta(s - \beta ct)$. Therefore, the wake potential $\vec{W}(z)$ for any given longitudinal line charge density $\lambda(z)$ can be obtained as the convolution of this

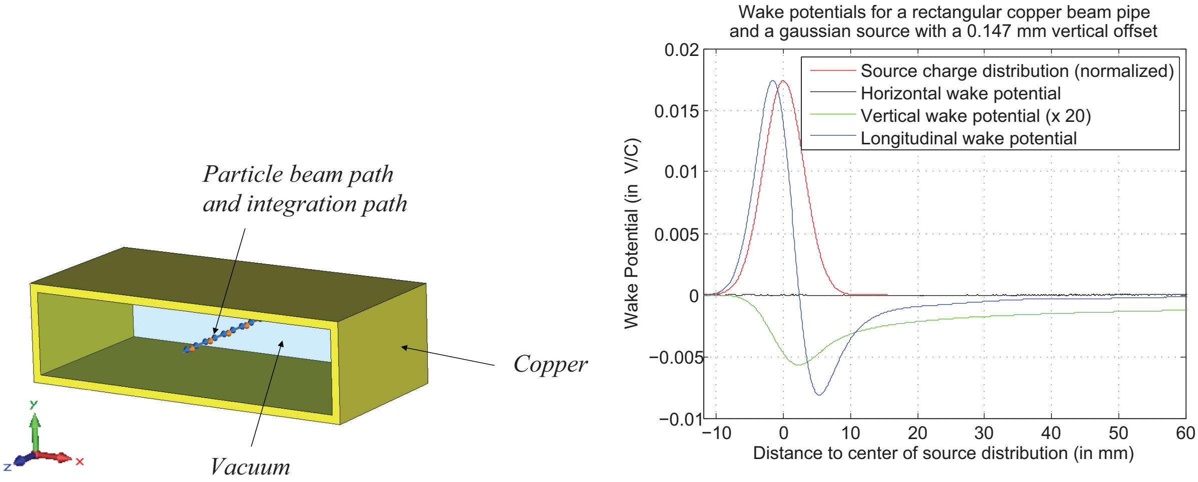

Figure 3.12: 3D Model of a rectangular beam pipe made of copper (left), and wake potentials simulated with *CST Particle Studio* (right): source bunch longitudinal Gaussian distribution (in red, normalized), longitudinal wake potential (in blue), horizontal wake potential (in black) and vertical wake potential (in green, magnified by a factor 20). The source bunch is displaced vertically by 0.147 mm, and the wake potentials were not normalized with respect to this displacement.

distribution with the wake function of the considered element.

$$\vec{W}(x_1, y_1, x_2, y_2, z) = \int_{z'=-\infty}^{+\infty} \vec{G}(x_1, y_1, x_2, y_2, z - z')\lambda(z')dz'. \tag{3.62}$$

If the considered particles are ultrarelativistic, then the integration needs to be performed only from longitudinal location z on, since the wake fields vanish in front of the bunch for causality reasons. The wake function is a fundamental characteristic of an accelerator element (or collection of accelerator elements) to study the collective effects that may arise from the interaction of an arbitrary bunch of particles with this element. Unfortunately, the wake function can be calculated analytically only for a few simple structures (please refer to Chapter 5 for illustrations of such calculations). On the other hand, simulation codes such as *CST Particle Studio* or *GdfidL* may provide numerical wake potentials, but not the wake functions since the source charge distribution can not be infinitely small. In some circumstances, we will see in Chapter 5 that the bunch can be made small enough to approach satisfyingly the wake function.

3.3.4 Beam Coupling Impedances

As it will be seen in Chapter 5, the electromagnetic fields are generally easier to compute in frequency domain than in time domain. We therefore define the longitudinal and transverse beam coupling impedances $Z_{//}$, Z_x,Z_y as the Fourier transform of the longitudinal and transverse wake functions $G_{//}$, G_x,G_y:

$$Z_{//}(\omega) = -\int_{z=-\infty}^{+\infty} G_{//}(z)\frac{e^{jkz}}{\beta c}dz, \tag{3.63a}$$

$$Z_x(\omega) = j\int_{z=-\infty}^{+\infty} G_x(z)\frac{e^{jkz}}{\beta c}dz, \tag{3.63b}$$

$$Z_y(\omega) = j\int_{z=-\infty}^{+\infty} G_y(z)\frac{e^{jkz}}{\beta c}dz. \tag{3.63c}$$

where $\omega = k\beta c$ is the angular frequency, and k is the wave number. As in the case of the wakes, different conventions are commonly used in both literature and codes. The convention used here, together with the convention used for the wakes, leads to a positive longitudinal impedance when the beam loses energy, and a positive transverse impedance for a capacitive contribution. The wake functions can also be obtained from the coupling impedance using the inverse Fourier Transform:

$$G_{//}(z) = -\frac{1}{2\pi}\int_{\omega=-\infty}^{+\infty} Z_{//}(\omega)e^{-jkz}d\omega, \tag{3.64a}$$

$$G_x(z) = -\frac{j}{2\pi}\int_{\omega=-\infty}^{+\infty} Z_x(\omega)e^{-jkz}d\omega, \tag{3.64b}$$

$$G_y(z) = -\frac{j}{2\pi}\int_{\omega=-\infty}^{+\infty} Z_y(\omega)e^{-jkz}d\omega. \tag{3.64c}$$

Defining this quantity as an impedance may lead to ambiguities as the classical definition of the electrical impedance of a circuit is also widely used in neighboring accelerator applications. In fact, the beam impedance shares many similarities with the electrical impedance.

- In both electrical circuit and collective effects, moving charges represent a current.
- Both of these currents propagate in a medium (passive circuit elements and beam pipe).
- The geometry and materials of this medium perturb the propagation of this current.
- This perturbation leads to the generation of a potential (voltage at the terminals of the circuit and wake potentials in the beam pipe).

This analogy can not be pushed too far: a perfect conductor in a circuit systematically leads to a vanishing resistance (real part of the circuit impedance). A beam pipe made of perfect conductor can lead to non zero real part of the beam impedance. In the following chapters of this manuscript, we will refer to the impedance as the beam coupling impedance, unless otherwise stated. Now that the wake fields have been introduced, some simple aspects of collective effects can be introduced. A more thorough treatment of one of these collective effects (TMCI) will then be given in Chapter 5.

3.4 Introduction to Collective Effects

References by S.Y. Lee [26], K.Y. Ng [34], A. Hofmann [39], J. Gareyte [40] and A. Koschik [41] have helped shape this section. We will focus here on transverse collective effects.

3.4.1 Transverse Equation of Motion

Let us recall Hill's equation in the smooth approximation in Eq. (3.24) perturbed by a vertical force F_y that was obtained in the frame of magnetic errors:

$$\ddot{y}(t) + \omega_0^2 Q_y^2 y(t) = \frac{F_y}{m_0 \gamma}, \tag{3.65}$$

where time t is used as variable. The unperturbed solution was of the form

$$\begin{aligned} y(t) &= A \cos\left(Q_y \omega_0 t\right), \\ &= \mathrm{Re}\left[A \; e^{j Q_y \omega_0 t}\right]. \end{aligned}$$

Let us now try and find a simplified expression for the vertical force acting on a test particle of vertical location y_2 within a bunch of particles of average vertical position $\bar{y}$. The evolution $\bar{y}(t)$ of the average vertical position is called coherent motion, as it represents the motion of the bunch as a whole. The deviation from this coherent motion $\Delta y = y_2 - \bar{y}$ is called the incoherent motion. As an immediate illustration of these concepts, an example of the vertical coherent motion and single particle vertical distribution simulated by the beam dynamics code *HEADTAIL* [42] for a kicked proton bunch is presented in Fig. 3.13. More details about the *HEADTAIL* code will be given in Chapter 6.

3.4.2 Direct Space Charge Force

For simplicity, let us assume as in [8], [39] and [43] a uniform continuous beam (also called coasting beam) of circular cross section of radius $r = a$, uniform charge density η_c, charge per unit length $\lambda = \eta_c \pi a^2$, velocity $\beta c \vec{u_z}$, then representing a current $I = \beta c \lambda$ in cylindrical coordinates $\{\vec{u_r}, \vec{u_\theta}, \vec{u_z}\}$. For symmetry reasons, the electric field only has a radial component E_r while the magnetic field only has an azimuthal component B_θ. Maxwell's equations [29] in the integral form applied to a cylinder of radius ρ and arbitrary length l yields for Gauss's law and Ampere's law:

$$E_r = \frac{I}{2\pi\varepsilon_0 \beta c}\frac{\rho}{a^2} \quad \text{and} \quad B_\theta = \frac{I}{2\pi\varepsilon_0 c^2}\frac{\rho}{a^2} \quad \text{for} \quad \rho < a.$$

As a consequence, the space charge force $\vec{F}^{sc}$ acting on a particle of charge q within the beam is

$$\vec{F}^{sc} = q\left(E_r - v_s B_\theta\right)\vec{u_r} = \frac{q\lambda}{2\pi\varepsilon_0\gamma^2}\frac{\rho}{a^2}\vec{u_r}. \tag{3.66}$$

In [8] and [39], it is shown that the space charge of a bunched beam with Gaussian longitudinal density of r.m.s. σ_z and Gaussian transverse density of r.m.s. σ_r can be approximated to first order in ρ by Eq. (3.66), where the radius of the uniform distribution a is replaced by $\sqrt{2}\sigma_r$ and λ is now a function of z:

$$\begin{aligned} \vec{F}^{sc} &= \frac{q}{2\pi\varepsilon_0\gamma^2}\lambda(z)\frac{\rho}{2\sigma^2}\vec{u_r} \\ &= \frac{q}{2\pi\varepsilon_0\gamma^2}\frac{qN_b}{\sqrt{2\pi}\sigma_z}e^{-\frac{z^2}{2\sigma_z^2}}\frac{\rho}{2\sigma_r^2}\vec{u_r}, \end{aligned} \tag{3.67}$$

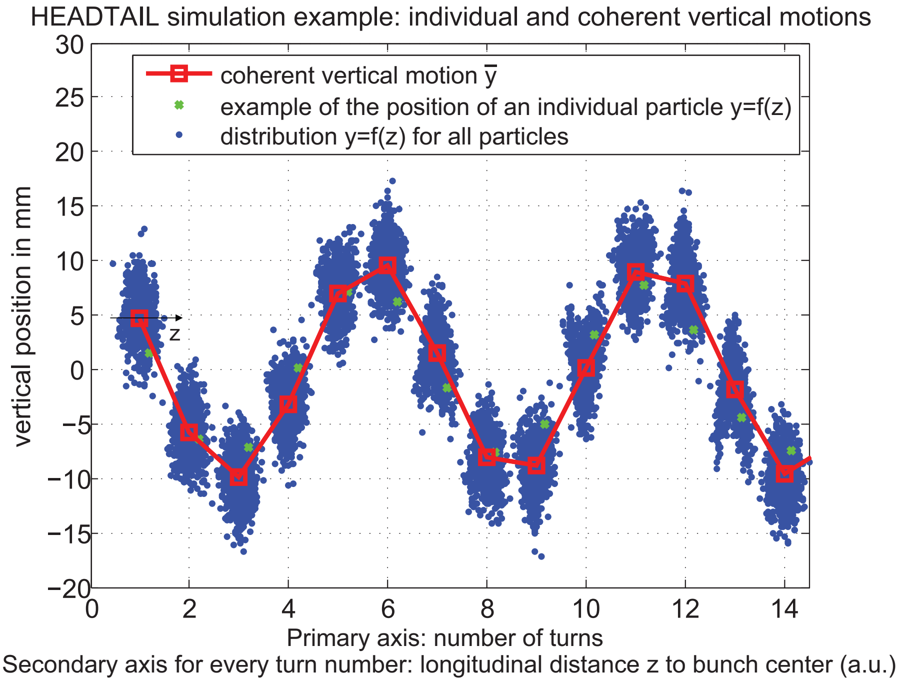

Figure 3.13: Example of the first 14 turns of a beam dynamics simulation with *HEADTAIL*. The red curve shows the vertical motion $\bar{y}$ of the bunch centroid as a function of the number of simulated turns. For each turn, the blue dots gives an idea of the vertical position of single particles in the bunch $y_2 = f(z)$ as a function of the longitudinal distance to bunch center. The green dots shows the simulated motion of one specific single particle. The vertical coherent motion $\bar{y}$ is represented by the red curve, whereas the incoherent motion for the green particle can be inferred by the difference between the green and red curves $y_2 - \bar{y}$. The main simulation parameters for this pedagogic example are the SPS injection parameters (see Tab. B.1 in appendix). The initial vertical kick (1 cm) was set intentionally large to distinguish the coherent and incoherent motions.

where N_b is the number of particles per bunch. For a bunched beam of protons, the maximum vertical space charge force is therefore:

$$\vec{F}_y^{sc}(y) = \frac{e^2 N_b}{4\pi\sqrt{2\pi}\varepsilon_0\gamma^2\sigma_z\sigma_y^2} y. \tag{3.68}$$

It is interesting to notice three important properties of this direct space charge force that can be concluded from Eq. (3.68):

- The direct space charge force increases linearly with the number of protons per bunch N_b.
- The direct space charge force is always defocusing.
- The direct space charge force vanishes for ultrarelativistic beams $\gamma \to \infty$.

In terms of position y_2 and $\bar{y}$, the vertical direct space charge force can therefore be expressed as a function of the deviation from the bunch centroid position only. The direct space charge force is a purely incoherent force.

$$F_y^{sc} = (y_2 - \bar{y})\, F_y^{sc,incoh}. \tag{3.69}$$

3.4.3 Forces due to the Beam Pipe Walls

Contrary to the direct space charge forces, the forces on a test particle due to the electromagnetic interactions of the bunch of particles with its surroundings will in general depend on the incoherent motion, but also on the global location of the bunch with respect to the beam pipe walls. If we come back to the vertical wake force of a source particle 1 acting on a trailing particle 2 following at a distance z_1 (in Fig. 3.10), and if we assume that these vertical positions are small enough, we can linearize the resulting force F_y on the test particle, ignore coupled terms between horizontal and vertical positions and separate the wake force into a dipolar contribution F_y^{dip} that depends on the source vertical location y_1 and a quadrupolar contribution F_y^{quad} that depends on the test particle vertical location y_2.

$$F_y(x_1, y_1, x_2, y_2, z) = y_1\ F_y^{dip}(z_1) + y_2\ F_y^{quad}(z_1). \tag{3.70}$$

This linearization can also be thought of as a first order Taylor expansion of the wake field as in Ref. [34], and was applied to several beam pipe geometries in Ref. [44]. The terms dipolar and quadrupolar have been chosen as the dipolar wake function acts on the test proton like a dipole magnet (the kick is the same whatever its transverse location), whereas the quadrupolar term acts like a quadrupole magnet (the kick increases linearly with the transverse offset of the test particle). This assumption may not be valid in practical cases where the source or the test particles are so far from the element center that nonlinear and coupled terms become significant. Also, and more importantly, many accelerator elements are not symmetric with respect to the vertical and longitudinal planes, so that even the center of symmetry of the device can not be defined. When considering a system of many particles, we need to sum contributions due to all particles in the beam. We can therefore write the total force $\langle F_y \rangle$ acting on the test particle of vertical position y_2 and longitudinal distance to bunch center z

$$\begin{aligned} \langle F_y(y_2,z) \rangle &= \sum_{i \neq 2} y_i \; F_y^{dip}(z_i) + \sum_{i \neq 2} y_2 \; F_y^{quad}(z_i), \\ &= \bar{y} \left\langle F_y^{dip}(z) \right\rangle + y_2 \; \left\langle F_y^{quad}(z) \right\rangle, \\ &= \bar{y} \left(\left\langle F_y^{dip}(z) \right\rangle + \left\langle F_y^{quad}(z) \right\rangle \right) + \Delta y \left\langle F_y^{quad}(z) \right\rangle, \end{aligned} \tag{3.71}$$

where $\left\langle F_y^{dip} \right\rangle$ and $\left\langle F_y^{quad} \right\rangle$ are the total dipolar and quadrupolar forces created by the beam on the trailing particle; $\bar{y}$ is the vertical location of the center of mass of the bunch (also called centroid), and $\Delta y = y_2 - \bar{y}$ is the incoherent motion of the trailing particle. We have therefore separated the wake force into a coherent force $\left\langle F_y^{coh} \right\rangle$

$$\left\langle F_y^{coh} \right\rangle = \bar{y} \left(\left\langle F_y^{dip} \right\rangle + \left\langle F_y^{quad} \right\rangle \right)$$

that depends only on the coherent position of the bunch $\bar{y}(t)$ and an incoherent force $\left\langle F_y^{incoh} \right\rangle$

$$\left\langle F_y^{incoh} \right\rangle = \Delta y \left\langle F_y^{quad} \right\rangle$$

that depends only on the incoherent position $\Delta y(t)$ of the considered particle.

3.4.4 Incoherent Tune Shift

Then we can write for any particle in the beam with Eq. (3.65) and Eq. (3.71)

$$\ddot{y_2}(t) + \left(\omega_0^2 Q_y^2 - \frac{\left\langle F_y^{quad} \right\rangle}{m_0 \gamma} \right) y_2(t) = \bar{y}(t) \; \frac{\left\langle F_y^{dip} \right\rangle}{m_0 \gamma}. \tag{3.72}$$

In the absence of coherent motion, we have $\bar{y}(t) = 0$, the r.h.s. of Eq. (3.72) vanishes and the quadrupolar force then creates an incoherent vertical tune shift ΔQ_y^{incoh}:

$$\begin{aligned} \omega_0^2 Q_y^2 - \frac{\left\langle F_y^{quad} \right\rangle}{m_0 \gamma} &= \omega_0^2 \left(Q_y + \Delta Q_y^{incoh} \right)^2 \\ &\approx \omega_0^2 Q_y^2 + 2 \omega_0^2 Q_y \Delta Q_y^{incoh}. \end{aligned}$$

where we assumed that the wake force is a small perturbation to the particle's motion. This leads to the incoherent vertical tune shift.

$$\Delta Q_y^{incoh} = - \frac{\left\langle F_y^{quad} \right\rangle}{2 m_0 \gamma \omega_0^2 Q_y}. \tag{3.73}$$

The perturbed solution is then of the form

$$y(t) = \mathrm{Re} \left[A \; e^{j \left(Q_y + \Delta Q_y^{incoh} \right) \omega_0 t} \right]. \tag{3.74}$$

Therefore, if the bunch has a finite vertical size, incoherent wake forces (such as the direct space charge and the quadrupolar component of the wake force) lead to incoherent tune shifts and therefore a tune spread. As we saw for the direct space charge effect in Eq. (3.68), these collective forces increases with the beam current, leading to larger incoherent tune shifts and a larger tune spread. As a direct application, the maximum value of the direct space charge tune shift for particles with small amplitudes in the SPS (circumference $L = 6.9$ km) can be obtained from Eq. (3.73) and (3.68) for a Gaussian proton beam of transverse size σ_y:

$$\begin{aligned}\Delta Q_y^{sc} &= -\frac{e^2}{4\pi\varepsilon_0 m_0 c^2}\frac{N_b R^2}{2Q_y\sqrt{2\pi}\beta^2\gamma^3\sigma_z\sigma_y^2} \\ &= -\frac{r_p N_b \beta_y L}{2\pi\sqrt{2\pi}\beta^2\gamma^3\sigma_z\sigma_y^2} \\ &= -\frac{r_p N_b}{2\pi B\beta\gamma^2\varepsilon_{y,N}},\end{aligned} \tag{3.75}$$

where we used the definition of the classical radius $r_p = e^2/4\pi m_0\varepsilon_0 c^2$, $\omega_0 = \beta c/R$, the normalized vertical emittance $\varepsilon_{y,N} = \beta\gamma\varepsilon_y$, the vertical emittance $\varepsilon_y = \sigma_y^2/\beta_y$, the bunching factor $B = \sqrt{2\pi}\sigma_z/L$ and the uniform focusing approximation $Q_y \approx R/\beta_y$. Using the parameters of the SPS at injection (see Tab. B.1) and assuming a beam with the same horizontal and vertical dimensions, we therefore obtain an order of magnitude for the direct space charge tune shift at injection in the SPS:

$$\Delta Q_y^{sc}(SPS) \approx -0.1. \tag{3.76}$$

3.4.5 Coherent Tune Shift

The average of single particle equation of motion Eq. (3.72) for all beam particles yields the equation of motion for the centroid of the particle distribution.

$$\ddot{\bar{y}}(t) + \left(\omega_0^2 Q_y^2 - \frac{\left\langle F_y^{quad}\right\rangle}{m_0\gamma}\right)\bar{y}(t) = \bar{y}(t)\,\frac{\left\langle F_y^{dip}\right\rangle}{m_0\gamma}, \tag{3.77}$$

leading to the coherent vertical tune shift

$$\begin{aligned}\Delta Q_y^{coh} &= -\frac{\left\langle F_y^{dip}\right\rangle + \left\langle F_y^{quad}\right\rangle}{2m_0\gamma\omega_0^2 Q_y} \\ &= \Delta Q_y^{incoh} - \frac{\left\langle F_y^{dip}\right\rangle}{2m_0\gamma\omega_0^2 Q_y}.\end{aligned} \tag{3.78}$$

With these notations, Eq. (3.72) for the single test particle takes the form

$$\ddot{y}_2(t) + \omega_0^2 Q_y^2 y_2(t) + 2\omega_0^2 Q_y\left[\Delta Q_y^{incoh}\left(y_2(t) - \bar{y}\right) + \Delta Q_y^{coh}\bar{y}\right] = 0, \tag{3.79}$$

as found in [45]. The perturbed solution for coherent motion is then of the form

$$\bar{y}(t) = \mathrm{Re}\left[A\ e^{j\left(Q_y + \Delta Q_y^{coh}\right)\omega_0 t}\right].$$

In this form, it becomes clear that a non zero imaginary part of the coherent tune shift ΔQ_y^{coh} leads to either damping of the coherent oscillations (for $\mathrm{Im}\big[\Delta Q_y^{coh}\big] > 0$) or exponential growth of the oscillations (for $\mathrm{Im}\big[\Delta Q_y^{coh}\big] < 0$). Expressing the tune shift as a function of the wake field or impedance could then inform us on whether the betatron oscillations can become unstable. The rigorous treatment will be given in Chapter 6, but interesting relationships can be found using a simplified framework. Using Eq. (3.60) and Eq. (3.63c), we have

$$\begin{aligned} Z_y(\omega) &= j\int_{z=-\infty}^{+\infty} G_y(z)\frac{e^{jkz}}{\beta c}dz \\ &= j\int_{z=-\infty}^{+\infty}\left(-\frac{1}{q_1q_2}\int_{s_2=0}^{L}\left[F_y\left(x_1,y_1,x_2,y_2,s_2,t\right)\right]_{t=(s_2+z)/c}ds_2\right)\frac{e^{jkz}}{\beta c}dz \\ &= \frac{j}{Iq_2}\int_{s_2=0}^{L}\mathcal{F}_y(s_2,\omega)ds_2, \end{aligned} \tag{3.80}$$

where we defined the beam current I and the Fourier Transform $\mathcal{F}_y$ of the vertical wake force F_y. The classical dipolar impedance Z_y^{dip} definition for a bunch of intensity I and centroid vertically displaced by $\bar{y}$ is normalized by the displacement $\bar{y}$:

$$\begin{aligned} Z_y^{dip}(\omega) &= \frac{j}{\bar{y}Iq_2}\int_{s_2=0}^{L}\mathcal{F}_y(s_2,\omega)ds_2 \\ &= \frac{j}{Iq_2}\int_{s_2=0}^{L}\mathcal{F}_y^{dip}(s_2,\omega)ds_2, \end{aligned} \tag{3.81}$$

with the dipolar force $\mathcal{F}_y^{dip} = \mathcal{F}_y/\bar{y}$. Assuming again a uniform coasting beam in a long enough impedance for simplicity leads the wake force $\mathcal{F}_y$ to be independent of s_2 and we can write in this case

$$Z_y^{dip} = \frac{jL}{Iq_2}\mathcal{F}_y^{dip}. \tag{3.82}$$

As a consequence, at a given frequency, the coherent tune shift in Eq. (3.78) becomes as in [40] and [46],

$$\Delta Q_y^{coh} = \Delta Q_y^{incoh} + j\frac{q_2 I Z_y^{dip}}{2Lm_0\gamma\omega_0^2 Q_y}. \tag{3.83}$$

From this mathematically simplified example, we see that a non zero real part of the impedance leads to an imaginary coherent tune shift (i.e. a damping or growth rate depending on the tune shift's sign), while a non zero imaginary part of the impedance leads to a real coherent tune shift. Both of these tune shifts are proportional to the beam intensity, which means that the disturbance to the beam increases with its intensity, until an instability growth rate is so large that it can not be managed by the damping mechanisms, or until the tune spread is so large that it leads to an unacceptable deterioration of the beam quality (beam loss and/or emittance blow up).

Now that the single particle dynamics and collective effects concepts have been defined, we will use them through the following chapters to improve our understanding of the impedance of the SPS ring and the LHC collimators.

Chapter 4

ZBASE, the CERN Impedance Database

As mentioned in the introductory chapter, the intensity performance of the LHC injector chain will need to be pushed far beyond its current limits in the frame of the LHC upgrade. In order to be able to implement this intensity upgrade, either stronger damping mechanisms have to be put in place or sources of collective effects have to be removed. This work is a part of a global project that focuses on identifying the main contributors to the total machine impedance of the LHC injectors. Once identified, these accelerator elements could be modified, replaced or removed to try and meet the requirements for the LHC upgrade. Since there can be thousands of accelerator elements in large machines, a database has been put in place to manage the large number of information involved [47].

4.1 Purpose

The ZBASE impedance database has been initially set up to compute the beam coupling impedance of LEP and then it was started for LHC. Since many LHC elements were still in the design phase, frequent modifications had to be checked, and a crucial feature of the database was to be able to redo impedance calculations quickly. The impedance of the accelerator elements could be obtained using various external computer codes (e.g. *URMEL*, *MAFIA*, *ABCI*), and links had been set up to launch these programs automatically from input files stored in the database.

Since then, some links, input files, libraries and even computer codes (e.g. *MAFIA*) became obsolete. New powerful computer programs have become available to compute the impedance of 3D structures (e.g. *CST Particle Studio*, *GdfidL*) as well as analytical calculation codes for simple geometries. More importantly, computer codes such as *HEADTAIL* have been developed to assess the complex dynamics of beams interacting with these impedances. Finally, it became clear that working with only the transverse dipolar impedances and wakes does not enable to satisfyingly predict the transverse collective effects observed in real accelerators.

As a consequence, the needed work on *ZBASE* covers two distinct but complementary areas:

- refurbish the underlying *ZBASE* code - restore the libraries, update the links - so that the LHC data stored over the years can be used

- assess the feasibility of using the new codes and new methods to generate new inputs for *ZBASE*, and link the impedance to a beam dynamics code, whose results could be compared with measurements with beam in the machine.

The work described in this thesis focuses on the latter objective, while the refurbishment of the code already started in Ref. [48] was initiated at the occasion of this thesis work and will be pursued in the following months [49].

4.2 Implementation

The functional diagram of the integration of the *ZBASE* impedance database into the iterative process of obtaining an impedance model for the SPS is given in Fig. 4.1. The aim of *ZBASE* is to compute an impedance model and use this impedance model to produce simulated observables (such as tune shifts and intensity thresholds for instabilities) that can be compared to machine measurements with beam. Obtaining an impedance model gathering several types of impedance contributors assessed with different methods (analytical, simulated or measured on a bench) requires a standardized procedure. Since the *HEADTAIL* macroparticle simulations was modified to be able to import the dipolar and quadrupolar wake function as a table, we chose to transform all the data available for single elements into wake functions. That involves transforming impedances into wake functions using Fourier Transforms, and deconvolving wake potentials into wake functions. Details of these transformations will be given in Chapter 5.

Once all data for single elements are obtained they need to be weighted by the corresponding relative beta function $\beta_{x,y}/\left\langle\beta_{x,y}\right\rangle$ at the location of the element before they can be summed into total wake functions. This step is needed since this version of *HEADTAIL* assumes a constant average transverse beta function $\left\langle\beta_{x,y}\right\rangle$ around the ring. If the beta function at the location of the considered impedance source is $\beta_{x,y}$ instead, the transverse amplitudes (resp. divergences) of the protons are larger (resp. smaller) by a factor $\sqrt{\beta_{x,y}/\left\langle\beta_{x,y}\right\rangle}$ for both the source and test charges, when compared to a location with average beta function $\left\langle\beta_{x,y}\right\rangle$. Then, two scaling factors need to be applied to the kick:

- The dipolar (resp. quadrupolar) kicks due to the wakefields are proportional to the source (resp. test) charge amplitude and the amplitude of the kicks should then also be scaled by $\sqrt{\beta_{x,y}/\left\langle\beta_{x,y}\right\rangle}$.
- The divergence of the test charge is scaled by $\sqrt{\left\langle\beta_{x,y}\right\rangle/\beta_{x,y}}$ at the location of the kick. After the kick is applied, this test charge divergence needs to be scaled back to be consistent with the average beta function in the rest of the ring, which means that the sum of the initial divergence and the applied kick should be divided by $\sqrt{\left\langle\beta_{x,y}\right\rangle/\beta_{x,y}}$.

The combination of these two effects explains the resulting scaling factor $\beta_{x,y}/\left\langle\beta_{x,y}\right\rangle$ that has to be included for a kick from an impedance source at a location where the beta function is $\beta_{x,y}$ instead of the average beta function $\left\langle\beta_{x,y}\right\rangle$.

As a consequence, *ZBASE* should be able to interact with several external programs:

- *MADX* to obtain relevant beam parameters and specific parameters of the element or ensemble of elements whose impedance is computed
- *Mathematica* or *Matlab* to perform impedance analytical calculations, and all post-processing steps (e.g. Fourier Transforms, deconvolution, weighted sums)
- *CST Studio Suite (Particle Studio and/or Microwave Studio)* or *GdfidL* to perform impedance simulations
- *HEADTAIL* macroparticle simulations to predict the collective effects associated to the computed impedance of an element or an ensemble of elements.

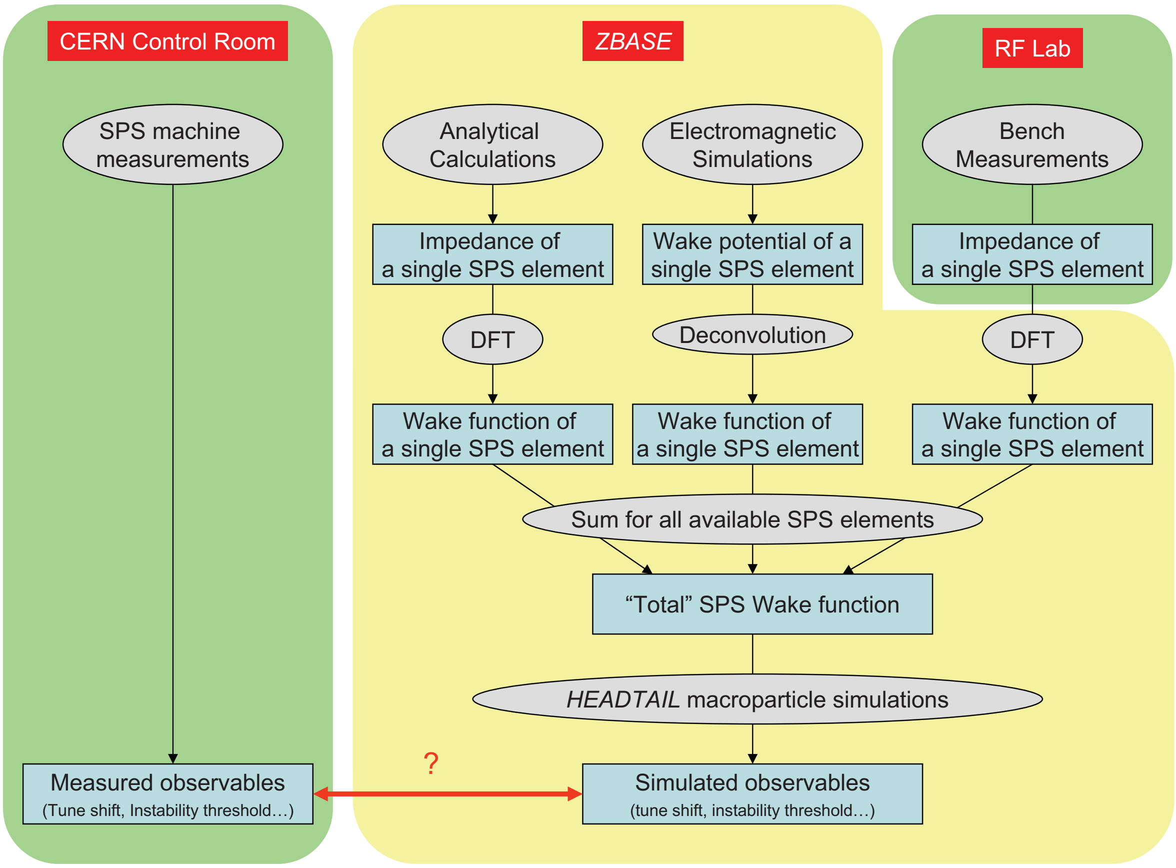

Figure 4.1: Functional diagram of the *ZBASE* impedance database. Apart from machine and bench measurements, all other impedance computations and postprocessing should be launched through *ZBASE*.

Now that the *ZBASE* framework is defined, Chapter 5 will be devoted to the various methods that were used to gather relevant beam coupling impedance data and obtain a improved SPS impedance model. Chapter 6 will focus on collective effects that result from this SPS impedance model.

Chapter 5

Obtaining Impedance Data for ZBASE

At the time of this study, several methods are available to obtain the impedance of an accelerator element.

- Maxwell's equations can be solved analytically to obtain the impedance for a small range of simple geometries. Infinite cylindrical beam pipes and rectangular kicker-like structures are addressed in sections 5.1 and 5.2.4.
- 2D or 3D powerful Finite Element codes can be used to simulate the wake potential generated by a bunch in a more complicated geometry. Simulations of several accelerator elements are reported in section 5.3
- Finally, when they are possible, dedicated RF measurements on a bench can be performed to obtain the impedance of actual accelerator elements. Reports of such measurements can be found in 5.4.

5.1 Theoretical Longitudinal Impedance of a Cylindrical Beam Pipe of Infinite Length

In the past, the impedance of many structures was calculated, simulated and measured. In particular, calculations of the impedance of a monolayer circular beam pipe of infinite thickness in the assumption of an ultrarelativistic beam [50], of a monolayer circular beam pipe of finite thickness [51], of a 2-layer-circular-beam-pipe of finite thickness [52], [53], [54] and [55] were reported. This section focuses on obtaining a formalism for calculating the longitudinal impedance of a cylindrical beam pipe made with any number of layers of materials with various electromagnetic properties. The following derivations of the longitudinal and transverse beam coupling impedance follow closely the formalism explained by R.L. Gluckstern [56] and applies to the longitudinal plane the field matching technique proposed by B. Zotter for the transverse plane [51]. It is important to note that numerous related papers were published on this subject during the course of this PhD work, in particular by M. Ivanyan et al. [57, 58], N. Wang et al. [59], E. Métral et al. [60], Hahn [61], F. Roncarolo et al. [62] and N. Mounet et al. [63]. In view of potential applications to LHC and CLIC impedance calculations, the focus of this section is to obtain a general formula for the impedance of multilayered structures with as little approximations as possible, and a computer implementation that could cope with the large range of frequencies covered by the CERN current machines and projects (from 1 kHz to 10 THz).

5.1.1 Choosing the Source Beam

As chosen by R. Gluckstern in Ref. [56], the source beam for longitudinal impedance computations is defined as an infinitely narrow ring moving with constant velocity $\vec{v}$ parallel to the z-axis, with radius a (see Fig. 5.1).

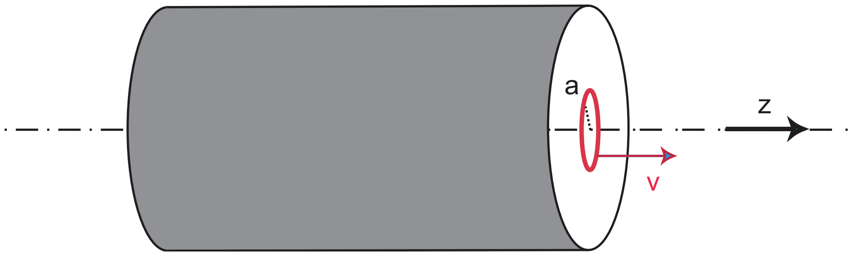

Figure 5.1: Sketch of an annular beam of radius a moving with velocity $\vec{v}$ parallel to the z-axis.

In time domain, the charge density ρ corresponding to this source beam of total charge

$$Q = \iiint \rho\left(r,\theta,z;t\right) rdrd\theta dz$$

can be written as:

$$\rho\left(r,z;t\right) = \frac{Q}{2\pi a}\delta\left(r-a\right)\delta\left(z-vt\right). \tag{5.1}$$

Using Fourier Transforms, the spatial Dirac delta function can be expressed as an integral :

$$\delta(z) = \int_{-\infty}^{+\infty} e^{-jkz}\frac{dk}{2\pi}, \tag{5.2}$$

where k is the wave number. Then we can write

$$\delta(z-vt) = \int_{-\infty}^{+\infty} e^{-jkz}e^{jkvt}\frac{dk}{2\pi}, \tag{5.3}$$

assuming that the velocity v is constant, $k=\omega/v$ leads to $dk=d\omega/v$, and we obtain:

$$\delta(z-vt) = \int_{-\infty}^{+\infty}\left[\frac{e^{-jkz}}{v}\right]e^{j\omega t}\frac{d\omega}{2\pi}. \tag{5.4}$$

From this relation, it can be concluded that $\left[\frac{e^{-jkz}}{v}\right]$ is the Fourier Transform of the Dirac function $\delta(z-vt)$. Then, in frequency domain, Eq. (5.1) can be rewritten as :

$$\boxed{\rho\left(r,z;\omega\right) = \tfrac{Q}{2\pi av}\delta\left(r-a\right)e^{-jkz}.} \tag{5.5}$$

As the current density is defined as $\vec{J}=\rho\vec{v}$, we also have the following relation:

$$\boxed{J_z\left(r,z;\omega\right) = \tfrac{Q}{2\pi a}\delta\left(r-a\right)e^{-jkz}.} \tag{5.6}$$

5.1.2 Deriving a Longitudinal Impedance Formula specific to our Source Beam

R. Gluckstern generalized the formula for the longitudinal coupling impedance $Z_{//}$[1] for a beam with non zero transverse size as an integral over the total volume V:

$$Z_{//}(\omega) = -\frac{1}{Q^2} \iiint_V \vec{E}\left(r,\theta,z;\omega\right) \cdot \vec{J}^*\left(r,\theta,z;\omega\right) dV. \tag{5.7}$$

The velocity of the chosen source beam is parallel to the z-axis, which means that the current density $\vec{J}$ is also parallel to the z-axis. As a consequence, we can write:

$$\vec{E}\left(r,\theta,z;\omega\right) \cdot \vec{J}^*\left(r,\theta,z;\omega\right) = E_z\left(r,\theta,z;\omega\right) J_z^*\left(r,\theta,z;\omega\right). \tag{5.8}$$

Using Eq. (5.6), we get

$$\vec{E}\left(r,\theta,z;\omega\right) \cdot \vec{J}^*\left(r,\theta,z;\omega\right) = \frac{Q}{2\pi a}\delta\left(r-a\right) E_z\left(r,\theta,z;\omega\right) e^{jkz}. \tag{5.9}$$

Integrating over the entire volume in cylindrical coordinate, and using Eq. (5.7) we obtain

$$Z_{//}(\omega) = -\frac{1}{2\pi a Q} \int_{z=-\infty}^{+\infty} \int_{\theta=0}^{2\pi} \int_{r=-\infty}^{+\infty} \delta\left(r-a\right) E_z\left(r,\theta,z;\omega\right) e^{jkz} r dr\ d\theta\ dz. \tag{5.10}$$

If we assume an axisymmetric structure and an axisymmetric source, then the field will also be independent of the angle θ around the z-axis, and the integral over the angle θ becomes 2π. Rearranging the previous equation yields:

$$Z_{//}(\omega) = -\frac{1}{aQ} \int_{z=-\infty}^{+\infty} \left(\int_{r=-\infty}^{+\infty} \delta\left(r-a\right) r E_z\left(r,z;\omega\right) dr \right) e^{jkz} dz. \tag{5.11}$$

Besides, a property of the the Dirac delta function is that for any function f:

$$\int_{r=-\infty}^{+\infty} \delta\left(r-a\right) f(r) dr = f(a). \tag{5.12}$$

It can be concluded that the integral over r in Eq. (5.11) reduces to

$$\int_{r=-\infty}^{+\infty} \delta\left(r-a\right) r E_z\left(r,z;\omega\right) dr = a E_z\left(r=a,z;\omega\right). \tag{5.13}$$

Finally, we get the longitudinal coupling impedance of an axisymmetric structure excited with a ring-shaped source:

$$\boxed{Z_{//}(\omega) = -\tfrac{1}{Q} \int_{-\infty}^{+\infty} E_z\left(r=a,z;\omega\right) e^{jkz} dz.} \tag{5.14}$$

In the following sections, we will use Eq. (5.14) to derive the longitudinal impedance of specific cylindric structures surrounding the source beam. It is important to notice that only the z-component of the electric field at a distance $r = a$ from the z-axis, $E_z\left(r=a,z;\omega\right)$, needs to be derived.

---

[1] The longitudinal impedance $Z_{//}$ is sometimes referred to as Z_{long} for legibility reasons.

5.1.3 Deriving an Expression for the Electric Field $E_z\left(r, z; \omega\right)$

From Eq. (5.14), only the longitudinal electric field needs to be derived. In this section, a general expression for the electric field will be obtained through solving the Maxwell equations with the chosen source beam. The physical cylindrical structure surrounding the beam does not need to be defined yet. As a consequence, an unknown constant α_2 will remain in the final expression for the electric field. This constant will be matched in subsequent sections by assuming a specific structure around the beam.

Getting a Convenient Set of Maxwell equations

As explained in section 5.1.2, Eq. (5.14) requires the calculation of the field component $E_z\left(r = a, z; \omega\right)$. The electromagnetic field components depend on the specific layout of the case studied, but all cases studied in this section share the same source beam circulating in vacuum surrounded by an axisymmetric structure. The source beam remains in vacuum and is assumed not to hit the surrounding structure. Let us first consider the region where the beam circulates, i.e. regions 1 and 2 of figure 5.2.

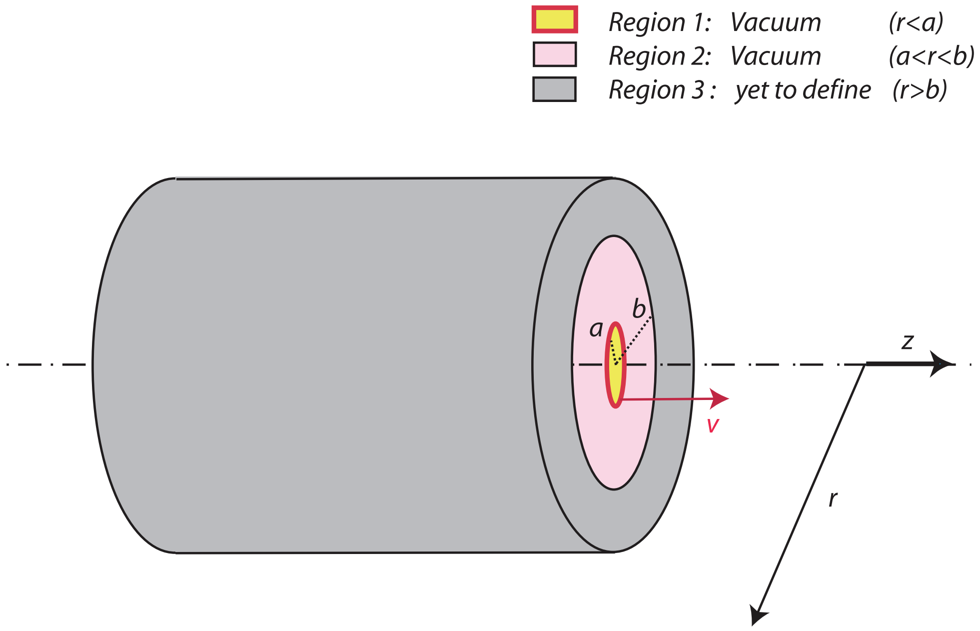

Figure 5.2: Layout of the generic case: ring shaped source beam at $r = a$ circulating in an infinitely long cylindric structure. Region 1 is defined by the cylindrical empty space contained inside the beam ($r < a$). Region 2 is defined by the annular space located between the beam and the structure ($a < r \leq b$). Region 3 does not need to be defined yet ($r \geq b$).

In any region of space, Maxwell's equations give [29]:

$$\vec{\nabla} \cdot \vec{D} = \rho, \tag{5.15a}$$

$$\vec{\nabla} \cdot \vec{B} = 0, \tag{5.15b}$$

$$\vec{\nabla} \times \vec{H} = \vec{J} + \frac{\partial \vec{D}}{\partial t}, \tag{5.15c}$$

$$\vec{\nabla} \times \vec{E} = -\frac{\partial \vec{B}}{\partial t}, \tag{5.15d}$$

where, in materials other than ferroelectric or ferromagnetic, and with small enough applied fields that the response of the material can be considered linear, $\vec{D} = \varepsilon \vec{E}$, and $\vec{B} = \mu \vec{H}$. ε is the electric permittivity of the considered material, and μ its magnetic permeability. $\vec{D}$ is the electric displacement, $\vec{H}$ is the magnetic field strength. In a medium of constant permittivity ε and constant permeability μ in time and space, Eq. (5.15) can be written as:

$$\vec{\nabla} \cdot \vec{E} = \frac{\rho}{\varepsilon}, \tag{5.16a}$$

$$\vec{\nabla} \cdot \vec{H} = 0, \tag{5.16b}$$

$$\vec{\nabla} \times \vec{H} = \vec{J} + \varepsilon \frac{\partial \vec{E}}{\partial t}, \tag{5.16c}$$

$$\vec{\nabla} \times \vec{E} = -\mu \frac{\partial \vec{H}}{\partial t}. \tag{5.16d}$$

In the frequency domain, Eqs. (5.16) become :

$$\vec{\nabla} \cdot \vec{E} = \frac{\rho}{\varepsilon}, \tag{5.17a}$$

$$\vec{\nabla} \cdot \vec{H} = 0, \tag{5.17b}$$

$$\vec{\nabla} \times \vec{H} = \vec{J} + j\omega\varepsilon \vec{E}, \tag{5.17c}$$

$$\vec{\nabla} \times \vec{E} = -j\omega\mu \vec{H}. \tag{5.17d}$$

Besides, the current density in a medium $\vec{J}$ can be split into two terms:

- the convection current density due to the intrinsic movement of the source charges: $\rho\vec{v}$, where $\vec{v}$ is the averaged velocity of the source charges.
- the conduction current density induced by the electric fields in the surrounding conducting materials: $\sigma\vec{E}$, where σ is the conductivity of the material.

Therefore:

$$\vec{J} = \rho\vec{v} + \sigma\vec{E}. \tag{5.18}$$

To gather all terms proportional to the electric field in Eq. (5.17c), the complex permittivity ε_c of the considered material is introduced:

$$\varepsilon_c = \varepsilon_0 \varepsilon_r = \varepsilon_0 \left(\varepsilon_r' - j\varepsilon_r''\right) = \varepsilon_0 \hat{\varepsilon}_r + \frac{\sigma}{j\omega}, \tag{5.19}$$

where $\varepsilon_r = \varepsilon_c/\varepsilon_0$ is the relative complex permittivity of the material with respect to the permittivity of vacuum ε_0. Depending on the material, it can be more convenient to write ε_r in terms of its real and imaginary parts ε_r' and ε_r'' or equivalently in terms of a the real dielectric constant $\hat{\varepsilon}_r = \varepsilon/\varepsilon_0$ and conductivity σ. We also take this opportunity to define the relative complex permeability μ_r with respect to the permeability of vacuum μ_0

$$\mu = \mu_0\mu_r = \mu_0\left(1 + \frac{\mu_i}{1 + j\omega\tau_\mu}\right). \tag{5.20}$$

where μ_r is the relative complex permeability of the material with respect to the permeability of vacuum μ_0, μ_i is the initial permeability of the material and τ_μ is the magnetic relaxation time. Finally, Eq. (5.17) can be written

$$\vec{\nabla} \cdot \vec{E} = \frac{\rho}{\varepsilon}, \tag{5.21a}$$

$$\vec{\nabla} \cdot \vec{H} = 0, \tag{5.21b}$$

$$\vec{\nabla} \times \vec{H} = \rho\vec{v} + j\omega\varepsilon_c\vec{E}, \tag{5.21c}$$

$$\vec{\nabla} \times \vec{E} = -j\omega\mu\vec{H}. \tag{5.21d}$$

The Maxwell equations in the form (5.21) will be used in the next section to calculate the general solutions of E_z and H_θ for the chosen source beam. At this point, in order to avoid confusion in the following calculations, it is important to notice that both the real permittivity ε and the complex permittivity ε_c appear in the set of equations (5.21).

Combining the Maxwell Equations to get a Differential Equation for $E_z(r)$

In this section, Eq. (5.21) will be used to derive general solutions for E_z within a homogeneous medium, in the presence of the source terms in Eqs. (5.5) and (5.6). The surrounding structure will not be defined yet. Therefore, in this section, we aim at obtaining equations for E_z with yet undefined parameters. These parameters will be calculated in the subsequent sections where various surrounding structures will be used through introducing boundary conditions. Applying the curl operator to both sides of Eq. (5.21d) yields:

$$\vec{\nabla} \times \left(\vec{\nabla} \times \vec{E}\right) = -j\omega\mu\left(\vec{\nabla} \times \vec{H}\right). \tag{5.22}$$

Substituting Eq. (5.21c) into Eq. 5.22, we obtain:

$$\vec{\nabla} \times \left(\vec{\nabla} \times \vec{E}\right) = -j\omega\mu\rho\vec{v} + \omega^2\mu\varepsilon_c\vec{E}. \tag{5.23}$$

Besides, a property of the Laplacian operator Δ is that for any vector $\vec{X}$,

$$\Delta\vec{X} = \vec{\nabla}\left(\vec{\nabla} \cdot \vec{X}\right) - \left(\vec{\nabla} \times \vec{\nabla}\right)\vec{X}. \tag{5.24}$$

Then, Eq. 5.23 becomes

$$\Delta\vec{E} + \omega^2\mu\varepsilon_c\vec{E} = \vec{\nabla}\left(\vec{\nabla} \cdot \vec{E}\right) + j\omega\mu\rho\vec{v}. \tag{5.25}$$

With Eq. (5.21a), we get:

$$\Delta \vec{E} + \omega^2 \mu \varepsilon_c \vec{E} = \frac{1}{\varepsilon} \vec{\nabla} \rho + j\omega\mu\rho\vec{v}. \tag{5.26}$$

Acknowledging that the velocity $\vec{v}$ of the source beam is parallel to the z-axis, the axial (z-)component of Eq. (5.26) is :

$$\Delta E_z + \omega^2 \mu \varepsilon_c E_z = \frac{1}{\varepsilon} \frac{\partial \rho}{\partial z} + j\omega\mu\rho v. \tag{5.27}$$

In cylindrical coordinates, the Laplacian applied to E_z is given by

$$\Delta E_z = \frac{1}{r} \frac{\partial}{\partial r} \left(r \frac{\partial E_z}{\partial r} \right) + \frac{1}{r^2} \frac{\partial^2 E_z}{\partial \theta^2} + \frac{\partial^2 E_z}{\partial z^2}. \tag{5.28}$$

Due to both axisymmetries of the source and the structure, the derivatives with respect to θ drop out. Then, injecting Eq. (5.28) into Eq. (5.27), we get a scalar Helmholtz equation

$$\frac{1}{r} \frac{\partial}{\partial r} \left(r \frac{\partial E_z}{\partial r} \right) + \frac{\partial^2 E_z}{\partial z^2} + \omega^2 \mu \varepsilon_c E_z = \frac{1}{\varepsilon} \frac{\partial \rho}{\partial z} + j\omega\mu\rho v. \tag{5.29}$$

Replacing the charge density ρ by its expression in Eq. (5.5), we obtain:

$$\frac{1}{r} \frac{\partial}{\partial r} \left(r \frac{\partial E_z}{\partial r} \right) + \frac{\partial^2 E_z}{\partial z^2} + \omega^2 \mu \varepsilon_c E_z = \frac{j\omega Q}{2\pi a \varepsilon v^2} \delta(r-a) \left(\beta^2 \mu_r \hat{\varepsilon}_r - 1 \right) e^{-jkz}, \tag{5.30}$$

where the relativistic $\beta = v/c$ was used. The fact that $\mu_0 \varepsilon_0 c^2 = 1$ was also used to get to this equation.

Deriving a Particular Solution for $E_z(r \neq a)$

This paragraph is devoted to obtain a possible solution for the electrical field E_z. Equation (5.30) is a partial differential equation, and the method of separation of variables is a powerful way to get trial solutions for the homogeneous equation:

$$\frac{1}{r} \frac{\partial}{\partial r} \left(r \frac{\partial E_z}{\partial r} \right) + \frac{\partial^2 E_z}{\partial z^2} + \omega^2 \mu \varepsilon_c E_z = 0. \tag{5.31}$$

It is useful to notice that, if $r \neq a$, then $\delta(r-a) = 0$, which means that the source terms vanish and Eq. (5.29) becomes the homogeneous Eq. (5.31). Let us assume that $E_z(r, z; \omega)$ can be expressed as the product of two functions of one variable each:

$$E_z(r, z; \omega) = R(r; \omega) Z(z; \omega). \tag{5.32}$$

Then the homogeneous Eq. (5.31) becomes:

$$\frac{1}{R(r)} \left(\frac{1}{r} \frac{d}{dr} \left(r \frac{dR(r)}{dr} \right) \right) + \omega^2 \mu \varepsilon_c = -\frac{1}{Z(z)} \frac{d^2 Z(z)}{dz^2}. \tag{5.33}$$

The left hand side of Eq. (5.33) is a function of r only, whereas the right hand side is a function of z only. Therefore, both sides are equal to a constant. To be consistent with the fact that source terms are a function of e^{-jkz}, this constant is taken to be k^2. As a consequence, we can write:

$$\frac{dZ(z)}{dz} + k^2 Z(z) = 0, \tag{5.34a}$$

$$\frac{1}{r}\frac{d}{dr}\left(r\frac{dR(r)}{dr}\right) + \left(\omega^2\mu\varepsilon_c - k^2\right) R(r) = 0. \tag{5.34b}$$

Equation (5.34a) gives solutions of the form (multiplicative constants aside)

$$Z(z) = e^{-jkz}. \tag{5.35}$$

Defining ν by

$$\nu = k\sqrt{1 - v^2\mu\varepsilon_c} = k\sqrt{1 - \beta^2\mu_r\varepsilon_r}, \tag{5.36}$$

we can rewrite Eq. (5.34b) as

$$r^2\frac{d^2R(r)}{dr^2} + r\frac{dR(r)}{dr} - r^2\nu^2 R(r) = 0, \tag{5.37}$$

for $r \neq 0$. Calling $u = \nu r$, and $U(u) = R\left(\frac{u}{\nu}\right)$ we finally get:

$$u^2\frac{d^2U(u)}{du^2} + u\frac{dU(u)}{du} - u^2 U(u) = 0. \tag{5.38}$$

Equation (5.38) is thus found to be the modified Bessel equation of order 0 [64] and its solutions are combinations of modified Bessel functions $J_0(u)$ and $K_0(u)$, of order 0 and argument $u = \nu r$:

$$R(r) = U(u) = AK_0(u) + BI_0(u), \tag{5.39}$$

where A and B are parameters that will be found out by applying boundary conditions later. As a consequence of Eqs. (5.32), (5.35) and (5.39), a possible solution for the electric field in any concentric homogeneous region of space where $r \neq a$ and $r \neq 0$ is:

$$\boxed{E_z(r, z; \omega) = \left[AK_0(u) + BI_0(u)\right] e^{-jkz},} \tag{5.40}$$

where A and B are yet unknown parameters.

5.1.4 Deducing an Expression of $H_\theta(r, z)$ from $E_z(r, z)$

When calculating the impedance of various structures, matching equations for both the longitudinal electric field $E_z(r, z)$ and the magnetic field strength $H_\theta(r, z)$ will be needed. This paragraph is then devoted to obtain an expression for $H_\theta(r, z)$ from equation (5.40) in any concentric homogeneous region of space where there is no beam. Coming back to Maxwell's equation (5.21c), and assuming that $r \neq a$, $\rho(r \neq a) = 0$ and

$$\vec{\nabla} \times \vec{H}(r, z; \omega) = j\omega\varepsilon_c\vec{E}(r, z; \omega), \tag{5.41}$$

which, projected on the z-axis, becomes:

$$\frac{1}{r}\left(\frac{\partial r H_\theta(r, z; \omega)}{\partial r} - \frac{\partial H_r(r, z; \omega)}{\partial \theta}\right) = j\omega\varepsilon_c E_z(r, z), \tag{5.42}$$

where the expression of the curl operator in cylindrical coordinates was used. The assumed axisymmetry of the structure leads again to the fact that all partial derivatives with respect to the azimuthal coordinate θ vanish. Therefore, we get:

$$\frac{1}{r}\frac{\partial r H_\theta(r,z;\omega)}{\partial r} = j\omega\varepsilon_c E_z(r,z). \tag{5.43}$$

Replacing $E_z(r,z)$ by its expression in (5.40), we get:

$$\frac{1}{r}\frac{\partial r H_\theta(r,z;\omega)}{\partial r} = j\omega\varepsilon_c \left(AK_0(u) + BI_0(u)\right) e^{-jkz}. \tag{5.44}$$

Changing variables in the left hand side $r = u/\nu$, we get

$$\frac{1}{u}\frac{\partial u H_\theta(u,z;\omega)}{\partial u} = \frac{j\omega\varepsilon_c}{\nu} \left(AK_0(u) + BI_0(u)\right) e^{-jkz}. \tag{5.45}$$

Besides, two interesting properties of the Bessel functions are [64]:

$$\begin{cases} \dfrac{1}{u}\dfrac{\partial u K_1(u)}{\partial u} = -K_0(u), \\ \dfrac{1}{u}\dfrac{\partial u I_1(u)}{\partial u} = I_0(u). \end{cases} \tag{5.46}$$

Then, one solution to equation (5.45) is of the form

$$H_\theta(u,z;\omega) = \frac{j\omega\varepsilon_c}{\nu}\left[-AK_1(u) + BI_1(u)\right] e^{-jkz}. \tag{5.47}$$

Acknowledging that [64] :

$$\begin{cases} K_0'(u) = -K_1(u), \\ I_0'(u) = I_1(u), \end{cases} \tag{5.48}$$

we finally obtain

$$\boxed{H_\theta(r,z;\omega) = \frac{j\omega\varepsilon_c}{\nu}\left[AK_0'(u) + BI_0'(u)\right] e^{-jkz}.} \tag{5.49}$$

Now that general forms for both electric and magnetic fields were obtained, the next step is to apply the boundary conditions. These boundary conditions all depend on the surrounding structure, except for the specific boundary condition at $r = a$, i.e. at the beam edge. In fact, as stated before and shown in Fig. 5.2, the beam is assumed not to hit any structure. As a consequence, a general form of the electric field E_z taking into account that there is beam at $r = a$ is derived in the following paragraph.

5.1.5 Field Matching at the Beam Location

Matching the Electric Field at the Beam Location ($r = a$)

We use the geometry of Fig. 5.2, where we only need to specify that $b > a$. Following the notations shown in this figure, and using Eq. (5.40), we can write that the electric field $E_z^{(1)}(r,z)$ in region 1 ($r < a$, inside the ring beam) is defined by:

$$E_z^{(1)}(r,z;\omega) = \left[A_1K_0(u) + B_1I_0(u)\right] e^{-jkz}. \tag{5.50}$$

The behavior of Bessel functions is known and in particular $K_0(u)$ diverges if $u \to 0$ (see Ref. [64]). The electrical field must remain finite on the z-axis, and, as a consequence, A_1 has to be set to 0. Equation (5.50) then simplifies to:

$$E_z^{(1)}(r, z; \omega) = B_1 I_0(u) e^{-jkz}. \tag{5.51}$$

The electric field $E_z^{(1)}(r, z)$ in region (2) ($a < r \leq b$, in the vacuum between the ring beam and the surrounding structure) is defined by:

$$E_z^{(2)}(r, z; \omega) = \left[A_2 K_0(u) + B_2 I_0(u)\right] e^{-jkz}. \tag{5.52}$$

The tangential components of the electric field across an interface are continuous [29], and that is why we can write that

$$E_z^{(1)}(r = a - \delta, z; \omega) = E_z^{(2)}(r = a + \delta, z; \omega), \tag{5.53}$$

where δ is infinitely small. Replacing $E_z^{(1)}(r, z)$ and $E_z^{(2)}(r, z)$ by their expressions in Eqs. (5.51) and (5.52), we get:

$$B_1 I_0(\nu_1 a) = A_2 K_0(\nu_2 a) + B_2 I_0(\nu_2 a), \tag{5.54}$$

where

$$\nu_1 = k\sqrt{1 - \beta^2 \mu_r^{(1)} \varepsilon_r^{(1)}}, \tag{5.55}$$

and

$$\nu_2 = k\sqrt{1 - \beta^2 \mu_r^{(2)} \varepsilon_r^{(2)}}, \tag{5.56}$$

with $\mu_r^{(i)}$ and $\varepsilon_r^{(i)}$ defined as the complex relative permeabilities and permittivities of the material in region i. With this expression for B_1, Eq. (5.51) then becomes

$$E_z^{(1)}(r, z; \omega) = \frac{A_2}{I_0(\nu_1 a)} \left(K_0(\nu_2 a) + \frac{B_2}{A_2} I_0(\nu_2 a) I_0(u) \right) e^{-jkz}. \tag{5.57}$$

Let us now define the function $F_0(u)$ such that

$$F_0(u) = K_0(u) - \alpha_2 I_0(u), \tag{5.58}$$

with $\alpha_2 = -\frac{B_2}{A_2}$. Equations (5.57) and (5.52) then become, with the definition of $A_2' = A_2 / I_0(\nu_1 a)$,

$$E_z^{(1)}(r, z; \omega) = A_2' F_0(\nu_2 a) I_0(u) e^{-jkz}, \tag{5.59a}$$
$$E_z^{(2)}(r, z; \omega) = A_2' I_0(\nu_1 a) F_0(u) e^{-jkz}. \tag{5.59b}$$

In this case, both regions 1 and 2 are made of the same material. Thus, we set $\nu_1 a = \nu_2 a = s$. We finally obtain:

$$E_z^{(1)}(r, z; \omega) = A_2' F_0(s) I_0(u) e^{-jkz}, \tag{5.60a}$$
$$E_z^{(2)}(r, z; \omega) = A_2' I_0(s) F_0(u) e^{-jkz}. \tag{5.60b}$$

Applying the Matching Condition for $\partial E_z(r,z)/\partial r$ at the Beam Location

The rest of this section is devoted to find an expression for constant A_2' in Eq. (5.60) by matching the partial derivatives of the electric field in regions 1 and 2. Contrary to the electric field, its partial derivative $\partial E_z(r,z)\partial r$ is not necessarily continuous at the beam location $r = a$. Let us come back to Eq. (5.30) to evaluate this discontinuity. Acknowledging the z-dependence of E_z in Eq. (5.35), we get:

$$\frac{1}{r}\frac{\partial}{\partial r}\left(r\frac{\partial E_z}{\partial r}\right) + k^2(\beta^2\mu_r\varepsilon_r - 1)E_z = \frac{j\omega Q}{2\pi a\varepsilon v^2}\delta(r-a)\left(\beta^2\mu_r\hat{\varepsilon}_r - 1\right)e^{-jkz}. \tag{5.61}$$

In fact, let us multiply both sides of Eq. (5.61) by r and integrate between $r = a - \Delta$ and $r = a + \Delta$, with Δ defined as a strictly positive number. We obtain:

$$\begin{aligned}\int_{r=a-\Delta}^{r=a+\Delta}\left[\frac{\partial}{\partial r}\left(r\frac{\partial E_z}{\partial r}\right)\right]dr + k^2(\beta^2\mu_r\varepsilon_r - 1)\int_{r=a-\Delta}^{r=a+\Delta}[rE_z]\,dr \\ = \frac{j\omega Q}{2\pi a\varepsilon v^2}\left(\beta^2\mu_r\hat{\varepsilon}_r - 1\right)e^{-jkz}\int_{r=a-\Delta}^{r=a+\Delta}[r\delta(r-a)]\,dr.\end{aligned} \tag{5.62}$$

If we remember the property of the delta function given in Eq. (5.12), we get:

$$\left[r\frac{\partial E_z}{\partial r}\right]_{r=a-\Delta}^{r=a+\Delta} + k^2(\beta^2\mu_r\varepsilon_r - 1)\int_{r=a-\Delta}^{r=a+\Delta}[rE_z]\,dr = \frac{j\omega Q}{2\pi\varepsilon v^2}\left(\beta^2\mu_r\hat{\varepsilon}_r - 1\right)e^{-jkz}. \tag{5.63}$$

The longitudinal electrical field $E_z(r)$ is continuous at $r = a$, and therefore the function $r \mapsto rE_z(r)$ is also continuous at $r = a$. Thus, the function $r \mapsto rE_z(r)$ is continuous on the interval $[a-\Delta; a+\Delta]$. Taking out the factor e^{-jkz} from the integral, this function takes real values. As a consequence, the function $r \mapsto rE_z(r)$ is integrable, and we define $r \mapsto F(r)$, one primitive function so that $F'(r) = rE(r)$, which is derivable by construction and then continuous on $[a-\Delta; a+\Delta]$. Then we have :

$$\begin{aligned}\lim_{\Delta\to 0}\int_{r=a-\Delta}^{r=a+\Delta}[rE_z]\,dr &= \lim_{\Delta\to 0}\left([F(r)]_{r=a-\Delta}^{r=a+\Delta}\right) \\ &= \lim_{\Delta\to 0}\left(F(a+\Delta) - F(a-\Delta)\right) \\ &= 0.\end{aligned} \tag{5.64}$$

As a consequence, we can write, acknowledging again that $\Delta \to 0$:

$$\left.\frac{\partial E_z(r,z)}{\partial r}\right|_{r=a+\Delta} - \left.\frac{\partial E_z(r,z)}{\partial r}\right|_{r=a-\Delta} = \frac{j\omega Q}{2\pi a\varepsilon v^2}\left(\beta^2\mu_r\hat{\varepsilon}_r - 1\right)e^{-jkz}. \tag{5.65}$$

If we replace $E_z(r,z)$ by its expression in Eq. (5.60), remembering that regions 1 and 2 are both vacuum, we obtain:

$$A_2'\nu_1\left[I_0(s)F_0'(s) - F_0(s)I_0'(s)\right] = \frac{j\omega Q}{2\pi a\varepsilon v^2}\left(\beta^2\mu_r\hat{\varepsilon}_r - 1\right). \tag{5.66}$$

Fortunately, the Wronskian of modified Bessel functions simplifies to this expression (see Ref. [64]):

$$\left[I_0(s)K_0'(s) - K_0(s)I_0'(s)\right] = -\frac{1}{s}. \tag{5.67}$$

We can get a similar expression for the Wronskian of F_0 and I_0

$$\begin{aligned} I_0(s)F_0'(s) - F_0(s)I_0'(s) &= I_0(s)\left(K_0'(s) - \alpha_2 I_0'(s)\right) - \left(K_0(s) - \alpha_2 I_0(s)\right) I_0'(s) \\ &= I_0(s)K_0'(s) - \alpha_2 I_0(s)I_0'(s) - K_0(s)I_0'(s) + \alpha_2 I_0(s)I_0'(s) \\ &= I_0(s)K_0'(s) - K_0(s)I_0'(s) \\ &= -\frac{1}{s}. \end{aligned} \tag{5.68}$$

Finally, we obtain the following expression for A_2':

$$A_2' = \frac{j\omega Q}{2\pi\varepsilon v^2}\left(1 - \beta^2\mu_r\hat{\varepsilon}_r\right). \tag{5.69}$$

As a consequence, whatever the axisymmetric surrounding structure at $r \geq b$, the general form for the longitudinal electric fields $E_z^{(2)}$ in region 2 is given by :

$$\boxed{E_z^{(2)}(r,z;\omega) = \tfrac{j\omega Q}{2\pi\varepsilon v^2}\left(1 - \beta^2\mu_r\hat{\varepsilon}_r\right) I_0(s)\left[K_0(u) - \alpha_2 I_0(u)\right] e^{-jkz}.} \tag{5.70}$$

From this equation, a general expression for the longitudinal impedance will be deduced in the following section.

5.1.6 General Expressions of the Longitudinal Impedance

Now that the electric field is given by Eq. (5.70), Eq. (5.14) becomes

$$Z_{//}(\omega) = -\frac{j\omega\left(1 - \beta^2\mu_r\hat{\varepsilon}_r\right) I_0(s)}{2\pi\varepsilon v^2}\int_{-\infty}^{+\infty}\left[K_0(s) - \alpha_2 I_0(s)\right] dz, \tag{5.71}$$

and, defining L as the length of this structure, we finally obtain a general expression for the total longitudinal impedance $Z_{//}^{total}(\omega)$:

$$\boxed{Z_{//}^{total}(\omega) = -\tfrac{j\omega L\left(1-\beta^2\mu_r\hat{\varepsilon}_r\right) I_0(s)}{2\pi\varepsilon v^2}\left[K_0(s) - \alpha_2 I_0(s)\right].} \tag{5.72}$$

As the structure around the beam is not yet defined, the constant α_2 is still unknown, but all other parameters are known. Now is the time to define the beam surroundings and determine the expression for α_2. We start by obtaining the expressions for the space charge impedance (direct and indirect contributions), and continue with the resistive wall impedance and wall impedance.

Longitudinal Space Charge Impedance

The direct space charge impedance can be obtained if one considers that the beam travels in vacuum. In this case, region (2) extends to infinity, and Eq. (5.70) has to remain finite when $r \mapsto \infty$, i.e. when $u \mapsto \infty$. The divergence of modified Bessel function $I_0(u)$ when $u \mapsto \infty$ imposes that $\alpha_2 = 0$. Therefore the longitudinal direct space charge impedance reads:

$$\boxed{Z_{//}^{direct\,SC}(\omega) = -\tfrac{j\omega L\left(1-\beta^2\mu_r\hat{\varepsilon}_r\right) I_0(s)}{2\pi\varepsilon v^2} K_0(s).} \tag{5.73}$$

The total space charge impedance is obtained by assuming that the beam pipe at $r = b$ is made of a perfect conductor (see Fig. 5.1). In that case, the matching conditions between regions 2 ($r < b$) and region 3 ($r \geq b$) for the electric fields $\vec{E}^{(2)}$ and $\vec{E}^{(3)}$ at $r = b$ impose that:

$$E_z^{(2)}(r = b) = E_z^{(3)}(r = b) = 0. \tag{5.74}$$

The general form of the electric field in region (2) given in Eq. (5.70) becomes at $r = b$:

$$E_z^{(2)}(r = b, z; \omega) = \frac{j\omega Q}{2\pi\varepsilon v^2}\left(1 - \beta^2\mu_r\hat{\varepsilon}_r\right) I_0(s)\left(K_0(\nu b) - \alpha_2 I_0(\nu b)\right) e^{-jkz} = 0, \tag{5.75}$$

from which the value for α_2 can be deduced:

$$\alpha_2 = \frac{K_0(\nu b)}{I_0(\nu b)}. \tag{5.76}$$

Finally, from Eq. (5.72), a general expression for the longitudinal space-charge impedance is

$$\boxed{Z_{//}^{SC}(\omega) = -\frac{j\omega L\left(1-\beta^2\mu_r\hat{\varepsilon}_r\right)I_0(s)}{2\pi\varepsilon v^2}\left(K_0(s) - \frac{K_0(x)}{I_0(x)}I_0(s)\right),} \tag{5.77}$$

where we have defined $x = \nu b$. The indirect space charge impedance is defined as the contribution due to the perfect conducting wall only and we can write

$$Z_{//}^{SC} = Z_{//}^{direct\,SC} + Z_{//}^{indirect\,SC}, \tag{5.78}$$

which leads to the expression of the indirect space charge impedance in our case:

$$\boxed{Z_{//}^{indirect\,SC}(\omega) = \frac{j\omega L\left(1-\beta^2\mu_r\hat{\varepsilon}_r\right)I_0(s)^2}{2\pi\varepsilon v^2}\frac{K_0(x)}{I_0(x)}.} \tag{5.79}$$

We now evaluate the longitudinal impedance of resistive structures.

Longitudinal Wall and Resistive-Wall Impedance

The resistive wall impedance is defined as the contribution of the resistive part of the beam pipe to the total longitudinal impedance. Therefore the space charge impedance $Z_{//}^{SC}(\omega)$ has to be subtracted from the total impedance in order to get the longitudinal resistive wall impedance $Z_{//}^{RW}(\omega)$

$$\begin{aligned} Z_{//}^{RW}(\omega) &= Z_{//}^{total}(\omega) - Z_{//}^{SC}(\omega), \\ &= -\frac{j\omega L\left(1 - \beta^2\mu_r\hat{\varepsilon}_r\right) I_0^2(s)}{2\pi\varepsilon v^2}\left(\frac{K_0(x)}{I_0(x)} - \alpha_2\right), \end{aligned} \tag{5.80}$$

where Eqs. (5.72) and (5.77) were used and the only unknown parameter α_2 is to be deduced from matching the fields at all material interfaces within the beam pipe. The wall impedance has been recently introduced to account for the fact that the ac magnetic images vanish when the frequency tends to 0 when performing classical simplifications [65]. The wall impedance $Z_{//}^{Wall}$ is defined as the sum of the impedance contributions due to the wall, including the resistive wall and indirect space charge, excluding only the direct space charge:

$$\begin{aligned} Z_{//}^{Wall}(\omega) &= Z_{//}^{total}(\omega) - Z_{//}^{direct\,SC}(\omega) \\ &= Z_{//}^{RW}(\omega) + Z_{//}^{indirect\,SC}(\omega), \end{aligned} \tag{5.81}$$

and we have finally

$$\boxed{Z_{//}^{Wall}(\omega) = \frac{j\omega L\left(1-\beta^2\mu_r\hat{\varepsilon}_r\right)I_0^2(s)}{2\pi\varepsilon v^2}\alpha_2.} \tag{5.82}$$

This general equation will be used in the following section to assess the longitudinal wall impedance of various axisymmetric structures composed of one or more layers of distinct materials. For any of these structures, matching the fields at the boundaries of each layer will lead to an expression of α_2, and as a consequence an expression for the longitudinal wall impedance.

5.1.7 Longitudinal Wall Impedance of Axisymmetric Multilayered Structures

Matching the electromagnetic fields at the boundaries of each layer leads to an expression for the longitudinal wall impedance for this structure. For this purpose, we need the general expression of $E_z^{(i)}$ and $H_\theta^{(i)}$ for any homogeneous axisymmetric layer (i) around the beam in Eqs. (5.40) and (5.49):

$$\left\{ \begin{aligned} E_z^{(i)}(r,z;\omega) &= \left[A_i K_0(\nu_i r) + B_i I_0(\nu_i r)\right] e^{-jkz} \\ H_\theta^{(i)}(r,z;\omega) &= \frac{j\omega\varepsilon_c^{(i)}}{\nu_i}\left[A_i K_0'(\nu_i r) + B_i I_0'(\nu_i r)\right] e^{-jkz}, \end{aligned} \right. \tag{5.83}$$

where $\varepsilon_c^{(i)} = \varepsilon_0\varepsilon_r^{(i)}$ and $\nu_i = k\sqrt{1-\beta^2\mu_r^{(i)}\varepsilon_r^{(i)}}$ are respectively the complex permittivity and the radial propagation constant of material (i). Similarly to paragraph 5.1.5, we define $\alpha_i = B_i/A_i$ and get:

$$\left\{ \begin{aligned} E_z^{(i)}(r,z;\omega) &= A_i\left[K_0(\nu_i r) + \alpha_i I_0(\nu_i r)\right] e^{-jkz}, \\ H_\theta^{(i)}(r,z;\omega) &= \frac{j\omega\varepsilon_0\varepsilon_r^{(i)}}{\nu_i}A_i\left[K_0'(\nu_i r) + \alpha_i I_0'(\nu_i r)\right] e^{-jkz}. \end{aligned} \right. \tag{5.84}$$

Finally, the interfaces between layer (i) and layer $(i+1)$ are defined to be located at $r = a_i$. As a consequence, the beam location is from now on defined as a_1, and we have $s = \nu_1 a_1 = \nu_2 a_1$. Now, we are ready to match the electromagnetic fields at each boundary.

Longitudinal Wall Impedance of a Monolayer Beam Pipe

In this paragraph, the beam pipe is assumed to be made of a single resistive layer extending from $r = a_2$ to $r = +\infty$. In Fig. 5.3, this infinite resistive layer is called region (3). At any boundary, the tangential components of the electric field $\vec{E}$ are continuous, and, in the absence of surface current, the tangential components of the magnetic field strength $\vec{H}$

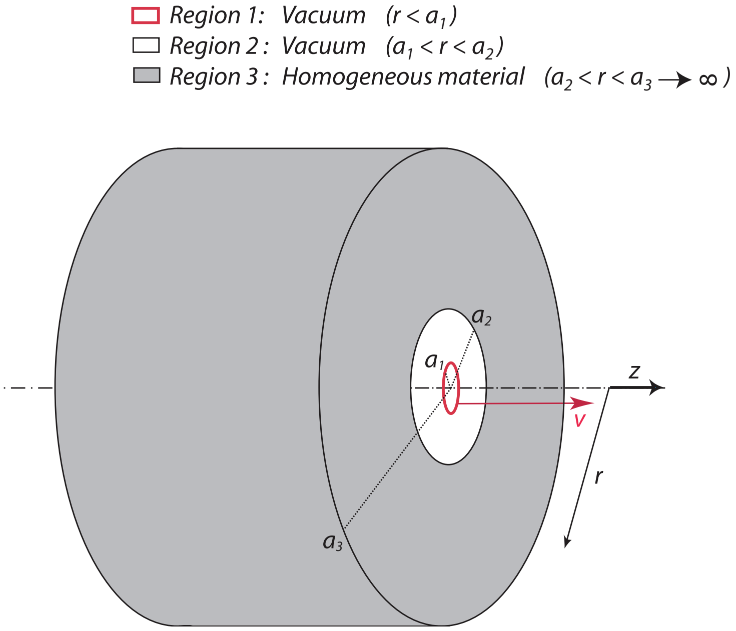

Figure 5.3: Sketch of a ring beam moving with velocity $\vec{v}$ parallel to the z-axis within a monolayer beam pipe extending to infinity ($a_3 \to \infty$).

are also continuous [29]. As a consequence, we can write the following matching equations for the longitudinal electric field E_z and the azimuthal magnetic field H_θ at $r = a_2$:

$$\begin{cases} E_z^{(2)}(a_2, z; \omega) = E_z^{(3)}(a_2, z; \omega), \\ H_\theta^{(2)}(a_2, z; \omega) = H_\theta^{(3)}(a_2, z; \omega). \end{cases} \tag{5.85}$$

Using general field expressions in Eq. (5.84), we obtain

$$\begin{cases} A_2 \left[K_0(\nu_2 a_2) + \alpha_2 I_0(\nu_2 a_2)\right] = A_3 \left[K_0(\nu_3 a_2) + \alpha_3 I_0(\nu_3 a_2)\right], \\ \dfrac{\varepsilon_r^{(2)} A_2}{\nu_2} \left[K_0'(\nu_2 a_2) + \alpha_2 I_0'(\nu_2 a_2)\right] = \dfrac{\varepsilon_r^{(3)} A_3}{\nu_3} \left[K_0'(\nu_3 a_2) + \alpha_3 I_0'(\nu_3 a_2)\right]. \end{cases} \tag{5.86}$$

To solve the linear system of two equations (5.86), it is useful to note that the electric field in region (3) must remain finite when $r \to \infty$. As the modified Bessel function $I_0(u)$ diverges when $r \to \infty$, its contribution in $E_z^{(3)}$ must vanish. Thus, $\alpha_3 = 0$, and the system (5.86) becomes

$$\begin{cases} K_0(\nu_2 a_2) + \alpha_2 I_0(\nu_2 a_2) = A_3' K_0(\nu_3 a_2), \\ \dfrac{\varepsilon_r^{(2)}}{\nu_2} \left[K_0'(\nu_2 a_2) + \alpha_2 I_0'(\nu_2 a_2)\right] = \dfrac{\varepsilon_r^{(3)} A_3'}{\nu_3} K_0'(\nu_3 a_2), \end{cases} \tag{5.87}$$

where we also defined $A_3' = A_3/A_2$, in order to get rid of A_2 in the system. This linear system of two equations (5.87) has two unknowns : A_3' and α_2. Solving this system yields the expression for α_2:

$$\boxed{\alpha_2 = \frac{\varepsilon_r^{(2)} \nu_3 K_0(\nu_3 a_2) K_0'(\nu_2 a_2) - \varepsilon_r^{(3)} \nu_2 K_0(\nu_2 a_2) K_0'(\nu_3 a_2)}{\varepsilon_r^{(2)} \nu_3 I_0'(\nu_2 a_2) K_0(\nu_3 a_2) - \varepsilon_r^{(3)} \nu_2 I_0(\nu_2 a_2) K_0'(\nu_3 a_2)}.} \tag{5.88}$$

Now that α_2 was derived from field-matching, we can reinject its expression in Eq. 5.82 applied to region (2) to get the longitudinal wall impedance formula for an infinite axisymmetric monolayer beam pipe:

$$\boxed{Z_{//}^{Wall}(\omega) = \frac{j\omega L\left(1-\beta^2\mu_r\hat{\varepsilon}_r\right)I_0^2(s)}{2\pi\varepsilon v^2}\alpha_2,} \tag{5.89}$$

where $\varepsilon_r^{(2)}$ and $\mu_r^{(2)}$ are respectively the real relative permittivity and relative permeability of the material composing both regions (1) and (2). In the usual case where regions (1) and (2) are vacuum, Eq. (5.89) simplifies to

$$Z_{//}^{Wall}(\omega) = \frac{j\omega L I_0^2(s)}{2\pi\gamma^2\varepsilon_0 v^2}\alpha_2. \tag{5.90}$$

This expression of the longitudinal impedance is compared to the expression found by Henry and Napoly in Ref. [50] for the total impedance of ultrarelativistic particles within a cylindrical beam pipe made of graphite in Fig. 5.4, where a very good agreement was obtained in this case. For numerical reasons, the expression in Eq. (5.90) turned out to be easier to compute for *Mathematica* at high frequencies than the expression derived by Henry and Napoly, which uses the Hankel functions. The effect of a non ultrarelativistic beam can be seen in Fig. 5.5, where the wall impedances due to a graphite beam pipe at injection and extraction in the SPS are plotted against the *classical thick wall impedance* $Z_{//}^{TW}$ (not to be confused with the *classical thick resistive wall impedance*), which is an

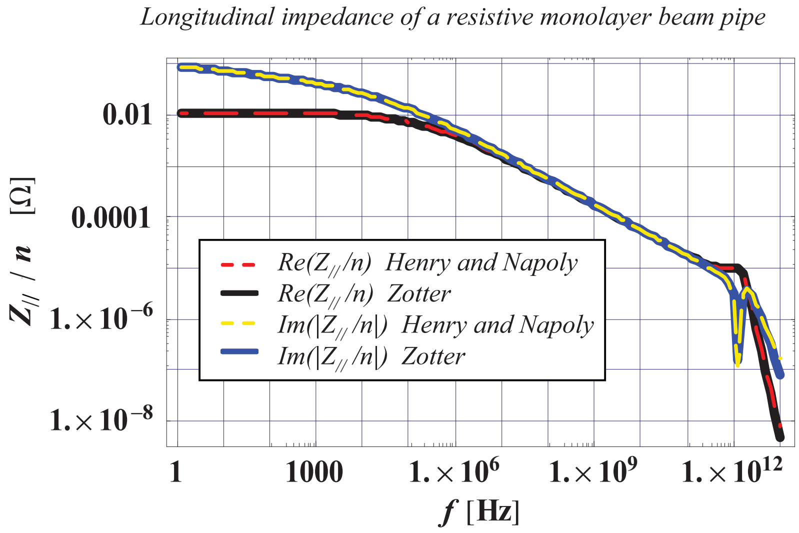

Figure 5.4: Total longitudinal impedance of a 1 m cylindrical beam pipe made of graphite of radius $a_1 = 2$ mm, and resistivity $\rho = 10\mu\Omega.m$. To be able to compare both formulae, the beam velocity has to be ultrarelativistic $v = c$, and the conductivity of graphite is assumed not frequency dependent. In this case, the space charge contribution vanish and the total impedance, wall impedance and resistive wall impedances are equal. It is usual to display the longitudinal impedance as $Z_{//}/n$, where $n = f/f_0$.

approximation of Eq. (5.90) when $\omega \ll \beta c\gamma/a_2$ that is known to be valid only in an intermediate range of frequencies [56]:

$$Z_{//}^{TW}(\omega) = (1+j)\frac{L}{2\pi b}\sqrt{\frac{\omega Z_0 \rho}{2c}} - j\frac{Z_0 L\omega}{2\pi\gamma^2\beta^2 c}\log\left(\frac{\omega b}{v\gamma}\right). \tag{5.91}$$

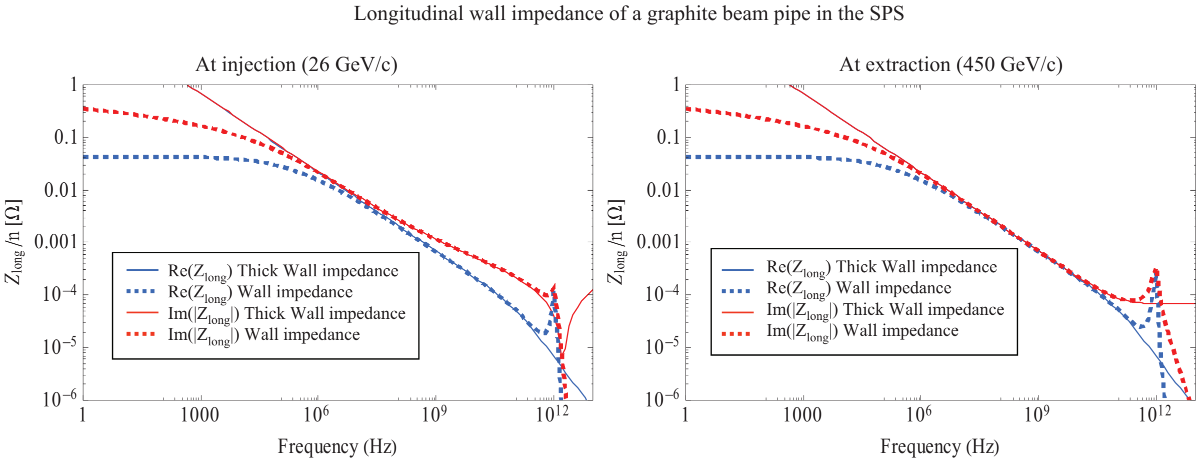

Figure 5.5: Longitudinal wall impedance of a 1 m cylindrical beam pipe made of graphite with radius $a_1 = 2$ mm, DC resistivity $\rho_{DC} = 10\ \mu\Omega.m$ and electron relaxation time $\tau_e = 8\ 10^{-13}$ s at SPS injection (left) and at SPS extraction (right). The approximations in the classical thick wall impedance are not valid anymore at low frequencies and high frequencies. The impact of using the wall impedance instead of the resistive wall impedance is observed at injection, as the imaginary part of the wall impedance is significantly higher than the resistive wall impedance from 100 MHz up to 0.1 THz. This difference can be explained by the significant indirect space charge contribution at injection energy in the SPS. We remind that the longitudinal impedance $Z_{//}$ is sometimes referred to as Z_{long} for legibility reasons.

Besides, to take into account the relaxation time of electrons in the conductor, the conductivity σ of graphite was assumed to follow Drude's model [66]

$$\sigma(\omega) = \frac{\sigma_{DC}}{1 + j\omega\tau_e}, \tag{5.92}$$

where $\sigma_{DC} = 1/\rho_{DC}$ is the DC conductivity and τ_e is the relaxation time of the electrons in the conductor.

In Ref. [67], K. Yokoya derived form factors that enable to compute the impedance for a resistive beam pipe of arbitrary cross section providing (a) the beam is ultrarelativistic, (b) the beam pipe is longitudinally uniform, and (c) the skin depth

$$\delta = \sqrt{\frac{2}{\omega\mu\sigma}},$$

is much smaller than the dimensions of the beam pipe and the thickness of the material. Between a circular cross section of radius a_1 and a geometry consisting of two parallel plates separated by a gap $2a_1$, the form factor for the longitudinal impedance is 1. Therefore, this cylindrical beam pipe made of graphite of radius $a_1 = 2$ mm could be considered a good approximation for a LHC collimator (see an example of collimator in Fig. 5.6), whose closed half gap (2 mm) is much smaller than the width of the jaws (about 10 cm). One such collimator was installed in the SPS, and we first chose this example to illustrate the effect of the indirect space charge impedance on the wall impedance.

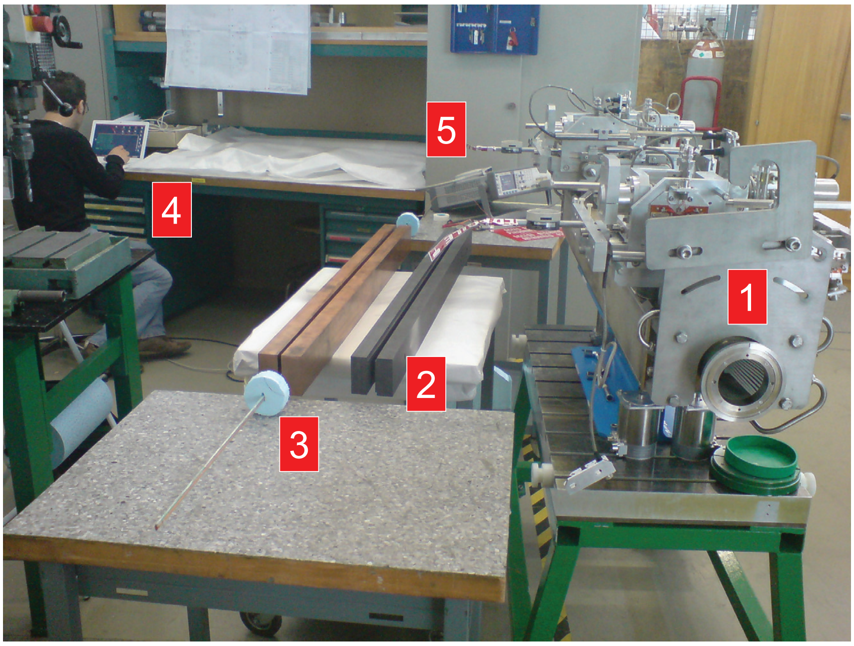

Figure 5.6: Picture of our setup for impedance measurements: $\boxed{1}$ full LHC collimator assembly (the graphite jaws inside are not visible); $\boxed{2}$ LHC collimator graphite jaws; $\boxed{3}$ LHC collimator copper jaws with 2 m long measurement coil; $\boxed{4}$ Federico with MacBook Pro; $\boxed{5}$ *Agilent* LCR meter.

Longitudinal Wall Impedance of a Bilayer Beam Pipe

In this section, the beam pipe is made of two concentric resistive layers : region (3) is made of a given homogeneous material and region (4) is made of another homogeneous material extending to infinity (see Fig. 5.7). To calculate the fields in this bilayer configuration, we will acknowledge again that the tangential components of both electric field $\vec{E}$ and magnetic field strength $\vec{H}$ are continuous at any interface where there is no charge and surface current. Then, the following matching equations for the longitudinal component of the electric field E_z and the azimuthal component of the magnetic field strength H_θ obtained in Eqs. (5.85) still hold at $r = a_2$, boundary between regions (2) and (3):

$$\begin{cases} E_z^{(2)}(a_2, z; \omega) = E_z^{(3)}(a_2, z; \omega), \\ H_\theta^{(2)}(a_2, z; \omega) = H_\theta^{(3)}(a_2, z; \omega). \end{cases} \tag{5.93}$$

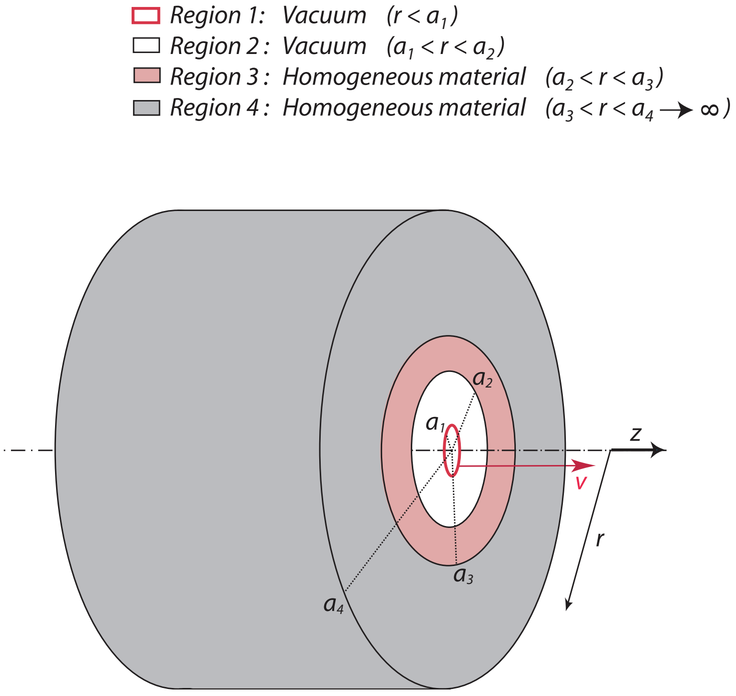

Figure 5.7: Sketch of a ring beam moving with velocity $\vec{v}$ parallel to the z-axis within a bilayer beam pipe, with its outer layer extending to infinity ($a_4 \to \infty$).

However in the bilayer case, fields also have to be matched at $r = a_3$, boundary between regions (3) and (4), which yields two additional equations.

$$\begin{cases} E_z^{(3)}(a_3, z; \omega) = E_z^{(4)}(a_3, z; \omega), \\ H_\theta^{(3)}(a_3, z; \omega) = H_\theta^{(4)}(a_3, z; \omega). \end{cases} \tag{5.94}$$

Using general field expressions in (5.84), we obtain the following linear system of four equations

$$\begin{cases} A_2 \left[K_0(\nu_2 a_2) + \alpha_2 I_0(\nu_2 a_2)\right] = A_3 \left[K_0(\nu_3 a_2) + \alpha_3 I_0(\nu_3 a_2)\right], \\ \dfrac{\varepsilon_r^{(2)} A_2}{\nu_2} \left[K_0'(\nu_2 a_2) + \alpha_2 I_0'(\nu_2 a_2)\right] = \dfrac{\varepsilon_r^{(3)} A_3}{\nu_3} \left[K_0'(\nu_3 a_2) + \alpha_3 I_0'(\nu_3 a_2)\right], \\ A_3 \left[K_0(\nu_3 a_3) + \alpha_3 I_0(\nu_3 a_3)\right] = A_4 \left[K_0(\nu_4 a_3) + \alpha_4 I_0(\nu_4 a_3)\right], \\ \dfrac{\varepsilon_r^{(3)} A_3}{\nu_3} \left[K_0'(\nu_3 a_3) + \alpha_3 I_0'(\nu_3 a_3)\right] = \dfrac{\varepsilon_r^{(4)} A_4}{\nu_4} \left[K_0'(\nu_4 a_3) + \alpha_4 I_0'(\nu_4 a_3)\right]. \end{cases} \tag{5.95}$$

As in the monolayer case, the electric field can not diverge when $r \to \infty$, and we can write $\alpha_4 = 0$ in order to suppress the diverging term $I_0(u)$ in region (4) which extends to infinity. Then, the system (5.95) becomes:

$$\begin{cases} K_0(\nu_2 a_2) + \alpha_2 I_0(\nu_2 a_2) = A_3' \left[K_0(\nu_3 a_2) + \alpha_3 I_0(\nu_3 a_2)\right], \\ \dfrac{\varepsilon_r^{(2)}}{\nu_2} \left[K_0'(\nu_2 a_2) + \alpha_2 I_0'(\nu_2 a_2)\right] = \dfrac{\varepsilon_r^{(3)} A_3'}{\nu_3} \left[K_0'(\nu_3 a_2) + \alpha_3 I_0'(\nu_3 a_2)\right], \\ A_3' \left[K_0(\nu_3 a_3) + \alpha_3 I_0(\nu_3 a_3)\right] = A_4' K_0(\nu_4 a_3), \\ \dfrac{\varepsilon_r^{(3)} A_3'}{\nu_3} \left[K_0'(\nu_3 a_3) + \alpha_3 I_0'(\nu_3 a_3)\right] = \dfrac{\varepsilon_r^{(4)} A_4'}{\nu_4} K_0'(\nu_4 a_3), \end{cases} \tag{5.96}$$

where we also defined $A_3' = A_3/A_2$ and $A_4' = A_4/A_2$, in order to get rid of A_2 in the system. We are left with a nonlinear system of four equations and four unknowns (α_2, α_3, A_3' and A_4'). However, in order to be able to use the tools designed to solve linear systems embedded in *Mathematica*, the non-linear system Eqs. (5.96) can be transformed into linear system (5.97) if we switch back from unknowns (α_2, α_3, A_3' and A_4') to unknowns (α_2, B_3', A_3' and A_4'), where $\alpha_i = B_i/A_i$ as already defined between Eqs. (5.83) and (5.84), and $B_i' = B_i/A_2$.

$$\begin{cases} K_0(\nu_2 a_2) + \alpha_2 I_0(\nu_2 a_2) = A_3' K_0(\nu_3 a_2) + B_3' I_0(\nu_3 a_2), \\ \dfrac{\varepsilon_r^{(2)}}{\nu_2} \left[K_0'(\nu_2 a_2) + \alpha_2 I_0'(\nu_2 a_2)\right] = \dfrac{\varepsilon_r^{(3)}}{\nu_3} \left[A_3' K_0'(\nu_3 a_2) + B_3' I_0'(\nu_3 a_2)\right], \\ A_3' K_0(\nu_3 a_3) + B_3' I_0(\nu_3 a_3) = A_4' K_0(\nu_4 a_3), \\ \dfrac{\varepsilon_r^{(3)}}{\nu_3} \left[A_3' K_0'(\nu_3 a_3) + B_3' I_0'(\nu_3 a_3)\right] = \dfrac{\varepsilon_r^{(4)} A_4'}{\nu_4} K_0'(\nu_4 a_3). \end{cases} \tag{5.97}$$

This system can then be solved symbolically for instance with *Mathematica*, and we obtain the following expression for the parameter α_2 :

$$\boxed{\alpha_2 = \frac{K_0(\nu_2 a_2)[SK_1(\nu_4 a_3) - QK_0(\nu_4 a_3)] - K_1(\nu_2 a_2)[PK_0(\nu_4 a_3) + RK_1(\nu_4 a_3)]}{I_1(\nu_2 a_2)[PK_0(\nu_4 a_3) + RK_1(\nu_4 a_3)] + I_0(\nu_2 a_2)[SK_1(\nu_4 a_3) - QK_0(\nu_4 a_3)]},} \tag{5.98}$$

with the parameters P, Q, R and S defined as:

$$\begin{aligned} P &= \varepsilon_r^{(2)} \varepsilon_r^{(3)} \nu_3 \nu_4 \left[I_1(\nu_3 a_3) K_0(\nu_3 a_2) + I_0(\nu_3 a_2) K_1(\nu_3 a_3)\right], \\ Q &= \left(\varepsilon_r^{(3)}\right)^2 \nu_2 \nu_4 \left[I_1(\nu_3 a_2) K_1(\nu_3 a_3) - I_1(\nu_3 a_3) K_1(\nu_3 a_2)\right], \\ R &= \varepsilon_r^{(2)} \varepsilon_r^{(4)} \left(\nu_3\right)^2 \left[I_0(\nu_3 a_3) K_0(\nu_3 a_2) - I_0(\nu_3 a_2) K_0(\nu_3 a_3)\right], \\ S &= \varepsilon_r^{(3)} \varepsilon_r^{(4)} \nu_2 \nu_3 \left[I_1(\nu_3 a_2) K_0(\nu_3 a_3) + I_0(\nu_3 a_3) K_1(\nu_3 a_2)\right]. \end{aligned} \tag{5.99}$$

As it was performed for a monolayer beam pipe, expression Eq. (5.98) for parameter α_2 can then be put into Eq. (5.82) applied to region (2) to obtain the analytic expression of longitudinal impedance of a bilayer beam pipe. Two examples of bilayer beam pipes (graphite+vacuum and a thin layer of copper+vacuum) are presented in Fig. (5.8).

Longitudinal Wall Impedance of a Trilayer Beam Pipe

In this paragraph, the beam pipe is made of three concentric resistive layers (see figure 5.9): region 3 made of a given homogeneous material, region 4 made of another homogeneous material, and region (5) made of yet another homogeneous material extending to

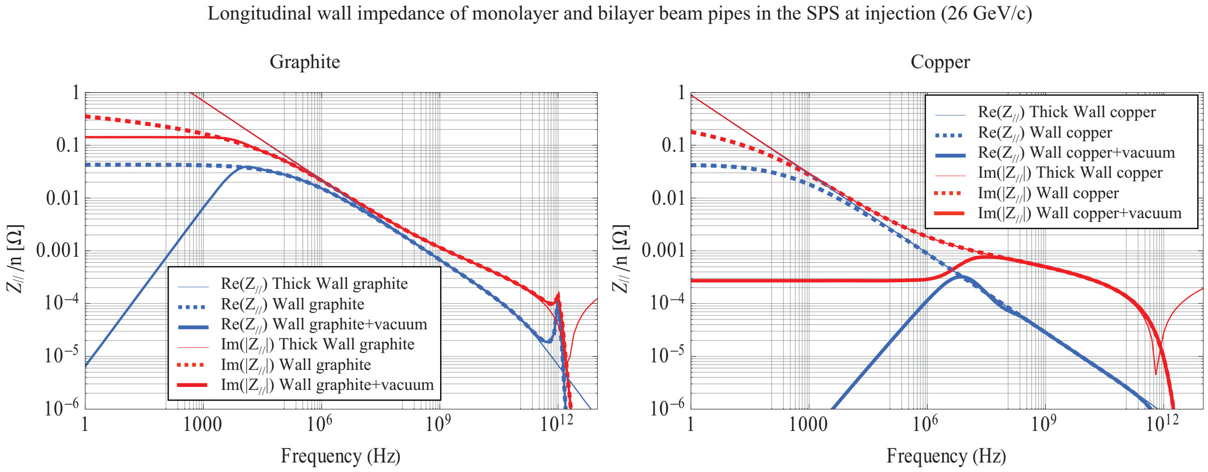

Figure 5.8: Longitudinal wall impedance of a 1 m cylindrical beam pipe with radius $a_1 = 2$ mm at SPS injection made of graphite of DC resistivity $\rho_{DC} = 10\ \mu\Omega.m$ and electron relaxation time $\tau_e = 8\ 10^-13$ s (left) and made of copper of DC resistivity $\rho_{DC} = 1.7\ 10^{-8}\ \Omega.m$ and electron relaxation time $\tau_e = 8\ 10^{-13}$ s (right). Reducing the thickness of the beam pipe (25 mm for graphite, 10 μm for copper) reduces the low frequency longitudinal wall impedance (up to 10 kHz for 25 mm of graphite, and up to 10 MHz for the 10 μm of copper).

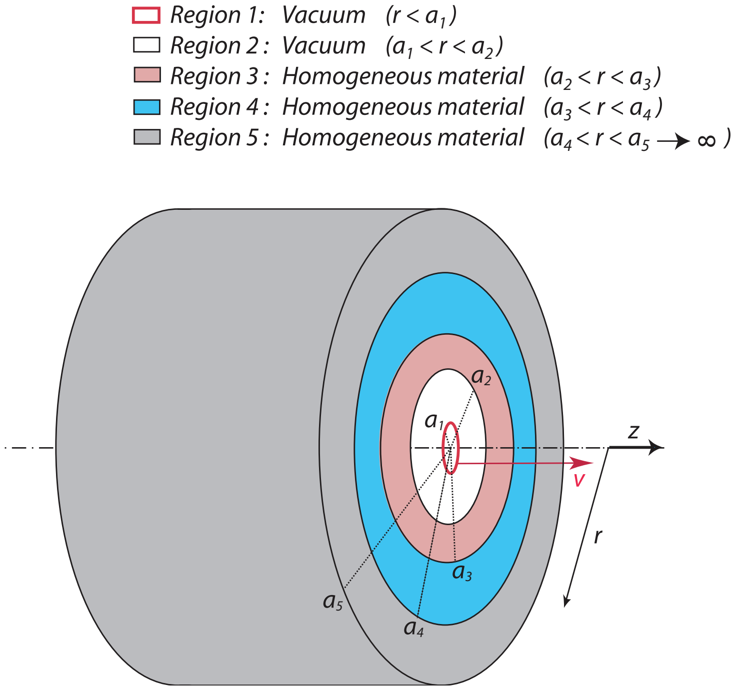

Figure 5.9: Sketch of a ring beam moving with velocity $\vec{v}$ parallel to the z-axis within a trilayer beam pipe, with its outer layer extending to infinity ($e \rightarrow \infty$).

infinity. To calculate the fields in this trilayer configuration, we will acknowledge again that the tangential components of both electric field $\vec{E}$ and magnetic field strength $\vec{H}$ are continuous at any interface where there is no charge and surface current. Then, the following matching equations for the longitudinal component of the electric field E_z and the azimuthal component of the magnetic field strength H_θ obtained in Eqs. (5.94) still hold at $r = a_2$, boundary between regions (2) and (3), and at $r = a_3$, boundary between regions (3) and (4):

$$\begin{cases} E_z^{(2)}(a_2, z; \omega) = E_z^{(3)}(a_2, z; \omega), \\ H_\theta^{(2)}(a_2, z; \omega) = H_\theta^{(3)}(a_2, z; \omega), \\ E_z^{(3)}(a_3, z; \omega) = E_z^{(4)}(a_3, z; \omega), \\ H_\theta^{(3)}(a_3, z; \omega) = H_\theta^{(4)}(a_3, z; \omega). \end{cases} \tag{5.100}$$

In the trilayer case, fields also have to be matched at $r = a_4$, boundary between regions (4) and (5), which yields two additional equations.

$$\begin{cases} E_z^{(4)}(a_4, z; \omega) = E_z^{(5)}(a_4, z; \omega), \\ H_\theta^{(4)}(a_4, z; \omega) = H_\theta^{(5)}(a_4, z; \omega). \end{cases} \tag{5.101}$$

Using general field expressions in (5.84), we obtain the following linear system of six equations

$$\begin{cases} A_2 \left[K_0(\nu_2 a_2) + \alpha_2 I_0(\nu_2 a_2)\right] = A_3 \left[K_0(\nu_3 a_2) + \alpha_3 I_0(\nu_3 a_2)\right], \\ \dfrac{\varepsilon_r^{(2)} A_2}{\nu_2} \left[K_0'(\nu_2 a_2) + \alpha_2 I_0'(\nu_2 a_2)\right] = \dfrac{\varepsilon_r^{(3)} A_3}{\nu_3} \left[K_0'(\nu_3 a_2) + \alpha_3 I_0'(\nu_3 a_2)\right], \\ A_3 \left[K_0(\nu_3 a_3) + \alpha_3 I_0(\nu_3 a_3)\right] = A_4 \left[K_0(\nu_4 a_3) + \alpha_4 I_0(\nu_4 a_3)\right], \\ \dfrac{\varepsilon_r^{(3)} A_3}{\nu_3} \left[K_0'(\nu_3 a_3) + \alpha_3 I_0'(\nu_3 a_3)\right] = \dfrac{\varepsilon_r^{(4)} A_4}{\nu_4} \left[K_0'(\nu_4 a_3) + \alpha_4 I_0'(\nu_4 a_3)\right], \\ A_4 \left[K_0(\nu_4 a_4) + \alpha_4 I_0(\nu_4 a_4)\right] = A_5 \left[K_0(\nu_5 a_4) + \alpha_5 I_0(\nu_5 a_4)\right], \\ \dfrac{\varepsilon_r^{(4)} A_4}{\nu_4} \left[K_0'(\nu_4 a_4) + \alpha_4 I_0'(\nu_4 a_4)\right] = \dfrac{\varepsilon_r^{(5)} A_5}{\nu_5} \left[K_0'(\nu_5 a_4) + \alpha_5 I_0'(\nu_5 a_4)\right]. \end{cases} \tag{5.102}$$

As in the monolayer and bilayer cases, the electric field can not diverge when $r \to \infty$, and we can write $\alpha_5 = 0$ in order to suppress the diverging term $I_0(u)$ in region (5) which extends to infinity. Then, the system (5.102) becomes:

$$\begin{cases} K_0(\nu_2 a_2) + \alpha_2 I_0(\nu_2 a_2) = A_3' \left[K_0(\nu_3 a_2) + \alpha_3 I_0(\nu_3 a_2)\right], \\ \dfrac{\varepsilon_r^{(2)}}{\nu_2} \left[K_0'(\nu_2 a_2) + \alpha_2 I_0'(\nu_2 a_2)\right] = \dfrac{\varepsilon_r^{(3)} A_3'}{\nu_3} \left[K_0'(\nu_3 a_2) + \alpha_3 I_0'(\nu_3 a_2)\right], \\ A_3 \left[K_0(\nu_3 a_3) + \alpha_3 I_0(\nu_3 a_3)\right] = A_4 \left[K_0(\nu_4 a_3) + \alpha_4 I_0(\nu_4 a_3)\right], \\ \dfrac{\varepsilon_r^{(3)} A_3'}{\nu_3} \left[K_0'(\nu_3 a_3) + \alpha_3 I_0'(\nu_3 a_3)\right] = \dfrac{\varepsilon_r^{(4)} A_4'}{\nu_4} \left[K_0'(\nu_4 a_3) + \alpha_4 I_0'(\nu_4 a_3)\right], \\ A_4' \left[K_0(\nu_4 a_4) + \alpha_4 I_0(\nu_4 a_4)\right] = A_5' K_0(\nu_5 a_4), \\ \dfrac{\varepsilon_r^{(4)} A_4'}{\nu_4} \left[K_0'(\nu_4 a_4) + \alpha_4 I_0'(\nu_4 a_4)\right] = \dfrac{\varepsilon_r^{(5)} A_5'}{\nu_5} K_0'(\nu_5 a_4), \end{cases} \tag{5.103}$$

where we again defined $A_3' = A_3/A_2$, $A_4' = A_4/A_2$ - as in the bilayer case - and $A_5' = A_5/A_2$ in order to get rid of A_2 in the system. We have obtained a nonlinear system of six equations and six unknowns (α_2, α_3, α_4, A_3', A_4' and A_5'). As in the bilayer case, this system can be transformed into a linear system by switching to the set of unknowns (α_2, B_3', B_4', A_3', A_4' and A_5').

$$\left\{ \begin{aligned} [K_0(\nu_2 a_2) + \alpha_2 I_0(\nu_2 a_2)] &= A_3' K_0(\nu_3 a_2) + B_3' I_0(\nu_3 a_2), \\ \frac{\varepsilon_r^{(2)}}{\nu_2} [K_0'(\nu_2 a_2) + \alpha_2 I_0'(\nu_2 a_2)] &= \frac{\varepsilon_r^{(3)}}{\nu_3} [A_3' K_0'(\nu_3 a_2) + B_3' I_0'(\nu_3 a_2)], \\ A_3' K_0(\nu_3 a_3) + B_3' I_0(\nu_3 a_3) &= A_4' K_0(\nu_4 a_3) + B_4' I_0(\nu_4 a_3), \\ \frac{\varepsilon_r^{(3)}}{\nu_3} [A_3' K_0'(\nu_3 a_3) + B_3' I_0'(\nu_3 a_3)] &= \frac{\varepsilon_r^{(4)}}{\nu_4} [A_4' K_0'(\nu_4 a_3) + B_4' I_0'(\nu_4 a_3)], \\ A_4' K_0(\nu_4 a_4) + B_4' I_0(\nu_4 a_4) &= A_5' K_0(\nu_5 a_4), \\ \frac{\varepsilon_r^{(4)}}{\nu_4} [A_4' K_0'(\nu_4 a_4) + B_4' I_0'(\nu_4 a_4)] &= \frac{\varepsilon_r^{(5)}}{\nu_5} A_5' K_0'(\nu_5 a_4). \end{aligned} \right. \tag{5.104}$$

This linear system can now be solved symbolically with for instance *Mathematica*, and we obtain a very lengthy expression for the parameter α_2, which is much too long to display in this note. However, this long expression can be substituted into Eq. (5.82) to yield the longitudinal wall impedance. An example for a finite thickness graphite SPS beam pipe coated with a thin layer of copper is given in Fig. 5.10. This formalism was

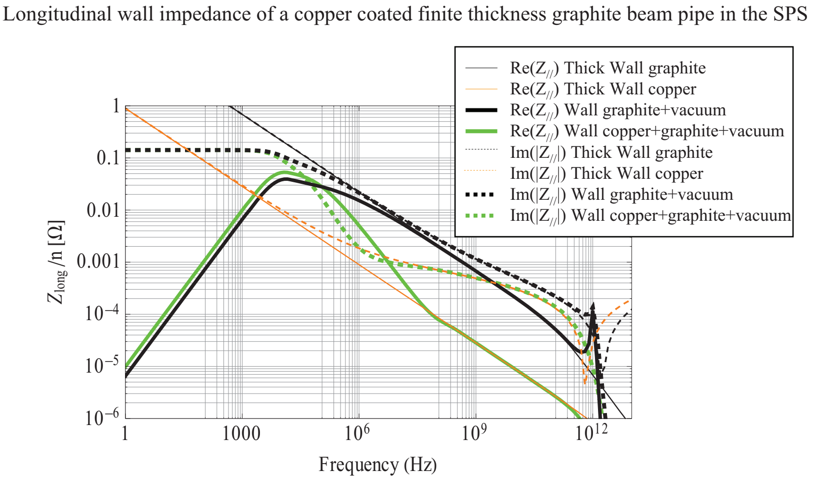

Figure 5.10: Longitudinal wall impedance of a 1 m cylindrical beam pipe with radius $a_1 = 2$ mm at SPS injection made of graphite of DC resistivity $\rho_{DC} = 10\ \mu\Omega.m$ and electron relaxation time $\tau_e = 8\ 10^{-13}$ s coated with 10 μm of copper of DC resistivity $\rho_{DC} = 1.710^{-8}\Omega.m$ and electron relaxation time $\tau_e = 2.7\ 10^{-14}$ s (right). The longitudinal wall impedance of this trilayer beam pipe (in green) follows the thick wall impedance of copper between 10 MHz and 100 GHz: in this frequency range, the fields are confined within the copper coating. At frequencies lower than 10 MHz, the fields penetrate into the graphite layer and the longitudinal wall impedance then follows the wall impedance of a graphite layer of finite thickness.

also used to compute the longitudinal impedance of an LHC TDI collimator, and its associated power loss in the ceramic [68]. It is important to note that the space charge impedance is negligible with respect to the resistive wall impedance at such energies. The longitudinal impedance of the first block in coated ceramic is plotted in Fig. (5.11). Following the outcome of these calculations among other studies, it was decided that the heat load in the ceramic was not low enough to be able to get rid of the dedicated water cooling system. Finally, this formalism was applied to obtain the longitudinal impedance of collimators with different potential materials for the upgrade of the LHC collimation system [69] see Fig. 5.12). The option of using ceramic collimators is studied due to their very low real impedance, and the wide range of mechanical, thermal and electrical properties accessible to ceramics. However, their large imaginary impedance contribution up to high frequency could be detrimental to the beam stability. A copper coating was then suggested, which reduces that imaginary impedance at high frequency, but also increases the real impedance. From these longitudinal impedance results only, the opportunity of using ceramics or copper coated ceramics is not obvious, and more studies should be performed to find a satisfying trade off between cleaning efficiency, beam impedance and mechanical stability.

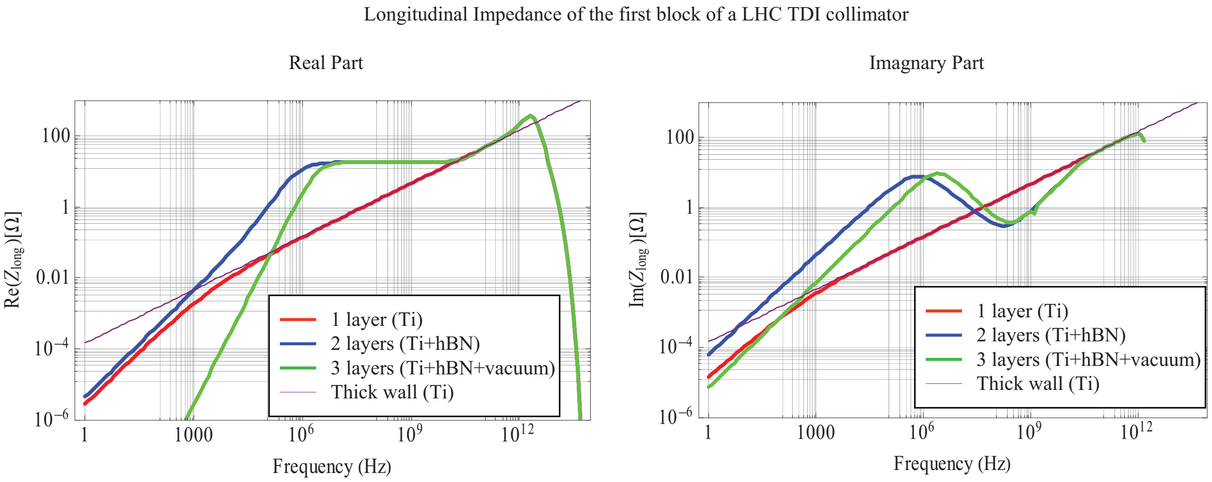

Figure 5.11: Longitudinal impedance of the 2.8 m long first block of an LHC TDI collimator with a beam pipe radius $a_1 = 4.4$ mm at LHC collision energy (7 TeV/c) made of a 54 mm thick ceramic layer of resistivity $\rho = 4\ 10^{12}\ \Omega.m$ and $\hat{\varepsilon}_r = 5$ coated with 3 μm of titanium of resistivity $\rho = 5.8\ 10^{-8}\ \Omega.m$.

Longitudinal Wall Impedance of a Multilayer Beam Pipe

An algorithm to calculate the longitudinal Resistive-Wall impedance of a beam pipe made of an arbitrary number of layers was implemented in *Mathematica*. This algorithm creates the linear system of equations and solves it symbolically. As the number of layers n increases, the number of equations in the system increases as $2n$. Solving large symbolic systems of equations yields lengthy expressions for the unknowns. These expressions need to be simplified in order to limit numerical issues during evaluation. This process in *Mathematica* becomes long and inefficient when the number of equations is larger than 15.

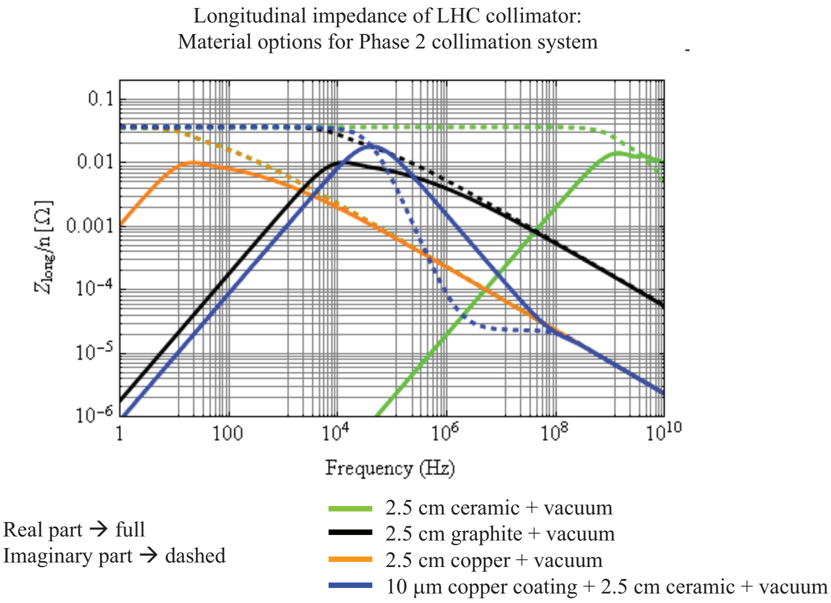

Figure 5.12: Longitudinal impedance of a 1 m long 2.5 cm thick LHC collimator made of different materials with a beam pipe radius $a_1 = 2$ mm at LHC collision energy (7 TeV/c): graphite ($\rho_{DC} = 10\ \mu\ \Omega.m$ and $\tau_e = 8\ 10^{-13}$ s), copper ($\rho_{DC} = 1.7\ 10^{-8}\Omega.m$ and $\tau_e = 2.7\ 10^{-14}$ s), ceramic ($\rho_{DC} = 1\ \Omega.m$, $\tau_e = 0$ s, and $\hat{\varepsilon}_r = 5$), and ceramic coated with 10 μm of copper.

An alternative algorithm based on the same formalism but using a matrix multiplication method instead of the solution of a linear system was implemented by N. Mounet and yields a more compact solution for the α_2 factor and is much more efficient to compute the impedance of a large number of layers [63].

To conclude this section on the derivation of the longitudinal impedance of a multi layer beam pipe, it is a good time to note that a major limitation to the application of these theoretical calculations to real beam pipes is in the coarse modeling of the material properties. Real materials used in real machines are in general heterogeneous and anisotropic. It is very common to find that materials with the same specifications but produced by different manufacturer will significantly differ. In addition, their properties may have been altered by machining, processing or exposure to radiation. Finally, the frequency dependence of electromagnetic properties - which is a crucial parameter for impedance assessment - is difficult and expensive to measure in the lab, not to mention on the production line. We therefore must be careful when applying the predictions computed from an ideal model to the real world, in particular when no crosscheck between several methods of predictions and measurements can be performed.

5.2 Theoretical Transverse Impedance

5.2.1 Field Matching Formalism

In Ref. [51], B. Zotter derived an algorithm applying the field matching technique to obtain the transverse impedance of a multilayer axisymmetric beam pipe of infinite length. This algorithm was implemented in *Mathematica* using the procedure mentioned in the previous section for the longitudinal impedance: the 4 field matching equations at each layer boundary are gathered into a system of linear equations that can be solved symbolically by *Mathematica*, and evaluated numerically in a second step for specific cases. An example of this implementation for the LHC graphite collimators can be found in [62] and will be benchmarked to RF impedance measurements in section 5.4. As an illustration, transverse impedance studies on potential materials for the upgrade of the LHC collimation system are shown in Fig. 5.13. Similarly to the longitudinal impedance studies shown in Fig. 5.12, the benefit of using this type of ceramic (with or without coating) as collimators jaws is not obvious from the transverse impedance point of view.

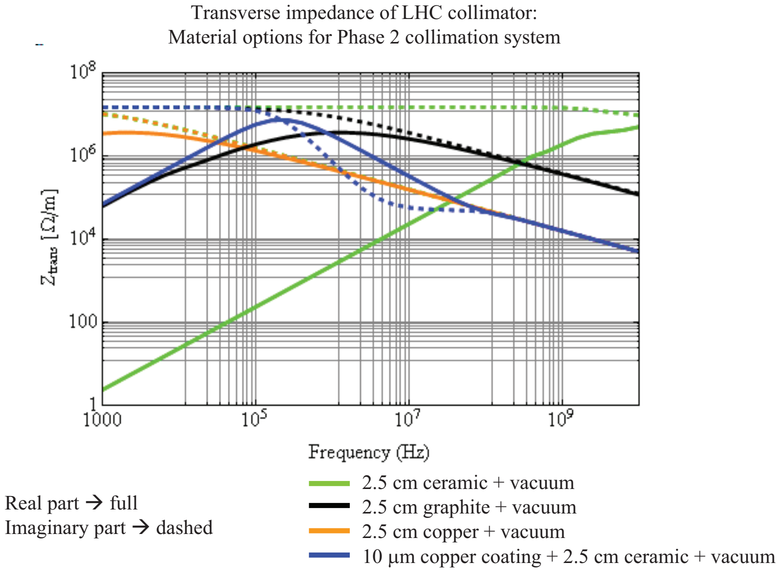

Figure 5.13: Transverse impedance of a 1 m long 2.5 cm thick circular beam pipe made of different materials with a beam pipe radius $a_1 = 2$ mm at LHC collision energy (7 TeV/c): graphite ($\rho_{DC} = 10\ \mu\Omega.m$ and $\tau_e = 8\ 10^{-13}$ s), copper ($\rho_{DC} = 1.7\ 10^{-8}\ \Omega.m$ and $\tau_e = 2.7\ 10^{-14}$ s), ceramic ($\rho_{DC} = 1\ \Omega.m$, $\tau_e = 0$ s, and $\hat{\varepsilon}_r = 5$), and ceramic coated with 10 μm of copper. The dipolar and quadrupolar components in the horizontal and vertical planes can be obtained using the Yokoya factors (see Tab. 5.1).

In Ref. [67], Yokoya also derived the transverse form factors. Between a circular cross section of radius a_1 and a geometry consisting of two horizontal parallel plates (also called flat chamber) separated by a gap $2a_1$, the transverse form factors are given in Tab. 5.1.

The two following applications of the field matching formalism will be used to build the transverse impedance model of the SPS.

vertical dipolar impedance	vertical quadrupolar impedance	horizontal dipolar impedance	horizontal quadrupolar impedance
$\pi^2/12$	$\pi^2/24$	$\pi^2/24$	$-\pi^2/24$

Table 5.1: Form factors to be applied to the transverse impedance obtained for a circular geometry in order to obtain the transverse impedance of a flat chamber [67].

5.2.2 Theoretical Transverse Impedance of the SPS Kickers

Among all the SPS elements, the kickers are suspected to contribute to a significant amount of the transverse impedance of the SPS [70]. A kicker is a special type of magnet designed to abruptly deflect the beam off its previous trajectory for instance to extract the beam to a transfer line or to a beam dump. For this reason, a crucial parameter for these kickers is their ramping time. There are several types of kickers installed in the SPS: injection kickers (MKP, MKPA, MKPC), extraction kickers to LHC transfer lines (MKE), extraction kickers to the SPS dump (MKDH, MKDV), tune measurement kickers (MKQH, MKQV). The layout of these kickers in the SPS ring is given in Fig. 5.14. In this section, we make a strong approximation and model the complicated geometry of each

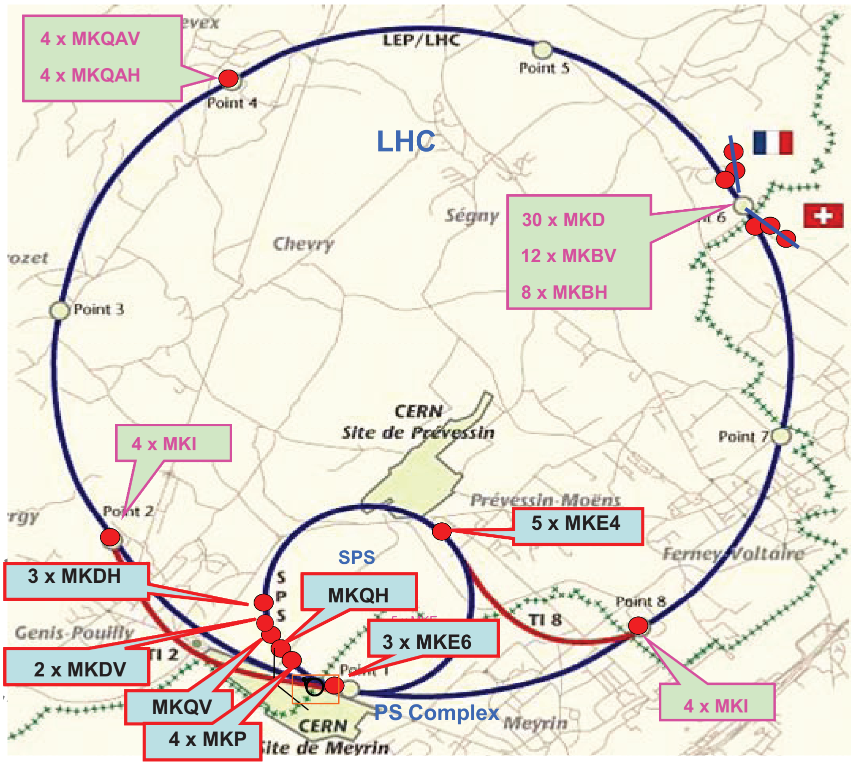

Figure 5.14: Geographical positions of the LHC kickers (green box) and SPS kickers (blue box). We can observe that the SPS kickers are not evenly distributed along the ring but are clustered around the injection zone from the PS (4 MKP), extraction zones to TI2 and TI8 (5+3 MKE), the tune measurement zone (MKDH+MKQH), and the beam dump (3 MKDV + 2MKDH). *Courtesy of M. Barnes.*

of these SPS kickers (see for instance the MKE geometry in Fig. 5.15) by a flat chamber made of two infinite blocks of ferrite in order to be able to compute the impedance of the kickers analytically with the field matching technique. We therefore neglect many features of the kicker magnets: hot and cold conductors on the side of the aperture, C-shape magnetic yoke, cell longitudinal structure, transitions between the ferrite blocks and the SPS beam pipe, external capacitor circuits and geometry outside the ferrite yoke. Besides, the MKDH kickers have been built with laminated silicon steel yokes instead of ferrite yokes [71]. Since relevant high frequency properties for this laminated silicon steel are not readily available, we make the approximation for now that all the kickers are made of ferrite. The model for the ferrite permeability μ as a function of frequency f was obtained from a first order dispersion fit on measured data up to 1.8 GHz [72]:

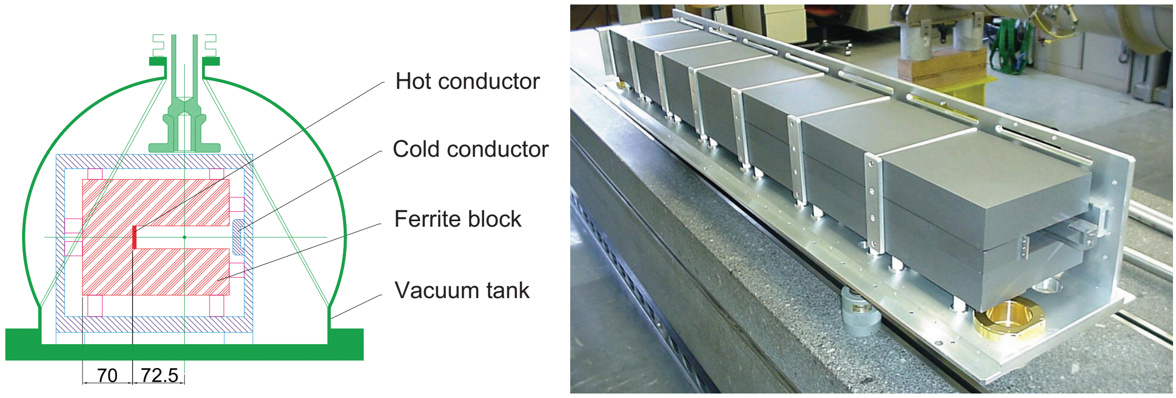

Figure 5.15: Drawing of the transverse cross-section of an SPS MKE kicker (left) and picture of the 7 assembled ferrite cells of an MKE kicker mounted with the hot and cold conductors (right). *Courtesy of T. Kroyer.*

$$\mu = \mu_0 \left(1 + \frac{\mu_i}{1 + j 2\pi f \tau_\mu} \right) \quad \text{with} \quad \mu_i = 460 \quad \text{and} \quad \frac{1}{2\pi\tau_\mu} = 20 \text{ MHz}. \tag{5.105}$$

The ferrite dielectric properties are characterized by a constant resistivity $\rho = 10^6\ \Omega.m$ and a real relative permittivity $\hat{\varepsilon}_r = 12$ yielding a complex permittivity ε_c

$$\varepsilon_c = \varepsilon_0 \left(\hat{\varepsilon}_r - \frac{j}{2\pi f \varepsilon_0 \rho} \right). \tag{5.106}$$

The ferrite used for these measurements was of type 4A4 made by *Philips Components* (now *Ferroxcube*). Most SPS kickers are however made of *Ferroxcube* ferrite type 8C11, but E. Métral in Ref. [73] showed that the resulting beam coupling impedance models obtained with ferrites 4A4 and 8C11 for kicker type structures were in fact very close. Finally, it is important to note that our model represents the kickers installed in the machine in 2006, as from 2007 on a campaign to shield the MKE kickers with serigraphed conducting stripes has been implemented in order to reduce their beam coupling impedance [74]. In the frame of all these approximations, we can apply the field matching formula and obtain the impedance for several axisymmetric structures made of ferrite 4A4. Scanning the ferrite layer thickness between 1 mm to infinity in Fig. 5.16, we realize that the impact of increasing the ferrite thickness above 6 cm is negligible in the frequency range of interest in single bunch collective effects, and that we may use indifferently an infinitely thick layer or a 6 cm thick ferrite layer. In addition to the SPS beam parameters at injection (see Tab. B.1 in the appendix) and the ferrite electromagnetic parameters, the half gap between the ferrite blocks, their thickness and their length are needed to compute this impedance. These parameters are given in Tab. B.2 in the appendix. In a last approximation, we assume Yokoya factors in Tab. 5.1 still hold in the case of ferrite to obtain the impedance for a flat chamber geometry. The outcome of the dipolar and quadrupolar impedance computations for all kickers for both horizontal and vertical planes is summarized in Fig. 5.17. As explained in chapter 4, the total wall impedance contribution for all the kickers can be obtained by weighting the impedance of each of the kickers by $\beta_{x,y}/\left<\beta_{x,y}\right>$ and summing these individual contributions. The weighted individual contributions are given in Fig. 5.18. Distortions from the Yokoya factors appear as beta functions are different in the horizontal and vertical planes. For instance, β_x are larger than β_y at the locations of the MKE kickers, yielding larger impedance contributions in the horizontal plane. On the contrary, β_y are larger than β_x at the locations of the MKP kickers, yielding larger impedance contributions in the vertical plane. The total impedance contributions of all these SPS kickers is given in Fig. 5.19. Different beta functions in both planes and rotated vertical kickers explain the deviation from the Yokoya form factors one would expect in the case of a single kicker. From these total impedance contributions for all the kickers, the total wake functions can be obtained using the discrete Fourier transform mentioned in Eq. (3.64). These total wake functions computed numerically with *Mathematica* are given in Fig. 5.20. The wake contributions of the modeled SPS kickers are now ready to be imported into *HEADTAIL* to assess their impact on the SPS beam dynamics.

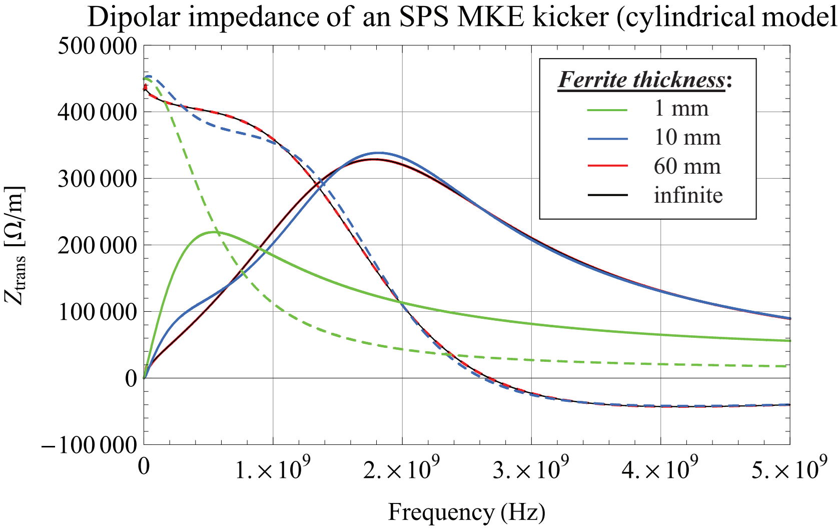

Figure 5.16: Transverse dipolar impedance of axisymmetric models of SPS kickers with various ferrite thicknesses. The layer closest to the beam is made of ferrite surrounded by an infinite layer of copper. Real parts of impedance are full lines, imaginary parts are dashed lines.

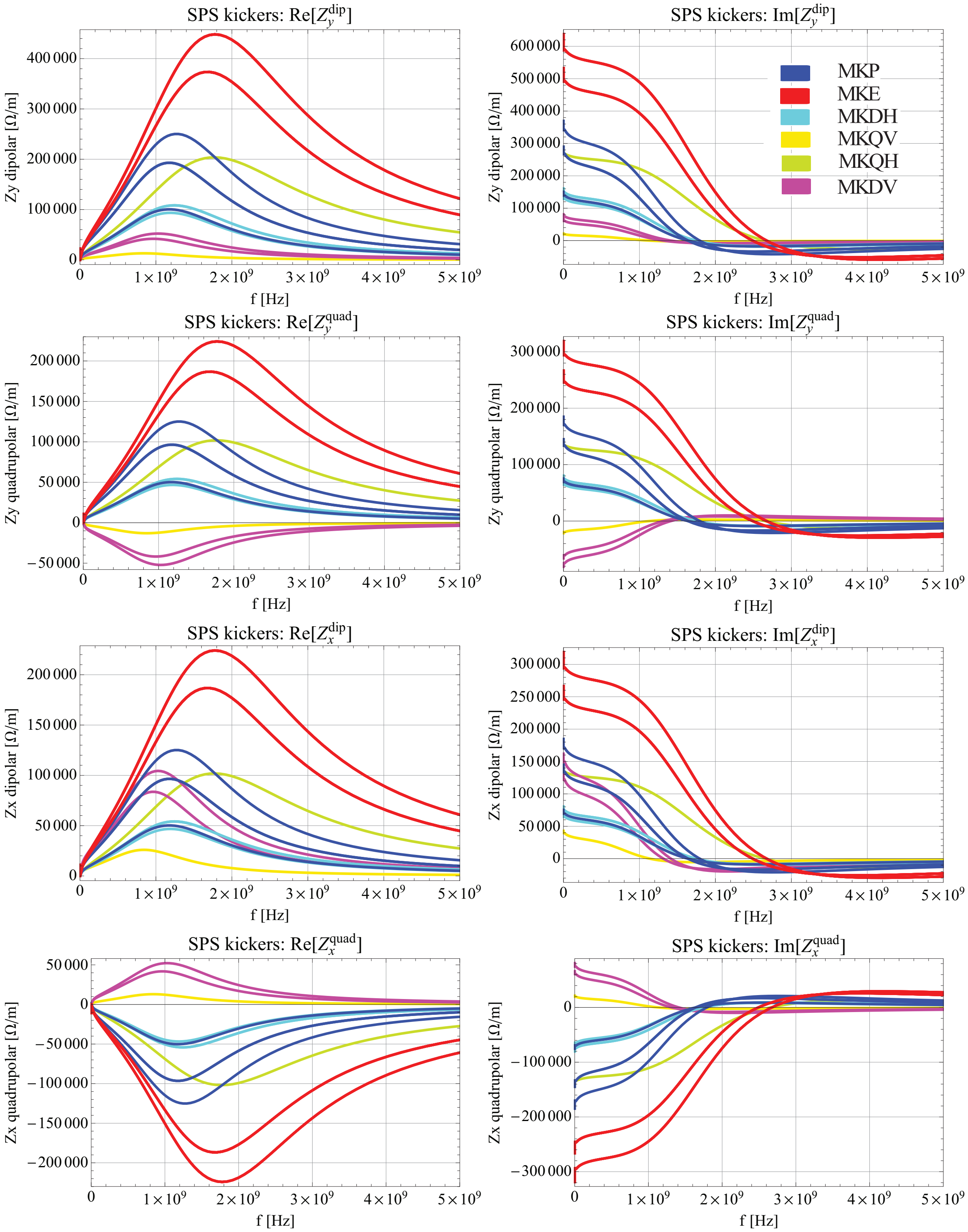

SPS kickers: Re[Z_y^{dip}]

SPS kickers: Im[Z_y^{dip}]

SPS kickers: Re[Z_y^{quad}]

SPS kickers: Im[Z_y^{quad}]

SPS kickers: Re[Z_x^{dip}]

SPS kickers: Im[Z_x^{dip}]

SPS kickers: Re[Z_x^{quad}]

SPS kickers: Im[Z_x^{quad}]

Figure 5.17: Real (left) and imaginary (right) dipolar and quadrupolar impedances of all the SPS kickers for both transverse planes. The same color was used for all kickers within a family. The SPS kickers are modeled as flat chambers made of ferrite.

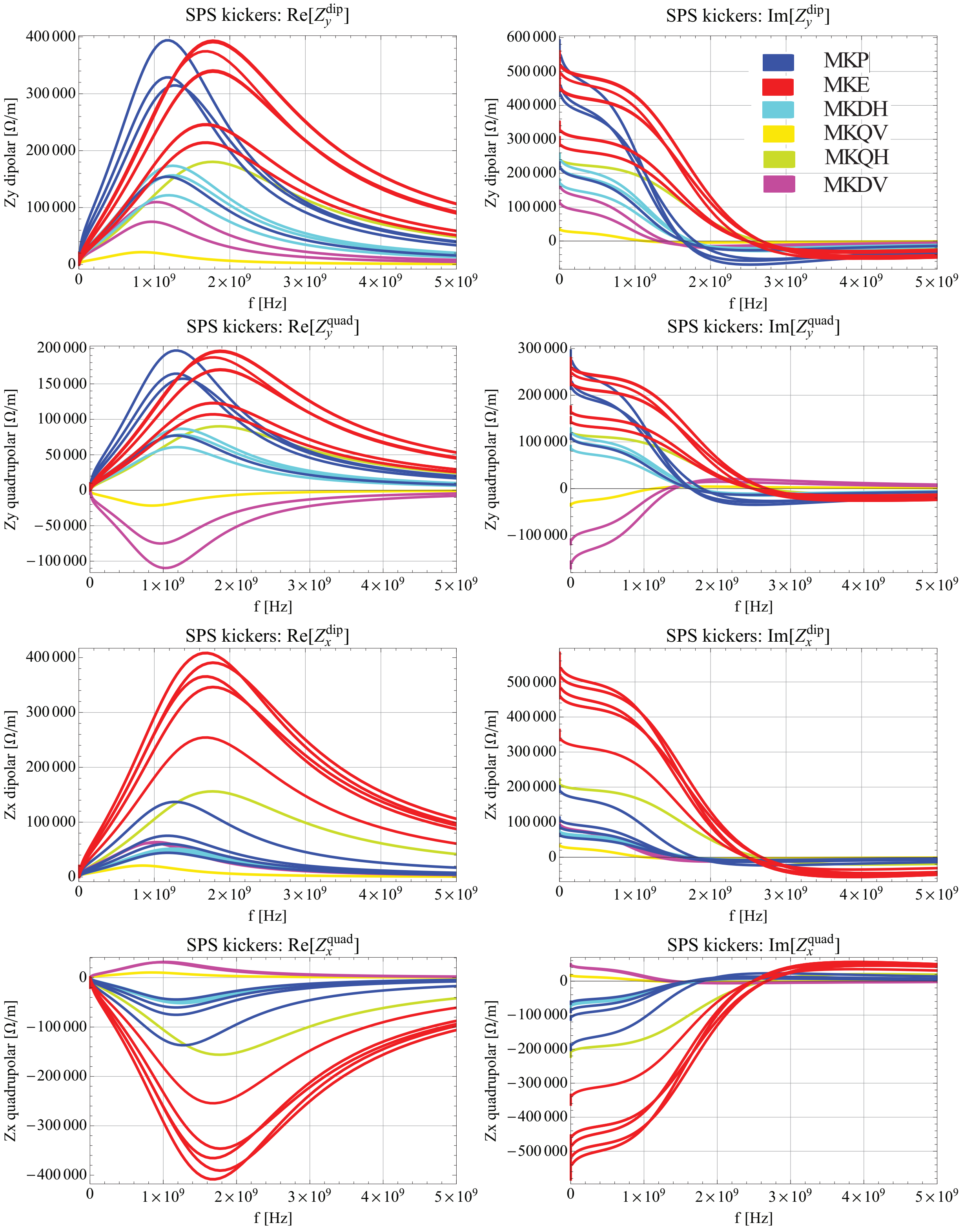

Figure 5.18: Real (left) and imaginary (right) dipolar and quadrupolar weighted impedances of all the SPS kickers for both transverse planes. The same color was used for all kickers within a family. The SPS kickers are modeled as flat chambers made of ferrite. The impedances were weighted by the relative transverse beta functions $\beta_{x,y}/\langle\beta_{x,y}\rangle$ to account for the larger impact of a transverse impedance source at a location with higher beta function $\beta_{x,y}$ than the average beta function $\langle\beta_{x,y}\rangle$.

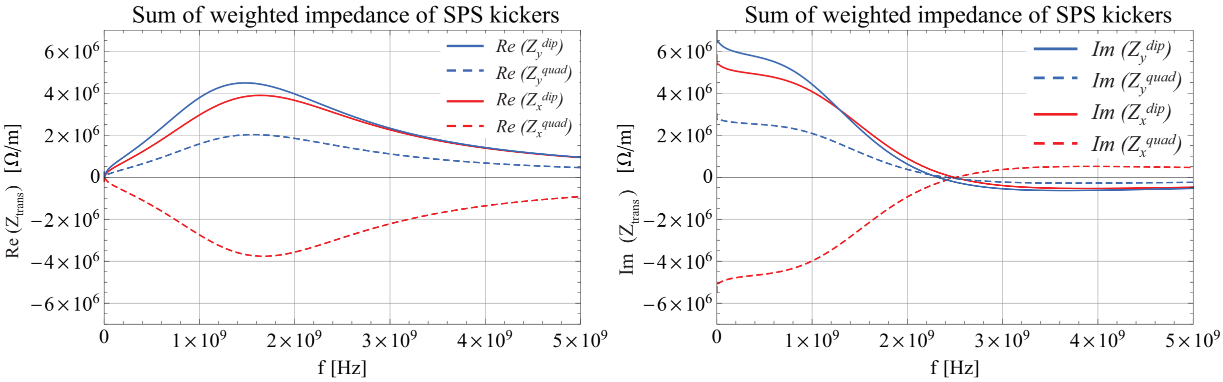

Figure 5.19: Total transverse dipolar and quadrupolar impedances in both planes of flat chamber models of SPS kickers.

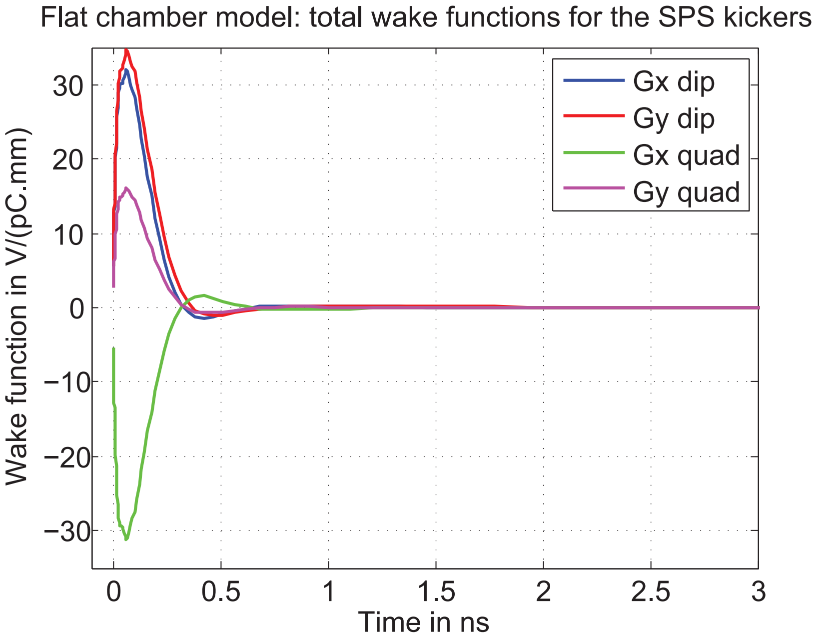

Figure 5.20: Total dipolar and quadrupolar wake functions for both planes of the SPS kickers modeled individually as flat chambers made of ferrite. The time span of this plot is of the order of the SPS total bunch length (2 to 3 ns).

5.2.3 Theoretical Transverse Impedance of the Beam Pipe

The field matching formalism was also applied to the 6.9 km long SPS stainless steel beam pipe. Even though there are many changes of cross section between elliptical chambers and round chambers, we modeled the SPS beam pipe by a flat chamber of half gap 2 cm. As for the SPS kickers, the first step is to obtain the wall impedance for the cylindrical beam pipe. A model with an infinitely thick layer of stainless steel and a model with a 2 mm thick stainless steel beam pipe surrounded by vacuum are compared in Fig. 5.21. The frequency dependence of conductivity was neglected in view of the frequency range of interest for the SPS. The typical permittivity $\hat{\varepsilon}_r \approx 1.5$ and permeability $\mu_r \approx 1.01$ of stainless steel vary with manufacturers and were not taken into account here. Taking them into account would yield a 3% increase of the impedance. The wake functions for the SPS beam pipe may be computed via inverse Discrete Fourier Transform (DFT) with Eq. (3.64). We take this opportunity to underline the fact that this step is not trivial, as the interesting impedance range spreads over many frequency decades. Built-in DFT with constant frequency sampling may reach the available memory limits. Wake functions obtained with several frequency ranges and frequency samplings are shown in Fig. 5.22. In this case, if the frequency sampling is too low (1 MHz), the long range wake is not correctly obtained (see Fig. 5.22(a)). Besides, if the impedance is truncated at too low frequencies (0.1 THz or lower), unphysical wake oscillations appear (see Fig. 5.22(b)). Even if tricks can be found to maximize the available memory and perform DFTs with billions of points in Matlab for instance, a fair trade-off has to be found. Another solution is to use DFTs on unevenly sampled data, mentioned in Ref. [75] and implemented in an elegant way by N. Mounet [63]. Besides it is interesting to note that high number of points DFT on an impedance with $\beta < 1$ beam enables to observe the wake in front

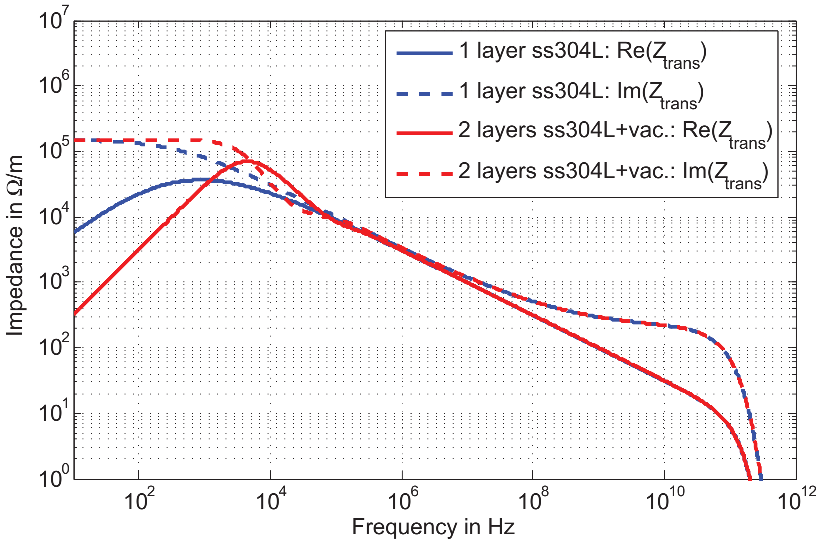

Figure 5.21: Transverse impedance of 1 m of the SPS beam pipe modeled as a circular chamber: 1 layer of infinitely thick stainless steel (1 layer in blue) and 1 layer of stainless steel surrounded by vacuum (2 layers in red). The DC resistivity $\rho_{DC} = 7.2\ 10^{-7}\ \Omega.m$ of standard stainless steel of grade 304L was used.

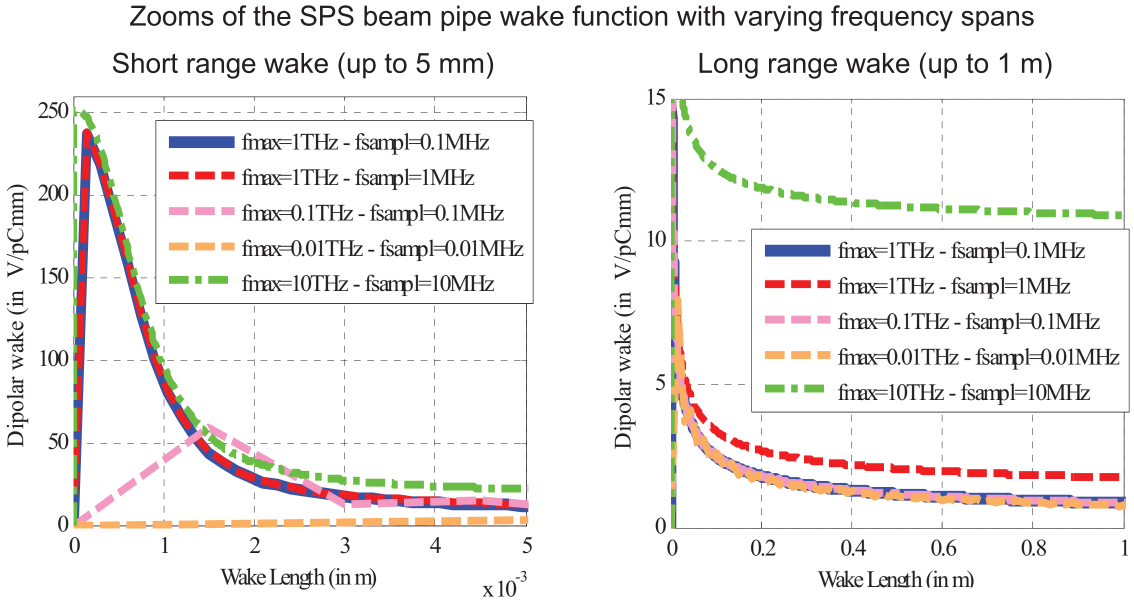

Figure 5.22: Transverse wake function obtained via inverse DFT of the SPS beam pipe impedance up to 5 mm (a), and up to 1 m (b) for different frequency samplings (0.01 MHz to 10 MHz) and frequency span (0.01 THz to 10 THz). The wake obtained from the largest number of impedance points (blue thick line, 0 to 1 THz with a sampling of 0.1 MHz, i.e. 10^7 points) seems to be a fair compromise at both low (a) and high (b) distance to the source charge.

of the bunch. In Fig. 5.23, the resistive wall and indirect space charge contributions to the wall wake function are disentangled. Using an infinite layer of stainless steel or a 2 mm stainless layer surrounded by vacuum yields the same wakes within 1 % over the SPS bunch length and is not plotted here. We observe that the indirect space charge contribution is symmetric and tends to a dirac distribution as beam energy increases, affecting mostly the short range wake (here up to 3 mm after the source charge). The resistive wall contribution is not symmetric and here affects mostly the medium to long range wake behind the charge. It is reminded that the SPS bunch length is of the order of 1 m. The wall impedance of the SPS beam pipe and the SPS kickers at injection are now

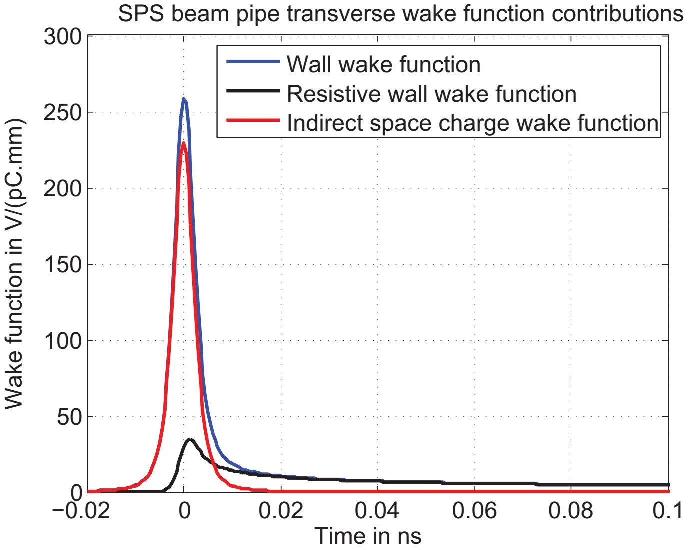

Figure 5.23: Transverse wake function obtained via inverse DFT of the impedance of a 2 cm radius 6911 m stainless steel 304L SPS cylindrical beam pipe at injection energy ($\gamma = 27.7$). The wake in front of the bunch (negative distance behind the bunch) can be observed for the wall impedance (in blue) and its contributions from resistive wall (in black) and indirect space charge (in red).

ready to be used as input of *HEADTAIL*. The following section mentions an alternative model to the Zotter/Métral model for computing the impedance of kickers.

5.2.4 An alternative Model for the Kicker's Impedance

The vertical dipolar impedance computed with the flat chamber model described in the previous section was successfully benchmarked to 2 wire impedance measurements up to 1 GHz for an SPS MKE kickers in Ref. [76]. The dipolar vertical impedance in this frequency range is expected to be the most critical as far as SPS single bunch transverse stability is concerned. However, this flat chamber model obtained from Zotter/Métral theory with Yokoya factors can not explain the negative total horizontal impedance measured on a PS kicker with a single wire in Ref. [77]. In fact, using Yokoya factors, the total horizontal impedance can only be positive or zero. Since this flat chamber model does not take into account the vertical metallic plates on each side of the ferrite blocks, E. Métral suspected the actual quadrupolar horizontal impedance could be quite different from the quadrupolar horizontal impedance predicted by theory (in Ref. [78]). Earlier, in order to refine the cylindrical model for the kickers, H. Tsutsui had already derived a field matching theory to obtain the longitudinal [79] and transverse dipolar [80] impedance of a geometrical model with vertical metal electrode plates described in Fig. 5.24 for an ultrarelativistic beam. In these references, his theoretical dipolar impedance calculations were compared to *HFSS* simulations and subsequently to measurements of PS and SPS kickers in Refs. [77], [81] and [82]. It would be interesting to be able to use this impedance formalism to generate transverse wake functions that could be imported into *HEADTAIL*. In his paper [80], H. Tsutsui only derived the transverse dipolar impedances. With the help of C. Zannini, we have derived the quadrupolar impedance from the source and electromagnetic fields obtained for the calculation of the longitudinal impedance in Ref. [79]. H. Tsutsui

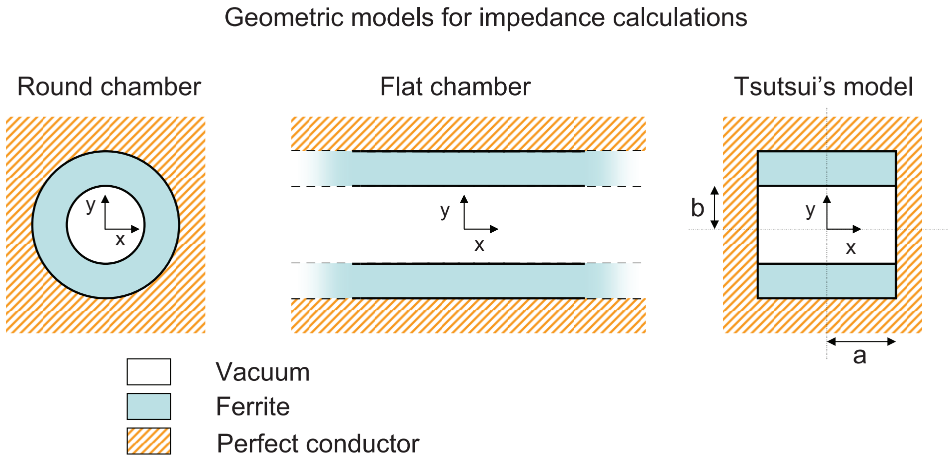

Figure 5.24: Geometric models for theoretical impedance calculations. The impedance for a multilayer cylindrical model (left) can be obtained with the field matching formalism put forward by Zotter and Métral. The impedance for a multilayer flat chamber model (center) can be obtained under certain assumptions by applying the Yokoya factors to the impedance of the cylindrical model. H. Tsutsui derived a formalism to obtain the impedance of a model that accounts for perfect conducting plates on both sides of the ferrite plates. The beam travels perpendicularly to the page.

computed the fields in the vacuum region $(y < bandx < a)$ (Eq. (17) in Ref. [79]):

$$\begin{cases} E_z(x,y) = \sum_n (A_n + B_n)\cos(k_{xn}x)\cosh(k_{xn}y)\,, \\ E_x(x,y) = \sum_n \frac{jk}{k_{xn}} A_n \sin(k_{xn}x)\cosh(k_{xn}y)\,, \\ E_y(x,y) = \sum_n \frac{jk}{k_{xn}} B_n \cos(k_{xn}x)\sinh(k_{xn}y)\,, \\ Z_0 H_z(x,y) = \sum_n (A_n + B_n)\sin(k_{xn}x)\sinh(k_{xn}y)\,, \\ Z_0 H_x(x,y) = j\sum_n \left(\frac{k_{xn}}{k}A_n + \left(\frac{k_{xn}}{k} - \frac{k}{k_{xn}}\right)B_n\right)\cos(k_{xn}x)\sinh(k_{xn}y)\,, \\ Z_0 H_y(x,y) = j\sum_n \left(\left(\frac{k_{xn}}{k} + \frac{k}{k_{xn}}\right)A_n + \frac{k_{xn}}{k}B_n\right)\sin(k_{xn}x)\cosh(k_{xn}y)\,, \end{cases} \tag{5.107}$$

with $k_{xn} = \frac{(2n+1)\pi}{2a}$, where $Z_0 = \mu_0 c$ is the vacuum impedance. The time and longitudinal dependences $\exp(j\omega(t - z/c))$ are omitted. Full derivations of electromagnetic fields in similar rectangular waveguide models loaded with dielectric slabs are given in Refs. [83] and [84]. At coordinate $(x,y) = (\xi, 0)$, fields E_x and H_y in the vacuum region can be written

$$\begin{cases} E_x(\xi,0) = \sum_n \frac{jk}{k_{xn}} A_n \sin(k_{xn}\xi)\,, \\ Z_0 H_y(\xi,0) = j\sum_n \left(\left(\frac{k_{xn}}{k} + \frac{k}{k_{xn}}\right)A_n + \frac{k_{xn}}{k}B_n\right)\sin(k_{xn}\xi)\,. \end{cases} \tag{5.108}$$

The horizontal detuning impedance per unit length is then obtained from the electromagnetic fields at $(x,y) = (\xi, 0)$ for the source current I_0 at $(x,y) = (0,0)$ given in Eq. (16) of Ref. [79]:

$$\begin{aligned} \frac{Z_h^{quad}}{L} &= \frac{j}{I_0\xi}\left(E_x(\xi,0) - Z_0 H_y(\xi,0)\right) \\ &= \frac{1}{I_0\xi}\sum_{n=0}^{\infty}\frac{k_{xn}}{k}(A_n + B_n)\sin(k_{xn}\xi) \\ &= -j\frac{Z_0}{2a\xi}\sum_{n=0}^{\infty}\frac{k_{xn}}{k}\frac{1}{\frac{\frac{k_{xn}}{k}(1+\mu_r\varepsilon_r)sh\,ch + \frac{k_{yn}}{k}(\mu_r sh^2 tn - \varepsilon_r ch^2 ct)}{\mu_r\varepsilon_r - 1} - \frac{k}{k_{xn}}sh\,ch}\sin(k_{xn}\xi)\,, \end{aligned} \tag{5.109}$$

with $sh = \sinh(k_{xn}b)$, $ch = \cosh(k_{xn}b)$, $tn = \tan[k_{yn}(b-d)]$ and $ct = \cot[k_{yn}(b-d)]$. The boundary conditions (Eq. (19) in Ref. [79]) are valid and we have used the expression of $(A_n + B_n)$ given in Eq. (21) and (27) of Ref. [79]. We finally choose a small displacement ξ so that we can write to first order:

$$\frac{Z_h^{quad}}{L} = -j\frac{Z_0}{2a}\sum_{n=0}^{\infty}\frac{k_{xn}^2}{k}\frac{1}{\frac{\frac{k_{xn}}{k}(1+\mu_r\varepsilon_r)sh\,ch + \frac{k_{yn}}{k}(\mu_r sh^2 tn - \varepsilon_r ch^2 ct)}{\mu_r\varepsilon_r - 1} - \frac{k}{k_{xn}}sh\,ch}. \tag{5.110}$$

We observe that the horizontal quadrupolar impedance at small transverse positions for each waveguide hybrid mode number is simply given by the longitudinal impedance multiplied by a factor $-\frac{k_{xn}^2}{k}$. Similarly, the vertical detuning impedance can be obtained. At coordinate $(x,y)=(0,\xi)$, fields E_y and H_x in the vacuum region can be written

$$\begin{cases} E_y(0,\xi) = \displaystyle\sum_n \frac{jk}{k_{xn}} B_n \sinh\left(k_{xn}\xi\right), \\ Z_0 H_x(0,\xi) = j \displaystyle\sum_n \left(\frac{k_{xn}}{k} A_n + \left(\frac{k_{xn}}{k} - \frac{k}{k_{xn}} \right) B_n \right) \sinh\left(k_{xn}\xi\right). \end{cases} \tag{5.111}$$

The vertical detuning impedance per unit length is obtained from the electromagnetic fields at $(x,y)=(0,\xi)$ for the source current I_0 at $(x,y)=(0,0)$.

$$\begin{aligned} \frac{Z_v^{quad}}{L} &= \frac{j}{I_0\xi}\left(E_y(0,\xi) + Z_0 H_x(0,\xi)\right) \\ &= -\frac{1}{I_0\xi} \sum_{n=0}^{\infty} \frac{k_{xn}}{k} \left(A_n + B_n\right) \sinh\left(k_{xn}\xi\right) \\ &= j\frac{Z_0}{2a\xi} \sum_{n=0}^{\infty} \frac{k_{xn}}{k} \frac{1}{\frac{\frac{k_{xn}}{k}(1+\mu_r\varepsilon_r) sh\, ch + \frac{k_{yn}}{k}(\mu_r sh^2 tn - \varepsilon_r ch^2 ct)}{\mu_r\varepsilon_r - 1} - \frac{k}{k_{xn}} sh\, ch} \sinh\left(k_{xn}\xi\right). \end{aligned} \tag{5.112}$$

We choose a small displacement ξ is so that we can write to first order:

$$\frac{Z_v^{quad}}{L} = j\frac{Z_0}{2a} \sum_{n=0}^{\infty} \frac{k_{xn}^2}{k} \frac{1}{\frac{\frac{k_{xn}}{k}(1+\mu_r\varepsilon_r) sh\, ch + \frac{k_{yn}}{k}(\mu_r sh^2 tn - \varepsilon_r ch^2 ct)}{\mu_r\varepsilon_r - 1} - \frac{k}{k_{xn}} sh\, ch}. \tag{5.113}$$

In this ultrarelativistic case for small amplitudes, we can observe that $Z_v^{quad} = -Z_h^{quad}$. The dipolar and quadrupolar impedances in both planes are presented in Fig. 5.25 for a single SPS MKE kicker (MKE.61651). Comparing the dipolar and quadrupolar contributions in each plane, we can conclude that the impedance contributions can not be related by simple Yokoya factors. Also, looking specifically at the low frequency imaginary impedance contributions, we observe that the quadrupolar impedance contributions are larger than the dipolar impedance contributions for each plane, inverting completely the picture obtained from the flat chamber model. The dipolar and quadrupolar impedances in both planes accounting for all the SPS kickers is given in Fig. 5.26. The importance of the quadrupolar contribution is confirmed. In fact, summing the dipolar and quadrupolar imaginary contributions in the horizontal plane yields a large negative horizontal impedance at low frequency, which could explain the positive tune shift observed in the SPS in the horizontal plane. As for the case of the flat chamber model, we use Eq.(3.64) to obtain the total dipolar and quadrupolar wake functions through inverse Fourier Transform of the dipolar and quadrupolar impedance contributions shown in Fig. 5.26. These wake functions are given in Fig. 5.27 together with the wake functions obtained with the flat chamber model in the previous paragraph. We see again the larger quadrupolar contributions in Tsutsui's model compared to Zotter/Métral's model, and we observe that their effect extends to trailing charges at larger distances from the source charge. These analytical calculations of the beam impedance using the models of Zot-

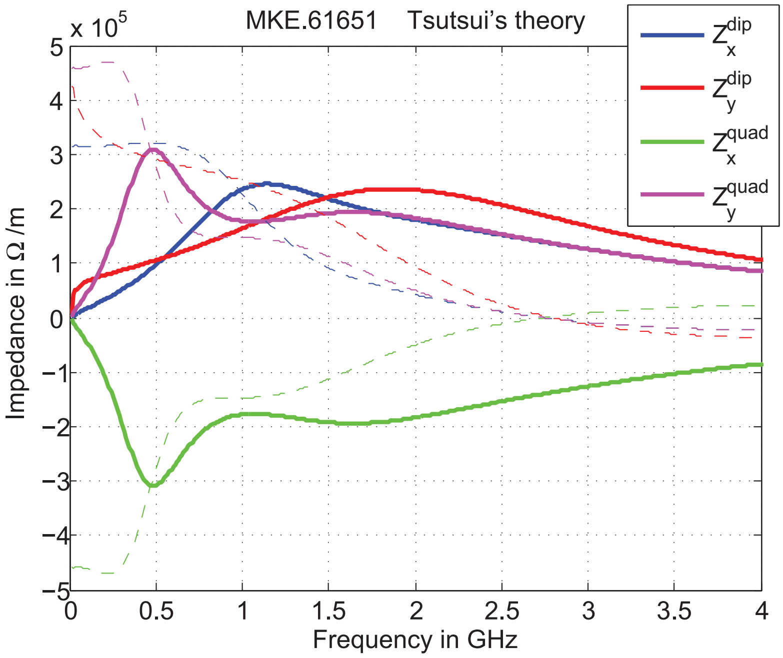

Figure 5.25: Dipolar and quadrupolar impedance in both transverse planes for SPS kicker MKE.61651. The real part impedance contributions are in full thick lines, while the imaginary part impedance contributions are thin and dashed.

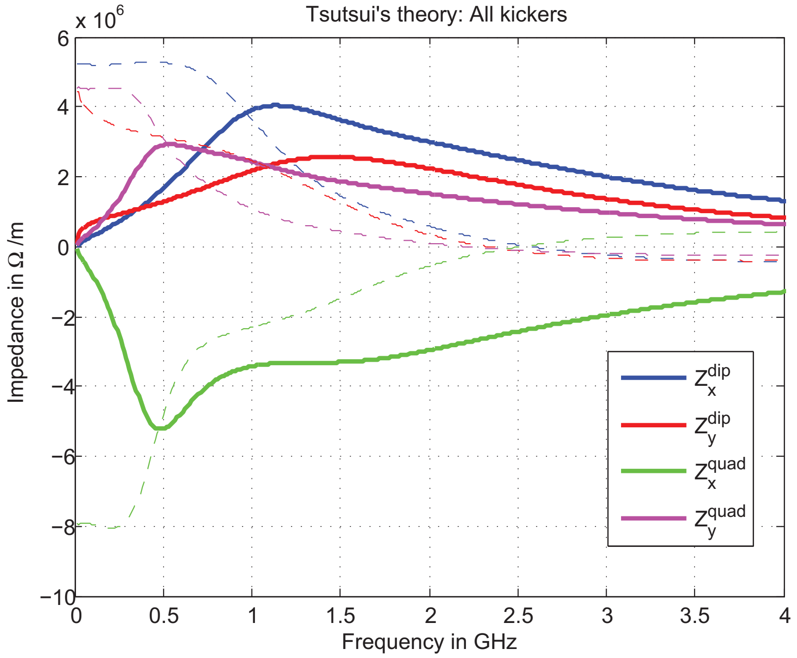

Figure 5.26: Dipolar and quadrupolar impedances in both transverse planes for the sum of the SPS kickers contributions weighted by their relative beta functions. The real part impedance contributions are in full thick lines, while the imaginary part impedance contributions are thin and dashed lines.

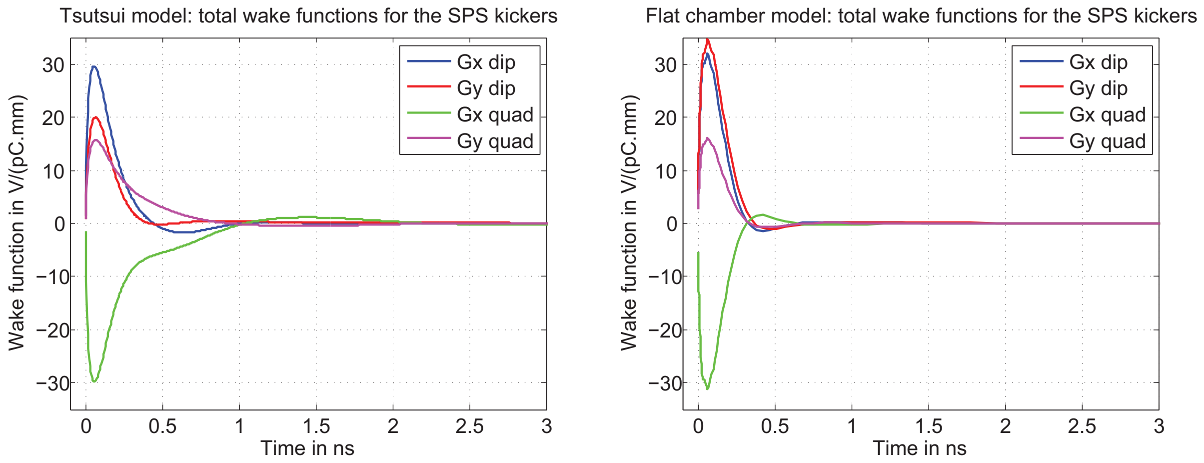

Figure 5.27: Total dipolar and quadrupolar wake functions in both transverse planes for all SPS kickers for Tsutsui's model (left) and the flat chamber model (right).

ter/Métral and Tsutsui are unfortunately restricted to simple geometrical models so that the equations can be solved analytically. Real accelerator devices are in general designed with complicated shapes optimized to give the best operating performance. The next section deals with 3D simulations of accelerator elements, a tool that allows to compute the electromagnetic fields of more complicated models.

5.3 Electromagnetic Simulations

A brief description of 3D electromagnetic simulation tools has been given in section 3.3, along with the example of wake fields calculated by *CST Particle Studio* for a simplified model of a CLIC collimator. In this section, we focus on :

- obtaining impedance and/or wake function contributions of SPS accelerator elements for the SPS impedance database *ZBASE*,
- assessing potential limitations of the simulation code in simulating accelerator components.

In fact, even though *CST Particle Studio* is based on *CST MAFIA* 4, a 2D and 3D simulation tool that was widely used at CERN in the years 1990-2003, little hand-on CERN experience was accumulated with *CST Particle Studio*. This is why we have tried to benchmark simulation results with analytical calculations and measurements whenever possible. We first mention simulations of simplified models of SPS kickers, performed in close collaboration with Carlo Zannini (Universita & INFN, Napoli and CERN, Geneva). These simulations are then compared to the analytical impedance calculations performed in the previous section. We then deal with the simulation and measurement studies of the SPS Beam Position Monitors, also reported in [85]. We would like here to acknowledge the helpful collaborations with colleagues from TU Darmstadt, CST AG, INFN Frascati and the CERN AB/RF and AT/BT groups.

5.3.1 3D Simulations of the Impedance of the SPS Kickers

Together with C. Zannini, we have performed *CST Particle Studio* simulations of simple 3D models of kickers. Carlo's report will describe the many types of simple models (collimators, steps, cavities, etc.) he has simulated with the help of the impedance team in order to benchmark theoretical computations and 3D simulations [86]. Here we briefly mention the team work that lead to the benchmark of the simulated impedance of Tsutsui's kicker geometrical model and the available theoretical computations described in sections 5.2.2 and 5.2.4.

Simulation Setup

The geometrical model described by H. Tsutsui was already shown in Fig. 5.24. The corresponding model generated with *CST STUDIO SUITE* is presented in Fig. 5.28.

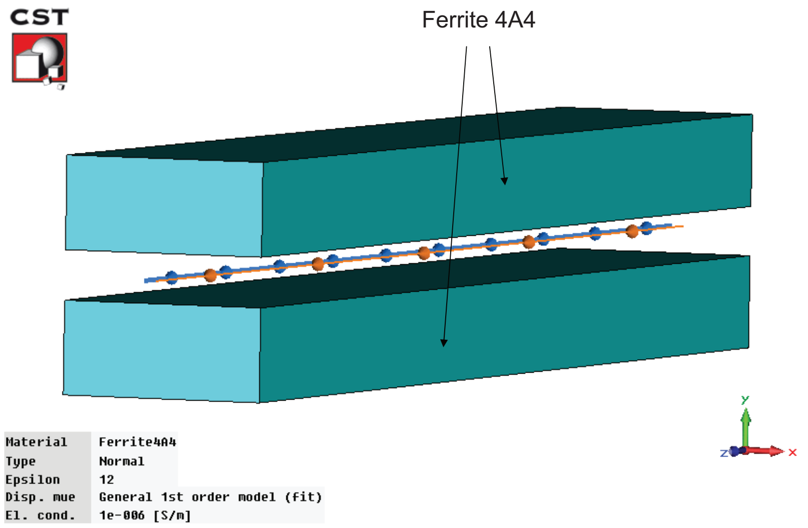

Material	Ferrite4A4
Type	Normal
Epsilon	12
Disp. mue	General 1st order model (fit)
El. cond.	1e-006 [S/m]

Figure 5.28: 3D model of the geometrical kicker model described by Tsutsui: 2 ferrite blocks (light blue) transversely surrounded by PEC (electric boundary conditions).

The dispersion model for the ferrite type 4A4 was already presented in section 5.2.2. The boundary conditions are set to electric around the ferrite except on the beam entrance and exit planes, for which the boundary condition is set to *Perfect Matching Layer*. A parameter study by C. Zannini showed that the simulated impedance is not linear with the length of the kicker, and we chose to simulate a kicker length of 80 cm, a reasonable trade off between the number of mesh cells needed to model the kicker and the convergence to impedance of larger lengths [87]. The results were then scaled to the length of the kicker given in Tab. B.2. An average of 2 million hexahedral mesh cells were used for the simulations (around 2 mm between 2 consecutive mesh points). Five simulations were performed per kicker with unique transverse aperture given in Tab. B.2 to obtain the longitudinal wake potential, as well as the dipolar and quadrupolar transverse wake potentials. The longitudinal wake potential was classically simulated by placing both beam and wake integration locations at the transverse center (x,y)=(0,0) of the kicker. The transverse dipolar wake potentials were obtained by displacing the beam transverse location to (x,y)=(a,0) while leaving the wake integration transverse location at the transverse center (x,y)=(0,0) of the kicker. The dipolar component is obtained by scaling the simulated transverse wake potential by this displacement a after the simulation. Similarly, the quadrupolar components are obtained by displacing the wake integration transverse location to (x,y)=(a,0) while leaving the beam transverse location at the transverse center (x,y)=(0,0) of the kicker. This procedure is illustrated in Fig. 5.29. We will focus here on the simulations to obtain the transverse impedance contributions. In fact, the successful longitudinal benchmark between Tsutsui's theory and simulations has been very recently presented in Ref. [87].

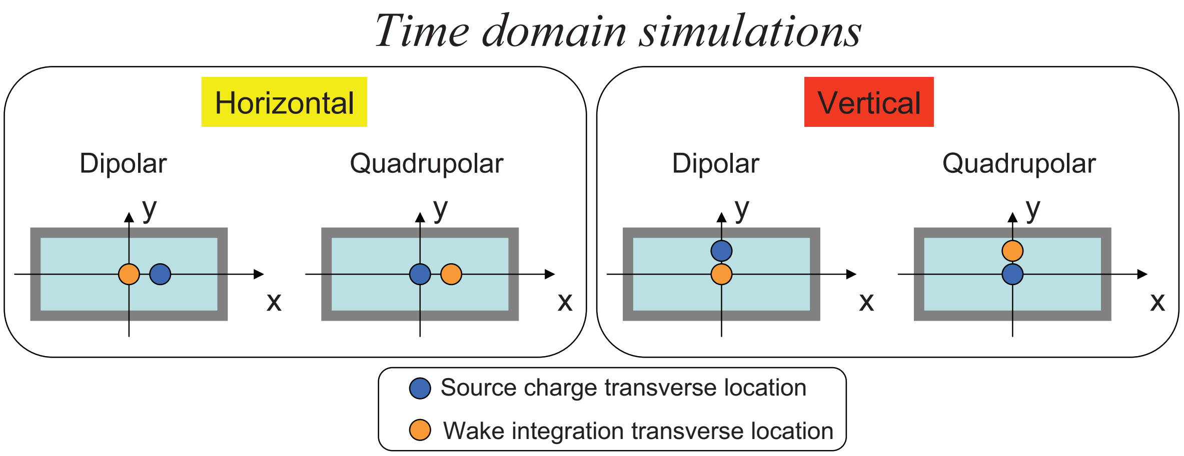

Figure 5.29: Procedure to obtain the dipolar and quadrupolar transverse wake potentials from 3D time domain simulations with a simulated beam.

Simulation Results and Comparison with Tsutsui's Theory

As an example, the simulated transverse wake potentials for a model of MKE kicker (MKE.61651) are presented in Fig. 5.30, together with the impedance derived from these simulated wake potentials with a DFT and a deconvolution from the source bunch distribution, as will be seen in Section 5.3.2.

These simulations can now be compared to the theoretical impedance obtained by H. Tsutsui for the dipolar contribution, and the new theoretical formulae we derived in section 5.2.4 for the quadrupolar impedance from Tsutsui's formalism (see Fig. 5.31). The theoretical predictions and simulations show almost identical behavior up to 2 GHz, frequency at which the theory and simulations start to differ significantly (more than 10%), in particular the imaginary vertical contributions (in red and magenta).

In view of the radically different methods to obtain these impedance contributions, this successful benchmark tends to confirm the validity of (1) the general method to obtain the dipolar and quadrupolar contributions of the impedance with *CST Particle Studio*, (2) the wake potentials simulated for the SPS kickers, and (3) the formulae for the dipolar (resp. quadrupolar) impedance contributions derived in Ref. [80] (resp. Section 5.2.4). The results for the summed contributions of all the SPS kickers are shown in Fig. 5.32, taking into account the local beta functions for each kicker as in Section 5.2.4.

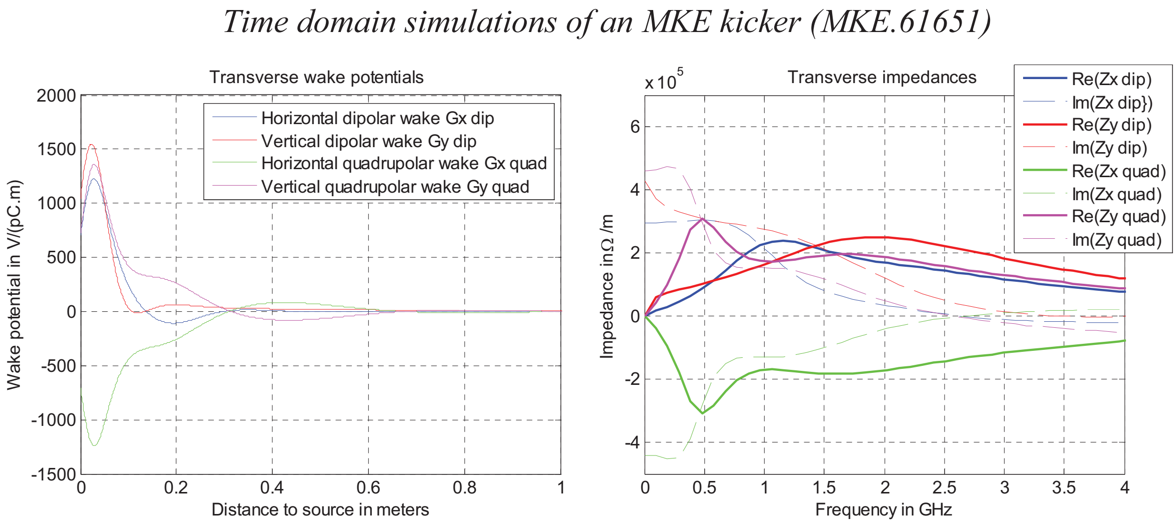

Figure 5.30: Simulated transverse wake potentials (left) and impedance (right) obtained from a DFT of these wake potentials deconvolved from the source charge distribution.

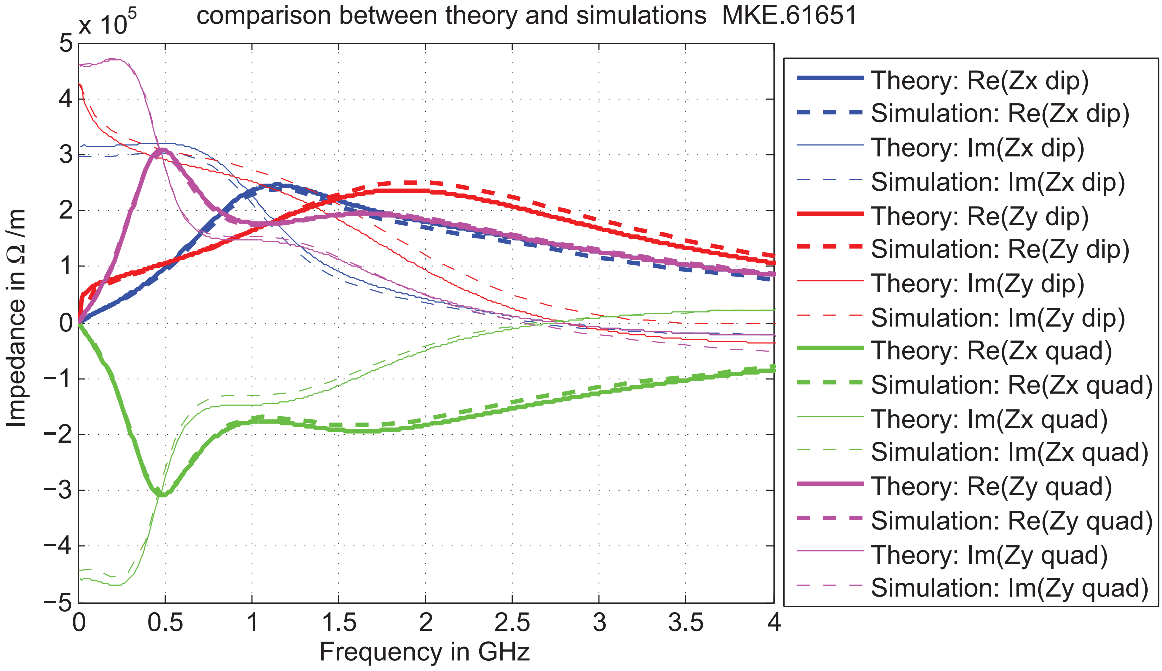

Figure 5.31: Comparison between dipolar and quadrupolar impedances from Tsutsui's theory (full lines) and *CST* simulations (dashed) for the MKE.61651 kicker. Real parts of the impedance are drawn thicker than the imaginary parts. The horizontal dipolar (Z_x^{dip}) contribution is in blue, the vertical dipolar (Z_y^{dip}) contribution is in red, the horizontal quadrupolar (Z_x^{quad}) contribution is in green, the vertical quadrupolar (Z_y^{quad}) contribution is in magenta.

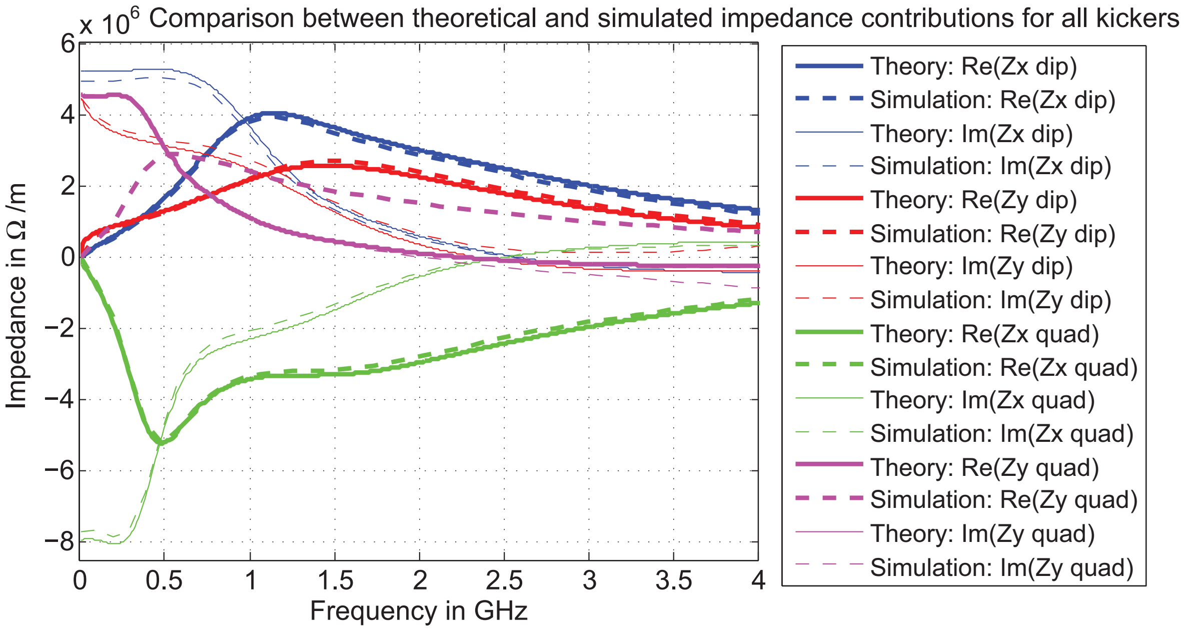

Figure 5.32: Comparison between the weighted sum of dipolar and quadrupolar impedances from Tsusui's theory (full lines) and *CST* simulations (dashed) for the 20 kickers installed in the SPS in 2006. Real parts of the impedance are drawn thicker than the imaginary parts. The horizontal dipolar (Z_x^{dip}) contribution is in blue, the vertical dipolar (Z_y^{dip}) contribution is in red, the horizontal quadrupolar (Z_x^{quad}) contribution is in green, the vertical quadrupolar (Z_y^{quad}) contribution is in magenta.

Similarly to the case of the single MKE kicker – and all other kickers for that matter –, the summed theoretical predictions and simulations show almost identical behavior up to 2 GHz. Contrary to the flat chamber, Tsutsui's model turns out to give very close results to the simulated kicker. This benchmark constitutes an important step towards gaining more confidence in both the new quadrupolar impedance formulae and the 3D simulations, before exporting these results into *HEADTAIL* for beam dynamics simulations.

Consequences for *HEADTAIL*

Such an agreement for the simulated and theoretical impedance gives an opportunity to assess the validity of importing a wake potential obtained with a finite length source instead of a real wake function. In fact, the short range simulated wake potentials are not valid due to the finite length of the source charge Gaussian distribution (here of r.m.s. length σ=2 cm). We then compare the simulated wake potentials and the theoretical wake functions to assess up to which point the wake potential can be considered as valid, if we make the assumption that we can trust the high frequency impedance obtained with Tsutsui's formalism (see Fig. 5.33).

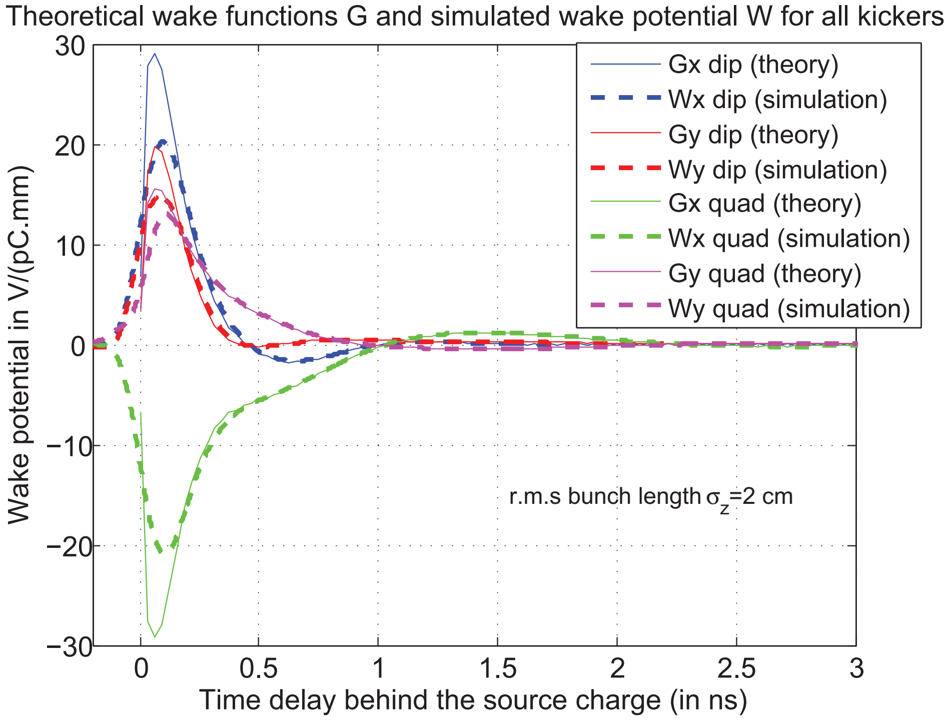

Figure 5.33: Comparison between dipolar and quadrupolar wake functions G obtained from Tsutsui's formalism (in thin full lines) and simulated dipolar and quadrupolar wake potentials W (in thick dashed lines with 2 cm r.m.s. bunch length) accounting for the 20 SPS kickers installed in the SPS in 2006 modeled with the geometry proposed by Tsutsui. The horizontal dipolar contribution is in blue, the vertical dipolar contribution is in red, the horizontal quadrupolar contribution is in magenta, the vertical quadrupolar contribution is in green.

In Fig. 5.33, the simulated wake potentials and theoretical wake functions are observed to be superimposed if the time delay between the source and the test particles is more than 0.15 ns (or a distance of 5 cm, i.e. 2.5 times the simulated r.m.s. bunch length). In these conditions, the wake potentials could be considered valid down to a distance corresponding to 2.5 r.m.s. bunch lengths. If we use an r.m.s. bunch length of 10 cm instead of 2 cm in Fig. 5.34, we can see that such a scaling law between the r.m.s. bunch length and the validity limit of the wake potential does not apply. In fact, the wake potentials and wake functions do not agree if the time delay between the source and the test particles is less than 2 ns (or a distance of 70 cm, i.e. 7 times the simulated r.m.s. bunch length). In fact, this graph shows that using an r.m.s. bunch length of 10 cm in *CST Particle Studio* simulations does not enable to sample the wake function correctly. Smaller bunch lengths have to be used at the expense of a denser mesh, which leads to longer CPU time or even simulation crash due to lack of memory.

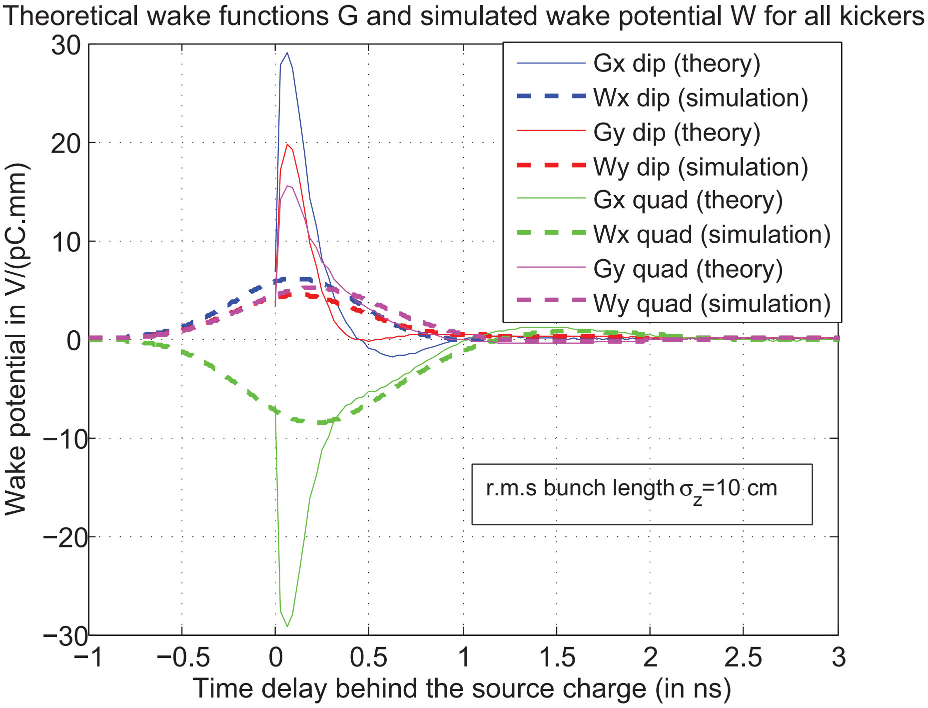

Figure 5.34: Comparison between dipolar and quadrupolar wake functions G obtained from Tsutsui's formalism (in thin full lines) and simulated dipolar and quadrupolar wake potentials W (in thick dashed lines with r.m.s. bunch length of 10 cm) accounting for the 20 SPS kickers installed in the SPS in 2006 modeled with the geometry proposed by Tsutsui. The horizontal dipolar contribution is in blue, the vertical dipolar contribution is in red, the horizontal quadrupolar contribution is in magenta, the vertical quadrupolar contribution is in green.

Finally, we compare the theoretical impedances of the flat chamber and Tsutsui's geometrical model with the simulations up to 13 GHz in Fig. 5.35. The divergence of the simulated impedances at higher frequencies due to the non zero bunch length is clearly visible. The imaginary part of the dipolar and quadrupolar impedance is observe to diverge at around 2 to 4 GHz, whereas the real part diverges at 8 GHz. Apart from the horizontal dipolar impedance, the flat chamber model is very different in both amplitude and shape from both the simulations and Tsutsui's formalism. The total (dipolar + quadrupolar) linear contribution to the impedance is also given at the bottom of Fig. 5.35. In contrast with the Zotter/Métral theory, we can observe the significant negative total contribution in the horizontal plane for both simulations and Tsutsui theory up to 500 MHz. On the other hand, the vertical total contribution is rather similar at low frequencies. In terms of beam dynamics, as we will see in Section 6.2.3, these total contributions will lead to (1) a positive tune shift in the horizontal plane for the Tsutsui theory (small negative tune shift for the Zotter/Métral theory), and (2) a similar negative vertical tune shift for both Zotter/Métral and Tsutsui theories. It is also interesting to notice that the diverging imaginary parts seem to compensate between the dipolar and quadrupolar parts in each plane, so that the total horizontal and vertical impedance contributions – both real and imaginary parts – are observed to diverge from the theoretical results after 8 GHz. This feature will be investigated further in the future, as it is most likely linked to a simulation issue.

At this occasion, we observe the convergence of all dipolar and quadrupolar theoretical contributions of both Zotter/Métral and Tsutsui formalisms at high frequencies, maybe indicating that the Yokoya factors are only valid in the high frequency range for the case of the geometry used by Tsutsui to obtain his theory. For this reason, the form factors relating the impedance obtained with the Tsutsui model (Tsutsui formalism) and the cylindrical model (Zotter/Métral formalism) is plotted for the dipolar and quadrupolar impedance contributions in both planes in Fig. 5.36. Due to the fact that all theoretical contributions become very small at very high frequency, strong numerical noise kicks in at around 100 GHz when performing the division $Z_{Tsutsui}/Z_{Zotter}$. However, we observe that the form factors relating the cylindrical model to the Tsutsui model are frequency dependent, and seem to tend towards $\pi^2/24$ for the horizontal dipolar and the vertical quadrupolar contributions and $-\pi^2/24$ for the horizontal quadrupolar contribution at high frequencies, which we could have expected if the Yokoya factors are valid at high frequencies. On the other hand, it is surprising to see that the dipolar vertical form factors seem to converge also to $\pi^2/24$ instead of $\pi^2/12$. Frequency dependent form factors have already been introduced by Burov and Lebedev in the case of a bilayer flat chamber made of metal surrounded by vacuum [52], and further studies are ongoing to derive these frequency dependent form factors in more general situations. The resonant-like behavior at a frequency around 3 GHz in the imaginary part is due to the zero crossing of the impedance contribution of the cylindrical chamber.

This convergence of Tsutsui's formula with the Zotter/Métral formalism, which is valid at all frequencies assuming given electromagnetic properties of the materials, could be an indication that the high frequency part of Tsutsui's formula is also valid. All these observations lead to the conclusion that with the current knowledge in our possession, Tsutsui's formalism would be the most accurate model of the SPS kickers.

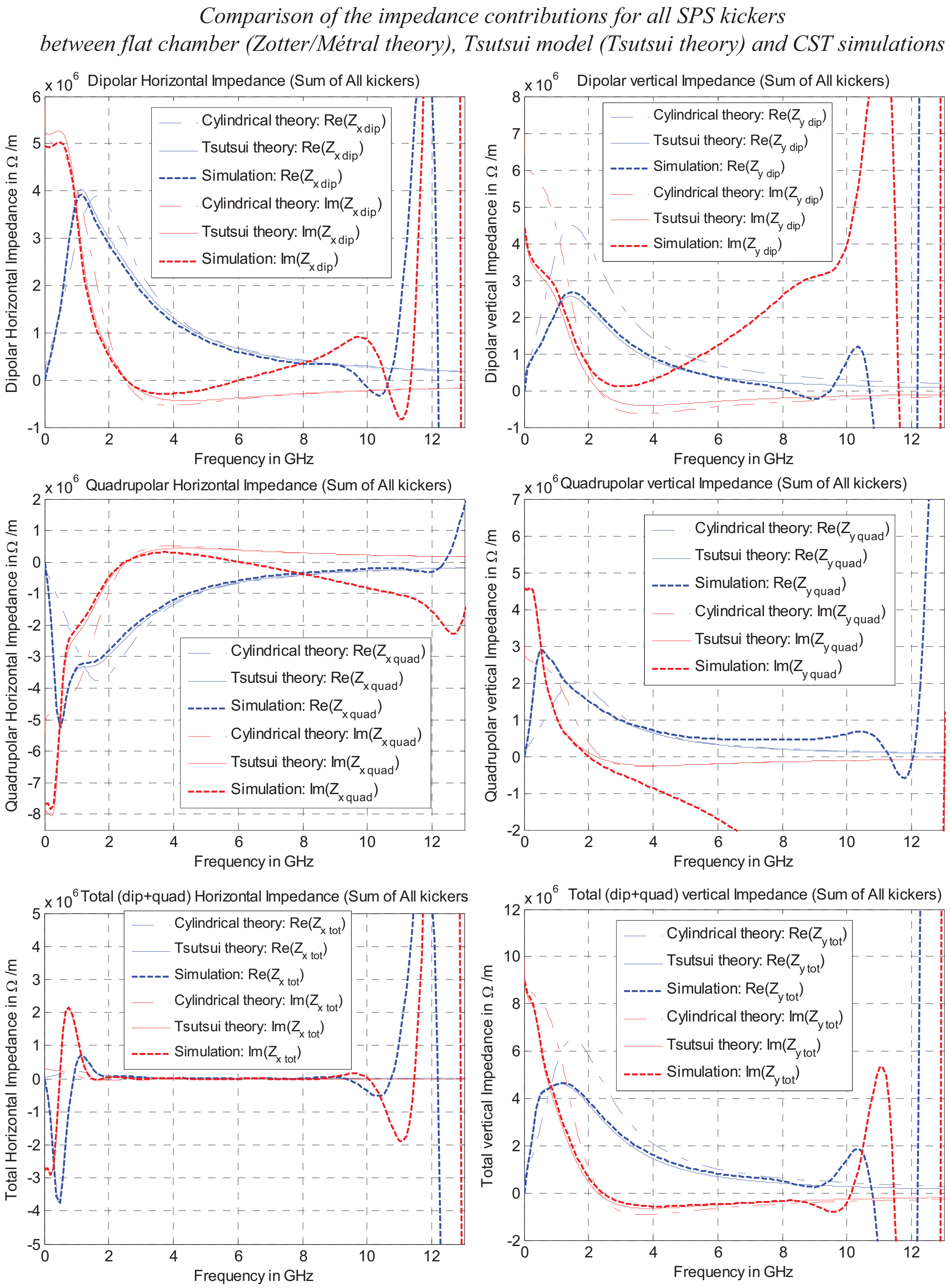

Figure 5.35: Comparison of the horizontal (left)/vertical (right) dipolar (top)/quadrupolar (middle)/total (bottom) impedance contributions for all SPS kickers between flat chamber (Zotter/Métral theory in thin dot dashed lines), Tsutsui's geometrical model (Tsutsui theory in thin full lines) and CST Particle Studio simulations (in thick dashed lines). Real parts are in blue and imaginary parts are in red.

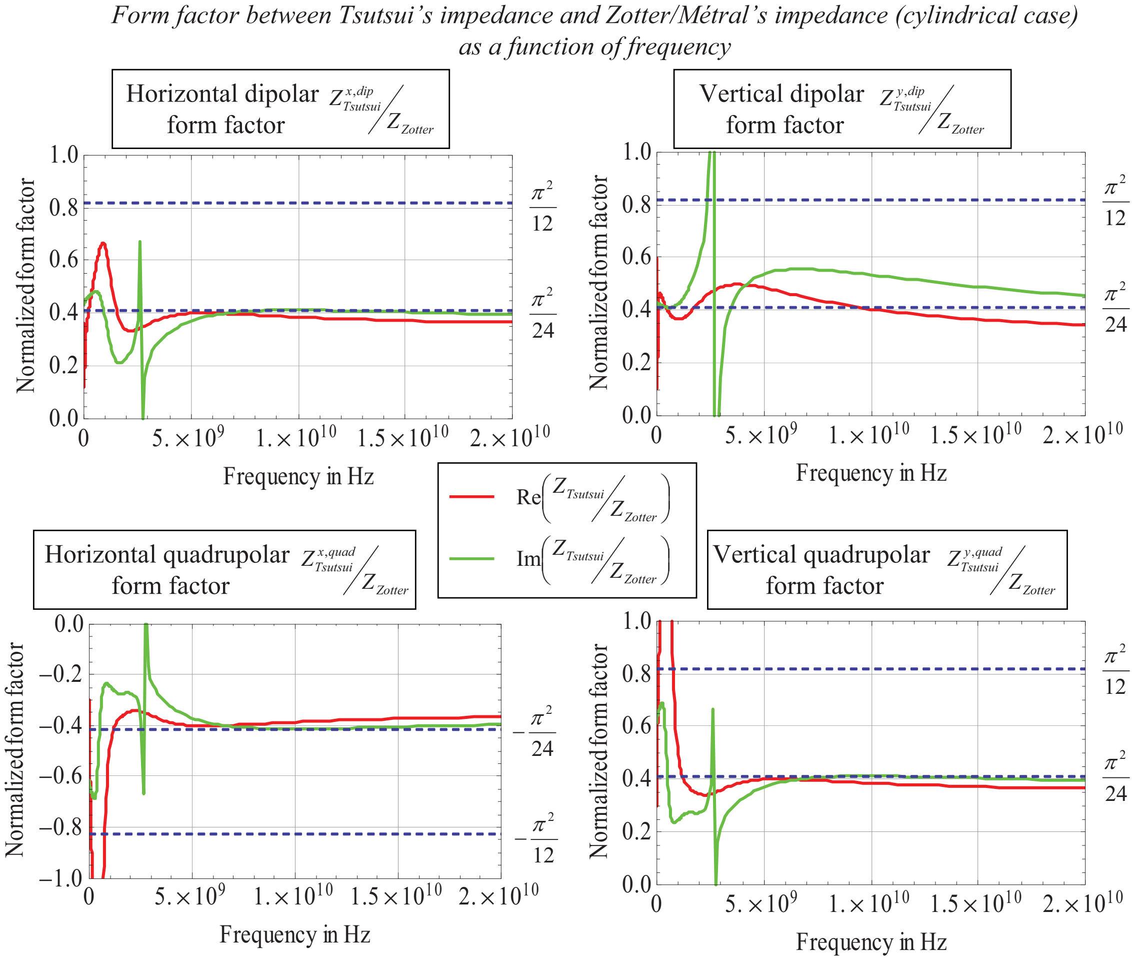

Figure 5.36: Form factors $Z_{Tsutsui}/Z_{Zotter}$ relating the horizontal (left)/vertical (right) dipolar (top)/quadrupolar (bottom) impedance contributions for an SPS MKE kicker calculated with the Tsutsui theory $Z_{Tsutsui}$ to the impedance of a cylindrical beam pipe made of ferrite calculated with the Zotter/Métral theory Z_{Zotter}. Real parts are in red and imaginary parts are in green.

5.3.2 3D Simulations of the Impedance of the SPS BPMs

The results of *CST Particle Studio* simulations of the Horizontal (BPH) and Vertical (BPV) SPS beam position monitors are discussed in this section. These elements have been chosen for studies because of their large number (106 BPH and 96 BPV during the run in 2006). As can be seen on Fig. 5.37, the shape and materials of these SPS BPMs are not trivial and to our knowledge there is no theory to predict their beam coupling impedance. As a consequence, bench RF measurements were also performed to benchmark the simulation results with available measured observables.

Figure 5.37: Pictures of an SPS BPH: partly dismantled BPH inner body (left and center) and full BPH assembly (right). The triangular-shape electrodes and the white ceramic spacers on top of the electrodes are visible on the pictures of the dismantled inner body.

Simulation Setup

The geometric structures of the BPH and BPV were first generated by B. Spataro and collaborators at INFN Frascati (Italy) with the very first version of *MAFIA* [88]. From these first attempts, updated 3D models were generated from archived technical drawings for simulations with *CST Particle Studio*. These new models for the BPH and BPV are presented in Fig. 5.38. Additional cross-sections of the BPH model are presented in Fig. 5.39 in order to show more details of the geometry of the inside casing.

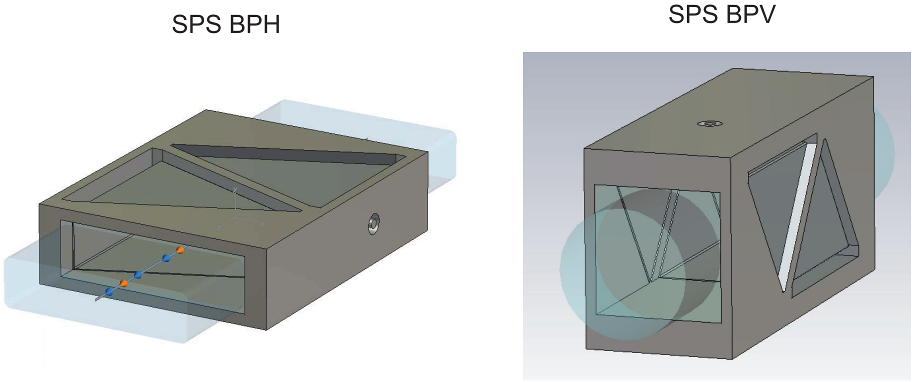

Figure 5.38: Models of the SPS BPH and BPV produced with *CST STUDIO SUITE* from technical drawings.

Many simplifications were applied to obtain the modeled geometry used for the simulations:

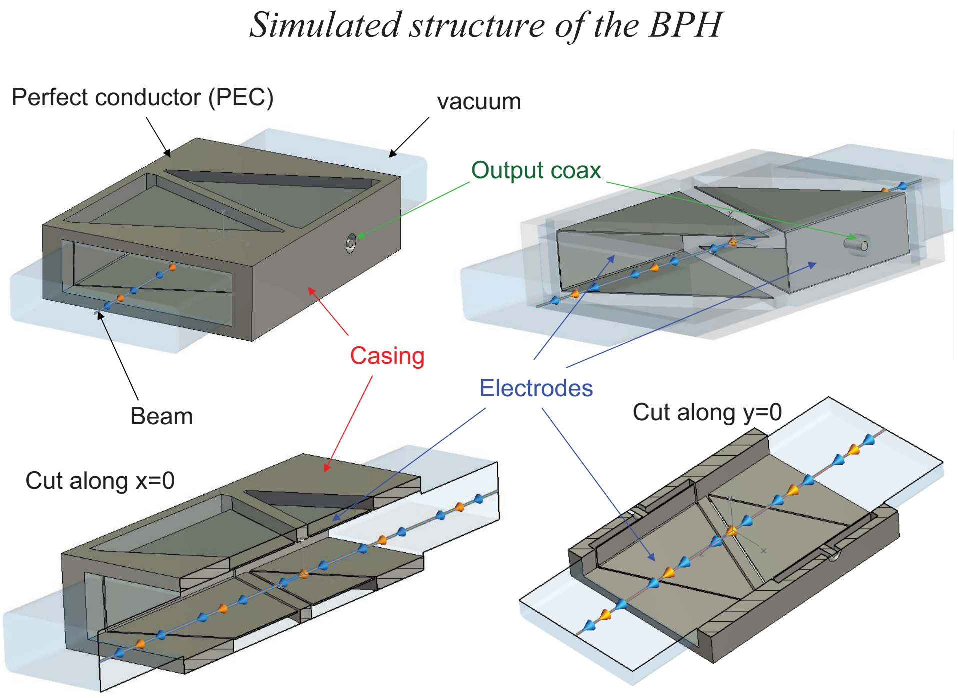

Figure 5.39: Cross-sections and transparent views of the BPH model revealing details of its geometry. Beam path and wake integration path are shown with blue and orange arrows. Hiding the casing (top right) and using a cut plane (bottom) reveals the details of the inner structure of the BPH body: a pair of bi-triangular shaped electrodes isolated from the rest of the casing with vacuum cavities. Beam entry and exit planes are perfect matching layers, and all other boundaries are perfect conductors (PEC).

- the outer cylindrical shell and the cavity between this shell and the rectangular inner body observed in Fig. 5.37 were not modeled, thereby assuming that the fields created by the beam can not reach beyond the inner body.
- Several features of the inner casing were removed (electrodes screws, brass calibration plates, ceramic spacers) or simplified (perfectly matched electrode coaxial port, casing to beam pipe transition, shape of the beam pipe cross-section, mechanical tolerances).
- The SPS BPM inner body is made of an aluminum alloy (Anticorodal B [89]), while both the electrodes and the beam pipe are made of Stainless Steel type 304L. However, all metallic parts of the simulated BPMs were initially assumed to be made of perfect conductors (PEC).
- The coaxial port geometry was simplified and matched to a 50 Ω load.
- To reduce computer time, 1 (resp. 2) transverse symmetry plane(s) was used to compute the transverse (resp. longitudinal) impedance. Comparisons on several cases showed very little effect of using the symmetry planes on the simulated wake potentials.
- Several important *CST Particle Studio* features (such as the *Perfect Matching Layer* boundary condition) are not available in the current version if the beam is not ultrarelativistic. We therefore only consider ultrarelativistic beams.
- The simulated beam is a pencil beam (i.e. with no transverse size).

We therefore make the assumption that these simplifications have a smaller impact on the simulated results than the coupling between the cavities behind the electrodes and the main cavity through which the beam traverses. *CST Particle Studio*s *Wakefield Solver* was then used to obtain the wake potential generated by the passage of a Gaussian bunch through the BPM. The Beam Coupling Impedance of the BPM is also automatically postprocessed from this wake potential. The Eigenmode solver of CST Microwave Studio was also used to obtain the parameters of the modes trapped in the structure (resonance frequency f_{res}, shunt impedance R_s and quality factor Q). Beam entry and exit planes are perfect matching layers, and all other boundaries are perfect conductors (PEC).

Time Domain Simulations

For the following *CST Particle Studio* simulations, the 15 meter wake potential left by a bunch of r.m.s. length $\sigma_z = 1$ cm and charge q= 1nC in BPH and BPV models made of 1 million hexahedral mesh cells was calculated using the *Indirect Testbeam* method to integrate the electromagnetic fields. This integration method is described briefly in [36] and computes the longitudinal wakes generated by test beams on the boundary of the transverse cross section of the beam pipe to obtain the longitudinal wake anywhere in the cross section of the beam pipe. In cases such as the BPMs, this method reduces the numerical noise when compared to a single *direct* integration of the electromagnetic fields with the source beam located at a given transverse location. The SPS BPH longitudinal wake potential was obtained by simulating a bunch passing at the transverse center of the beam pipe, and calculating the longitudinal wake along z also at (x,y)=(0, 0), as depicted in the top left sketch within Fig. 5.40. The SPS BPH total transverse wake potential is obtained by displacing the transverse locations of both the beam location and the wake integration location from the center of the beam pipe (see middle and center sketches within Fig. 5.40). The simulated wake potential oscillations are observed not to decay within a reasonable simulated time. This is why additional frequency domain simulations are needed to obtain more accurate parameters for each of the resonance modes. Finally, it is important to realize that CST Particle Studio uses a different sign convention in the definition of the impedance that leads to a sign change of the transverse impedance. We chose to keep CST Particle Studio's convention in the graphs, but the numerical results are given in the convention defined in Chap. 3 for which inductive contributions are positive.

The order of magnitude of the frequencies of the longitudinal impedance peaks for the BPH agrees with the 3 sharp peaks measured in Ref. [90]. Similar simulations for the BPV model gave the simulation results presented in Fig. 5.41.

Before moving to the frequency domain simulations, several remarks need to be made on these frequency domain simulations.

- The length of the wake potential should be increased to obtain a sufficient frequency resolution for the impedance. This is why 15 m of wake potentials were simulated, at the expense of longer computation times.

- In the simulations, matching at the coaxial ports extracting the signals from the electrodes appears to be fundamental to damp the reflected modes. Wrong matching leads to very strong oscillations as can be seen on Fig. 5.42.

- The cause for large resonance peaks observed in time domain simulations can be understood by observing the EM field contributions at their resonance frequencies. For instance, thanks to Fig. 5.43, the peak at 1.06 GHz in the longitudinal plane can be linked to the coupling through the 2mm width slits between the main cavity where the beam passes and the empty space behind the electrodes.

- The DFT embedded in *CST Particle Studio* appears to create artificial ripple. This has been reported to the *CST* customer support team in Darmstadt, which acknowledged that the embedded DFT should be modified in the next versions. This is why we use here a homemade DFT inspired from the DFT used in the impedance computation code *ABCI* from Y.H. Chin [91].

- Studies carried out in close collaboration with Carlo Zannini and the CERN impedance team revealed that a factor 4 could be observed between theoretical computations and *CST Particle Studio 2009* simulations of the transverse wake potential of a resistive beam pipe when using the indirect testbeam wakefield solver. After numerous checks on our side, that issue was finally brought up to the *CST* customer support team (in particular M. Balk and U. Becker), who quickly performed their own checks and acknowledged an issue with that particular solver. This wake integration issue will be solved in the next *CST Particle Studio 2010* release, which is currently under development (see for instance a slide in Fig. 5.44 provided by M. Balk from *CST AG* showing the large factor obtained when running the same BPH input file with released 2009 and unreleased 2010 versions).

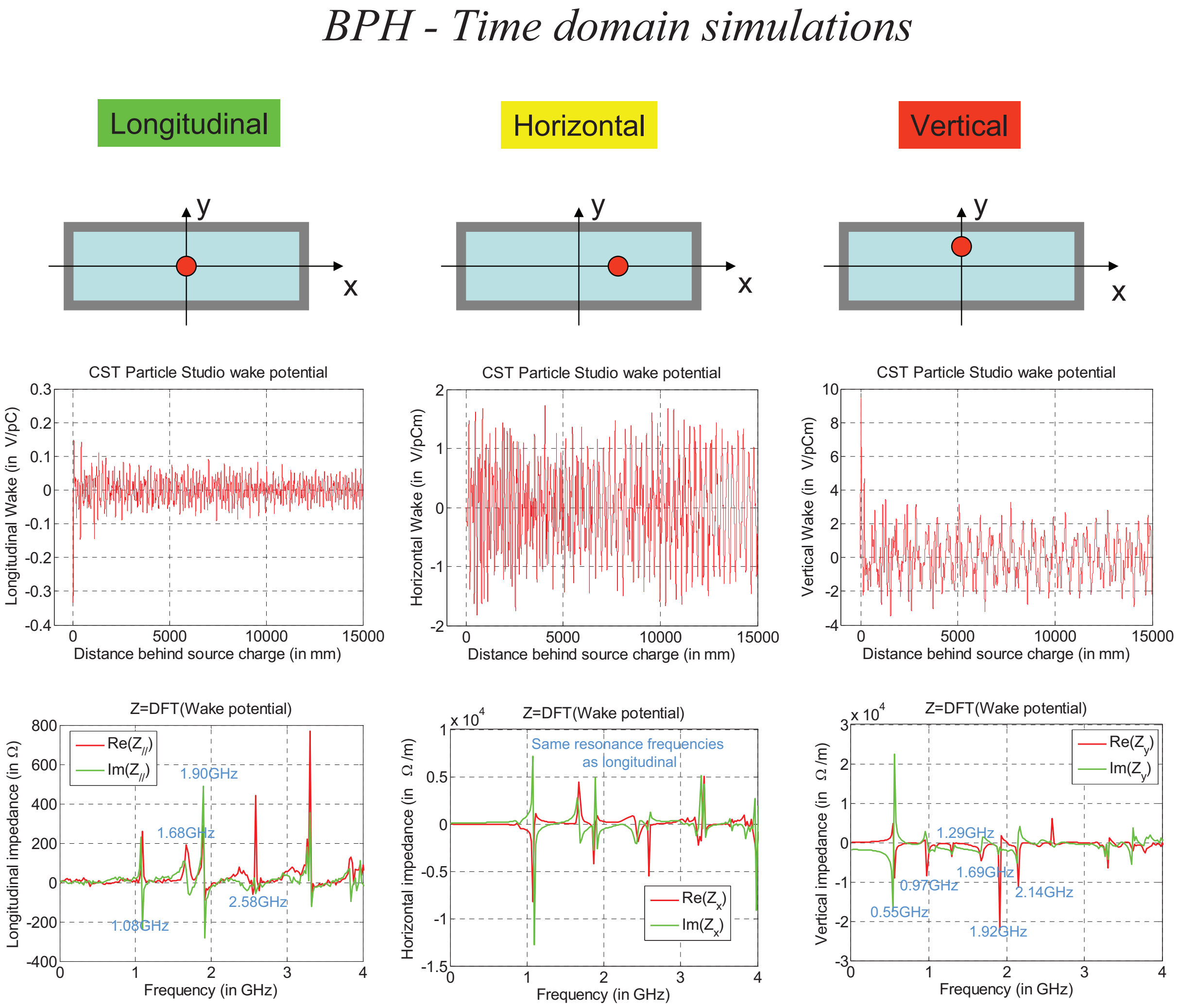

Figure 5.40: Simulated wake potentials (middle) and impedances (bottom) of a 3D model of an SPS BPH. The sketch of the transverse locations of the beam path and wake integration path (top) are shown for the simulation of the longitudinal impedance (left), total horizontal impedance (center) and total vertical impedance (right). In a linear approximation, the total transverse impedances is the sum of both dipolar and quadrupolar contributions. The main resonance frequencies are displayed next to the peaks. The total transverse impedance is normalized to the 5 mm transverse source and test displacement used in the simulation.

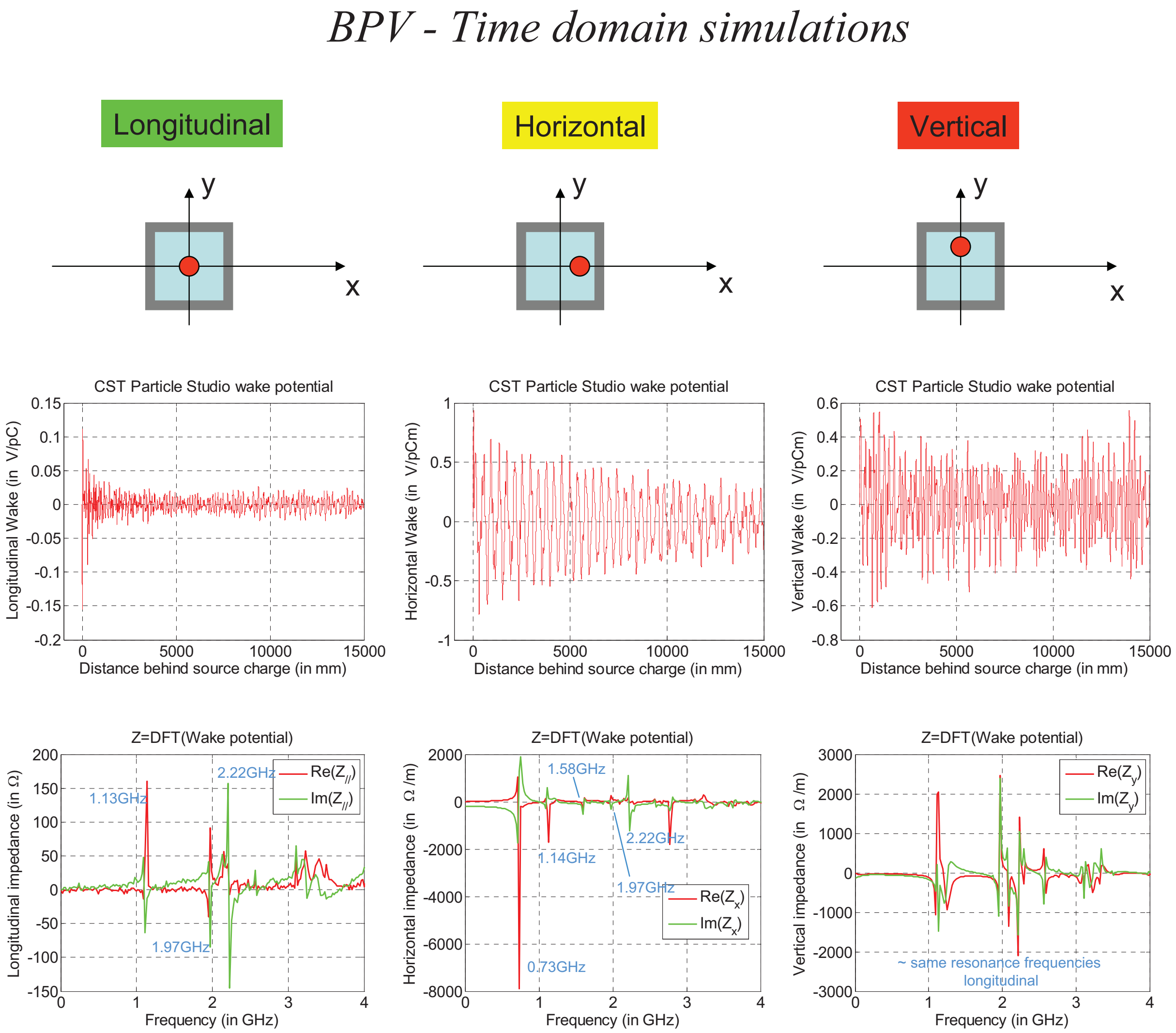

Figure 5.41: Simulated wake potentials (middle) and impedances (bottom) of a 3D model of an SPS BPV. The sketch of the transverse locations of the beam path and wake integration path (top) are shown for the simulation of the longitudinal impedance (left), total horizontal impedance (center) and total vertical impedance (right). In a linear approximation, the total transverse impedances is the sum of both dipolar and quadrupolar contributions. The main resonance frequencies are displayed next to the peaks. The total transverse impedance is normalized to the 5 mm transverse source and test displacement used in the simulation.

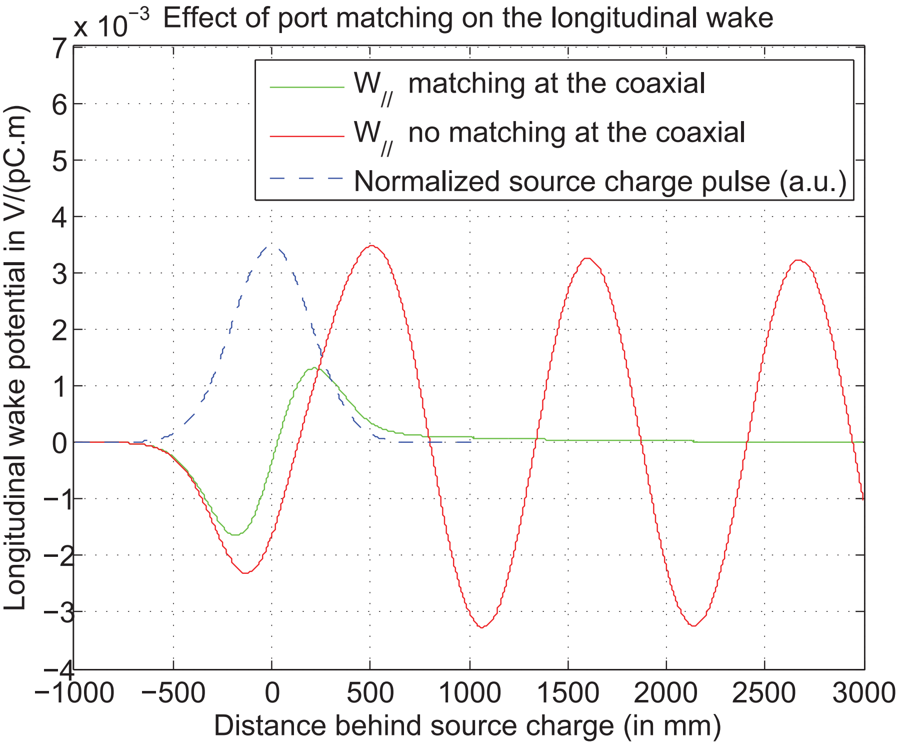

Figure 5.42: Effect of matching at the two coaxial ports on the longitudinal wake. Here, adequate matching (in green) enables to damp an otherwise strong resonance around 280 MHz (in red) due to reflexions at the coaxial port. The source charge distribution amplitude (in blue) is arbitrarily normalized to the maximum amplitude of the longitudinal wake (not matched in red) for display purposes.

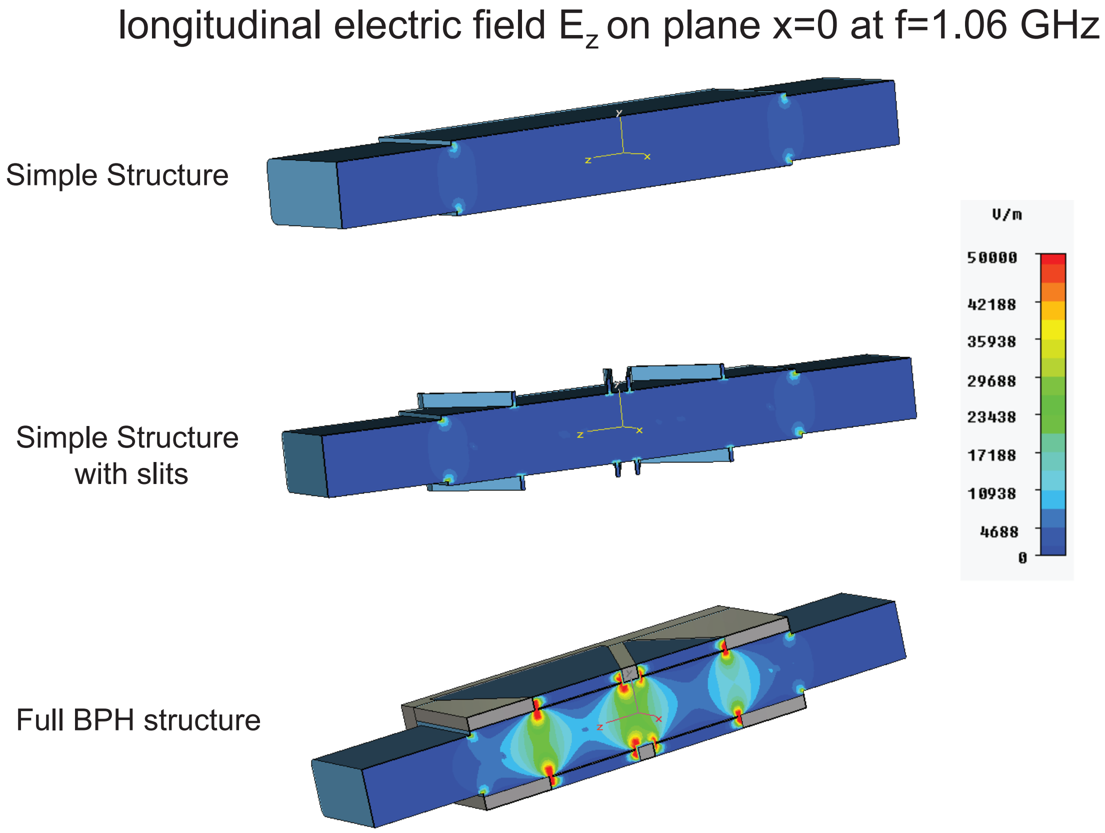

Figure 5.43: Longitudinal electric field E_z on plane $x = 0$ at f=1.06 GHz for a simple BPH casing without slits (top), a structure with 2 mm wide 9 mm deep slits but no cavity behind the electrode (middle) and a full BPH model with slits and cavities behind the electrodes (bottom). The gaps between the electrodes and the casing are thin (2 mm), but these electrodes are so thin that the cavities behind the electrodes couple with the main aperture to perturb the EM fields around the beam down to lower frequencies than expected from the size of the slits (around 1 GHz).

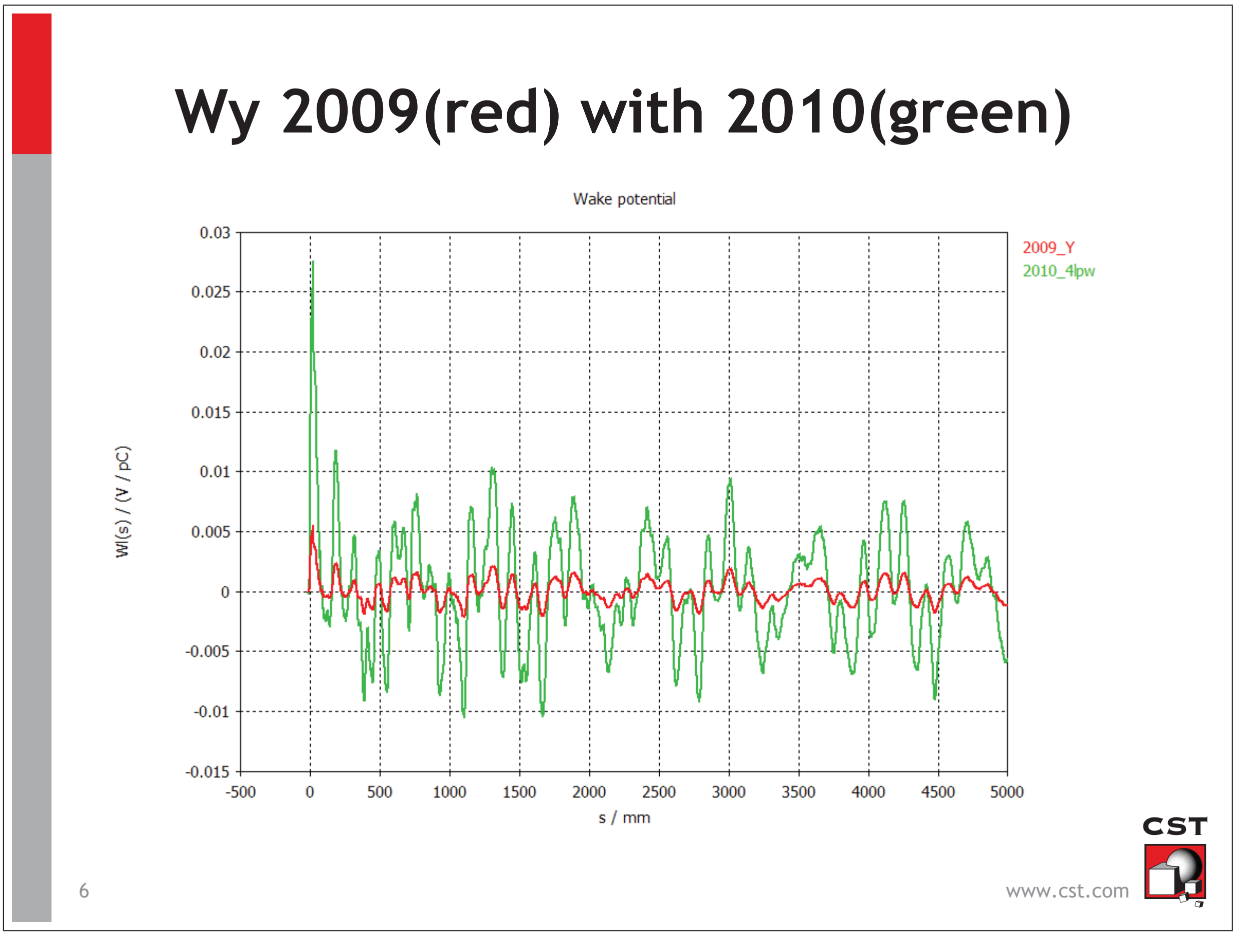

Wy 2009(red) with 2010(green)

www.cst.com

Figure 5.44: Slide extracted from a PowerPoint file sent by M. Balk (*CST AG*) on May 19, 2009 showing the large factor obtained between a simulation of the SPS BPH dipolar wake potential with the released 2009 version of *CST Particle Studio* (in red) and a simulation of that same input file with an unreleased version of *CST Particle Studio 2010* (in green). Apart from this factor, the general behavior of the wake is conserved. We provided the input file but these simulations were kindly performed by M. Balk. *Courtesy of M. Balk, CST AG.*

In the meantime, M. Balk from the customer support team kindly helped us and ran some of our input files on their own clusters with the new unreleased 2010 version. The results from these simulations of dipolar and quadrupolar contributions of the wake potentials are presented in Fig. 5.45 together with the wake functions $G(t)$ obtained by deconvolution of these wake potential $W(t)$ from the source charge distribution $\rho(t)$. The deconvolution step is performed in frequency domain by dividing the Discrete Fourier Transform (DFT) of the wake potential by the DFT of the source charge to obtain the impedance $Z(f)$. The wake function is then classically obtained by inverse DFT (iDFT) of the impedance.

$$G(t) = \mathrm{iDFT}\left(Z(f)\right) = \mathrm{iDFT}\left(\frac{\mathrm{DFT}\left(W(t)\right)}{\mathrm{DFT}\left(\rho(t)\right)}\right). \qquad (5.114)$$

In this not so trivial step described in more details in Ref. [92], it is particularly important to correctly synchronize the time coordinates for the wake potential and the source charge. Also, the frequency spectrum of the source charge vanishes at high frequencies, while the wake potential remains finite due to numerical errors. The impedance then diverges and it is necessary to window the impedance before performing the iDFT. The source charge frequency spectrum vanishes at lower frequencies if the bunch length is increased. Therefore, it is crucial to use as small bunches as possible to increase the frequency range over which the impedance is not affected by numerical noise, and thereby increase the time resolution of the wake function results. It is also important to note that we took the opportunity to refine several features of the BPH and BPV models for these simulations, such as the addition of ceramic spacers that will be justified from frequency domain measurements and simulations as well as an improved shape for the flat SPS beam pipe attached to the BPH. For these simulations we could profit from the powerful dedicated MPI (parallel computing) cluster at *CST AG* and we were able to model a mesh with more than 4 millions cells that would not have otherwise been possible to simulate on a single PC. In Fig. 5.45, we observe that the wake function and wake potentials obtained with a 1 cm r.m.s. bunch length share similar behaviors. The impedance had to be truncated at 15 GHz to avoid spoiling the results with the diverging high frequency contribution, and we observe the resulting loss in time resolution. These wake functions represent the contribution from all the SPS BPMs present in the machine in 2006 (106 BPHs and 96 BPVs). As for the SPS kickers, these wake potentials and wake functions have been weighted by the relative beta functions at which these BPMs are located. The individual beta functions available from *MAD-X* aperture files for each of these 202 BPHs and BPVs have been used. Finally, we notice that the quadrupolar wake functions are not opposite in sign as expected by E. Métral in Ref. [93], but this could be due to the strong asymmetry of the BPM structure, which makes it hard to define a *center* of the structure.

These dipolar and quadrupolar wake functions are now ready to be imported into *HEADTAIL*. However, we were not very experienced with these 3D simulations and it seemed important to perform some checks before using these results in *ZBASE*. Since theory can not be applied to the complex geometry of the BPH, classical bench RF impedance measurements with wire could be performed on an SPS BPH and an SPS BPV [94]. However,

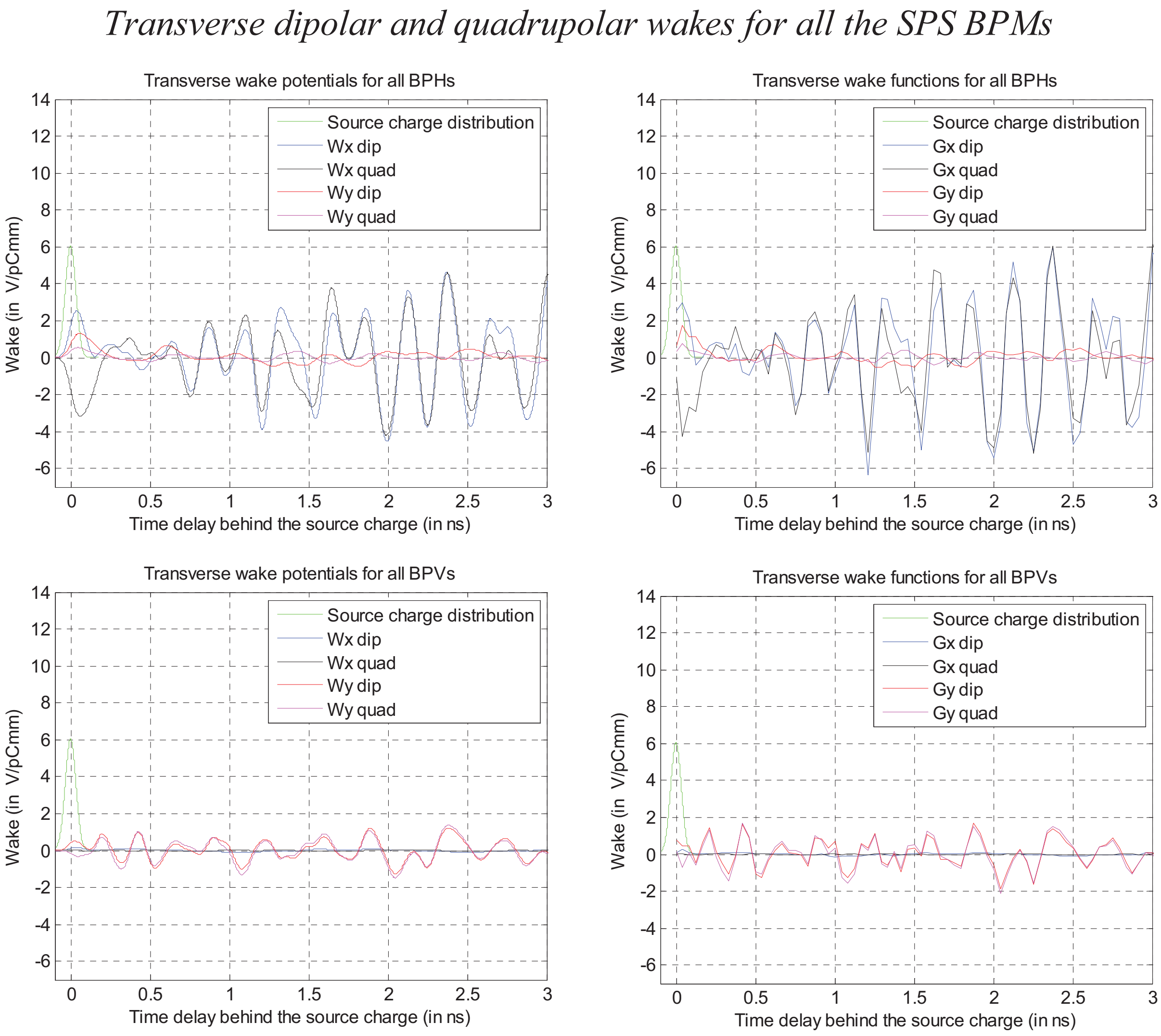

Figure 5.45: Transverse dipolar and quadrupolar wake potentials $W(t)$ (left) and wake functions $G(t)$ (right) accounting for all the SPS BPHs (top) and SPS BPVs (bottom). The beta functions of each BPM was taken into account.

the conditions were not ideal to measure the impedance with a wire: the expected detected signal would be small, the SPS BPMs available from storage are radioactive, and tampering with the device would mean reconditioning before being able to put it back in the machine. A nice feature of the BPM is however the possibility to measure scattering parameters (S-parameters) through the available N-ports normally used to extract the signals from the beam. A convenient crosscheck of the validity of the model would be to compare frequency domain simulations and RF bench measurements of the S-parameters for both a BPH and a BPV.

Frequency Domain Simulations and Bench RF Measurements as a Crosscheck of Time Domain Simulations

It is important to note that these S-parameters simulations and measurements are not direct impedance measurements, but they could help validate or invalidate the assumptions and modeling choices. CST Microwave Studio Frequency Domain solver is used to obtain the S-parameters of the models of BPH and BPV shown in Fig. 5.38 in the frequency range 0.5 GHz to 4 GHz using adaptative mesh refinement. In parallel, a Vector Network Analyzer (VNA) is used to excite one of the coaxial ports (port 1) with an RF wave of sweeping frequency and simultaneously acquiring the signal transmitted to the other coaxial port (port 2). This is the classical S_{21} measurement. Pictures of the BPMs and the measurement setup with the VNA are shown in Fig. 5.46 and Fig. 5.47.

Figure 5.46: SPS BPV (left) and SPS BPH (right) used for the S-parameter measurements. The sealing plastic bag around the BPMs had to be pierced to plug the cable in the N ports connected to the electrodes.

The measurements were realised with a linear frequency sweep between 1 MHz and 3 GHz (20000 points). Using a low *IF bandwidth* (1 kHz) turned out to be necessary to enhance the resolution of the signal. Port 1 is defined as the port next to the beam pipe and port 2 is the port next to the flange. The transmission S_{21} simulation and measurements for the SPS BPH and BPV are gathered in the left part of Fig. 5.48.

Up to 2 GHz, the same $S_(21)$ general pattern can be observed in both measurements and simulations, even if a 10 to 100 MHz frequency shift is observed. Besides, it is interesting to observe that resonance peaks are present in both S_{21} simulations and measurements

Figure 5.47: S-parameter measurement setup for the BPH.

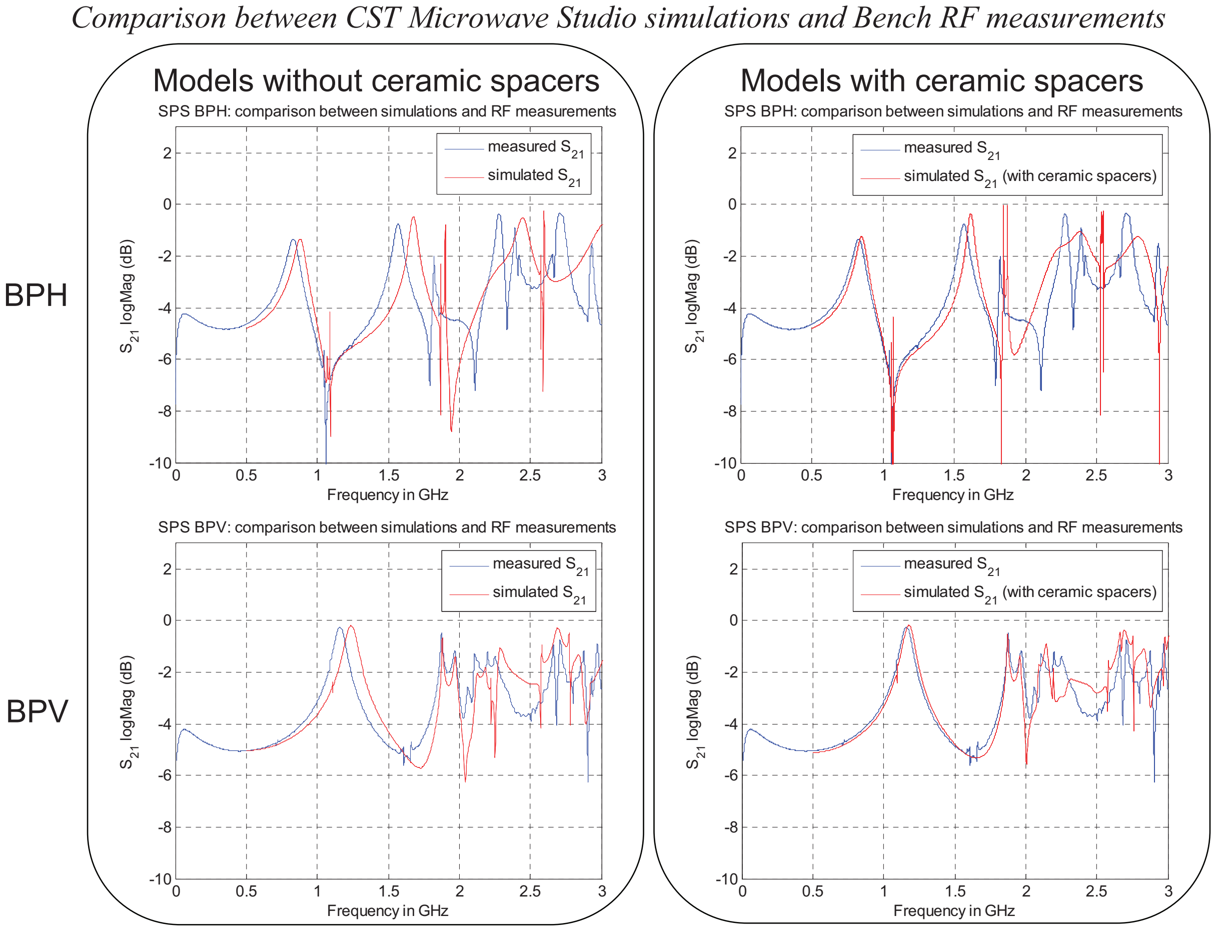

Figure 5.48: Comparison between *CST Microwave Studio* simulations (in red) and bench RF measurements (in blue) of transmission parameter S_{21} for the SPS BPH (top) and BPV (bottom). A first set of models without ceramic spacers (left) was used for the simulations. A frequency-dependent frequency shift is observed between measurements and simulations. The BPM models were therefore refined and in particular ceramic spacers were included (right).

at longitudinal or vertical impedance resonance frequencies previously obtained in time domain. BPH longitudinal impedance resonances can be clearly seen at 1.1 GHz, 1.7 GHz, 1.9 GHz and 2.6 GHz for instance. Other peaks need a very close zoom and a smith chart to check that they indeed are resonances, as the peaks at 0.7 GHz (horizontal), 1.1 GHz (horizontal or longitudinal), 1.6 GHz (horizontal), 2 GHz (longitudinal) for the BPV. This interesting observation on both BPMs leads to the conclusion that (1) the simulated BPM models are close to the real BPMs, and (2) this kind of indirect RF measurements without wire can give relevant information on the impedance of a device.

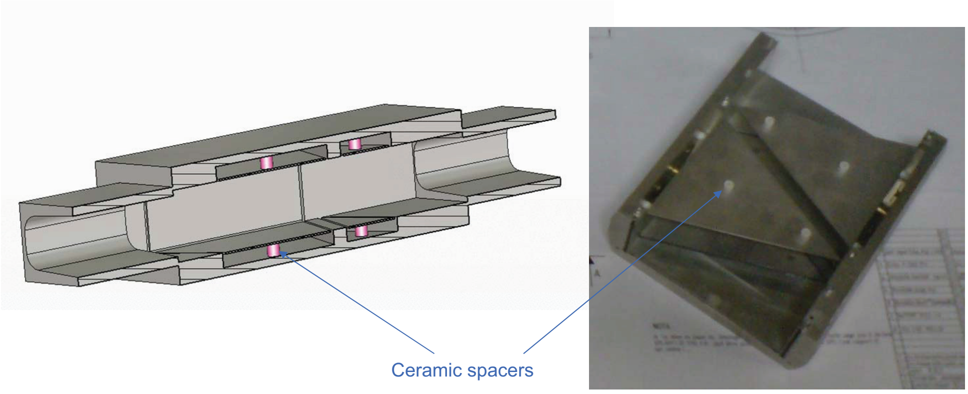

Figure 5.49: Improved model of the SPS BPH (left) and picture of the SPS BPH (right) highlighting the presence of the ceramic insulator spacers designed to mechanically stabilize the thin electrodes. The cross section of the SPS beam pipe and the transition with the BPH as well as other minor geometrical details were also improved.

In order to improve the model, the small white ceramic spacers visible on the top of the electrode on Fig. 5.49 have been included in the simulations (see results on the right side of Fig. 5.48). As expected by waveguide theory [29], the $\hat{\varepsilon}_r$=10 ceramic decreased the frequency of the modes, and improved the agreement between simulations and RF measurements. In Ref. [95], similar simulations and measurements of the transmission parameter S_{11} were reported as well as S-parameter measurements on a BPV prototype equipped with a wire. These other measurements also confirm that the 3D model we used to obtain the wake functions for *HEADTAIL* simulations is reasonably close to the real SPS BPMs installed in the machine, in spite of all the approximations mentioned at the start of this section. As for theoretical computations, 3D models can never represent fully the reality of an accelerator device, in particular the material properties and the inevitable deviations to the specifications. The main challenge of simulations is to decide which approximations can be made and which can not be made. This is why RF measurements will always be needed to benchmark the simulations and validate or invalidate the chosen set of approximations.

5.4 RF Bench Measurements

Similarly to electromagnetic simulations, impedance measurements involve being able to excite the device under test (DUT) with an RF wave simulating the beam and measuring the resulting EM fields along the beam path (or with an offset for transverse measurements). A classical way to perform these measurements consists in using a stretched thin conducting wire along the reference beam trajectory inside the DUT as both RF source and RF receiver. The theoretical and experimental aspects of this classical method are addressed in Refs. [96] and [94]. Such RF measurements of many accelerator components have been reported. Of particular relevance to this work are several measurement campaigns of the PS and SPS kickers presented in [74], [77], [82], [97] and [98]. Specific dedicated RF measurements to assess the dipolar and quadrupolar contributions of ferrite blocks and full SPS kicker magnets are in preparation and are not discussed here. We however focus this discussion on dedicated measurements performed to assess the transverse dipolar impedance of LHC components in the low frequency range (1 kHz to 1 MHz), a critical range for the stability of the beam in the LHC. Two families of elements are studied in the following paragraphs: the LHC collimators and the LHC beam vacuum interconnects, also known as Plug-In Modules (PIMs).

5.4.1 Measurements of the Impedance of an LHC Collimator

In 2004, L. Evans, LHC project leader, stressed in Ref. [99] that the LHC graphite collimators were major contributors to the transverse machine impedance and will be a limitation to the total beam current that can be accumulated in the LHC. That same year, the LHC Collimation Review Committee “would urge extensive beam and wire impedance measurements of the prototype (uncoated) collimators as planned” in order to assess the validity of the “modified theories (that) predict significantly lower impedance from the carbon collimators than does the normal resistive wall theory”. This *normal resistive wall theory*, also referred to as *classical thick resistive wall impedance* in this paper, was derived in the 1960s [100]. As mentioned in Chapter 5.1.7 for the longitudinal plane, this expression is only valid in a limited frequency range, and in particular when the skin depth in the conductor is larger than conductor’s thickness and also larger than the beam aperture [101]. In the case of the collimators, the latter condition is not fulfilled. Several theories with fewer approximations have been developed to extend the classical thick wall formula to the low frequency regime (see references in introductory paragraph of Chapter 5.1). However, as stressed by the LHC Collimation Review Committee, these formulae needed validation with simulations and measurements before they could be trusted to make strategic decisions for LHC operation. The low frequency part of the impedance spectrum is not easily accessible with beam measurements before LHC starts up as this low frequency regime would only be revealed in a machine that would be the size of LHC. This is why the management strongly pushed to

- get as much information as possible from beam based measurements with the prototype collimator installed in the SPS (see Refs [102] and [103])
- launch a campaign of EM simulations and RF measurements of an LHC collimator.

This section reports selected aspects of the successful teamwork with F. Caspers, E. Métral and F. Roncarolo that lead to the benchmark of the RF measurements with the Zotter/Métral theory. Details of the EM simulations can be found in Ref. [104], while the RF measurements are reported in [105]. All these theoretical studies, simulations and RF measurements were gathered and published in [62].

Measurement Technique

The measured signal obtained with the classical single wire techniques is expected to be very small at low frequencies and it was decided to use the loop measurement method described by Nassibian and Sacherer in [106]. From Eq. (3.81), we can write the vertical dipolar impedance Z_y^{dip} of a device of length L as

$$Z_y^{dip} = \frac{jL}{2\bar{y}I}\left(E_y + \beta c B_x\right), \tag{5.115}$$

where $2\bar{y}I$ is the dipole moment of the beam and the beam is assumed ultrarelativistic. At this point, an important approximation is made: the electric field contribution E_y to the transverse impedance Z_y^{dip} is neglected compared to the magnetic field B_x. In Ref. [62], this approximation is shown to be only valid for the real part of the impedance at low frequencies. Besides, the increase of the electrical impedance ΔZ_{loop} of a loop of width $2\bar{y}$ and length L_{loop} can be obtained using the Faraday law of induction, which is the integral form of Eq. (5.15d) (called the Maxwell-Faraday equation). This equation links the magnetic flux Φ_B through the surface defined by a loop to the line integral of the electric field along the loop circumference (i.e. the voltage $U = \Delta Z_{loop} I_{loop}$ with I_{loop} the electrical current running through the loop):

$$\oint \vec{E}\cdot\vec{dl} = -\frac{\partial \Phi_B}{\partial t} \quad \text{which leads to} \quad \Delta Z_{loop} I_{loop} = -2j\omega B_x \bar{y} L_{loop}, \tag{5.116}$$

for a loop orthogonal to the x direction, and assuming the magnetic field B_x is constant over the surface of the loop (i.e. neglecting edge effects). We now assume the EM fields created by a current $I_{loop} = I$ in the loop of width $d = 2\bar{y}$ are simulating the EM fields created by a beam of dipole moment $I \cdot d$. We can then identify the horizontal magnetic field B_x in Eq. (5.115) and Eq. (5.116) to relate the loop electrical impedance increase ΔZ_{loop} to the transverse dipolar beam impedance Z_y^{dip}

$$Z_y^{dip} = \frac{c\Delta Z_{loop}}{\omega d^2}, \tag{5.117}$$

where we chose $L_{coil} = L$. Due to the presence of angular frequency ω in the denominator of Eq. (5.117), this method can not be very sensitive at low frequencies. However, the loop can be replaced by a coil made of several turns N, as suggested in [107]. In this case, the magnetic field picked up by the coil is magnified by a factor N^2 if the coil is strongly coupled and we can write

$$Z_y^{dip} = \frac{c\Delta Z_{coil}}{\omega N^2 d^2}. \tag{5.118}$$

In order to measure the loop electrical impedance increase, we need to perform a reference measurement.

$$\Delta Z_y^{dip} = Z_y^{dip\ (DUT)} - Z_y^{dip\ (\mathrm{ref})} = \frac{c\left(Z_{coil}^{DUT} - Z_{coil}^{\mathrm{ref}}\right)}{\omega N^2 d^2}. \tag{5.119}$$

This formula can now be used to evaluate transverse impedances with a relevant measurement setup able to measure the electrical impedance of a coil.

Building the Coils

To perform this measurement, we needed to build probe coils and measure their electrical impedance at low frequency. A picture of a the detail of a typical homemade coil is shown in Fig. 5.50.

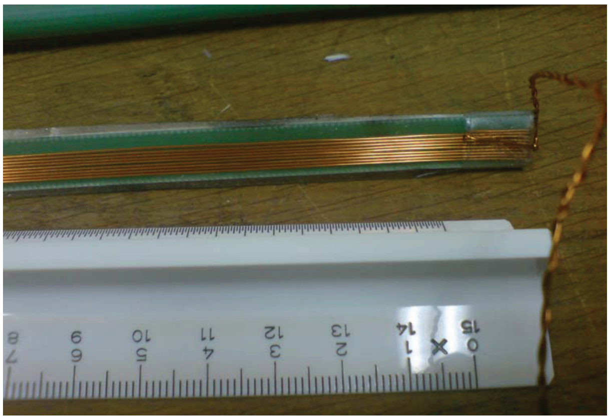

Figure 5.50: Picture of one end of a 30 cm long coil with 9 turns made on a 2 mm wide fiberglass support used in the impedance measurements of 15 cm long graphite plates.

The difference between signals from the DUT and the reference were very small (variation of fractions of mΩ on top of constant coil electrical impedance of several Ω as can be seen for instance in Fig. 5.52). As a consequence, measurement parameters have to be optimized, and in particular the probe coil. Here is a list of the main constraints:

- the coil support needs to be made of isolating material to minimize perturbation to the magnetic field. To this end, stiff fiber glass vetronite provided by the RF workshop was used as coil support.
- the total transverse geometrical size of the coil had to be small enough to be inserted into the DUT aperture (a few mm). Reducing the width d of the coil leads to a decrease of the signal with d^2 from Eq. (5.119). Also on a purely mechanical point of view, thin coils are more subject to unwanted sagging during the measurement and unwanted bending during the coil making process. This becomes a major concern for the coils used for the collimator assembly in particular (2 m long coil).
- the diameter of the insulated conducting wire had to be small enough to reduce the total size of the probe coil, but large enough so that the coil electrical impedance without field remains low.
- increasing the number of turns N increased the signal with N^2 from Eq. (5.119), but it also decreased the frequency of the first coil resonance (observed for instance at 1 MHz in Fig. 5.53), thereby reducing the frequency range over which the electrical impedance can be accurately measured.
- the minimum coil length L_{coil} has to be larger than the DUT length to avoid edge effects at the coil's ends. As the reference and the DUT share the same geometry, the electric impedance contribution coming from the parts outside of the DUT

should cancel out when subtracting the reference. Longer coils also facilitate the coil placement and alignment inside the DUT. On the other hand, each portion of the coil outside the DUT is affected by external fields, potentially variable between DUT and reference measurements.

As a consequence, a trade off has to be found to accommodate all these constraints. This is why many coil prototypes were built before satisfactory coil parameters could be found. Besides, it turned out that it was more efficient to move the coils than move the DUT. This is an obvious statement for the 50 kg copper jaws and the full LHC collimator assembly. Since the coil had to manipulated between DUT and reference measurement, the reproducibility of the measurements were then affected if the wires were not fixed to the fiberglass support with a layer of adhesive tape. Length aside, typical parameters chosen for these measurements were 0.5 mm diameter conducting wire surrounded by thin insulation and wound on a 2 to 3 mm wide fiberglass support to a total of 5 to 15 turns.

Measurement Setup and Results for Small Plates

Following the method presented in Ref. [107], a low frequency VNA (*Agilent* HP 8751) was first used to measure the coil electrical impedance. As can be seen in Ref. [62], it turned out that an LCRmeter (*Agilent* E4980A) was less sensitive to noise at low frequency. The VNA presents the advantage that the frequency of interest is automatically scanned while the LCRmeter has no built-in frequency scan capabilities. The LCRmeter was then set to be controlled remotely from any computer on the CERN network through a GPIB/LAN adapter that enables to scan the frequencies automatically, read out the impedance measurements and store the results. The bench measurements were first performed on small graphite plates (15 cm x 10 cm x 1 cm) with copper plates as reference (see Fig. 5.51). An example of postprocessing from the raw data of the real part of the coil electrical impedance to the real part of the beam impedance of graphite with copper as reference is shown in Fig. 5.52. The raw data signal difference between copper and graphite becomes very small and subject to noise at low frequency. We also observe that the impedance of the coil is lower with graphite than with copper at frequencies lower than 40 kHz. This leads to a negative graphite beam impedance with copper as reference. The coil used for these measurements was built with N=9 turns and a width d=2.5 mm. No coil resonance is observed ti lie within the frequency range scanned by the VNA (100 Hz to 2 MHz). The Zotter/Métral field matching formalism described in section 5.2.1 was applied to the case of the small graphite and copper plates, modeled as flat chambers of length 15 cm and thickness 1 cm (or 2 cm) surrounded by vacuum. The DC resistivity of the graphite used for the graphite plates was measured using the Four-point probe method [108] to $\rho_{DC} = 1.7\ 10^{-8}\ \Omega.m$ and an electron relaxation time of $\tau_e = 2.7\ 10^{-14}$ s, with relative permittivity and permeability equal to unity. The copper parameters are assumed to be $\rho_{DC} = 13\ \mu\Omega.m$. As in the procedure described for the SPS kickers and the SPS beam pipe, the first step was to obtain the wall impedance for the cylindrical case, and then use the Yokoya factors to obtain the dipolar wall impedance of LHC collimators. A summary of the benchmarks between the beam impedance results and these theoretical predictions can be observed in Fig. 5.53). In these results, we see that the real part of the impedance variation $\Delta Z_y^{dip} = Z_y^{dip,graphite} - Z_y^{dip,copper}$ follows the theory in a frequency range between 4 kHz and 200 kHz. Contrary to the results in Fig. 5.52,

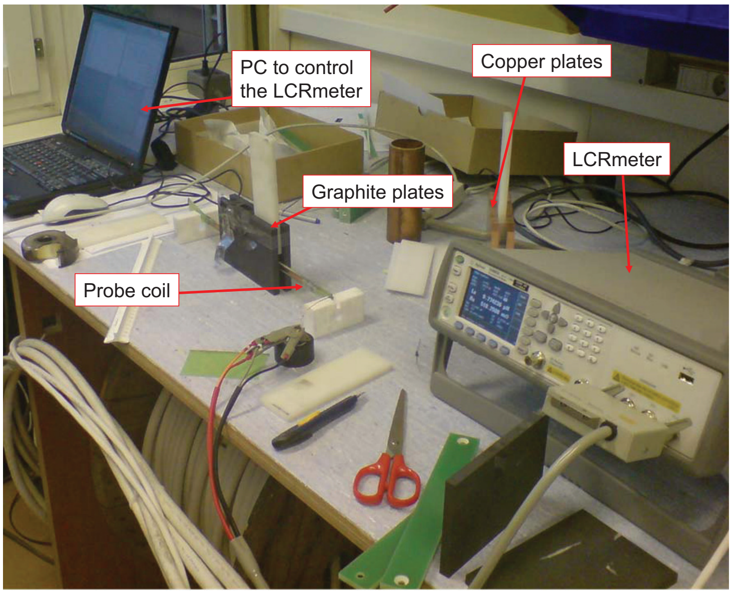

Figure 5.51: Measurement setup for low frequency impedance measurements. A home-made probe coil is inserted inside the 1 cm gap between 2 graphite plates, and its impedance is measured with an LCRmeter remotely controlled by a PC on the CERN network. The copper plates used as reference are also visible. The Kelvin clips connected to the input of the LCRmeter are plugged to the end of each coil.

the coil used had 14 turns instead of 9 turns. A direct consequence of this is that the coil resonance is observed around 1MHz and affect significantly the measurements from 200 kHz on. The low frequency range is also affected by noise. Since the setup was next to a window, we realized that closing and opening the window lead to abrupt significant changes of the signal at low frequency. Unfortunately, the temperature varies significantly during the day (see Fig. 5.54) in the measurement room, and this is why we decided to move the measurement setup to a room with controlled temperature and to be as quick as possible when measuring the impedance of the graphite plates and the copper reference. This decision enabled to largely reduce low frequency noise, as can be seen on Fig. 5.55. These results show the successful benchmark between Zotter/Métral theory of transverse impedance and RF measurements down to 3 kHz for two different gaps (10 mm and 14 mm).

Measurement Setup and Results for Standalone Jaws

Standalone graphite jaws could be borrowed for measurements from the Collimation Project team. The measurement setup is shown in Fig. 5.56. The alignment of the coil was carefully checked from above, using insulator spacers when necessary, but the coils were so long that inevitable bending could be observed.

As for the small plates, the Zotter/Métral field matching formalism was applied to the case of the LHC graphite and copper jaws modeled as flat chambers of length 1.2 m and thickness 2.5 cm surrounded by vacuum. The same electromagnetic properties of the materials as for the small plates were used. The measurement results are compared with theoretical predictions in Fig. 5.57. The better agreement and reproducibility of the

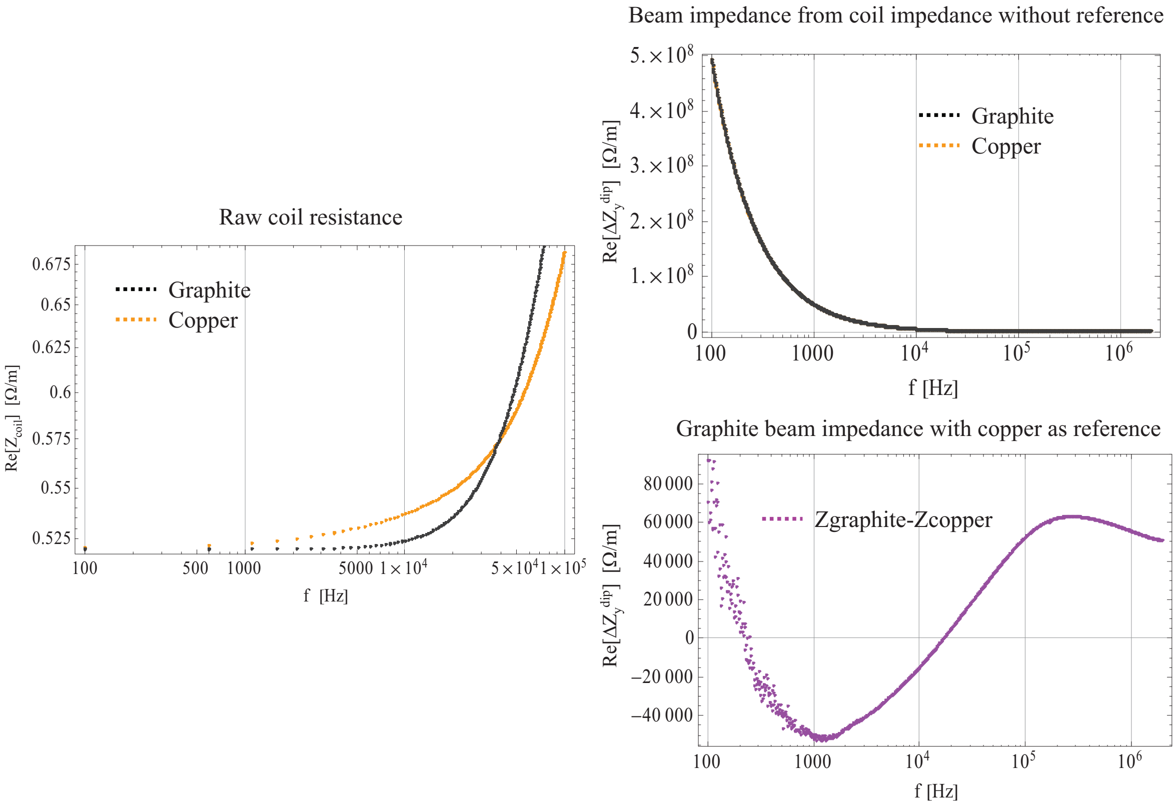

Figure 5.52: Example of the postprocessing steps from the raw data of coil electrical resistance measured with the LCRmeter (left) for the graphite plates (black) and copper plates (orange). The real part of the dipolar beam impedance without reference (top right) can be obtained from Eq. (5.118) for the graphite plates (black) and the copper plates (orange, here superimposed with the black). The graphite plates beam impedance with copper as reference (bottom right) is obtained by the subtraction of the graphite and copper beam impedances in Eq. (5.119) (violet).

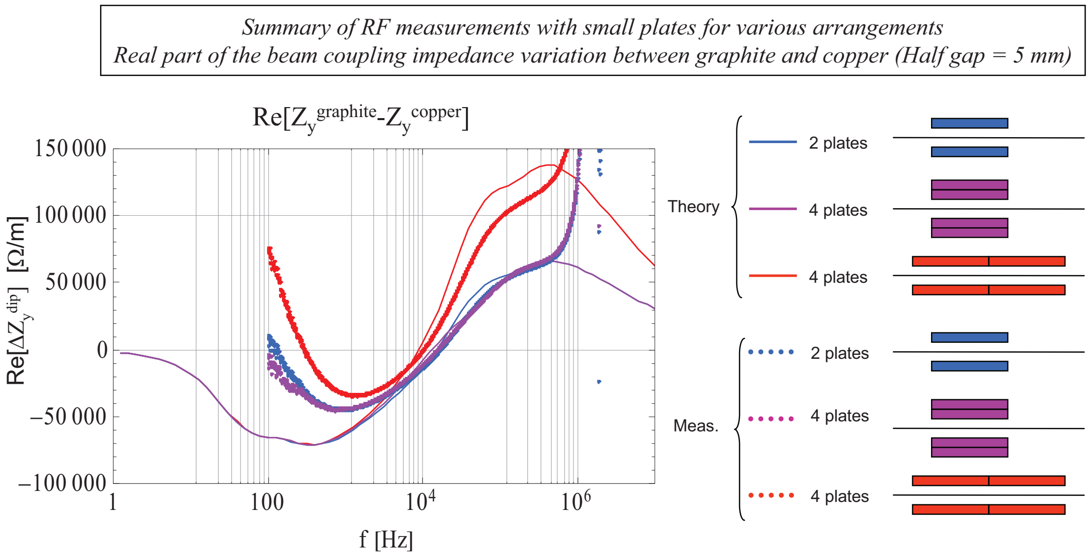

Figure 5.53: Summary of the beam impedance measurement results (thick dots) and theoretical predictions (thin lines) obtained for several arrangements of the small graphite and copper plates: 2 plates (blue), 4 plates juxtaposed in thickness (violet), or in length (red). Only the real part of the impedance is showed.

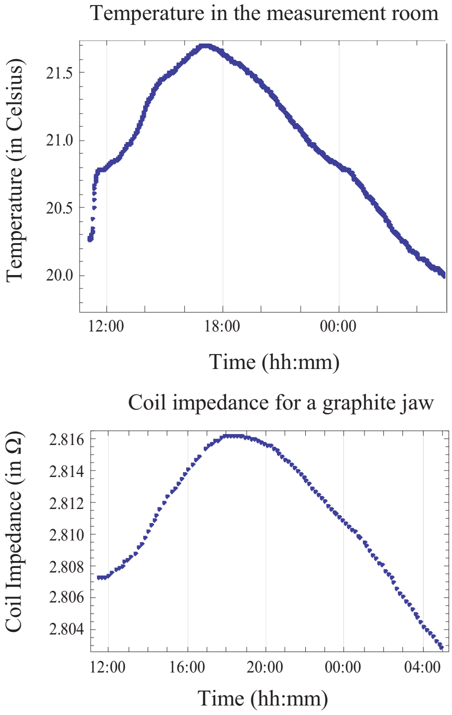

Figure 5.54: Simultaneous acquisition of the temperature in the room (top) and the coil impedance in copper jaws (bottom). It is important to note we were not in the room during these measurements, and that the temperature increased by a few degrees if we were working in there. Since the difference between graphite and copper jaws is around 0.01 Ω, an increase of a fractions of degrees generates fluctuations that are of the order the signal amplitude.

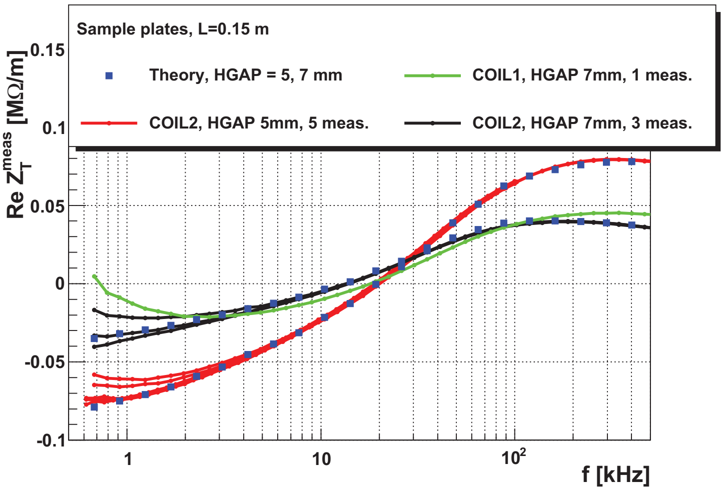

Figure 5.55: Comparison between RF measurements (thin lines) and theoretical predictions (blue dots) of the transverse impedance at half gaps HGAP=5 mm (red) and 7 mm (green and black). Several reproducibility measurements without tampering with the setup show that the noise affects frequencies lower than 3 kHz. The green line at half gap 7mm was measured with a different coil. *(courtesy of F. Roncarolo et al. [62]).*

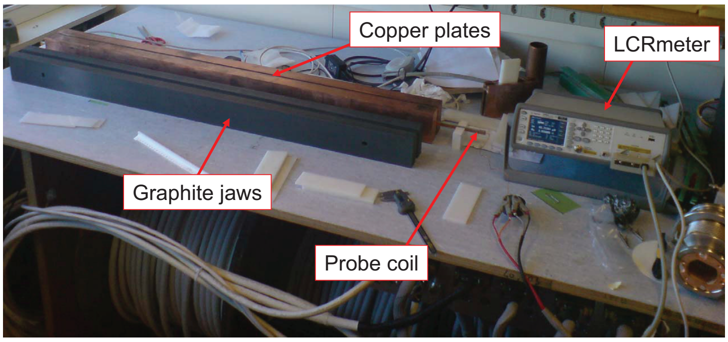

Figure 5.56: Measurement setup for low frequency impedance measurements of graphite and copper jaws. A 1.4 m long homemade probe coil is inserted inside a 1 cm gap between 2 copper jaws, and its impedance is measured with an LCRmeter remotely controlled by a PC on the CERN network. The graphite jaws are also visible.

measurements at low frequencies for the standalone jaws compared to the small plates can be explained by the larger length of the jaws, which leads to a larger picked up impedance signal, and a better signal to noise ratio.

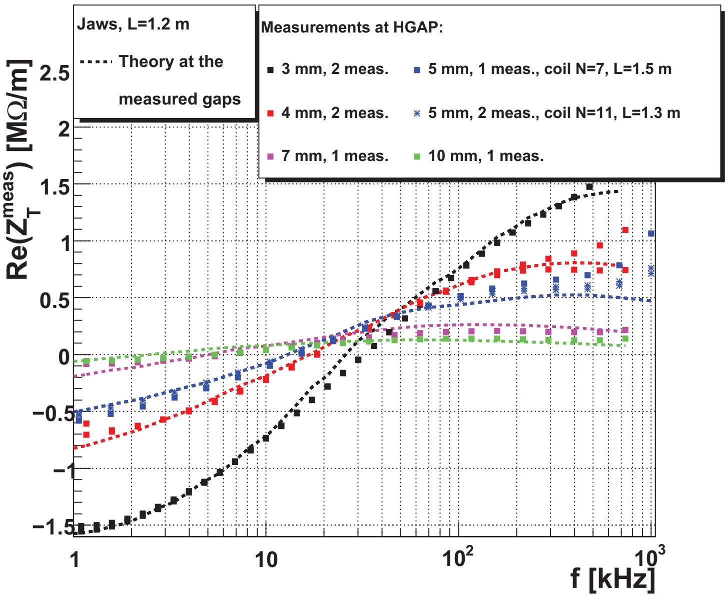

Figure 5.57: Comparison between RF measurements (dots) and theoretical predictions (dashed lines) of the transverse impedance at half gaps HGAP=3 mm (black), 4 mm (red), 5 mm (blue), 7 mm (pink) and 10 mm (green). The number of reproducibility measurements superimposed is indicated. Two separate coils with different length and number of turns were used for HGAP= 5 mm. *(courtesy of F. Roncarolo et al. [62]).*

Now that the benchmarks with theory have been performed for naked material blocks (small plates or standalone jaws), it is interesting to measure the impedance of a full collimator assembly, to check (1) if also there the decrease of the transverse dipolar beam impedance with frequency expected by the Zotter/Métral and Burov/Lebedev [52] theories is observed and (2) assess the effect of the elements surrounding the jaws on the impedance.

Measurement Setup and Results for Collimator Assembly

A TCS phase 1 collimator was made available for the RF measurement and the measurement setup can be seen in Fig. 5.58 . The procedure for inserting and aligning the coil from above could not be applied with this closed assembly. Insulating centering pieces were improvised to center as precisely as possible the 1.5 m coil in the collimator assembly, and to try to prevent a mechanical bending of the coil. A close-up of the coil inserted in the collimator can be seen in Fig. 5.59.

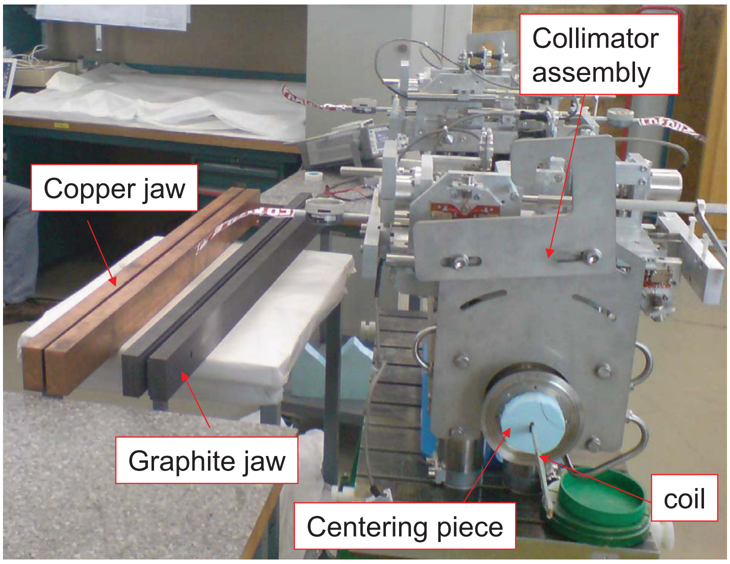

Figure 5.58: Measurement setup for low frequency impedance measurements of graphite jaws, copper jaws and CFC graphite collimator assembly. A 2 m long homemade probe coil with N=7 turns and a support of 3 mm fiberglass is inserted inside the collimator gap, and its impedance is measured with an LCRmeter remotely controlled by a PC on the CERN network. The graphite jaws and copper jaws are also visible.

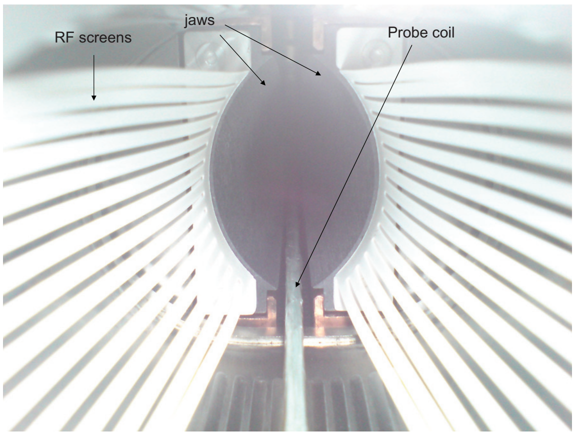

Figure 5.59: Close-up on the coil inserted into the collimator gap.

As for the small plates and the jaws, the Zotter/Métral field matching formalism was applied to the case of the LHC graphite collimator modeled as flat chambers of length 1.2 m and thickness 2.5 cm surrounded by vacuum. The collimator jaws in the assembly are not in graphite but in CFC composite (Carbon Fiber reinforced Carbon) of decreased resistivity ($\rho_{DC} = 5\ \mu\Omega$.m instead of 13 $\mu\Omega$.m for classical graphite.). The other electromagnetic properties of the materials were kept the same as for the small plates and the jaws. The RF measurement results are compared with theoretical predictions for the real part of the transverse impedance of the collimator assembly in Fig. 5.60. As already discussed above, theory and measurements are in very good agreement for the standalone jaws. The agreement is poorer in the case of the collimator assembly, especially for frequencies above 10 kHz. Consequently, comparing the measured traces of the standalone jaws and the collimator assembly, their difference can only be partially attributed to the difference in material resistivity (i.e. the difference between the red and black lines). The remaining difference could come from many sources of discrepancy between the model for the theoretical calculations and the RF measurements (e.g. the impact of the elements surrounding the jaws, the frequency dependent EM properties of the CFC, the coarse alignment and sagging of the coil in the collimator). The precision of these measurements could be increased with a stiffer coil and with dedicated holding end-plates.

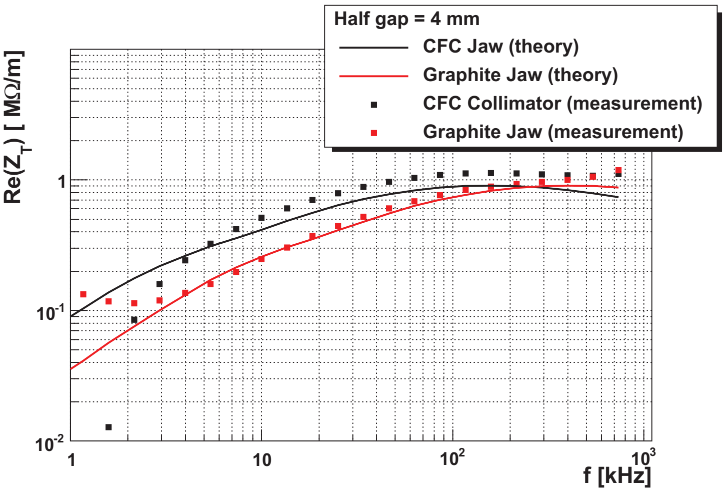

Figure 5.60: Comparison between RF measurements (dots) and theoretical predictions (lines) of the transverse impedance of graphite jaws (red) and CFC collimator assembly (black) at half gaps HGAP=4 mm. The copper jaw measurements were subtracted and from the DUT measurements, and the theory for the copper jaw was added to obtain an estimate of the impedance of the graphite collimators. *(courtesy of F. Roncarolo et al. [62]).*

As a conclusion, the measurement campaign aiming at benchmarking novel analytical transverse impedance theories in a low frequency regime was successful as the measurement results agree within 1% with theory down to f=3 kHz. This agreement is also confirmed by low frequency *Ansoft Maxwell* numerical simulations [104].

Implications for the LHC Impedance

This measurement campaign confirmed the recent theoretical calculations obtained by Burov/Lebedev and Zotter/Métral that predict a decreasing transverse impedance when the frequency decreases. Accounting for this beneficial effect, the LHC collimators still dominate the LHC impedance, and an upgrade of the collimation system aimed at reducing its transverse impedance is being studied [109]. Ideas to reduce the transverse impedance of collimators includes in particular tuning the properties of the material of the collimator jaws to find an optimum trade-off between beam impedance, mechanic stability and cleaning efficiency.

5.4.2 Measurements of the Impedance of the LHC Beam Vacuum Interconnects (PIMs)

The LHC beam vacuum interconnects are flexible bellow plug-in modules located between LHC cold elements. These PIMs are designed to ensure continuity of the vacuum chamber, both at room temperature and at operational cryogenic temperature [110]. Much effort has been made to reduce the beam impedance of these bellows - there are around 1700 PIMs per ring -, and RF contact fingers were designed to shield the distorted geometry of the bellows from the beam, while still enabling longitudinal flexibility of the whole module [111]. These contact fingers should then significantly reduce the longitudinal impedance at high frequency. However, the resulting contact resistance between these fingers and the beam pipe was a concern, as it could lead to an increase of the transverse impedance at low frequency, and therefore to a drop in the threshold for coupled bunch instability. The same coil probe measurement method as in the previous paragraph was applied to assess the transverse beam impedance of a PIM in various configurations at low frequency. The results are given in Ref. [112], and we highlight here the main differences with the collimator setup.

Measurement Setup

In contrast to the aperture of the collimators, the transverse aperture of a PIM is large (full gap 4 cm), and thick low resistance copper wires of diameter 1 mm can be used in order to maximize the signal to noise ratio. Coils were wound around fiberglass rods of rectangular section. The number of turns N and thickness of the coil d were tuned to obtain a satisfying trade-off between the amplification of the measured signal (i.e. high N, high d), and a frequency of the lowest coil resonance outside of the frequency range of interest (i.e. low N, low d). The coil was inserted into the PIM and centered using polyethylene and fiberglass blocks of known thickness.

A copper round tube of similar length and diameter as the PIM and thickness 1 mm was chosen as reference. Again, the impedance of copper cannot be considered negligible within a great part of the frequency range of interest [100 Hz, 10 kHz]. This is why subtracting the impedance of the reference from the impedance of the PIM can lead to negative values at low frequencies.

Measurement Results

The RF measurements were aimed at precisely observing the impact on beam impedance of the nominal change of configuration of the PIM between warm and cold temperatures, as well as different types of non-conforming contacts. The first set of measurements was performed at cold nominal length (elongated to 19.9 cm at cryogenic temperature) and

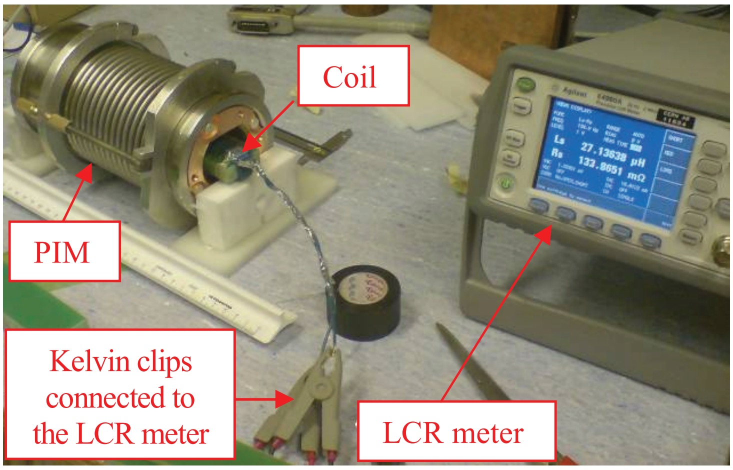

Figure 5.61: Measurement setup for the low frequency measurement of a PIM. Note the large size of the coil and wires compared to the coil used for the collimator like structures.

warm nominal length (closed to 16.5 cm at room temperature) on an LHC SSS/MB-type PIM see Fig. 5.61. It is observed that the general shape of the transverse beam impedance

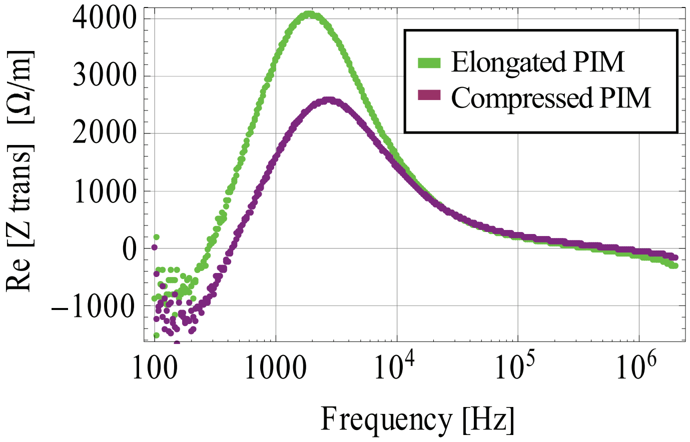

Figure 5.62: Comparison of the real part of the transverse beam impedance of a PIM at nominal length for cryogenic temperature (19.9 cm in green), and the same PIM at nominal length for room temperature (16.5 cm in purple). Measurement with the reference copper tube is subtracted.

of a PIM is conserved when it is elongated. However, we can see that elongating the PIM by 20% leads to a 40% higher impedance contribution, with a peak at about the same frequency (≈ 2 kHz). In fact, from contracted to elongated position, a larger length of RF fingers are exposed to the coil and these RF fingers (with the bellow behind them) could be responsible for this significant contribution to the global PIM transverse beam impedance in the operating LHC conditions. The second set of measurements was performed at cold nominal length with either bad or no electrical contact between some or all of the RF fingers and the vacuum chamber. The bad electrical contact were obtained inserting a thin (≈ 100 μm) copper sheet between the CuBe fingers and the coated vacuum chamber to reproduce an erosion of the thin gold/rhodium coating layer (see Fig. 5.63(a)). Isolation of the RF fingers from the vacuum chamber was obtained by inserting several 0.5-mm-thick-fiberglass plates. This configuration simulates bent fingers that lost contact with the vacuum chamber (see Fig. 5.63(b)). The measurements results using these non conforming configurations are presented in Fig. 5.64. It is observed that the general shape of the real part of the impedance is conserved. Note that the difference between the 3 green curves in Fig. 5.62 and Fig. 5.64 can be explained by slightly different measurement conditions (temperature). In the case of copper contacts, the peak frequency is shifted to higher frequencies. As lower conductivity materials exhibit higher beam impedance peak frequency (see for instance the comparison between copper and graphite in Fig. 5.13), this observation is consistent with a global lower conductivity of the PIM due to this bad contact. If only 8 fingers out of 30 fingers are isolated, the global conductivity of the PIM is not affected too much, and the beam impedance peak is again slightly shifted to higher frequencies. When all fingers are isolated with fiberglass, the impedance peak is now clearly shifted by two orders of magnitude in frequency and smeared on a much wider range of frequencies. The impedance is then significant on a large range of frequencies, which can be detrimental to the beam transverse stability.

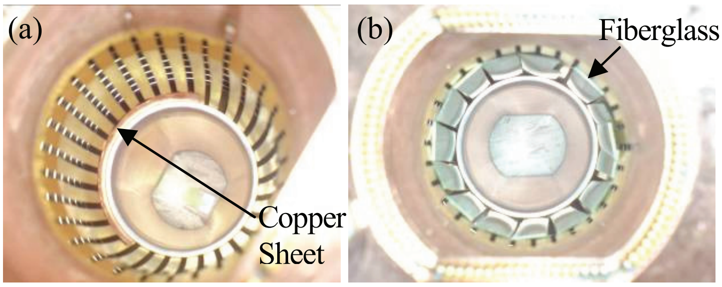

Figure 5.63: Pictures of the inside of a PIM with (a) a thin copper sheet inserted between the RF fingers and the vacuum chamber (copper contacts), (b) all RF contacts isolated from the vacuum chamber with thin plates of fiberglass.

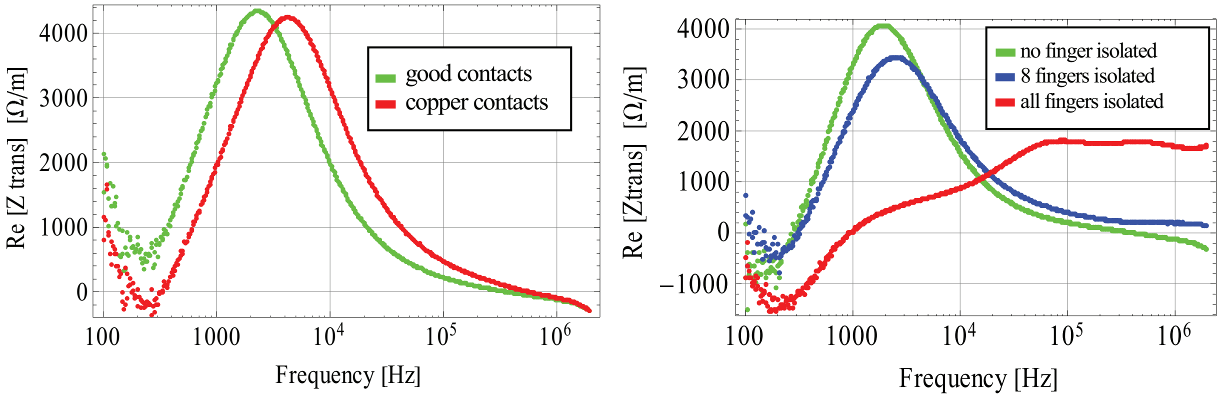

Figure 5.64: Comparison of the real part of the transverse beam impedance of a PIM with conform good contacts (left and right graphs, in green), and the same PIM with a thin sheet of copper between half of the RF fingers and the vacuum chamber (left, in red), and the same PIM with 8 fingers isolated out of 30 (right graph, in blue), and all fingers isolated (right graph, in red). Measurement with the reference copper tube is subtracted.

Implications for the LHC Impedance

In the case of a nominal PIM at operating cryogenic temperature the peak of the transverse beam impedance is observed to be ≈ 4 kΩ/m at ≈ 2 kHz. This peak value is consistent with a crude estimate deduced from Ref. [111], in which Eq. (1) used with the operating value of the contact resistance of 1 finger (3 mΩ in Fig. 1 in Ref. [111]) - i.e. 0.1 mΩ for 30 contacts in parallel - yields a transverse beam impedance of 3.4 kΩ/m for one PIM (i.e. 5.8 MΩ/m for all 1700 PIMs). In addition to being consistent with crude estimates, this measurement displays the frequency spectrum of the beam impedance, which is observed to become negligible for frequencies higher than 1MHz. It is interesting to notice that, for the lowest betatron line frequency (8 kHz), the transverse beam impedance is lower when all contacts are removed. In addition, the peak value is divided by 2 at 2 kΩ/m (3.4 MΩ/m for all 1700 PIMs). However, as already mentioned, the peak is broader, and a larger transverse beam impedance over 1 MHz may lead to more detrimental to beam stability than a larger transverse beam impedance at 8 kHz. Finally, the transverse beam impedance of the rest of the machine is estimated to be 300 MΩ/m at 2 kHz, and constant at 100 MΩ/m between 20kHz and 1 MHz [103]. Therefore, in the measured frequency range, the transverse beam impedance of the PIMs accounts for less than 4% of the total LHC beam impedance, even if all contacts are removed. As a consequence, if a solution is found to reduce the transverse beam impedance of the LHC collimators, which largely dominate over all the rest of the machine around 1 MHz [113], non-conforming PIMs could then become the major contributor to the LHC impedance around 1 MHz.

Methods to estimate the beam impedance of a given accelerator device have been described in this chapter. Depending on the complexity of the structure, the availability of the physical device for measurement and the frequency range of interest, theoretical calculations, electromagnetic simulations and/or bench measurements will be the method(s) of choice to obtain the beam impedance. Effects of the transverse beam impedance on the single-bunch motion are studied in the next chapter.

Chapter 6

Impact of impedance on Beam Dynamics: case of the CERN SPS

The effect of the beam coupling impedance on beam dynamics can be studied with analytical formalisms, macroparticle simulations and dedicated measurements with beam. We focus here on the coherent tune shifts and instabilities affecting single bunches in the SPS at injection.

6.1 Analytical Calculations of Beam Instabilities

This section follows the theory derived by Y. H. Chin to compute the coherent betatron tune shifts and predict coherent instabilities in his code MOSES (MOde-coupling Single bunch instability in an Electron Storage ring) [114]. Fundamental insight in this mode coupling formalism was also found in contributions by G. Besnier et al [115], A. W. Chao [116, 33], Y.H. Chin [117, 118], J.L. Laclare [119], E. Métral and G. Rumolo [8], F. Ruggiero [120], and F. Sacherer [121].

6.1.1 Recalling the Mode Coupling Formalism

Vlasov Equation

The motion of protons in an accelerator follows the Liouville theorem (a volume of a phase space element expressed in canonical variables is conserved along its motion). The evolution of a distribution of protons Ψ in an accelerator is therefore governed by the Vlasov equation [122]:

$$\frac{d\Psi}{dt} = 0. \tag{6.1}$$

For a distribution Ψ that depends on transverse coordinates u, $\dot{u}$ and longitudinal coordinates θ, $\dot{\theta}$, the Vlasov equation becomes (we neglect coupling between transverse planes)

$$\frac{\partial\Psi}{\partial\tau} + \dot{u}\frac{\partial\Psi}{\partial u} + \ddot{u}\frac{\partial\Psi}{\partial\dot{u}} + \dot{\theta}\frac{\partial\Psi}{\partial\theta} + \ddot{\theta}\frac{\partial\Psi}{\partial\dot{\theta}} = 0, \tag{6.2}$$

where we define the horizontal (resp. vertical) displacements normalized to the beta function

$$u = \frac{(x,y)}{\sqrt{\beta_{(x,y)}(s)}},$$

and the longitudinal angular coordinate θ with respect to the synchronous particle. Here the dot means that the derivative is taken with respect to the quasi time

$$\tau = \frac{1}{\omega_\beta} \int \frac{ds}{\beta_{(x,y)}(s)},$$

where the angular betatron frequency is written[1]

$$\omega_\beta = Q_{(x,y)}\omega_0 = \frac{\omega_0}{2\pi} \int_s^{s+L} \frac{ds}{\beta_{(x,y)}(s)},$$

using Eq. (3.19) and ω_0 as the revolution angular frequency. We now need to write the single particle motion in these coordinates. We will consider from now on the vertical plane y only to simplify the expressions, but the same equations can be applied to the horizontal plane.

Single Particle Motion

From Eq. (3.17b), Hill's single particle equation of motion in the vertical plane in the presence of a focusing term $K(s)$ and a vertical perturbing force F_y is

$$y'' + K(s)y = \frac{F_y}{m_0\gamma v^2}. \tag{6.3}$$

In the following, we do not use the smooth approximation and we write the second derivative in the new variables u and τ as

$$\begin{aligned} \frac{d^2u}{d\tau^2} &= \frac{d}{ds}\left(\frac{d}{ds}\left(\frac{y}{\sqrt{\beta_y}}\right)\frac{ds}{d\tau}\right)\frac{ds}{d\tau} \\ &= \omega_\beta^2\beta_y\frac{d}{ds}\left(\frac{\alpha_y y}{\sqrt{\beta_y}} + y'\sqrt{\beta_y}\right) \\ &= \omega_\beta^2\left(y''\beta_y^{3/2} + \alpha_y' y\sqrt{\beta_y} + \alpha_y^2\frac{y}{\beta_y}\right). \end{aligned} \tag{6.4}$$

where we used $\alpha_y = -\beta_y'/2$. Substituting the expression for y'' in Eq. (6.3) into Eq. (6.4), we obtain

$$\begin{aligned} \frac{d^2u}{d\tau^2} &= \omega_\beta^2\left(\frac{F_y}{m_0\gamma v^2}\beta_y^{3/2} - K(s)\beta_y^{3/2}y + y\alpha_y'\sqrt{\beta_y} + \alpha_y^2\frac{y}{\beta_y}\right) \\ &= \frac{F_y\omega_\beta^2\beta_y^{3/2}}{m_0\gamma v^2} + \omega_\beta^2 u\left(\alpha_y'\beta_y - K(s)\beta_y^2 + \alpha_y^2\right). \end{aligned} \tag{6.5}$$

---

[1] The transverse (x,y) index is dropped in $\omega_{\beta_{(x,y)}}$ for legibility reasons.

Using the Floquet transformation in Ref. [26], we can check that the beta function $\beta_y = w^2$ is the solution of equation

$$w'' + K(s)w - \frac{1}{w^3} = 0,$$

which yields, replacing w with $\sqrt{\beta_y}$

$$\alpha_y'\beta_y + \alpha_y^2 - K(s)\beta_y^2 + 1 = 0.$$

As a consequence, substituting $K(s)$ by its expression in Eq. (6.5), we obtain

$$\frac{d^2u}{d\tau^2} + \omega_\beta^2 u = \frac{F_y \omega_\beta^2 \beta_y^{3/2}}{m_0\gamma v^2}. \tag{6.6}$$

In coordinates u and τ, the Hill's equation of motion is a harmonic oscillator. Accounting for the vertical chromaticity $\xi = \frac{\Delta Q_y/Q_y}{\Delta p/p}$, we can write the betatron angular frequency shift due to chromaticity to first order as [123]

$$\Delta\omega_\beta \approx \omega_0\Delta Q_y + Q_y\Delta\omega_0 = Q_y\left(\omega_0\xi\frac{\Delta p}{p} + \Delta\omega_0\right) = Q_y\Delta\omega_0\left(1 - \frac{\xi}{\eta}\right) = Q_y\omega_0\frac{d\theta}{d\theta_L}\left(1 - \frac{\xi}{\eta}\right),$$

where we have used the definition of the slip factor η from Eq. (3.37), as well as

$$\frac{d\theta}{d\theta_L} = \frac{\dot{\theta}}{\omega_0} = \frac{\Delta\omega_0}{\omega_0},$$

where we defined $\theta_L = s/R$, with R the radius of the machine. If we assume $\xi/\eta \gg 1$, the transverse equation of motion with chromaticity becomes

$$\frac{d^2u}{d\tau^2} + \left(\omega_\beta - \frac{\xi Q_y}{\eta}\frac{d\theta}{d\theta_L}\omega_0\right)^2 u = \frac{F_y\omega_\beta^2\beta_y^{3/2}}{m_0\gamma v^2}. \tag{6.7}$$

In the longitudinal plane, we use the small amplitude approximation for the equation of synchrotron motion in Eq. (3.50). In the notations of this chapter, $\Delta\phi = -h\theta$, and we can write

$$\frac{d^2\theta}{d\tau^2} + \tilde{\omega}_s^2\theta = 0. \tag{6.8}$$

with the angular synchrotron frequency in the quasi time coordinate τ defined as

$$\tilde{\omega}_s = \frac{\omega_s}{\omega_\beta^2\beta_y^2 v^2},$$

compared to the synchrotron frequency used in Section 3.2.2.

Transformation of Vlasov Equation in Polar Variables

Changing variables from $(u, \dot{u}, \theta, \dot{\theta})$ to polar coordinates (r_y, ϕ_y, r, ϕ) defined by

$$\begin{cases} u = r_y\cos\phi_y, \\ \dot{u} = -\left(\omega_\beta - \omega_\xi\right) r_y \sin\phi_y, \\ \theta = r\cos\phi, \\ \dot{\theta} = -\tilde{\omega}_s r\sin\phi, \end{cases}$$

with

$$\omega_\xi = \frac{\xi Q}{\eta}\frac{d\theta}{d\theta_L}\omega_0.$$

As a consequence, for the longitudinal plane, we can write

$$\begin{cases} r = \sqrt{\theta^2 + \dot{\theta}^2}, \\ \phi = -\arctan\left(\dfrac{\dot{\theta}}{\tilde{\omega}_s\theta}\right). \end{cases}$$

and the partial derivatives are

$$\begin{cases} \dfrac{\partial r}{\partial \theta} = \dfrac{\theta}{\sqrt{\theta^2 + \frac{\dot{\theta}^2}{\tilde{\omega}_s^2}}} = \cos\phi, \\ \dfrac{\partial r}{\partial \dot{\theta}} = \dfrac{\dot{\theta}}{\tilde{\omega}_s^2\sqrt{\theta^2 + \frac{\dot{\theta}^2}{\tilde{\omega}_s^2}}} = -\dfrac{\sin\phi}{\tilde{\omega}_s}, \\ \dfrac{\partial \phi}{\partial \theta} = \dfrac{\dot{\theta}}{\tilde{\omega}_s\left(\theta^2 + \frac{\dot{\theta}^2}{\tilde{\omega}_s^2}\right)} = -\dfrac{sin\phi}{r}, \\ \dfrac{\partial \phi}{\partial \dot{\theta}} = -\dfrac{\theta}{\tilde{\omega}_s\left(\theta^2 + \frac{\dot{\theta}^2}{\tilde{\omega}_s^2}\right)} = -\dfrac{\cos\phi}{r\tilde{\omega}_s}. \end{cases}$$

We can obtain similar equations for the transverse plane, and the Vlasov equation Eq. (6.2) can be rewritten in the polar coordinates

$$\frac{\partial \Psi}{\partial \tau} = -\left(\omega_\beta - \omega_\xi\right)\frac{\partial \Psi}{\partial \phi_y} + \frac{F_y\omega_\beta^2\beta_y^{3/2}}{m_0\gamma v^2}\left(\frac{\partial \Psi}{\partial r_y}\frac{\sin\phi_y}{\omega_\beta - \omega_\xi} + \frac{\partial \Psi}{\partial \phi_y}\frac{\cos\phi_y}{r_y(\omega_\beta - \omega_\xi)}\right) - \tilde{\omega}_s\frac{\partial \Psi}{\partial \phi}, \quad (6.9)$$

where we have used the chain rule to express the partial derivatives, as well as Eq. (6.7) and (6.8). Now that a compact expression of the Vlasov equation has been derived, we now change the independent variable from τ to $\theta_L = s/R$, and get

$$\frac{\omega_\beta\beta_y}{R}\frac{\partial \Psi}{\partial \theta_L} + \left(\omega_\beta - \omega_\xi\right)\frac{\partial \Psi}{\partial \phi_y} - \frac{F_y\omega_\beta^2\beta_y^{3/2}}{m_0\gamma v^2}\left(\frac{\partial \Psi}{\partial r_y}\frac{\sin\phi_y}{\omega_\beta - \omega_\xi} + \frac{\partial \Psi}{\partial \phi_y}\frac{\cos\phi_y}{r_y(\omega_\beta - \omega_\xi)}\right) + \tilde{\omega}_s\frac{\partial \Psi}{\partial \phi} = 0. \quad (6.10)$$

We consider the beta function constant around the ring except for the source term, so that we can write $\omega_\beta = \omega_0 R/\beta_y$ from the definition of the angular betatron frequency, and obtain

$$\omega_0\frac{\partial \Psi}{\partial \theta_L} + \left(\omega_\beta - \omega_\xi\right)\frac{\partial \Psi}{\partial \phi_y} - \frac{F_y\omega_\beta\omega_0 R\sqrt{\beta_y}}{m_0\gamma v^2}\left(\frac{\partial \Psi}{\partial r_y}\frac{\sin\phi_y}{\omega_\beta - \omega_\xi} + \frac{\partial \Psi}{\partial \phi_y}\frac{\cos\phi_y}{r_y(\omega_\beta - \omega_\xi)}\right) + \tilde{\omega}_s\frac{\partial \Psi}{\partial \phi} = 0. \quad (6.11)$$

As already mentioned in Section 4.2, the beta function at the location of the impedance source affects the amplitude of the perturbation to the beam, and this is why the dependence with β_y is kept in the source term of Eq. (6.11).

Defining the Perturbation

If we assume that the perturbation to the beam is small, the distribution function can be decomposed into a stationary distribution $\Psi_0(r_y, \phi_y, r, \phi)$ and a perturbed distribution $\Delta\Psi(r_y, \phi_y, r, \phi, t)$. From the Vlasov equation without source term for the stationary distribution (i.e. independent of τ), we can conclude that the stationary distribution is a function of r and r_y only. Assuming that the distribution functions can be separated into functions of longitudinal or transverse coordinates only and we write

$$\begin{aligned}\Psi(r_y, \phi_y, r, \phi) &= \Psi_0(r_y, r) + \Delta\Psi(r_y, , \phi_y, r, \phi, t)\\ &= f_0(r_y)g_0(r) + f(r_y, \phi_y)g(r, \phi)e^{-j\left(\frac{\Omega}{\omega_0}\theta_L - \frac{\xi}{\eta}\theta\right)},\end{aligned} \tag{6.12}$$

in which the density perturbation simulates a coherent beam oscillation of angular frequency Ω that already includes the head-tail phase shift due to chromaticity [123]. The goal of the rest of this section is to determine the coherent modes of oscillation and find the angular frequencies Ω.

Linearizing the Vlasov Equation

Substituting the distribution Eq. (6.12) into Vlasov equation Eq. (6.11), we obtain

$$\left(-j\Omega fg + (\omega_\beta - \omega_\xi)\frac{\partial f}{\partial \phi_y}g + \tilde{\omega}_s f\frac{\partial g}{\partial \phi}\right)\exp^{-j\left(\frac{\Omega}{\omega_0}\theta_L - \frac{\xi}{\eta}\theta\right)} - \frac{F_y\omega_\beta\omega_0 R\sqrt{\beta_y}}{m_0\gamma v^2}\frac{df_0}{dr_y}g_0\frac{\sin\phi_y}{\omega_\beta - \omega_\xi} = 0, \tag{6.13}$$

where we kept only the first order terms with respect to the perturbation. In the following, we neglect ω_ξ with respect to ω_β, but the head-tail phase shift is kept. We obtain:

$$\left(-j\Omega fg + \omega_\beta\frac{\partial f}{\partial \phi_y}g + \tilde{\omega}_s f\frac{\partial g}{\partial \phi}\right)e^{-j\left(\frac{\Omega}{\omega_0}\theta_L - \frac{\xi}{\eta}\theta\right)} - \frac{F_y\omega_0 R\sqrt{\beta_y}}{m_0\gamma v^2}\frac{df_0}{dr_y}g_0\sin\phi_y = 0. \tag{6.14}$$

Dipole Moment and Deflecting Force

We assume the distribution executes coherent dipole oscillations of amplitude $De^{-j\left(\frac{\Omega}{\omega_0}\theta_L - \frac{\xi}{\eta}\theta\right)}$, where D is the transverse dipole displacement defined by

$$D = \frac{\iint yf(r_y, \phi_y)r_y dr_y d\phi_y}{\iint f_0(r_y)r_y dr_y d\phi_y} = \sqrt{\beta_y}\frac{\iint uf(r_y, \phi_y)r_y dr_y d\phi_y}{\iint f_0(r_y)r_y dr_y d\phi_y} = \sqrt{\beta_y}D_n.$$

The dipole moment $< Iy >$ at location θ_L can then be written as the product of the amplitude of the oscillations at this location with the beam current

$$< Iy(\theta_L, \theta) >= De^{-j\left(\frac{\Omega}{\omega_0}\theta_L - \frac{\xi}{\eta}\theta\right)}\omega_0\rho(\theta),$$

where the longitudinal charge distribution per unit angle $\rho(\theta)$ can be obtained by projecting the stationary distribution $g(r, \phi)$ onto the θ axis:

$$\rho(\theta) = \int_{\dot{\theta}=-\infty}^{+\infty} g(r, \phi)d\dot{\theta}. \tag{6.15}$$

The force generated by this source charge distribution $\rho(\theta)$ felt by a test particle at a position $z = R\theta$ due to a localized impedance source can be expressed using the wake function $G(z' - z)$ and Eqs. (3.60) and (3.62)

$$\begin{aligned} F_y(\theta_L, z) &= -\frac{e}{2\pi R}\int_{z'=-\infty}^{+\infty} < Iy(\theta_L, z) > G_y^{dip}(z - z')dz' \\ &= -\frac{De\omega_0}{2\pi R} e^{-j\frac{\Omega}{\omega_0}\theta_L}\int_{z'=-\infty}^{+\infty} \rho(z') e^{j\frac{\xi}{\eta}\frac{z'}{R}} G_y^{dip}(z - z')dz', \end{aligned} \tag{6.16}$$

where we have taken into account only the vertical dipolar wake function G_y^{dip}, and neglected all other terms. Taking into account contributions for all turns k,

$$F_y(s, z) = -\frac{De\omega_0}{2\pi R}\sum_{k=-\infty}^{+\infty} e^{-j\frac{\Omega}{R\omega_0}(s-kL)}\int_{z'=-\infty}^{+\infty} \rho(z') e^{j\frac{\xi}{\eta}\frac{z'}{R}} G_y^{dip}(z - z' - kL)dz'. \tag{6.17}$$

We will now switch to frequency domain, and this is why we define the Fourier Transform $\tilde{\rho}(p)$ of the longitudinal charge distribution $\rho(\theta)$

$$\tilde{\rho}(p) = \frac{1}{2\pi}\int_{\theta=-\infty}^{+\infty} \rho(\theta) e^{-ip\theta} d\theta.$$

Using the definition of $\rho(\theta)$ in Eq. (6.15), we note that we can substitute polar longitudinal variables in the double integral with $\theta = r\cos\phi$ and $\dot{\theta} = -\tilde{\omega}_s r \sin\phi$ to obtain

$$\tilde{\rho}(p) = \frac{\tilde{\omega}_s}{2\pi}\int_{r=-\infty}^{+\infty}\int_{\phi=0}^{2\pi} e^{-ipr\cos\phi} g(r, \phi) r dr d\phi. \tag{6.18}$$

Coming back to Eq. (6.17), the Poisson summation formula can be used to switch to frequency domain. For any function $F(\omega)$ and its Fourier Transform $\tilde{F}(\omega/c)$, we have

$$\sum_{k=-\infty}^{+\infty} F(kL) = \frac{c}{L}\sum_{p=-\infty}^{+\infty} \tilde{F}(\frac{2p\pi c}{L}),$$

where $L = 2\pi R$ is the length of the machine. The vertical deflecting force Eq. (6.17) can therefore be obtained as

$$F_y = -\frac{jDe\omega_0}{2\pi R T_0} e^{-j\frac{\Omega}{\omega_0}\theta_L}\sum_{p=-\infty}^{+\infty} \tilde{\rho}\left(p + \frac{\Omega}{\omega_0} - \frac{\xi}{\eta}\right) Z_y^{dip}\left(p\omega_0 + \Omega\right) e^{j\left(p + \frac{\Omega}{\omega_0}\right)\theta}. \tag{6.19}$$

Dispersion Relation

With this expression of the vertical perturbing force, the Vlasov equation Eq. (6.14) then becomes

$$\begin{aligned} & e^{j\left(\frac{\xi}{\eta} - \frac{\Omega}{\omega_0}\right)\theta}\left(-j\Omega f g + \omega_\beta \frac{\partial f}{\partial \phi_y} g + \tilde{\omega}_s f \frac{\partial g}{\partial \phi}\right) \\ & \qquad + \frac{jD_n\omega_0\beta_y e}{T_0 m_0 \gamma v^2}\sum_{p=-\infty}^{+\infty} \tilde{\rho}\left(p + \frac{\Omega}{\omega_0} - \frac{\xi}{\eta}\right) Z_y^{dip}\left(p\omega_0 + \Omega\right) e^{jp\theta}\frac{df_0}{dr_y} g_0 \sin\phi_y = 0. \end{aligned} \tag{6.20}$$

For a rigid rotation in the betatron phase space with a small displacement D, we have the solution for $f(r_y)$

$$f(r_y, \phi_y) = f_0(r_y - De^{j\phi_y}) - f_0(r_y) = -De^{j\phi_y}\frac{df_0}{dr_y}.$$

Besides, as justified in Refs. [34] and [124], we have dropped the $\exp(-j\phi_y)$ component of $\sin\phi_y$ because it corresponds to a rotation with angular frequency $-\omega_\beta$ in the transverse phase space, which is too far to couple with the unperturbed rotation of angular frequency ω_β provided the frequency shift due to the wake force is much smaller than the betatron frequency. The linearized Vlasov equation can then be rewritten

$$-j\lambda g + \frac{\partial g}{\partial \phi} = \frac{\omega_0\beta_y e}{2T_0 m_0\gamma v^2\tilde{\omega}_s}\sum_{p=-\infty}^{+\infty}\tilde{\rho}\left(p + \frac{\Omega}{\omega_0} - \frac{\xi}{\eta}\right)Z_y^{dip}\left(p\omega_0 + \Omega\right)e^{j\left(p - \frac{\xi}{\eta} + \frac{\Omega}{\omega_0}\right)r\cos\phi}g_0, \tag{6.21}$$

where we have defined $\lambda = (\Omega - \omega_\beta)/\tilde{\omega}_s$. Since $g(r,\phi)$ is 2 π periodic in ϕ, it can be expanded into Fourier series of azimuthal mode numbers m:

$$g(r,\phi) = \sum_{m=-\infty}^{+\infty} g_m(r)e^{jm\phi}.$$

Substituting this expression of $g(r,\phi)$ into Eq. (6.21), we then multiply by $\exp(jm_0\phi)$ and integrate from $\phi = 0$ to $\phi = 2\pi$ so that all the terms in the summation over m vanish except for $m = m_0$. We then get, dropping the index of azimuthal mode m

$$\begin{aligned}&(\lambda - m)g_m(r) = \\ &\frac{j\omega_0\beta_y e}{2T_0 m_0\gamma v^2\tilde{\omega}_s}g_0\sum_{p=-\infty}^{+\infty}\tilde{\rho}\left(p + \frac{\Omega}{\omega_0} - \frac{\xi}{\eta}\right)Z_y^{dip}\left(p\omega_0 + \Omega\right)J_m\left(\left(p - \frac{\xi}{\eta} + \frac{\Omega}{\omega_0}\right)r\right)j^m,\end{aligned} \tag{6.22}$$

where we have used one of the the Bessel integrals [64] to compute the integral of the exponential factor in the left hand side

$$\int_{\phi=0}^{2\pi} e^{j(x\cos\phi - m\phi)}d\phi = 2\pi j^m J_m(x).$$

Reconstructing $g(r,\phi)$ from Eq. (6.22) by multiplying by $\exp(jm\phi)$ and summing over m we obtain:

$$\begin{aligned}g(r,\phi) = &\frac{j\omega_0\beta_y e}{2T_0 m_0\gamma v^2\tilde{\omega}_s}\sum_{m=-\infty}^{+\infty}\frac{j^m g_0}{(\lambda - m)} \\ &\sum_{p=-\infty}^{+\infty}Z_y^{dip}\left(p\omega_0 + \Omega\right)\tilde{\rho}\left(p + \frac{\Omega}{\omega_0} - \frac{\xi}{\eta}\right)J_m\left(\left(p - \frac{\xi}{\eta} + \frac{\Omega}{\omega_0}\right)r\right)e^{jm\phi},\end{aligned} \tag{6.23}$$

We now reconstruct the Fourier transform $\tilde{\rho}(q)$ defined in Eq. (6.18) from the expression of $g(r, \phi)$ in Eq. (6.22):

$$\tilde{\rho}(q) = \frac{j\omega_0\beta_y e}{2T_0 m_0 \gamma v^2} \sum_{m=0}^{+\infty} \frac{\lambda\varepsilon_{m,0}}{(\lambda^2 - m^2)}$$
$$\sum_{p=-\infty}^{+\infty} Z_y^{dip}(p\omega_0 + \Omega)\, \tilde{\rho}\left(p + \frac{\Omega}{\omega_0} - \frac{\xi}{\eta}\right) \int_{+\infty}^{r=-\infty} g_0(r) J_m\left(\left(p - \frac{\xi}{\eta} + \frac{\Omega}{\omega_0}\right) r\right) J_m(qr)\, r dr, \tag{6.24}$$

with $\varepsilon_{m,0} = 1$ if $m = 0$ and $\varepsilon_{m,0} = 2$ if $m \neq 0$.

Eigenvalue Problem for a Longitudinal Gaussian Distribution

We further assume a gaussian longitudinal distribution given by

$$g_0(r) = \frac{Ne}{2\pi\tilde{\omega}_s\sigma_\theta^2} e^{-\frac{r^2}{2\sigma_\theta^2}},$$

where N is the number of particles per bunch and σ_θ is the bunch length defined as $\sigma_\theta = \sigma_z / R$. In this case, the integral in Eq.(6.23) can be expanded in series

$$\int_{+\infty}^{r=-\infty} e^{-\frac{r^2}{2\sigma_\theta^2}} J_m(pr)\, J_m(qr)\, r dr = \sigma_\theta^2 \sum_{k=0}^{+\infty} C_{mk}(p\sigma_\theta) C_{mk}(q\sigma_\theta),$$

with

$$C_{mk}(p\sigma_\theta) = \frac{1}{\sqrt{(m+k)!k!}} e^{-\frac{1}{2}p^2\sigma_\theta^2} \left(\frac{p\sigma_\theta}{\sqrt{2}}\right)^{m+2k} \quad \text{for} \quad m \geq 0.$$

These $C_{mk}(p\sigma_\theta)$ represent the frequency spectra of the azimuthal modes $\pm m$ and radial mode k. Coming back now to Eq.(6.24), we have

$$\begin{aligned} \tilde{\rho}(q) = j\frac{N\omega_0\beta_y e^2}{4\pi T_0 m_0\gamma v^2 \tilde{\omega}_s} \sum_{p=-\infty}^{+\infty} Z_y^{dip}(p\omega_0 + \Omega)\, \tilde{\rho}\left(p + \frac{\Omega}{\omega_0} - \frac{\xi}{\eta}\right) \\ \sum_{m=0}^{+\infty} \frac{\lambda\varepsilon_{m,0}}{(\lambda^2 - m^2)} \sum_{k=0}^{+\infty} C_{mk}\left(\left(p - \frac{\xi}{\eta} + \frac{\Omega}{\omega_0}\right)\sigma_\theta\right) C_{mk}(q\sigma_\theta). \end{aligned} \tag{6.25}$$

Besides we can check that

$$C_{mk}(p\sigma_\theta) = \frac{\sqrt{m+2k}}{\sqrt{(m+k)!k!}} C_{(m+2k)0}(p\sigma_\theta),$$

and the double summation with azimuthal mode m and radial mode k in (6.25) can be replaced with a summation with a hybrid mode $h = |m| + 2k$, that contains all modes for which $|m| + 2k = h$. We define

$$\beta_h(\lambda) = \sum_{m+2k=h} \frac{\lambda\varepsilon_{m,0}}{(\lambda^2 - m^2)} \frac{h}{(m+k)!k!} \quad \text{and} \quad F_h(q\sigma_\theta) = C_{h0}(q\sigma_\theta),$$

to obtain

$$\begin{aligned}\tilde{\rho}(q) = j\frac{N\omega_0\beta_y e^2}{4\pi T_0 m_0 \gamma v^2 \tilde{\omega}_s} \sum_{p=-\infty}^{+\infty} Z_y^{dip}\left(p\omega_0+\Omega\right)\tilde{\rho}\left(p+\frac{\Omega}{\omega_0}-\frac{\xi}{\eta}\right) \\ \sum_{h=0}^{+\infty}\beta_h(\lambda)F_h\left(\left(p-\frac{\xi}{\eta}+\frac{\Omega}{\omega_0}\right)\sigma_\theta\right)F_h(q\sigma_\theta).\end{aligned} \tag{6.26}$$

We look for an eigenmode frequency spectrum given by the linearly independent functions F_h

$$\tilde{\rho}(q) = \sum_{h=0}^{+\infty}\alpha_h F_h(q\sigma_\theta).$$

Substituting this expression of $\tilde{\rho}(q)$ into Eq. (6.26), we obtain

$$\alpha_h = j\frac{N\omega_0\beta_y e^2}{4\pi T_0 m_0\gamma v^2\tilde{\omega}_s}\beta_h(\lambda)\sum_{h=0}^{+\infty}M_{hl}(\lambda)\alpha_l,$$

where

$$M_{hl}(\lambda) = \sum_{p=-\infty}^{+\infty} Z_y^{dip}\left(p\omega_0+\Omega\right)F_h\left(\left(p-\frac{\xi}{\eta}+\frac{\Omega}{\omega_0}\right)\sigma_\theta\right)F_l\left(\left(p-\frac{\xi}{\eta}+\frac{\Omega}{\omega_0}\right)\sigma_\theta\right).$$

As a consequence, solving the determinant equation

$$det\left(\delta_{hl} - j\frac{N\omega_0\beta_y e^2}{4\pi T_0 m_0\gamma v^2\tilde{\omega}_s}\beta_h(\lambda)M_{hl}(\lambda)\right) = 0,$$

where δ_{hl} is the Kronecker delta, yields λ and therefore the mode frequencies $\Omega = \lambda\omega_s + \omega_\beta$ for the chosen radial and azimuthal modes. This computation can be performed numerically if we choose a finite number of modes to compute, i.e. if the matrix $M_{hl}(\lambda)$ is truncated. This mode coupling formalism is at the root of the MOSES code. In MOSES, Y. H. Chin included the possibility of a distribution with betatron tune spread in Refs. [125] and [114]. An application of the MOSES code to the SPS transverse single-bunch instability at injection is presented in the next section.

6.1.2 *MOSES* Results for the SPS Parameters

In Ref. [126], E. Métral used MOSES v3.3 to generate the bunch mode spectrum as a function of bunch current, for a bunch interacting with a transverse impedance of a round chamber modelled as a broadband resonator model $Z_\perp(f)$ (see Ref. [35])

$$Z_\perp(f) = \frac{f_{res}}{f}\frac{R_s}{1+jQ\left(\frac{f}{f_{res}}-\frac{f_{res}}{f}\right)}, \tag{6.27}$$

where f is the frequency, R_s is the transverse resonator shunt impedance, f_{res} is the resonator frequency and Q is the resonator quality factor. The parameters for the LHC-type beam in the SPS at injection used for these calculations are listed in Tab. B.3 in the appendix. As can be seen from the parameters used by *MOSES*, the horizontal and vertical planes are here completely equivalent, and we arbitrarily choose to refer to the horizontal plane.

Tune Shift of the Bunch Coherent Modes

The relative tune shift $Re\left(Q - Q_x\right)/Q_s$ with respect to the 0-current tune Q_x is normalized to the synchrotron tune Q_s to identify each of the bunch azimuthal modes, and is plotted as a function of bunch intensity (I_b) in Fig. 6.1. The azimuthal modes of the bunch are observed to separate into several radial modes, which shift with their own pace as the bunch intensity is increased. Some azimuthal modes are observed to couple, in particular modes 0 and -1 at $I_b \approx 0.3$ mA, which also decouple if the bunch current is increased further. Modes -1 and -2, as well as modes -2 and -3 also couple between $I_b \approx 0.45$ mA and $I_b \approx 0.5$ mA.

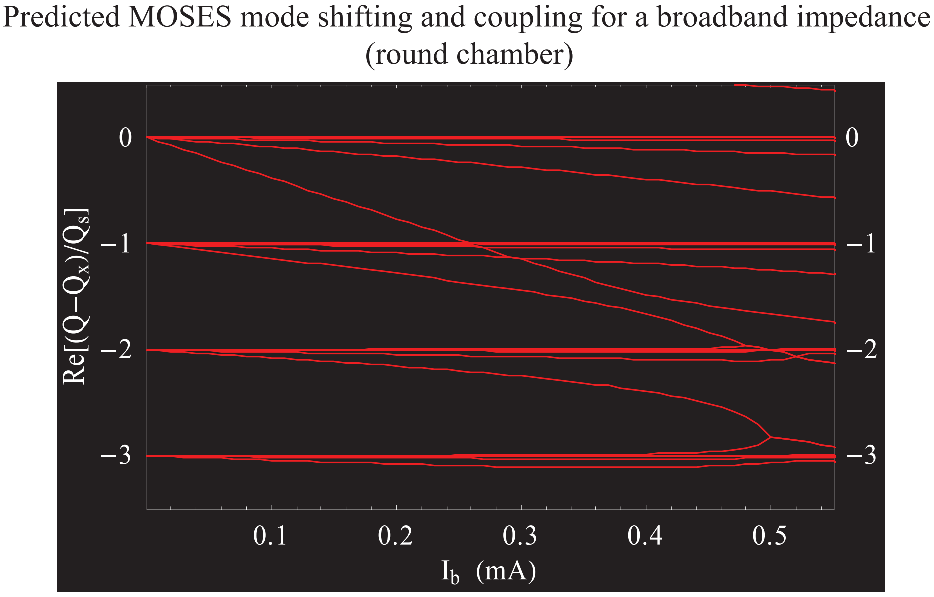

Figure 6.1: Zoom of the normalized real part of the mode spectrum of the bunch (from azimuthal mode 0 to azimuthal mode -3) as a function of the bunch intensity calculated with *MOSES* for the LHC bunch in the SPS at injection (see parameters in Tab. B.3). Courtesy of E. Métral.

Instability Rise Time

The rise time [2] τ and growth rate $1/\tau$ of the instability are derived from the imaginary part of the normalized mode spectrum, which is displayed in Fig. 6.2. The instability growth rate is observed to be particularly significant for large beam intensities ($I_b > 0.47$ mA). Taking into account the observations made for the real part of the mode spectrum, it can be concluded that this instability growth rate is due to coupling between azimuthal modes -1 and -2 from $I_b \approx 0.47$ mA, followed by an even stronger coupling between azimuthal modes -2 and -3 from $I_b \approx 0.5$ mA. The coupling observed between modes 0 and -1 at $I_b \approx 0.3$ mA on Fig. 6.1 leads to a smaller growth rate on Fig. 6.2. This growth rate vanishes as soon as the two modes decouple. From these observations, it can be concluded

---

[2] Through the remaining sections of this manuscript, τ is used to refer to the instability rise time.

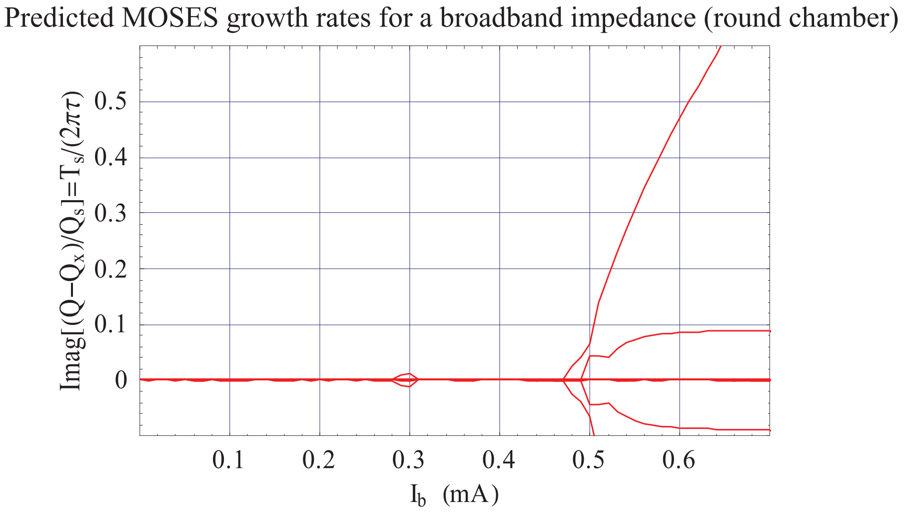

Figure 6.2: Imaginary part of the normalized mode spectrum of the bunch as a function of the bunch intensity calculated with *MOSES* for the LHC bunch in the SPS at injection (see parameters in Tab. B.3). Courtesy of E. Métral.

that the instability modelled by MOSES in these conditions is the result of the coupling of transverse modes, and therefore can be referred to as a TMCI.

6.2 Macroparticle Simulations

As seen in the previous section, many assumptions need to be made on the impedance dependence with frequency and the bunch distribution to be able to apply theoretical formulae for collective phenomena to practical cases. On the other hand, two particle models can give a simple physical picture of the mechanisms involved in collective instabilities, but the underlying assumptions do not allow them either to give a more detailed quantitative description of the complex phenomena occurring in bunches of more than 100 bilion particles. Unfortunately, the capacity of current computers do not allow us to simulate the coupled dynamics of 100 billion particles. This is why a trade off somewhere between 2 and 100 billion needs to be found. Driven by the maximum computing power and memory available, this trade off settles in general between 1000 and 10 million simulated macroparticles depending on the complexity of the interactions that need to be taken into account, and the simulated time needed to observe the phenomena of interest (e.g. coherent motion, emittance growth or instabilities). In this section, we complement the theoretical description of beam instabilities by macroparticle simulations with the *HEADTAIL* code applied to several collective effects in the PS or the SPS.

6.2.1 The *HEADTAIL* Code

The *HEADTAIL* code is a simulation code developed by G. Rumolo and is aimed at simulating the interaction on successive turns of a bunch of macroparticles with an impedance source, an electron cloud or other disturbance phenomena [127]. We are interested here in the interaction of a proton bunch with a transverse impedance source. This interaction is modeled by one or more kicks given at each turn to each of the macroparticles of charge Q. The bunch is sliced longitudinally and each of the macroparticles in a slice gets a kick due to the wake fields generated by the preceding slices[3]. From section 3.2.1, a vertical angle kick $\Delta y'$ due to a vertical force F_y can be expressed as

$$\Delta y' = \int y'' ds = \int \frac{F_y}{m_0 \gamma \beta^2 c^2} ds.$$

For the case of a vertical wake force generated by a source charge Q_1 on a test charge Q_2, assuming that the momentum remains constant during the interaction, we use the definition of the wake potential W_y in Eq. (3.60)

$$\Delta y' = \int \frac{F_y}{m_0 \gamma \beta^2 c^2} ds = \frac{\int F_y ds}{m_0 \gamma \beta^2 c^2} = Q_1 Q_2 \frac{W_y}{m_0 \gamma \beta^2 c^2}.$$

Let us number the slices from head ($i = 1$) to tail ($i = N_{slice}$). At a given turn, a given slice i contains $N(i)$ macroparticles of charge Q, amounting to a charge $Q_1 = N(i)Q$. The center of mass position of slice i is located at $(\langle x(i) \rangle, \langle y(i) \rangle)$ at interaction location. A macroparticle of charge $Q_2 = Q$ at transverse location (x, y) within a following slice $j > i$ receives the total vertical angle kick $\Delta y'(i)$ from slice i

$$\Delta y'(i) = \frac{N(i) Q^2}{m_0 \gamma v_s^2} G_y \left((j-i) \Delta z, y, \langle y(i) \rangle \right), \tag{6.28}$$

where Δz is the longitudinal size of a slice and $G_y \left((j-i) \Delta z, y, \langle y(i) \rangle \right)$ is the wake function generated by source slice at vertical center of mass location $\langle y(i) \rangle$ on a test macroparticle at distance $(j-i) \Delta z$ from the source slice and vertical location x. Equation (6.28) assumes that the transverse motions in the horizontal and vertical planes are decoupled. Decomposing the wake function into dipolar and quadrupolar components as mentioned in Eq. (3.70) and summing the contributions from all the slices preceding the slice of the test macroparticle, we obtain the kicks due to the wakes in both planes

$$\begin{aligned} \Delta x'(i) &= \frac{Q^2}{m_0 \gamma \beta^2 c^2} \sum_{i=1}^{j-1} N(i) \left[\langle x(i) \rangle G_x^{dip} \left((j-i) \Delta z \right) + x G_x^{quad} \left((j-i) \Delta z \right) \right], \\ \Delta y'(i) &= \frac{Q^2}{m_0 \gamma \beta^2 c^2} \sum_{i=1}^{j-1} N(i) \left[\langle y(i) \rangle G_y^{dip} \left((j-i) \Delta z \right) + y G_y^{quad} \left((j-i) \Delta z \right) \right]. \end{aligned} \tag{6.29}$$

We remind here the single kick approximation already mentioned in section 4.2 that requires weighting the impedance input into *HEADTAIL* by a scaling factor $\beta_{x,y} / \langle \beta_{x,y} \rangle$ for an impedance source located at a given beta function $\beta_{x,y}$. Once the angle kick is given to the macroparticles, the simulation code transports the macroparticle transverse positions from one interaction point to the next using the ring linear optics and chromaticity

---

[3] This statement is only true in the ultrarelativistic case for which strictly no wake field can be generated in front of the bunch. If $\beta < 1$, the wake field should also be taken into account. The current versions of *HEADTAIL* only take into account the wake following the source charge.

provided in an input file. The longitudinal coordinates of the macroparticles are obtained by simple transport in the case of a linear longitudinal restoring force valid for small amplitude synchrotron oscillations as described in 3.2.2, and by solving the non linear equations of longitudinal motion with the Runge-Kutta method in case the non linear restoring force is taken into account. Recent updates and benchmarks of the *HEADTAIL* code can be found in Refs. [128] and [129]. In this section, the *HEADTAIL* code was applied to several practical situations, in which collective phenomena in the SPS and the PS can be observed.

6.2.2 Benchmark with *MOSES* for a SPS Broadband Impedance

A benchmark between theoretical mode coupling calculations with *MOSES* and *HEADTAIL* simulations predicting a single bunch fast instability at injection in the SPS was reported in [130]. We start by recalling briefly the context of these TMCI studies in the SPS.

Context of the Fast Transverse Instability in the SPS

Since 2003, beam measurements reported in Refs. [131], [126] and [132] have shown that the SPS intensity is now limited by a fast vertical single bunch instability at injection energy ($p = 26$ GeV/c) if the bunch longitudinal emittance is low ($\varepsilon_l < 0.2$ eVs), and the vertical chromaticity is set as low as possible ($\xi_y \approx 0$). This vertical instability presented the signature of the Transverse Mode Coupling Instability (TMCI) mentioned in section 3.3:

(a) resulting heavy losses appeared within less than a synchrotron period (see the plot on the left of Fig. 6.3),

(b) these losses could be avoided if the vertical chromaticity was increased to $\xi_y = 0.8$ (see both plots on Fig. 6.3),

(c) a traveling-wave pattern propagating from the head to the tail of the bunch could be observed on the data recorded on the SPS Headtail monitor (a wide band SPS strip line pickup).

Besides, as mentioned in the previous chapter, MOSES had predicted a TMCI would occur in the SPS at injection. However, the classical feature of a mode coupling instability that predicts the onset of the instability when the beam current is such that the coherent tune shift of mode 0 is equal to the synchrotron tune (used for instance in Refs. [120] and [34]) is not verified in the case of the SPS. Transverse mode coupling instabilities have already been observed with leptons in many machines (for instance in CERN EPA in Ref. [124] and SLAC PEP in Ref. [33]) or with protons crossing transition (for instance in the CERN PS in Ref. [133]), but to our knowledge they had not been observed with hadron machines far from transition. This is why more arguments are needed to conclude that the fast instability observed in the SPS is indeed a TMCI, and *HEADTAIL* simulation studies were performed.

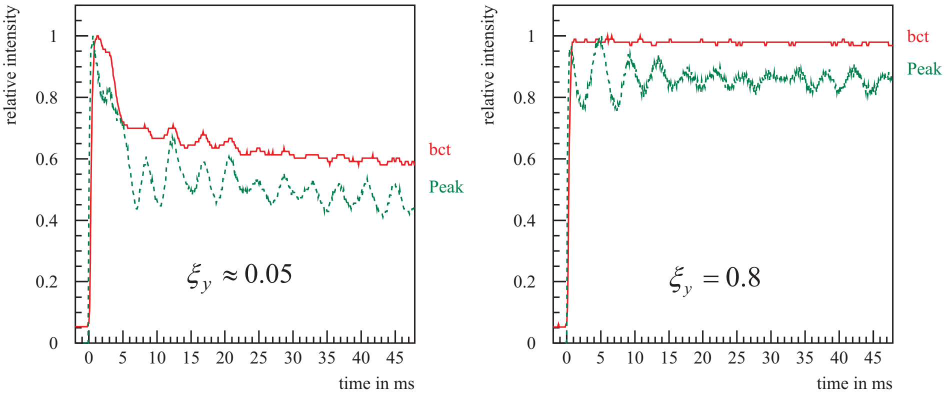

Figure 6.3: Measured relative bunch intensity vs. time in the SPS machine in 2003. Relative bunch intensity was normalized to the bunch intensity measured at injection. *bct* stands for beam current transformer (in red) and *Peak* stands for peak intensity (in green). The bunch, which is unstable when $\xi_y \approx 0.05$ (left) is stabilized by increasing the chromaticity to $\xi_y \approx 0.8$ (right). Courtesy of E. Métral et al [126]

.

HEADTAIL Simulations of the TMCI in the SPS for a Round Chamber

In Refs. [132] and [134], E. Métral and G. Rumolo compared calculations of the coherent bunched-beam modes with *MOSES* and simulated the coherent behavior of a single bunch with the *HEADTAIL* code. A very good agreement was found in predicting the intensity threshold of a single bunch interacting with an SPS transverse impedance modeled as a broadband. In this paragraph, a further frequency analysis of the bunch spectrum of the *HEADTAIL* simulation output is performed and compared with the bunch mode spectrum predicted by MOSES for a round chamber. The main simulation parameters are given in Tab. B.4 in the appendix, and are chosen to reproduce the situation modeled by *MOSES* in the previous section. The transverse tunes (Q_x , Q_y) are set to the working points used before 2006. The transverse betatron tunes have since been exchanged to enhance the lifetime. Also, assumptions include no space charge, no amplitude detuning, a linearized RF bucket, and a frozen wake field i.e. the wake field is only calculated for the first turn, and remains unchanged for all remaining turns. This approximation holds because the bunch is assumed to be well matched to the bucket and no longitudinal impedance is included in the simulation. In this paragraph, the chamber is round so that the horizontal and vertical planes are equivalent, except for the betatron tune. The instability growth rate is calculated from the exponential growth of the amplitude of the bunch centroid oscillations as a function of time. The growth rate as a function of bunch intensity calculated from the output of the *HEADTAIL* simulations is compared with *MOSES* results in Fig. 6.4. Apart from a small non-zero growth rate at $I_b = 0.38$ mA, and a slightly lower growth rate in the range $I_b \in [0.45;\ 0.5]$ mA, *HEADTAIL* simulations reproduce the instability growth rates predicted by *MOSES* calculations for the explored range of bunch intensities. However, this observation is necessary but not sufficient to prove that the transverse instability predicted by HEADTAIL is of the same nature as the one predicted by MOSES, i.e. a TMCI. To learn more about the nature

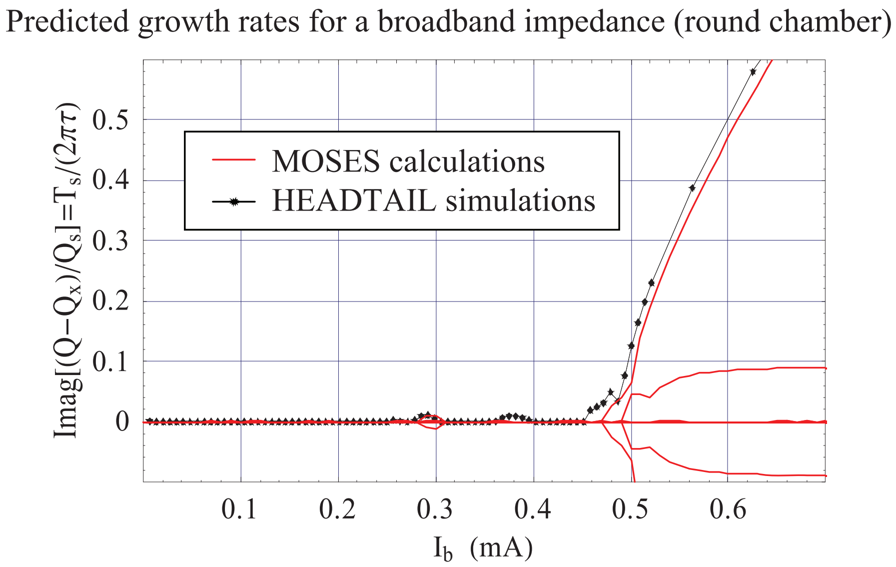

Figure 6.4: Comparing *HEADTAIL* (black full line with dots) and *MOSES* (red full line) growth rates as a function of bunch intensity for the LHC bunch in the SPS at injection (see parameters in Tabs. B.3 and B.4).

of the fast transverse instability predicted by HEADTAIL, the behavior of the transverse modes is also analyzed in the frequency domain. For each of the bunch intensities, the mode spectrum is obtained by applying a frequency analysis to the bunch transverse coherent oscillations as a function of time, which is an output of the HEADTAIL code. Two frequency analysis techniques were used to process the raw simulation data into normalized mode spectra: the classical FFT algorithm or the SUSSIX program [135]. The theory behind *SUSSIX* can be found in Refs. [136] and [137]. The *SUSSIX* algorithm uses an iterative method to identify the main frequency contributions of the spectrum by interpolation in the frequency range of interest. The *SUSSIX* program is applied to the complex phase space normalized coordinate $x - jp_x$ in the phase space whereas simple FFT is only applied to the coherent transverse position x of the bunch centroid, the transverse momentum p_x being left unused. To better observe the difference between the two methods, raw time domain simulation data is plotted for several bunch populations $N_b = I_b L/(ec)$ in Fig. 6.5, and the resulting Fourier analysis is displayed in Fig. 6.6. It can be observed in the examples in Fig. 6.6 that the *SUSSIX* algorithm (results in red) is more sensitive to smaller peaks in the frequency spectrum than a classical FFT (results in green). For instance, the coherent motion analyzed with *SUSSIX* enables to recognize azimuthal modes -2, -1, 0, 1, and 2. The same coherent motion analyzed with a classical Mathematica FFT algorithm only enables to observe azimuthal mode 0. More generally, the *SUSSIX* algorithm is found to be more powerful to analyze the behavior of simulated transverse modes than a classical FFT. This is why we will use exclusively the *SUSSIX* algorithm to analyze both simulated and measured coherent motion data. A closer look at the raw time domain plots in Fig. 6.5 leads to the observations that increasing the bunch population leads to stronger beating visible on the beam envelope and a clear coherent instability at 4.1 10^{10} p/b that dies out if the current is increased

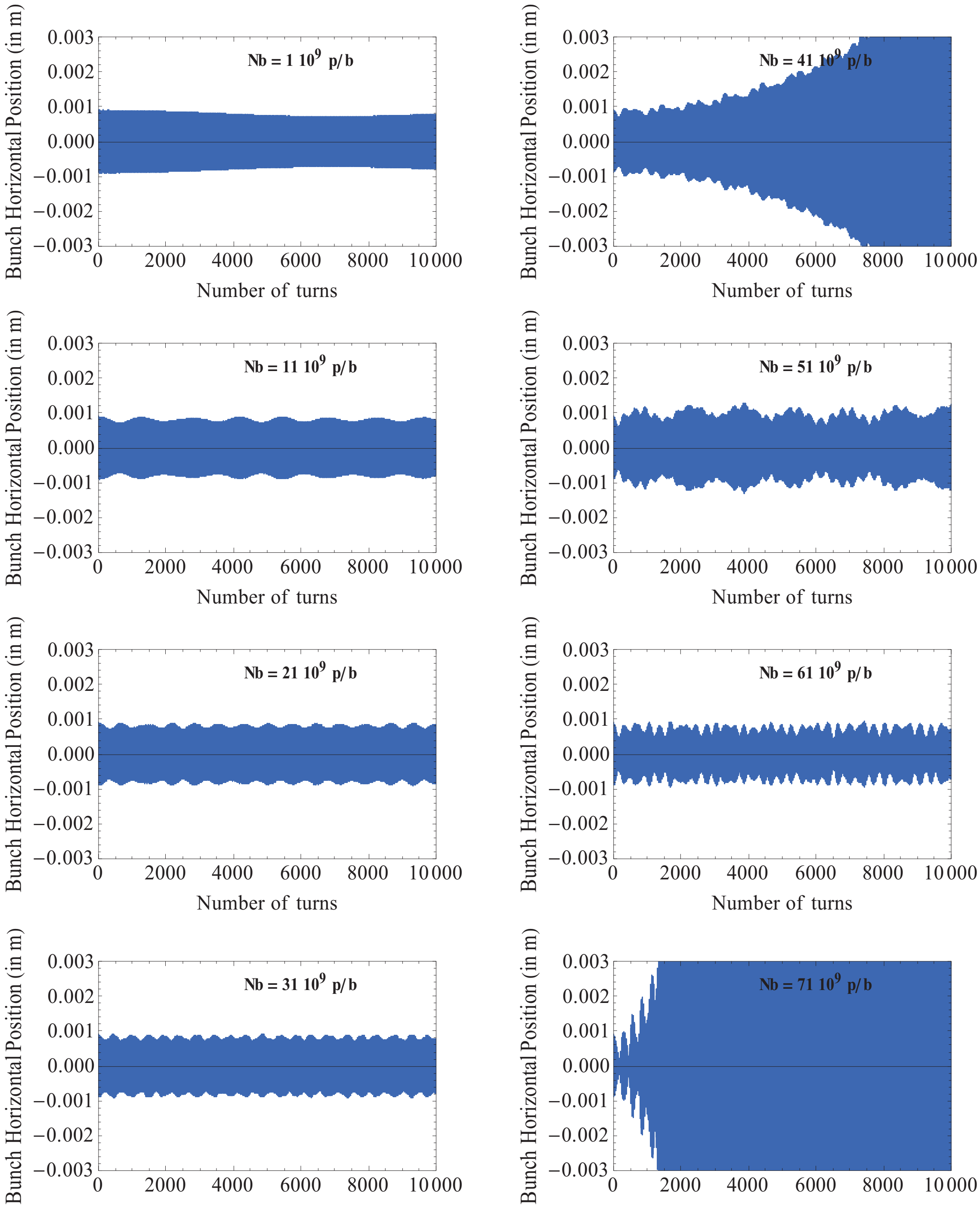

Figure 6.5: Coherent horizontal motion simulated by *HEADTAIL* for the LHC bunch in the SPS at injection (see parameters in Tab. B.4). Bunch population $N_b = I_b L/(ec)$ is increased from (top left) $N_b = 1\ 10^9$ protons per bunch (p/b) to (bottom right) $N_b = 71\ 10^9$ p/b. Since the fractional tune is 0.18, the center of mass betatron oscillations have a period of less than 6 turns and are not visible on this 10000 turns scale.

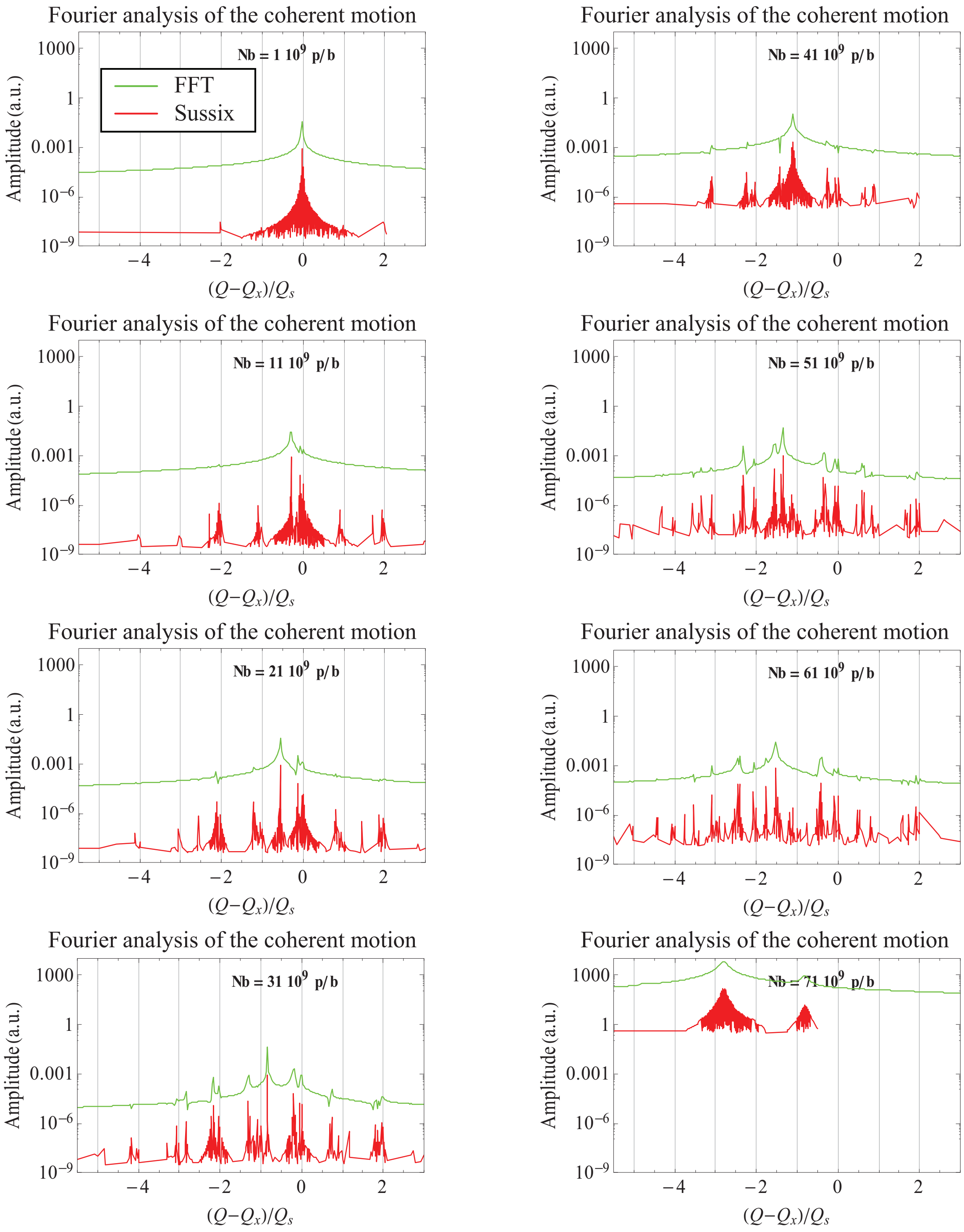

Figure 6.6: Comparing the classical FFT and *SUSSIX* algorithms for Fourier analyzing the coherent horizontal motion simulated by *HEADTAIL* for the LHC bunch in the SPS at injection displayed in Fig. 6.5. Bunch population $N_b = I_b L/(ec)$ is increased from (top left) $N_b = 1\ 10^9$ protons per bunch (p/b) to (bottom right) $N_b = 71\ 10^9$ p/b.

further. The mode spectra obtained from a large number of simulations (80 in this case) with bunch intensities ranging from $I_b = 0.01$ mA to $I_b = 0.55$ mA are gathered on a flattened 3-D plot in Fig. 6.7 (together with a zoom between azimuthal modes -3 and 0 where we changed the x-axis to bunch current to be able to compare with *MOSES* results). The sensitivity of the *SUSSIX* frequency analysis enables to follow the behavior of radial modes that separate when the bunch current is increased. The mode 0 is clearly observed to couple and decouple twice at I_b=0.3 mA and 0.37 mA before a stronger coupling occurs between modes -1 and -2 at I_b=0.43 mA and an even stronger coupling between modes -2 and -3. These mode spectra simulated with *HEADTAIL* are compared with theoretical calculations from *MOSES* in Fig. 6.8. From this comparison, it can be concluded that *MOSES* and *HEADTAIL* quantitatively agree in predicting most of the transverse modes shifting with increasing intensity, and transverse mode coupling at bunch intensities $I_b =$ 0.3 mA (modes 0 and -1), $I_b = 0.47$ mA (modes -1 and -2) and $I_b = 0.5$ mA (modes -2 and -3). This latter coupled mode between modes -2 and -3 is clearly the main contribution to the spectrum amplitude for $I_b > 0.5$ mA, whereas the azimuthal mode 0 also referred to as the transverse tune - carries most of the spectral power for $I_b < 0.5$ mA. This swift power swap between these two spectral lines, along with the large instability growth rate observed in the time domain (see Fig. 6.4), which both occur at $I_b = 0.5$ mA, proves that the resulting instability observed in *HEADTAIL* simulations is indeed a TMCI. The agreement between the two codes is not perfect as it can be seen in Fig. 6.8 that some simulated transverse modes from *HEADTAIL* are not predicted by *MOSES*. In particular, a -2 spectral line undergoes a shift with intensity that is comparable to the shift of the main tune. Along with other features of the *HEADTAIL* simulated mode spectrum, this tends to indicate that the mode spectrum contains echoes of the main lines translated by $\pm 2Q_s$, which do not seem to couple with other modes. The imperfect matching of the longitudinal parameters leading to synchrotron oscillations at $\pm 2Q_s$ could explain these echoes in the mode spectrum. Besides, as opposed to *MOSES*, the main tune couples twice with two different radial modes -1 at $I_b = 0.38$ mA in *HEADTAIL*, which explains the non-zero growth rate at this current in Fig. 6.4. Work on understanding the reasons behind these discrepancies is ongoing. In addition, a benchmark of *MOSES* and *HEADTAIL* increasing by steps the chromaticity has been performed and the results are presented in Appendix C.1.

HEADTAIL **Simulations of the TMCI in the SPS for a Flat Chamber**

Now that the simulations with *HEADTAIL* have been benchmarked with MOSES calculations for the round chamber case, we feel more confident to simulate the case of the flat chamber, i.e. two infinite horizontal parallel plates. This flat chamber case is closer to the elliptic chamber of the CERN SPS, but it is not yet possible to solve it with *MOSES*. The simulation parameters in Tab. B.4 were left unchanged but the Yokoya factors in Tab. 5.1 were used to transform the broadband impedance of a round chamber into a broadband impedance for a flat chamber. The comparison between the simulated growth rates for both horizontal and vertical planes of the flat chamber, and the growth rate for the round chamber simulated in the previous section, is shown in Fig. 6.9. The instability threshold for the vertical plane of the flat chamber is slightly higher than the threshold for the round chamber case. Besides, although a factor 2 higher than that of the vertical

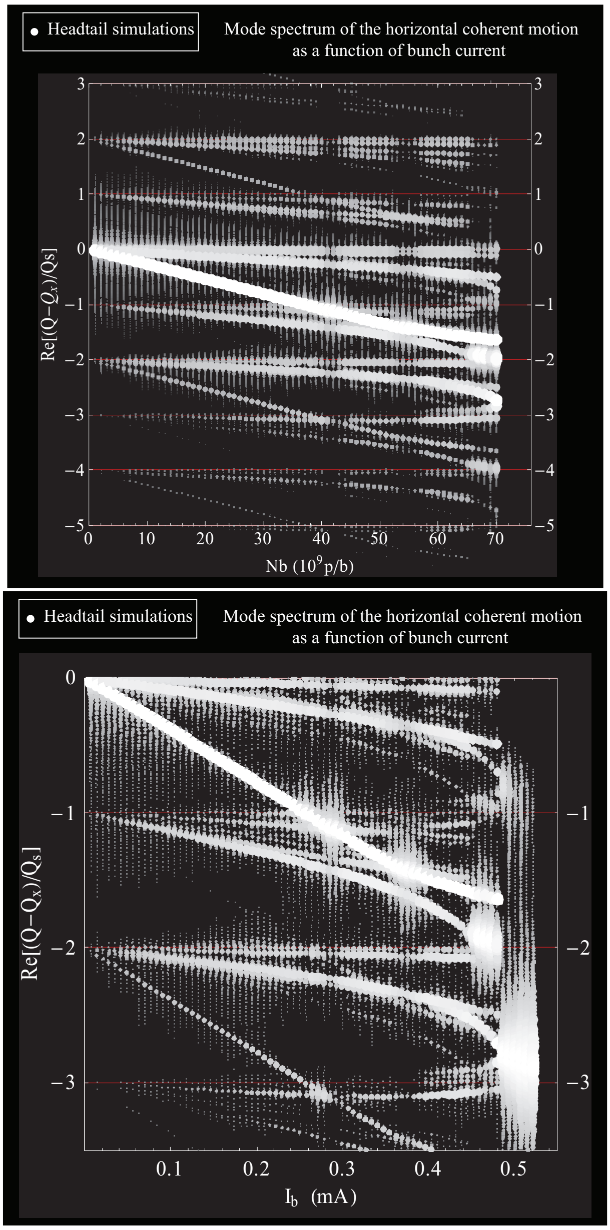

Figure 6.7: Mode spectrum of the horizontal coherent motion simulated by *HEADTAIL* (white dots) as a function of bunch population (top), and as a function of bunch intensity (bottom, zoomed to enhance the behavior of azimuthal modes 0, -1, -2 and -3). The coherent motion as simulated with HEADTAIL was post-processed with SUSSIX and displayed using white dots, whose size and brightness are both non-linear functions of their spectral amplitude (bigger brighter dots have a higher amplitude than smaller darker dots).

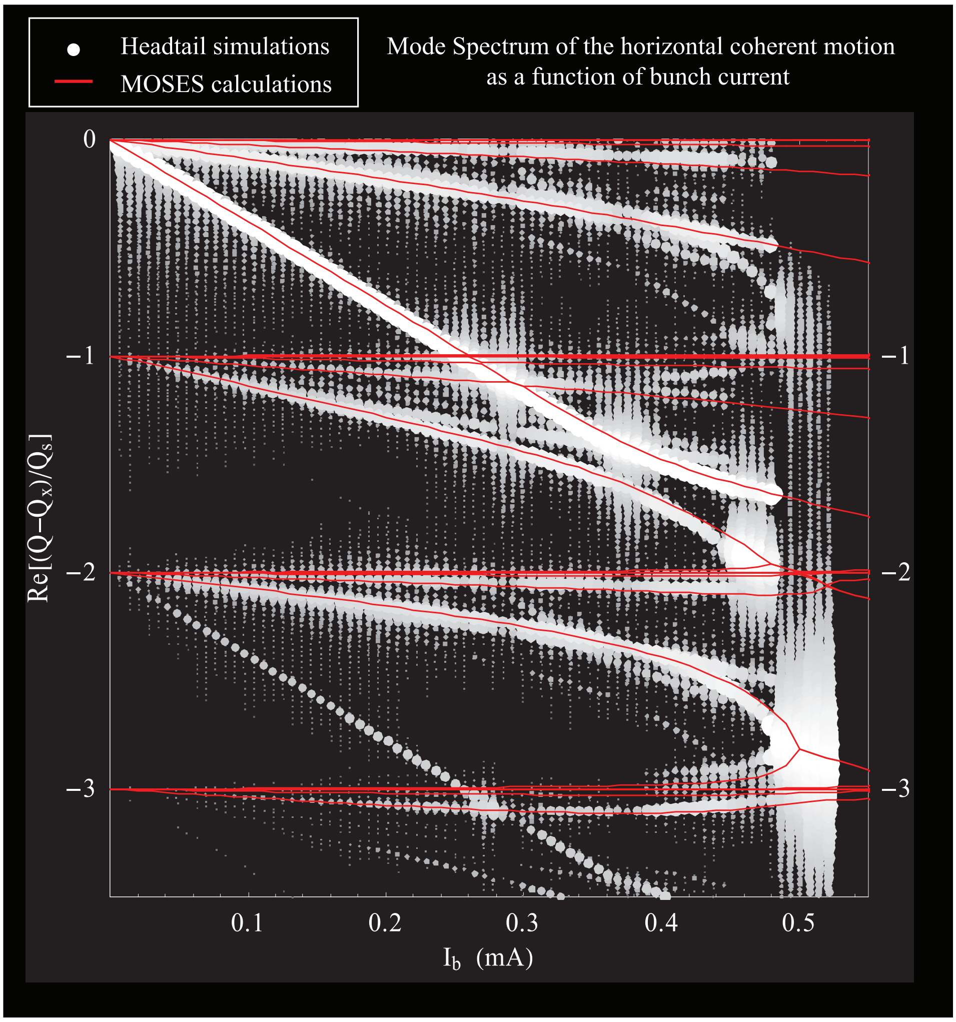

Figure 6.8: Comparing mode spectra as a function of bunch intensity obtained with *HEADTAIL* simulations (white dots) and *MOSES* theoretical calculations (red lines). The coherent motion simulated with *HEADTAIL* was post-processed with *SUSSIX* and displayed using white dots, whose size and brightness are both non-linear functions of their spectral amplitude (bigger brighter dots have a higher amplitude than smaller darker dots).

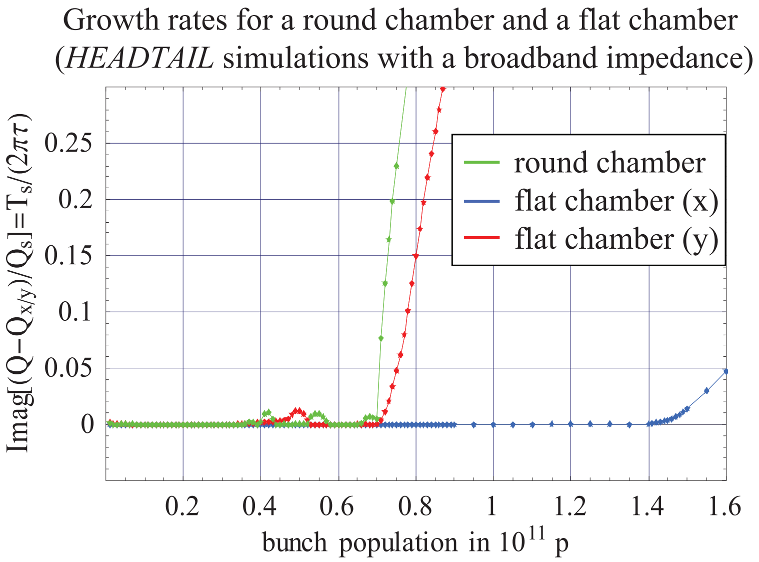

Figure 6.9: Comparison *HEADTAIL* simulated growth rates of a bunch interacting with the broadband impedance of a round chamber (in green) and the broadband impedance of a flat chamber (x plane in blue and y plane in red) as a function of bunch population.

plane, an instability threshold is found for the horizontal plane of the flat chamber. The thresholds for the vertical and horizontal planes of the flat chamber are scaled from the round chamber threshold by the respective vertical ($\pi^2/12$) and horizontal ($\pi^2/24$) dipolar factors obtained by K. Yokoya for the case of a resistive pipe and Laslett for a perfect conductor [138]. Besides, simulated mode spectra as a function of bunch population for both horizontal and vertical planes are presented in Fig. 6.10. A coupling between modes -2 and -3 in the vertical plane is observed. In the horizontal plane, the origin of the instability can not be proven, but a coupling between azimuthal modes -1 and -2 can be guessed. Moreover, the slope of the tune shift with intensity (main radial mode of azimuthal mode 0) for the vertical plane of the flat chamber case is observed to be higher by a factor $\pi^2/8$ than for the round chamber case. The slope of the tune shift with intensity for the horizontal plane of the flat chamber case is observed to be zero. These observations can be understood if we assume that both dipolar and quadrupolar parts of the flat chamber impedance have an impact on the tune shift [139]. Actually, for the vertical plane the two contributions add up resulting in a factor $\pi^2/12+\pi^2/24 = \pi^2/8$ with respect to the round chamber, whereas for the horizontal plane, the two contributions are subtracted and, in this specific case, they cancel out ($\pi^2/24-\pi^2/24=0$).

***HEADTAIL* Simulations of the TMCI in the SPS for a Flat Chamber with Linear Coupling**

Linear coupling between the transverse planes can be introduced in the transport matrix of the coordinates from one interaction point to the next interaction point in *HEADTAIL* simulations. *HEADTAIL* simulations performed in Ref. [134] showed that linear coupling between the transverse planes was observed to increase the TMCI threshold in the case of a flat chamber as predicted theoretically in Ref. [140], when the transverse tunes are set to

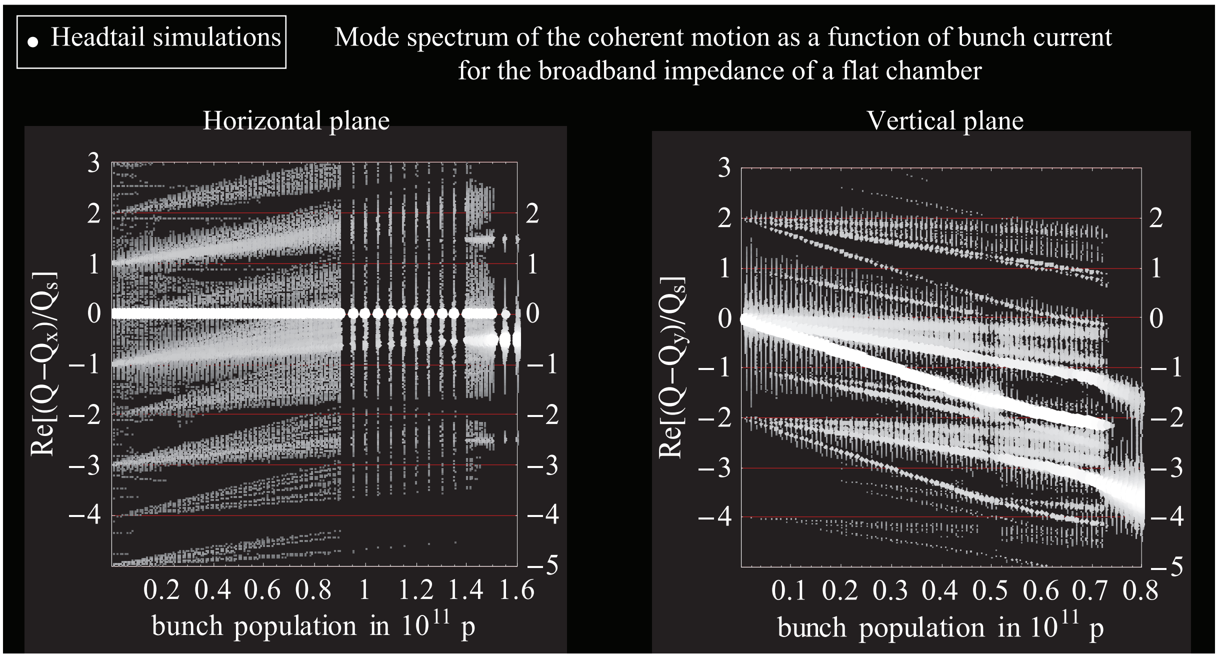

Figure 6.10: HEADTAIL horizontal (left) and vertical (right) mode spectra as a function of bunch population for a flat chamber and a broadband impedance. It is important to notice that the horizontal scale range is larger, and that the density of simulations covering the population range Nb ∈ [0.9;1.6] 10^{11} protons is reduced. Simulated mode spectra are displayed using white dots, whose size and brightness are both non-linear functions of their spectral amplitude (bigger brighter dots have a higher amplitude than smaller darker dots).

$Q_x = 26.18$ and $Q_y = 26.185$. As can be seen in Fig. 6.11, a 30% threshold increase can be obtained with a linear coupling coefficient K=0.005 m^{-1}, corresponding to a closest-tune approach $C \approx 0.033$. It is important to note that the shunt impedance was doubled to R_s = 20 MΩ/m compared to the studies in the previous paragraph. The mode spectrum with linear coupling obtained in Fig. 6.12 is not normalized, so that the absolute values of the coupled tunes can be observed. Mode coupling is again observed to take place between mode -2 and mode -3 when linear coupling is present. Now that benchmarks have been performed for several types of broadband impedance models, we will use more realistic impedance models of SPS elements from theory and EM simulations obtained in Chapter 5 as input of *HEADTAIL* simulations. Comparing the results of these *HEADTAIL* simulations with observables measured during Machine Development studies (MDs) with the SPS beam presented in Section 6.3 will then enable us to assess the relevance of the current transverse impedance model of the SPS. In particular, this comparison should tell us which of the modeled impedance sources are major contributors to the total transverse SPS impedance and whether large contributions are still unaccounted for in the model.

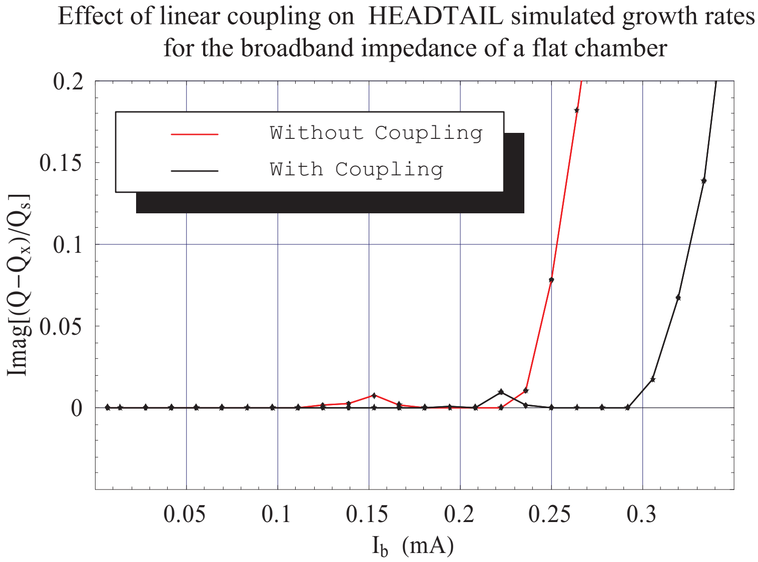

Figure 6.11: Comparison between *HEADTAIL* simulated growth rates for the vertical plane of a flat chamber without linear coupling between the two transverse planes (red), and with linear coupling (black) as a function of bunch intensity, for a shunt impedance R_s = 20 MΩ/m.

6.2.3 Improved SPS Impedance Models from ZBASE

In this section, we will use the wakes obtained in Chapter 5 for several SPS elements (20 kickers in 2006, beam pipe and BPMs) as inputs of *HEADTAIL* simulations in order to obtain simulated beam dynamics observables (e.g. coherent tune shift and instability growth rate). We start with the theoretical models for the SPS kickers, which are assumed to be major contributors to the SPS transverse impedance, before adding the wake contributions obtained for the beam position monitors and the beam pipe.

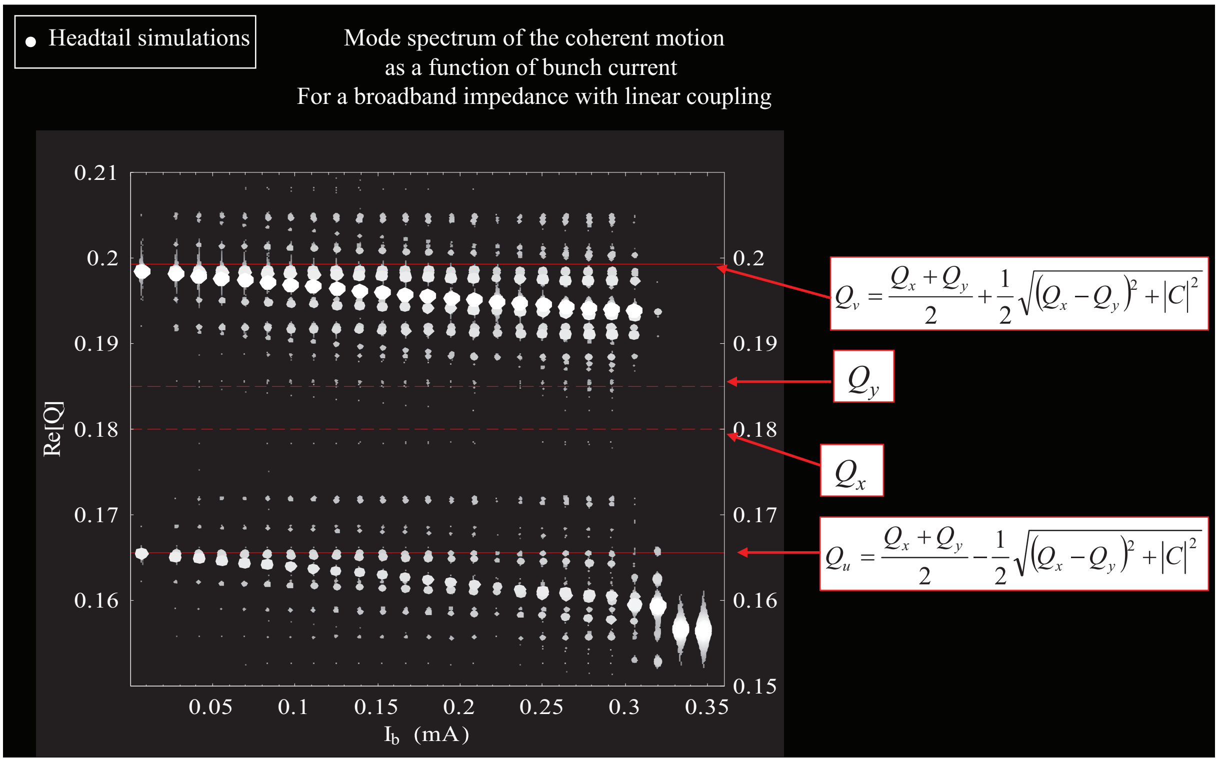

Figure 6.12: *HEADTAIL* mode behavior as a function of bunch intensity for a flat chamber in the vertical plane, for a shunt impedance $R_s = 20$ MΩ/m, and in the presence of linear coupling between the transverse planes with a closest-tune approach $C = 0.033$. Dashed red lines indicate the uncoupled fractional parts of the vertical (Q_y=0.185) and horizontal tunes (Q_x=0.18). Full red lines are the coupled tunes Q_u and Q_v predicted in Ref. [141]. Simulated mode spectra are displayed using white dots, whose size and brightness are both non-linear functions of their spectral amplitude (bigger brighter dots have a higher amplitude than smaller darker dots).

HEADTAIL Simulations for the Zotter/Métral Model for the SPS Kickers

In section 5.2.2, we obtained the dipolar and quadrupolar wake functions accounting for the 20 SPS kickers modeled with the Zotter/Métral model present in the SPS in 2006. *HEADTAIL* was modified to allow importing dipolar and quadrupolar wake functions separately, in order to study collective phenomena resulting from a lumped impedance source, which dipolar and quadrupolar wake functions can not be related simply by applying the Yokoya factors. The *HEADTAIL* input parameters were chosen to be as close as possible to the SPS machine measurements parameters (see Tab. B.5). However, the simulated bunch needs to be longitudinally matched to the simulated linear SPS longitudinal restoring force in order to minimize bunch length oscillations and observe the modes more clearly. This linear restoring force was preferred to a more realistic non-linear bucket to avoid introducing synchrotron frequency spread and non-linearities. Besides, at such low longitudinal emittance, the SPS beam is small in the RF bucket and the linear and the difference between the linear and non linear longitudinal motions are small (see Fig. 3.5). As a consequence, the bunch length can not be fixed to the measured value of $\sigma_t = 0.7$ ns, but to $\sigma_t = 0.5$ ns instead. The results of these *HEADTAIL* simulations are presented in Fig. 6.13. As can be seen on Fig. 6.13, a weak coupling between azimuthal modes 0 and -1 is observed for a bunch population N_b=6.5 10^{10} p/b, resulting in a slow instability. These modes decouple for $N_b = 7.5$ 10^{10} p/b, resulting in a stabilization of the

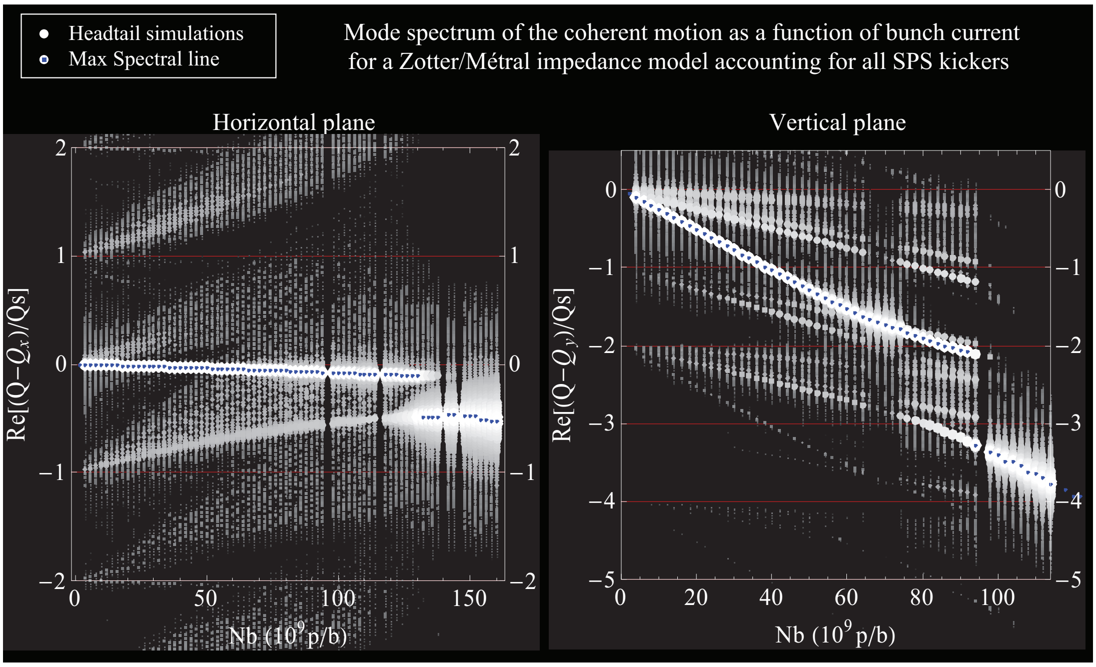

Figure 6.13: Simulated horizontal (left) and vertical (right) mode spectra of the coherent motion as a function of bunch population for a Zotter/Métral impedance model accounting for all SPS kickers. Four simulated mode spectra are missing on the horizontal plot, and one on the vertical plot. Simulated mode spectra are displayed using white dots, whose size and brightness are both non-linear functions of their spectral amplitude (bigger brighter dots have a higher amplitude than smaller darker dots). For each bunch population, the main spectral line is indicated by a blue spot.

vertical motion. Finally a strong coupling between azimuthal modes -2 and -3 occurs for $N_b = 9.3\ 10^{10}$ p, leading to a significant growth rate. This general behavior is similar to the case of a simulated broadband impedance in a flat chamber studied in section 6.2.2. Therefore, in this case of a more realistic transverse impedance model taking into account the 20 SPS kickers, we can again conclude that a TMC instability is observed. A new "Multi kick" version of *HEADTAIL* was implemented to import a machine lattice from a MAD-X output file, and to let the bunch interact with multiple impedance sources [128]. The individual wake functions obtained from *ZBASE* for each SPS kicker were then input into *HEADTAIL*. Over one turn, the *HEADTAIL* simulated bunch could then interact separately with each of these 20 kickers taking into account the beta function at their location. The horizontal and vertical coherent motions simulated with the single kick version of *HEADTAIL* used in the previous simulations, and the new multi kick version are displayed in Fig. 6.14. The comparison of the growth rates for the single kick and multi kick versions are presented in Fig. 6.15. The good agreement between the two approaches for both mode spectra and growth rate validates the single kick approach that was used in previous impedance studies with HEADTAIL.

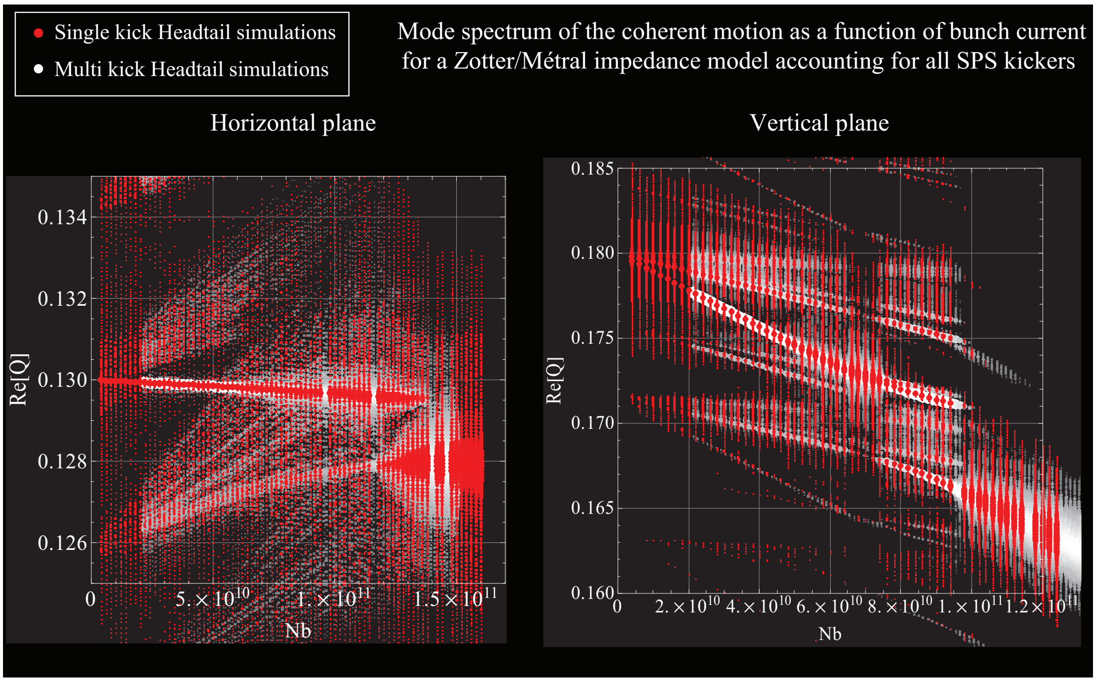

Figure 6.14: Simulated horizontal (left) and vertical (right) mode spectra of the coherent motion as a function of bunch population for a Zotter/Métral impedance model accounting for all SPS kickers. Simulated mode spectra are displayed using white dots, whose size and brightness are both non-linear functions of their spectral amplitude (bigger brighter dots have a higher amplitude than smaller darker dots) for the multi-kick approach, and with red dots for the single-kick approach.

HEADTAIL Simulations for Tsutsui's Model of the SPS Kickers

In section 5.2.4, the dipolar and quadrupolar wake functions accounting for the 20 SPS kickers were obtained with Tsutsui's formalism. These wakes were lumped into a single

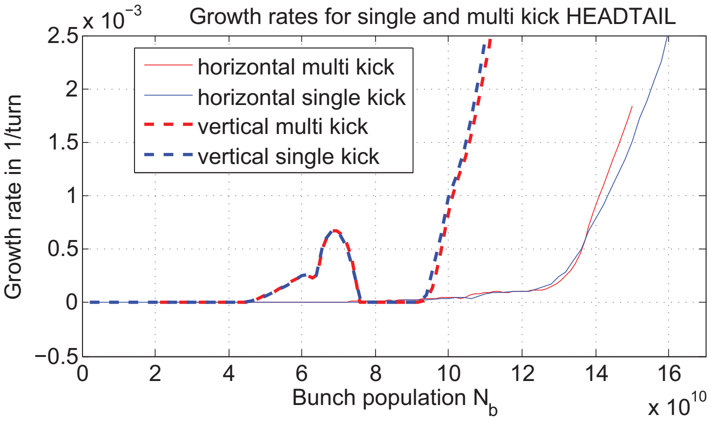

Figure 6.15: *HEADTAIL* simulated growth rates vs. bunch population N_b using the multi-kick approach (red) and the single-kick approach (blue) for the horizontal plane (in thin full lines) and the vertical plane (in dashed thick lines).

localized impedance source in *HEADTAIL* simulations with the same simulation parameters as in the previous paragraph (see Tab. B.6). The growth rates obtained from these simulations are presented in Fig. 6.16 and the mode spectra in Fig. 6.17. On Fig. 6.16, a negative growth rate means that the amplitude of the coherent oscillations decays. As we will see in the Qmeter measurements in Chapter 6.3, a quantitative automated exponential fit turns out to be tricky to perform on large number of data sets in which both coherent damping and coherent growth are present. Depending on the chosen range of simulated turns, the exponential fit gives a radically different result. This is why we decided to use a simple uniform fit on the whole 8192 simulated turns. In this case, a negative growth rate can be interpreted as damping, but a lower value of this negative growth rate does not necessarily mean stronger damping, due to the quick convergence to numerical noise for very strong damping (as for instance for N_b=178 10^9 p/b). However, a positive growth rate is representative of both the presence of a coherent instability and its quantitative strength. Issues may come up in obtaining the growth rate when the onset of the instability takes a significant number of turns before happening (due to damping in particular as for N_b=158 10^9 p/b). It is interesting to note that the simulated coherent motion in both planes appears to be strongly damped when the bunch population is increased, even though no non linearity or spread is present in the simulations (no direct space charge, no amplitude dependent tune shift, no synchrotron tune spread). This damping is observed to be strongly intensity dependent (negligible at low bunch populations such as N_b=14 10^9 p/b for instance). Besides, this damping disappears when the same simulations are performed setting to zero the quadrupolar components of the wake functions, and we can conclude that the strong quadrupolar component of the wake in Tsutsui's model creates enough tune spread to damp the coherent oscillations in both planes and generate emittance growth (see an illustration for N_b = 8 10^{10} p/b in Fig. 6.18). Moreover, when comparing Fig. 6.17 to Fig. 6.13, a striking feature is that the coherent tune shift in the horizontal plane is small and negative for the Zotter/Métral model but large and positive for the Tsutsui model, as predicted in Section 5.2.4. This can be understood when observing that the quadrupolar horizontal wake function is larger than the dipolar horizontal wake function for the model of Tsutsui. Even though the ver-

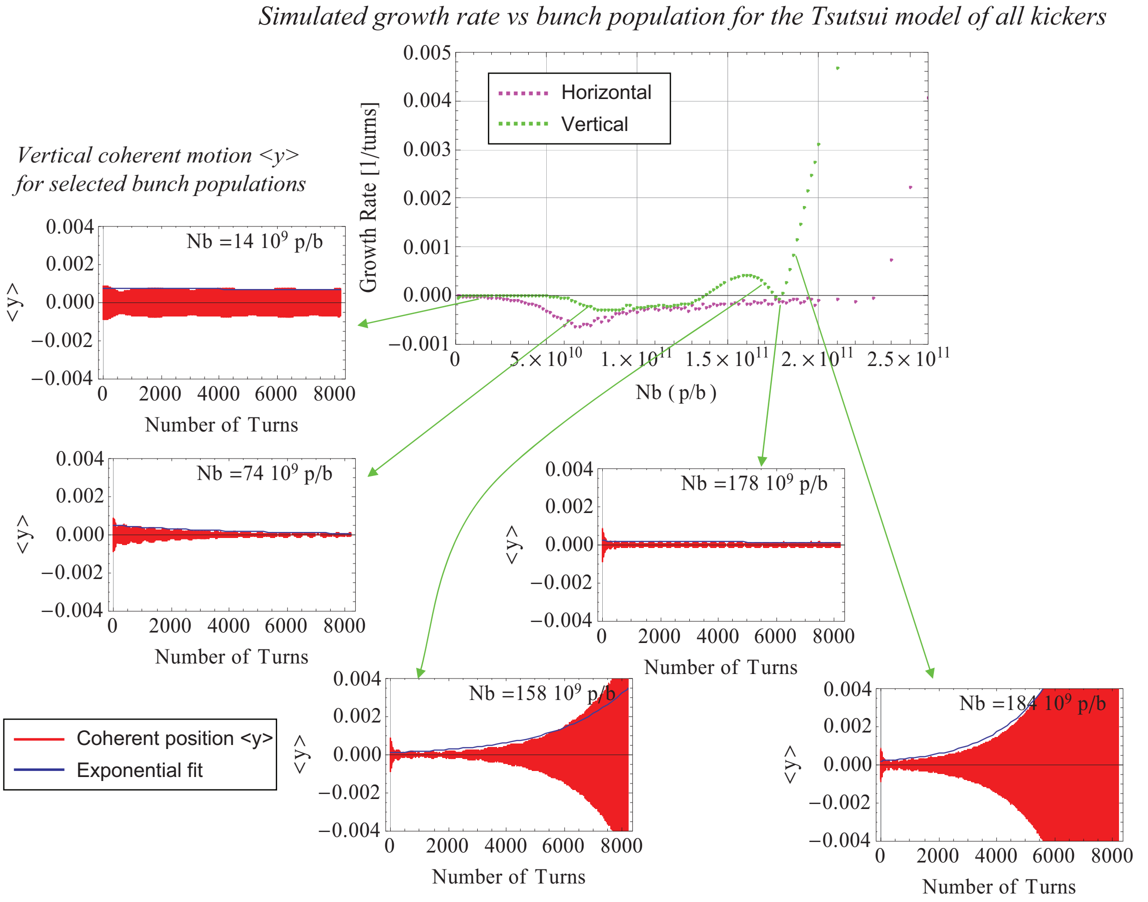

Figure 6.16: Horizontal (pink dots) and vertical (green dots) growth rates simulated with *HEADTAIL* of the contributions of the 20 SPS kickers (top large graph). The vertical coherent motion (in red) for selected bunch populations is also displayed to realize that for low bunch currents the amplitude of the motion is stable, whereas it is subject to damping and/or growth at higher bunch currents. The exponential fit of the coherent motion is also displayed for these selected bunch populations (in blue).

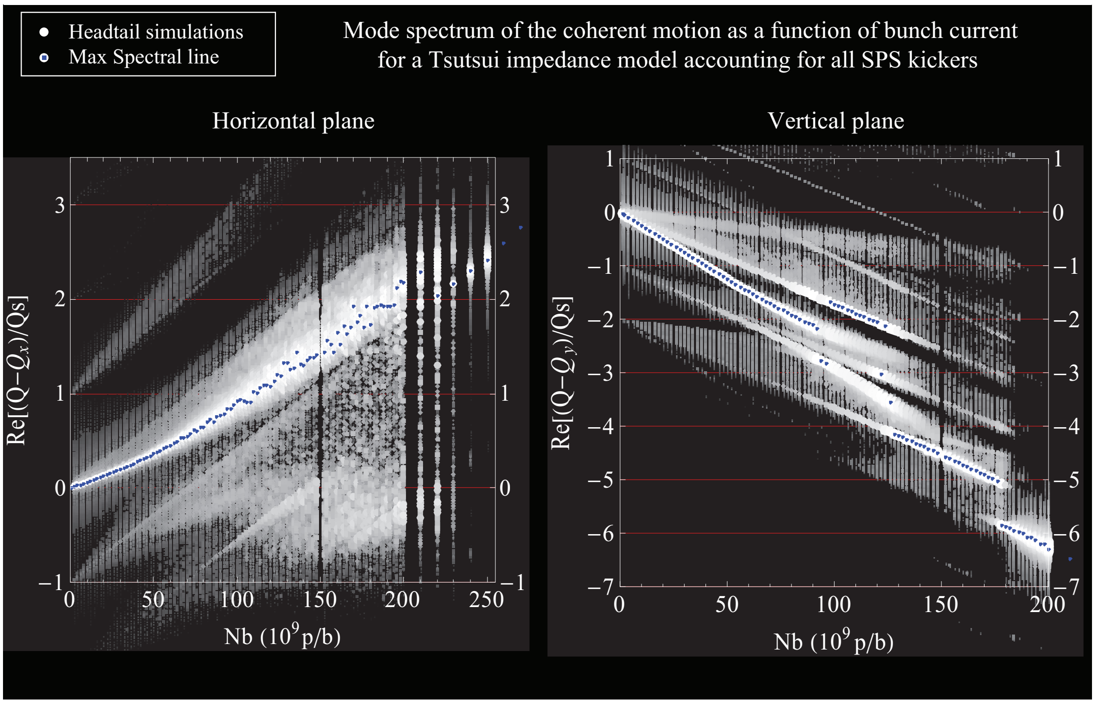

Figure 6.17: Simulated horizontal (left) and vertical (right) mode spectra of the coherent motion as a function of bunch population for a Tsutsui impedance model accounting for all SPS kickers. Simulated mode spectra are displayed using white dots, whose size and brightness are both non-linear functions of their spectral amplitude (bigger brighter dots have a higher amplitude than smaller darker dots). For each bunch population, the main spectral line is indicated by a blue spot.

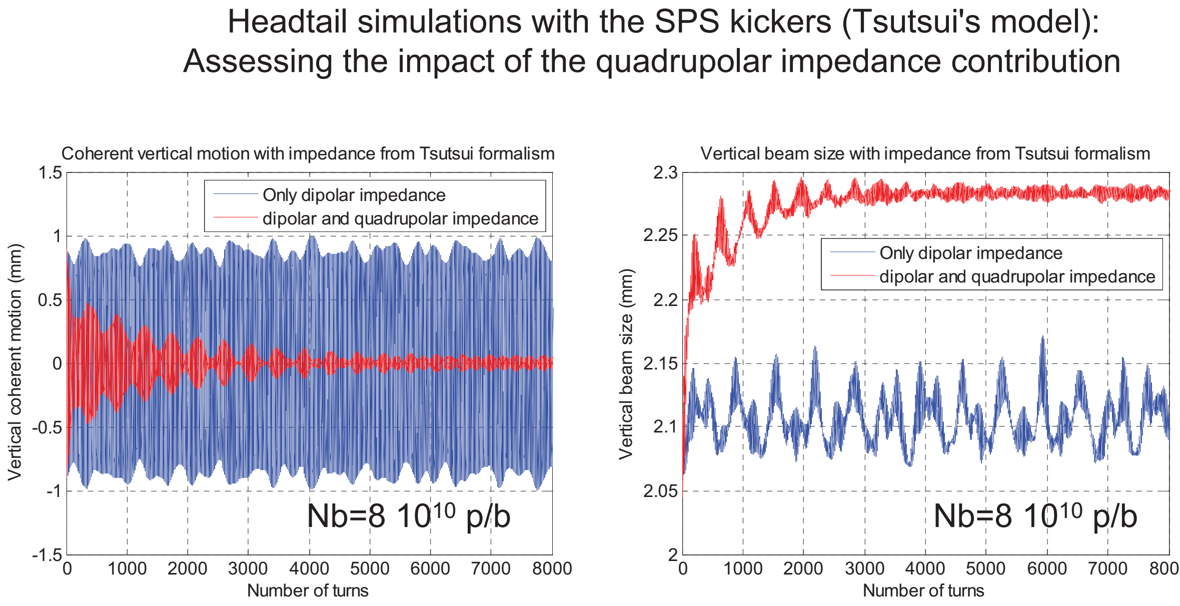

Figure 6.18: Evolution of the vertical coherent bunch position (left) and vertical emittance (right) simulated with *HEADTAIL* for an impedance model accounting for 20 SPS kickers: dipolar contribution only (in blue) and total (dipolar + quadrupolar) contributions in red.

tical coherent tune shift is similar for both the Tsutsui and the Zotter/Métral model, the intensity thresholds in both planes are much larger for the Tsutsui model. As already mentioned above when analyzing the growth rates, the quadrupolar components create tune spread, which in turn damps the coherent oscillations and delays the onset of the instability. Another interesting feature of the vertical mode spectra is the fact that the main spectral line oscillates between several radial modes of azimuthal modes 0 and -1 in the range $N_b \in [9;12.5]$ 10^{10} p/b , even though no coherent instability can be observed. The observables extracted from these plots of the Tsutsui model and the Zotter/Métral model for the SPS kickers are gathered for comparison purposes in Tab. 6.1.

Observable	Zotter/Métral model	Tsutsui model
Horizontal effective impedance Z_x^{eff}	0.3 MΩ/m	-2.3 MΩ/m
Vertical effective impedance Z_y^{eff}	9.3 MΩ/m	9.0 MΩ/m
Horizontal instability threshold $N_{b,x}^{th}$	8-13 10^{10} p/b	24 10^{10} p/b
Modes involved in horizontal instability	-1 (maybe 0 or -2)	-1 (maybe 0)
First vertical instability threshold $N_{b,y}^{th\ (1)}$	6 10^{10} p/b	15 10^{10} p/b
Modes involved in first vertical Instability	0 and -1	-2 and ?
Intermediate stable region	7.5 to 9.5 10^{10} p/b	17 to 18 10^{10} p/b
Second vertical instability threshold $N_{b,y}^{th\ (2)}$	9.5 10^{10} p/b	18 10^{10} p/b
Modes involved in second vertical Instability	-2 and -3	-3 and ?
Damping of coherent oscillations	no	yes

Table 6.1: Comparison of beam dynamics observables simulated with *HEADTAIL* for the Zotter/Métral model and Tsutsui model accounting for the 20 kickers in the SPS present in 2006. The effective impedances are estimated with the Sacherer formula for the mode 0 assuming a Gaussian bunch [46].

Adding the Beam Pipe and BPMs to the SPS Impedance Model

The tools set up for the database *ZBASE* were used to add the transverse dipolar and quadrupolar wake functions obtained for the SPS beam pipe in section 5.2.3 and for the SPS BPMs in section 5.3.2. After an interpolation step, all the wake contributions are summed for each interpolation frequency and presented in Fig. 6.19 for both the Zotter/Métral model and the Tsutsui model of the SPS kickers. The contribution of the SPS BPMs to the total SPS wake model (from blue curves to red curves) is an oscillation that affect significantly (30 %) the long range single bunch wakes (from 1 ns to 3 ns). It also leads to a 10 % increase of the absolute value of the short range wakes (up to 1 ns). The contribution of the SPS beam pipe (from red curves to green curves) is strong in the very short range of the single bunch wakes (the direct space charge contribution tends to a Dirac distribution at high energies), but it also leads to a significant increase of the long range single bunch wakes (from 1 ns to 3 ns), in particular for the dipolar vertical wake functions due to the Yokoya factors. Simulations with the two SPS impedance models (kickers+BPMs+beam pipe) were performed for the kicker models of both Zotter/Métral and Tsutsui. The growth rates for both sets of simulations are presented in Fig. 6.20 and the mode spectra are presented in Fig. 6.21 for the Zotter/Métral kickers model and

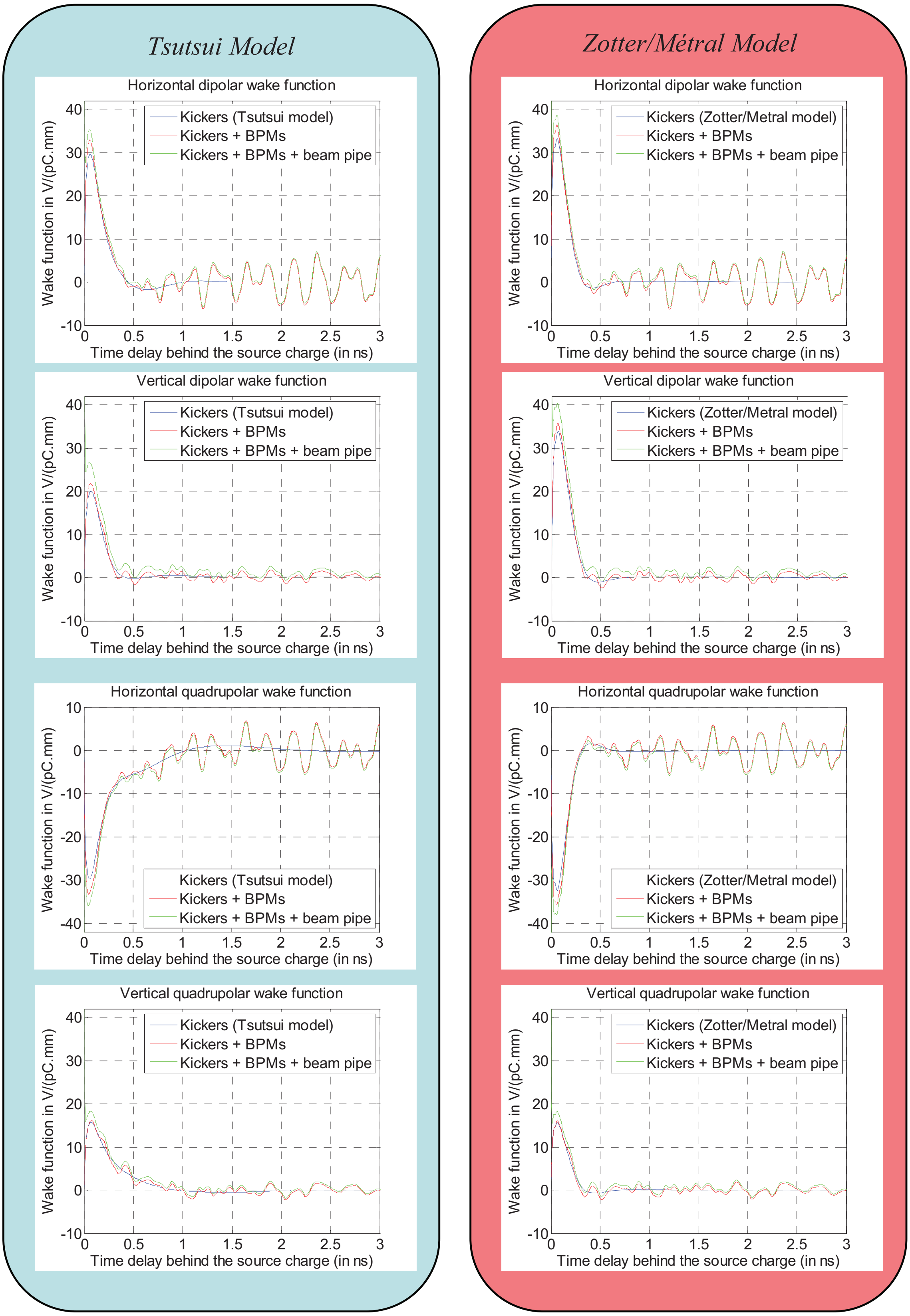

Figure 6.19: Summed wake functions for an SPS impedance model composed of the 20 SPS kickers present in 2006, the 6911 m long SPS beam pipe, the 106 SPS BPHs and 96 SPS BPVs (in green), together with the summed wake functions for the kickers and BPMs (in red), and the kickers alone (in blue). The SPS impedance model based on the Tsutsui model for the kickers contribution is on the left while SPS impedance model based on the Zotter/Métral model for the kickers contribution is on the right

in Fig. 6.22 for the Tsutsui kickers model. Comparing the instability thresholds in

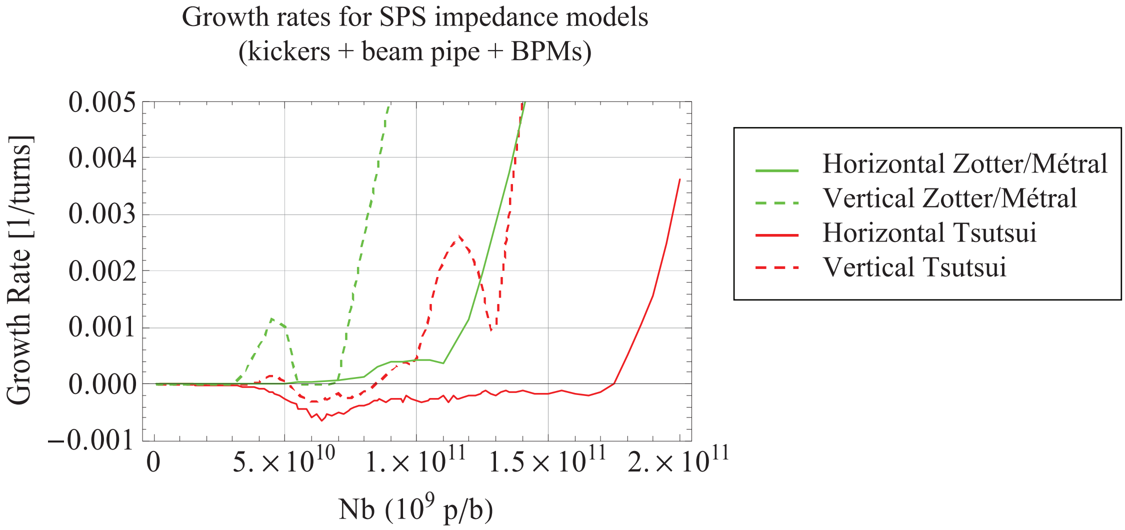

Figure 6.20: Summed wake functions for an SPS impedance model composed of the 20 SPS kickers present in 2006, the 6911 m long SPS beam pipe, the 106 SPS BPHs and 96 SPS BPVs (in green), together with the summed wake functions for the kickers and BPMs (in red), and the kickers alone (in blue). The SPS impedance model based on the Tsutsui model for the kickers contribution is on the left while SPS impedance model based on the Zotter/Métral model for the kickers contribution is on the right.

Fig. 6.20 to those in Fig. 6.15 and 6.16, including the beam pipe and the BPMs leads to significantly lower instability threshold (20% for the Zotter/Métral kickers model and 30 % for the Tsutsui model). This observation is the result of an increase of the dipolar components in both planes. Significant damping of the coherent oscillations with the Tsutsui model of the kickers can still be observed. The horizontal tune shift with intensity is not changed but the vertical tune shift increases from 9 MΩ/m to 13 MΩ/m, a 40 % increase, acknowledging that the quadrupolar components also increased. The mode spectra show similar behaviour in both SPS impedance models, but the the strongest spectral line is not carried by the same modes in the case of the Tsutsui kicker model. We also observe the presence of a first instability around 4 10^{10} p/b due to a coupling between modes 0 and -1 in the vertical plane of the SPS impedance model with Tsutsui kickers model, that was absent with the kickers alone. A summary of the main observables that can be extracted from these simulations is gathered in Tab 6.2. These *HEADTAIL* simulations of updated SPS impedance models show the complexity of the behavior of the modes with increasing bunch population. It will now be interesting to compare these simulated observables with measurements with the LHC beam in the SPS.

6.3 Measurements with Beam in the SPS

Following initial studies on the fast instability in the SPS [142], dedicated measurements to observe the TMCI at injection with the LHC beam in the SPS were performed in 2007 and

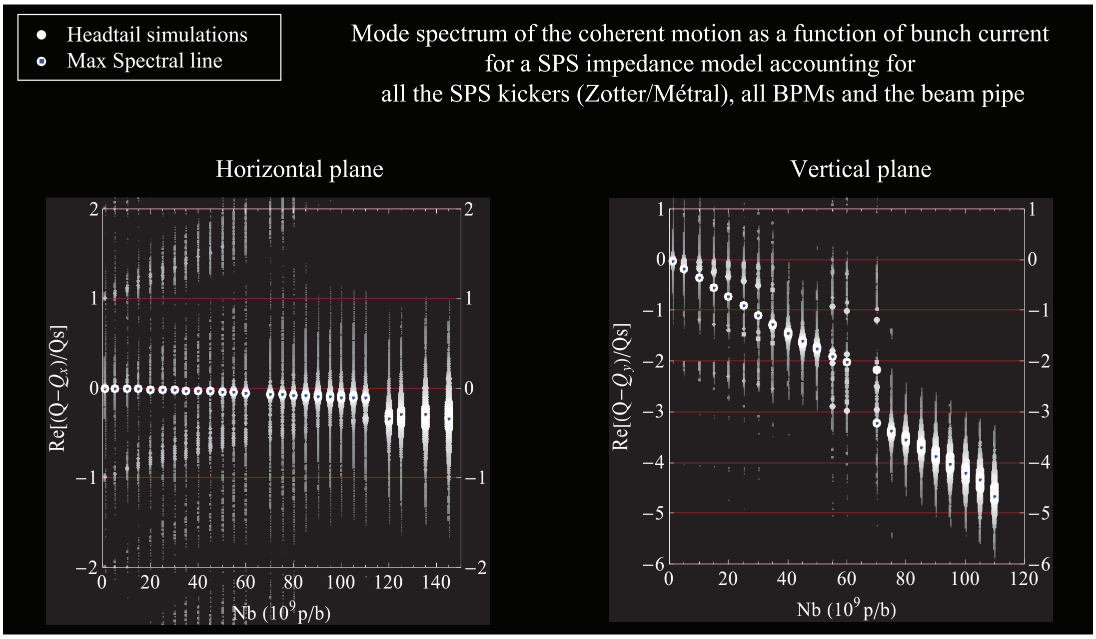

Figure 6.21: Simulated horizontal (left) and vertical (right) mode spectra of the coherent motion as a function of bunch population for a Zotter/Métral impedance model accounting for all SPS kickers. Simulated mode spectra are displayed using white dots, whose size and brightness are both non-linear functions of their spectral amplitude (bigger brighter dots have a higher amplitude than smaller darker dots). For each bunch population, the main spectral line is indicated by a blue spot.

Observable	Zotter/Métral model	Tsutsui model
Horizontal effective impedance Z_x^{eff}	0.3 MΩ/m	-2.3 MΩ/m
Vertical effective impedance Z_y^{eff}	12.9 MΩ/m	12.7 MΩ/m
Horizontal instability threshold $N_{b,x}^{th}$	8-11 10^{10} p/b	1.8 10^{11} p/b
Modes involved in horizontal instability	-1 (maybe 0 or -2)	-1 (maybe 0)
First vertical instability threshold $N_{b,y}^{th\ (1)}$	3.5 10^{10} p/b	4 10^{10} p/b
Modes involved in first vertical Instability	0 and -1	0 and -1
Intermediate stable region	5.0 to 7.5 10^{10} p/b	5 to 8.5 10^{10} p/b
Second vertical instability threshold $N_{b,y}^{th\ (2)}$	7.5 10^{10} p/b	8.5 10^{10} p/b
Modes involved in second vertical Instability	-2 and -3	-2 and -1
Third vertical instability threshold $N_{b,y}^{th\ (3)}$	no	1.3 10^{11} p/b
Modes involved in third vertical Instability	N/A	-2 and -3
Damping of coherent oscillations	no	yes

Table 6.2: Comparison of beam dynamics observables simulated with *HEADTAIL* for SPS models accounting for the 20 kickers in the SPS present in 2006 (both models from Zotter/Métral and Tsutsui), the beam pipe and the BPMs. The effective impedances are estimated with Sacherer's formula for the mode 0 assuming a Gaussian bunch [46].

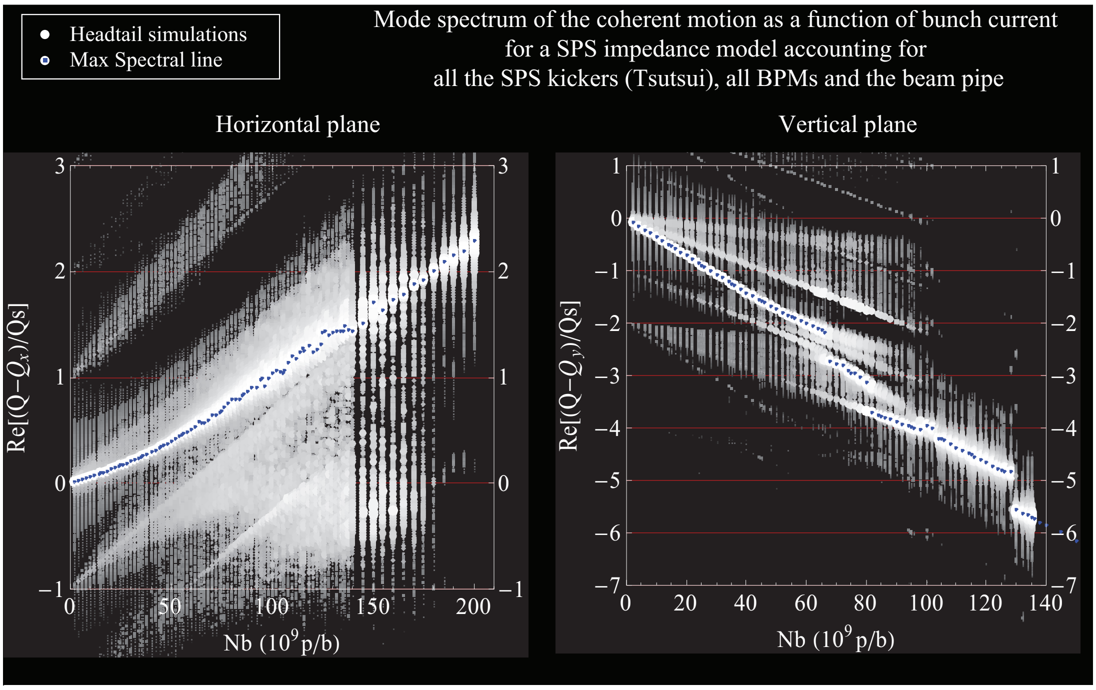

Figure 6.22: Simulated horizontal (left) and vertical (right) mode spectra of the coherent motion as a function of bunch population for a Tsutsui impedance model accounting for all SPS kickers. Simulated mode spectra are displayed using white dots, whose size and brightness are both non-linear functions of their spectral amplitude (bigger brighter dots have a higher amplitude than smaller darker dots). For each bunch population, the main spectral line is indicated by a blue spot.

2008 to try and gather observables that could give useful information on the impedance of the SPS, and its contributors. These measurements have been possible thanks to the collaboration of many colleagues from the operation, instrumentation, radio frequency and beam physics groups.

6.3.1 Measurement Setup

As mentioned in Chapter 2.2, the LHC injector complex is composed of several machines and transfer lines amounting to thousands of magnetic and electrical elements that need to be individually tuned to obtain the desired measurement conditions. The machines and their parameters are constantly changing due to e.g. physical parameter drifts, replacement of hardware, needed change of beam parameters, reset of servers. In these conditions, exactly reproducing the measurement conditions of an experiment from one day to the next is an illusion.

Beam Parameters

Single bunches of protons with LHC nominal parameters – apart from a low longitudinal emittance ($\varepsilon_l = 0.16$ eV.s) – were prepared by the PS complex and injected into the SPS. The bunch intensity was varied by applying vertical shaving in the PS Booster. Such a scan is shown in Fig. 6.23. The main parameters used for these measurements are summarized in Tab. B.6.

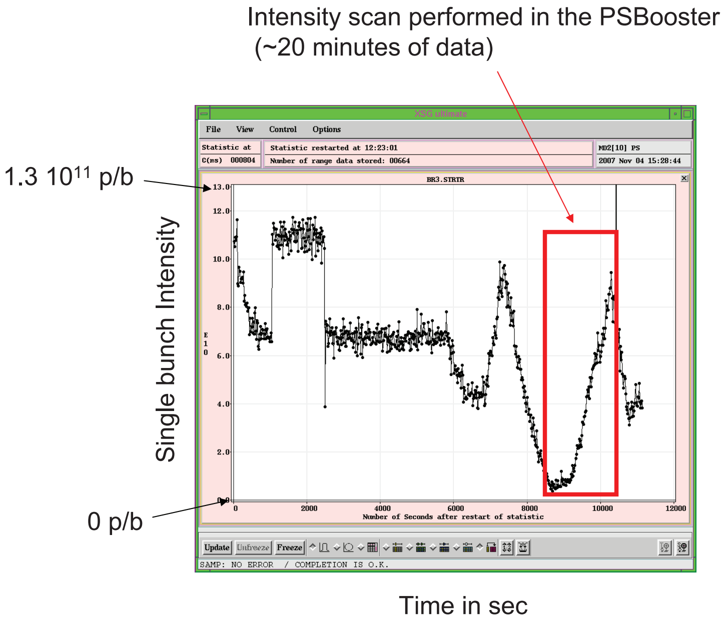

Intensity scan performed in the PSBooster (~20 minutes of data)

Statistic at
C(ms) 000804
Statistic restarted at 12:23:01
Number of range data stored: 00664
MD2[10] PS
2007 Nov 04 15:28:44

SAMP: NO ERROR / COMPLETION IS O.K.

Figure 6.23: Screen capture from a CCC operation console on which the PSB operator could monitor the bunch intensity sent to the PS. An intensity scan, of which results will be presented in the following paragraphs, is framed in red.

Machine Parameters

The machine had to be as linear as possible to prevent damping and spreads, which push the instability threshold to high intensities and prevent clear observation of the modes in *HEADTAIL* simulations. As a consequence, the linear chromaticity in the vertical plane was measured and corrected to very small positive values using the sextupole magnets ($\xi_y \approx 0.05$). Both chromaticities however should always remain positive during the measurements to prevent the onset of another type of instabilities (the Head-tail instability). Another significant source of spread is the detuning with amplitude. Detuning with amplitude leads to strong damping of coherent oscillations even at very low bunch currents, and this is why we tuned the octupole magnets to maximize the coherence time after which the coherent oscillations generated by a kick are damped. We also tried to minimize linear coupling by fine tuning the skew quadrupole magnets to reduce as much as possible the peak of the horizontal tune in the vertical BPM signals. Finally, the longitudinal matching of the bunch to the SPS RF bucket by changing the RF voltage is crucial to the success of these measurements. An improper longitudinal matching results in filamentation and longitudinal emittance blow up that perturbs the onset of the instability. Unfortunately, the complex RF gymnastics performed in the PS just before extraction leads to a strongly distorted longitudinal bunch shape, to which the RF bucket can not be matched by simply changing the RF voltage. This was in particular true during the measurement sessions in 2008.

Instrumentation

For these measurements in the SPS, we could monitor:

- the bunch current N_b with the SPS BCT for low currents (SPS.BCTDC.41435) which measures the bunch current every 10 ms (i.e. every 430 turns),
- the coherent motion $< y >$ in the horizontal and vertical planes with the SPS Qmeter system (the excitation was not used since the beam was already subject to a transverse kick at injection from the transfer line),
- the complex coherent motion $< y > +j < p_y >$ for *SUSSIX* Fourier analysis with the 2 pickups of the BBQ system [143],
- the longitudinal bunch distribution with the wall current monitor,
- the transverse motion over the longitudinal bunch distribution was recorded with the Head-Tail monitor [144] or the directional couplers [145].

6.3.2 Measurement Results

The results of measurements performed on November 4^{th} 2007 are presented here. We first checked that the observations already made in 2003 and 2006 could be reproduced [142].

Effect of Vertical Chromaticity at Maximum Bunch Population

For the maximum injected current (more than 1.2 10^{11} p/b), bunches were injected with different vertical chromaticity settings, and fast severe losses could be observed unless the chromaticity was increased over $\xi_y = 0.52$, as could be measured with the SPS BCT in Fig. 6.24. As already mentioned in [142], this is a first signature of a TMCI.

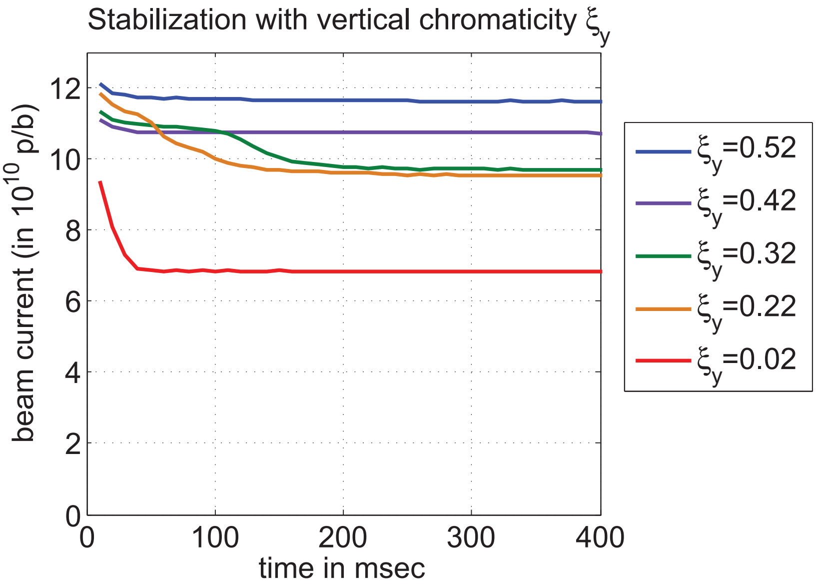

Figure 6.24: BCT measurements of the current of a single bunch injected in the SPS as a function of time after injection for different chromaticity settings.

Travelling Wave Pattern along the Bunch

The vertical Delta signal of the SPS Head-Tail monitor revealed a traveling wave pattern along the bunch for low vertical chromaticity, and the instability could be avoided if the SPS vertical chromaticity was increased (see successive acquisitions of the Head-Tail monitor for non consecutive turns in Fig. 6.25). These traveling wave patterns at low chromaticity are also typical of TMC instabilities.

Effect of Bunch Population at Low Vertical Chromaticity

Setting the chromaticity to a low but positive value ($\xi_y = 0.02$), the bunch population was varied from a few 10^9 p/b to 1.2 10^{12} p/b in the PS Booster as shown in Fig. 6.23. The resulting evolution of bunch current as a function of time after injection are presented in the left graph of Fig. 6.26. For $N_b \in [1;6]$ 10^{10} p/b, negligible losses are visible : the bunch motion is stable. For $N_b \in [6; 6.3]$ 10^{10} p, slow proton losses occur. However, for $N_b \in [6.3; 7.6]$ 10^{10} p, the bunch motion becomes again stable. Finally, for $N_b > 7.5$ 10^{10} p, fast heavy losses occur. It should be noted that the first point measured by the SPS Beam Current Transformer (BCT) is performed 10 ms after injection, and not right at injection. Beam losses may then have occurred before the first measurement point. As found in *HEADTAIL* simulations discussed in section 6.2.3, a threshold for a slow instability is

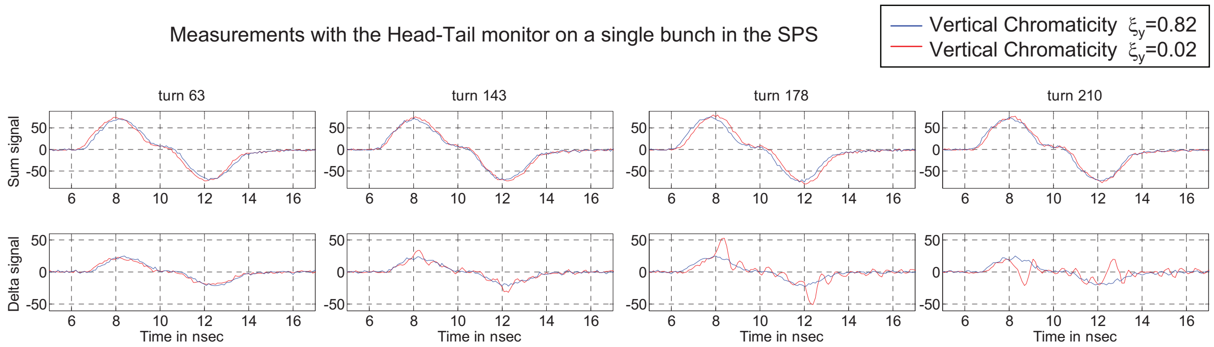

Figure 6.25: Measurement of the transverse sum signal (top) and delta signal (bottom) along the longitudinal bunch distribution at turns 63, 143, 178 and 210. The sextupoles were set to have a high chromaticity (≈ 0.82) in blue, and a low chromaticity (≈ 0.02) in red.

followed by a stable range, and finally by a threshold for a fast instability. In order to compare the measured and simulated losses, the Zotter/Métral model of the SPS kickers was used as SPS impedance model for *HEADTAIL* simulations with losses. Single-kick *HEADTAIL* simulations were performed, in which macroparticles are lost if their distance from the beam pipe axis gets over 2 cm (approximating the position of the vacuum chamber). The bunch population over the simulated 10,000 turns (i.e. 230 ms) is presented in the right graph of Fig. 6.26. It should be reminded that this SPS impedance model is coarse and many contributors were not included. This comparison is then not relevant quantitatively. Besides, *HEADTAIL* simulations do not take into account space charge, amplitude detuning and other stabilization mechanisms which may damp instabilities in the machine, and therefore reduce the bunch population ranges for which the beam is unstable. Nevertheless, as in *HEADTAIL* simulations, measurements show that a threshold for a slow instability is followed by a stable range, and finally by a threshold for a fast instability. The fact that this rather unusual instability pattern can be explained by coupling/decoupling mechanisms is another argument for a TMCI.

Instability Growth Rates

The coherent motion acquired by the BBQ (or the Qmeter) enable to assess the growth rates of potential instabilities, as shown in Fig. 6.27. It was already mentioned that computing the simulated growth rates can be tricky when several phenomena act together on the bunch motion. In simulations, some damping terms and the time taken for the instability to develop were perturbing the accuracy of the growth rate calculations. With measurements, several other mechanisms worsened the situation:

- non zero chromaticity generating periodic coherence and recoherence of the envelope of the bunch coherent motion,
- strong transverse injection oscillations affecting the first 50 turns after injection,
- imperfect longitudinal matching generating longitudinal dipolar oscillations, and sometimes additional strong distortions of the longitudinal bunch shape.

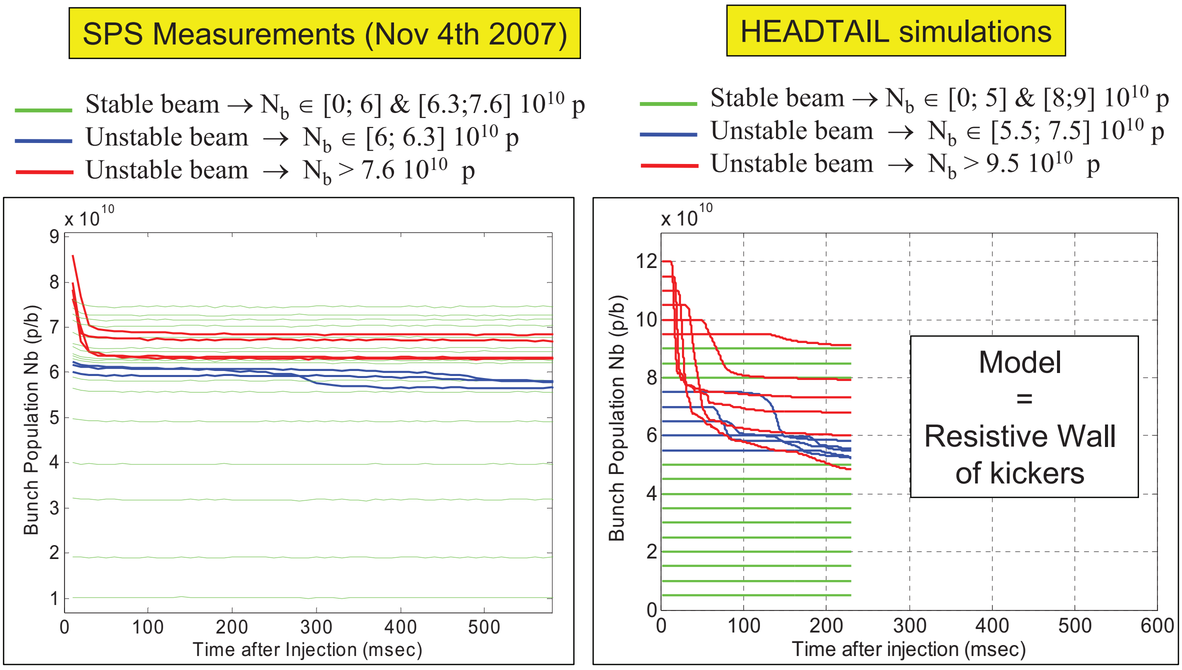

Figure 6.26: Bunch population measured by the SPS BCT for various cycles, SPS parameters $\varepsilon_l = 0.16$ eV.s, $\sigma_t = 0.7$ ns, and $\xi_y \approx 0$ (left), simulated with *HEADTAIL* for $\varepsilon_l = 0.16$ eV.s, $\sigma_t = 0.5$ ns, and $\xi_y = 0$ (right). Low bunch currents lead to stable bunch motion (in green). In both simulations and measurements, two distinct unstable ranges (slow instability in blue and fast instability in red) are separated by a stable range of bunch population (in green).

- in case of losses, the number of particles in the bunch is not constant and both the tune and the growth rate will be strongly perturbed after the first losses occur.

For all these reasons, we rely only on the 200 to 300 turns that lie between the end of the injection oscillations and the first maximum of the coherent motion to compute the growth rate (shown in red in Fig. 6.27). This method to compute growth rates can now be computed for both the measurements and for the Zotter/Métral model of the SPS kickers that was used as SPS impedance model for *HEADTAIL* simulations. The comparison of simulated and measured growth rates calculated for these 200 turns immediately following the injection oscillations is shown in Fig. 6.28. A very similar - however shifted in N_b – sharp growth rate decrease before the onset of the main instability can be observed. The shift can be explained by the coarse impedance model, which only takes into account the SPS kickers. As a consequence, the TMC typical pattern of stable and unstable ranges predicted by the *HEADTAIL* simulations, is observed right after injection with the BBQ, and later with the BCT.

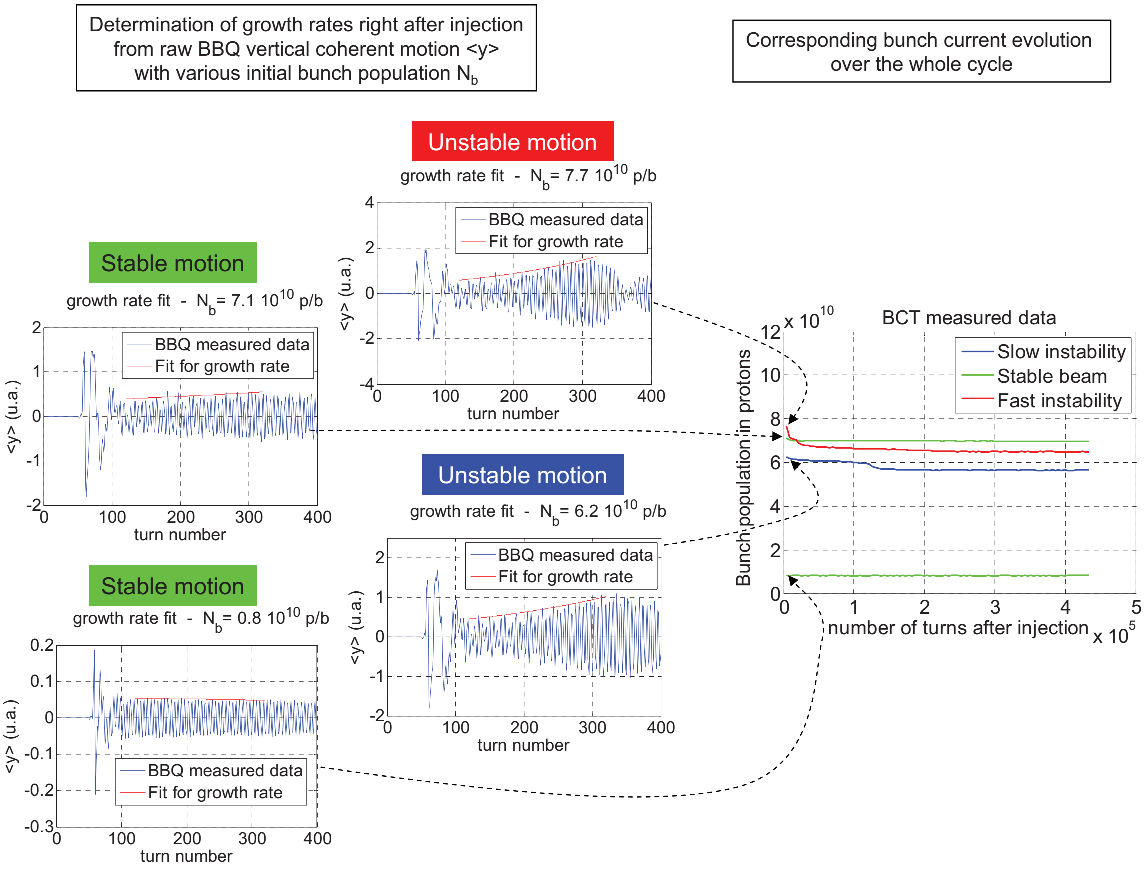

Figure 6.27: For each of the supercycles (only four examples shown here) corresponding to the BCT data on the left, the BBQ data is plotted (in blue) together with the exponential fit to obtain the initial growth rate (in red).

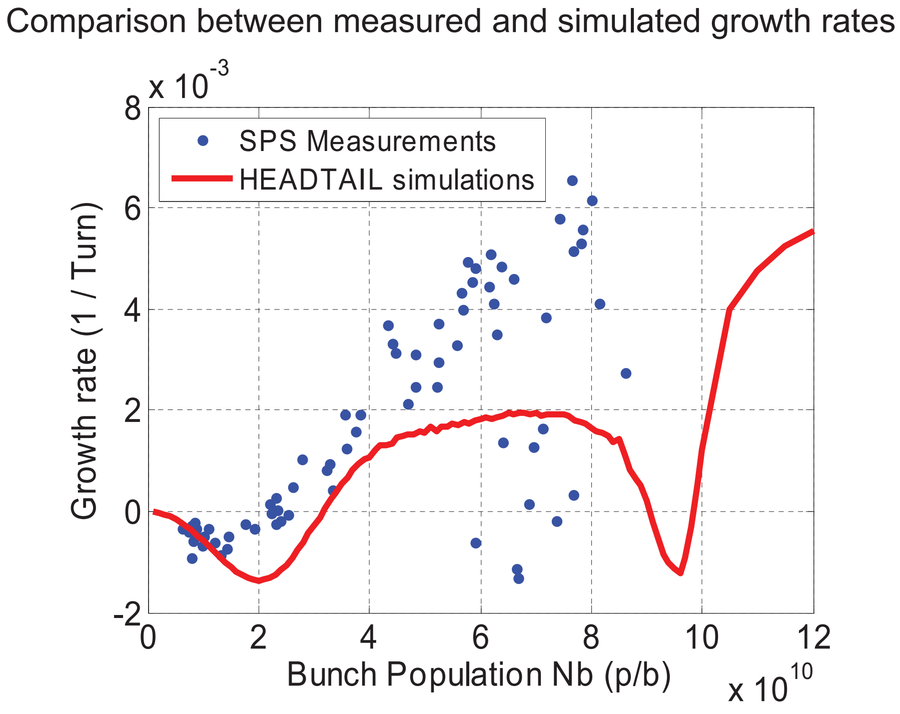

Figure 6.28: Comparison of growth rate vs. bunch population N_b for a 2007 SPS experiment (blue dots) and *HEADTAIL* simulations for the 20 2006 SPS kickers (red line). The simulated SPS model only accounts for the 20 SPS kickers (Zotter/Métral model).

Tune Shift, Tune Step and Mode Spectra

The vertical coherent motion picked up by the 2 BBQ in two different locations were Fourier analyzed with SUSSIX to obtain the tunes and similar mode spectra as the ones presented in Section 6.2. The measured mode spectra are presented in Fig. 6.29. For the same reasons mentioned above for the growth rate calculations, we limited the Fourier analysis to a very small number of turns after injection (256 turns), thereby strongly reducing the accuracy of the frequency analysis. As can be seen in Fig. 6.29, the mode spectrum is much noisier than in simulations, and more difficult to interpret. For low bunch intensities $N_b < 2\ 10^{10}$ p/b, strong spectral lines can be observed clustered around many azimuthal modes around mode 0 at low frequency. As we can see in Section C.1 in the appendix, this could be an indication of non zero chromaticity. It is interesting to note that the main spectral lines are carried by the mode 0, while the second peaks are carried exclusively by mode 1. As current increases, the tune shifts down and is subject to more spread. Around $N_b = 4\ 10^{10}$ p/b, the second main line is now carried by mode -1 and by the spectral line corresponding to the horizontal tune Q_x (outside the graph), which is a sign that the linear coupling was not perfectly corrected. For $N_b > 5\ 10^{10}$ p/b, the main line's shift slows down and seems to be carried alternatively by mode 0

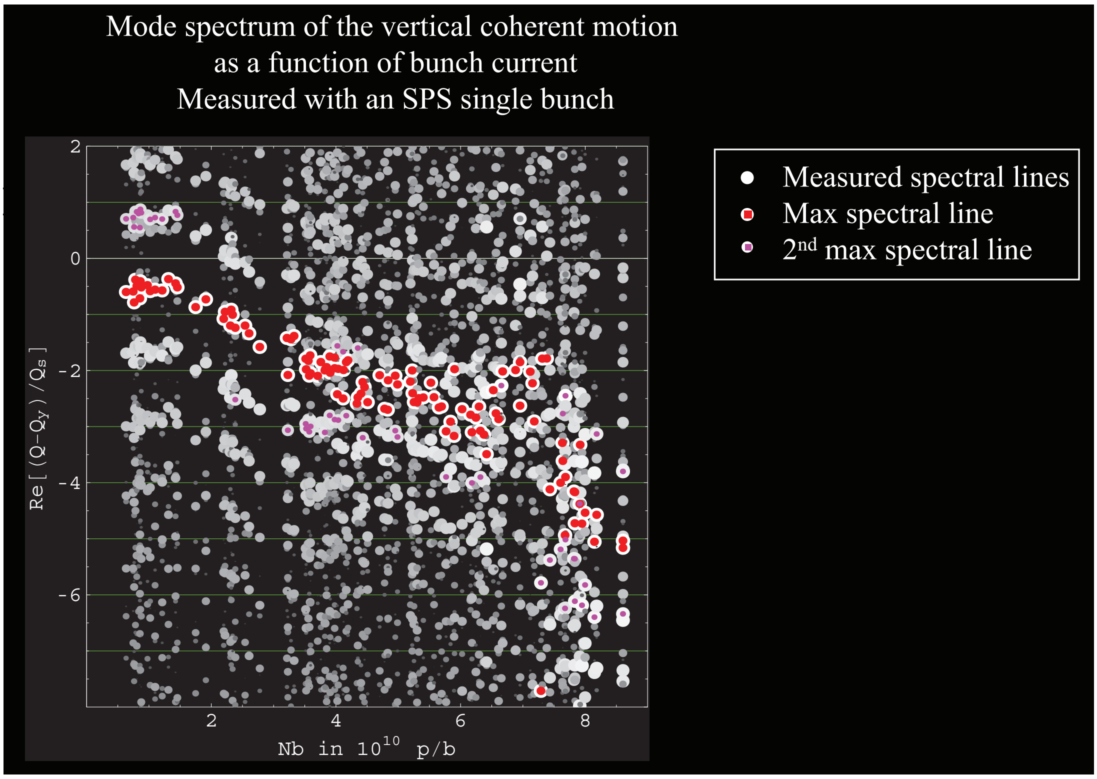

Figure 6.29: Measured mode spectra of the vertical coherent motion as a function of bunch current. The coherent motion as measured by the BBQs was post-processed with SUSSIX and displayed using white dots, whose size and brightness are both a linear function of their spectral amplitude (bigger brighter dots have a higher amplitude than smaller darker dots). For each bunch population, the main spectral line is indicated by a red spot, and the second main spectral line is indicated by a magenta spot.

and another mode above it. Between N_b =6.5 and 7.5 10^{10} p/b, the main mode does not carry significant spectral power. After N_b = 7.5 10^{10} p/b, the main spectral line shifted to a mode lower than mode 0, most likely a combination of modes -1 and -2. It is interesting to notice that the second line is then carried consistently by an even lower mode or combination of mode, that could be modes -2 and -3. Although very noisy, this measured mode spectrum shows similar qualitative behavior to the simulated mode spectrum shown in Fig. 6.13 and Fig. 6.17: the main spectral line is mode 0, it shifts quickly down with increasing current, before it slows down, and becomes smaller than other modes above or below it, leading to damping. Finally, when a certain current threshold is reached a coupling between modes -1 and -2 or -2 and -3 drives the instability. Qualitatively, we compare in Fig 6.30 the main spectral lines from measurements and simulations of the bunch interacting with the impedance of SPS kickers computed with the Zotter/Métral formalism. As already mentioned for the full mode spectra, the main

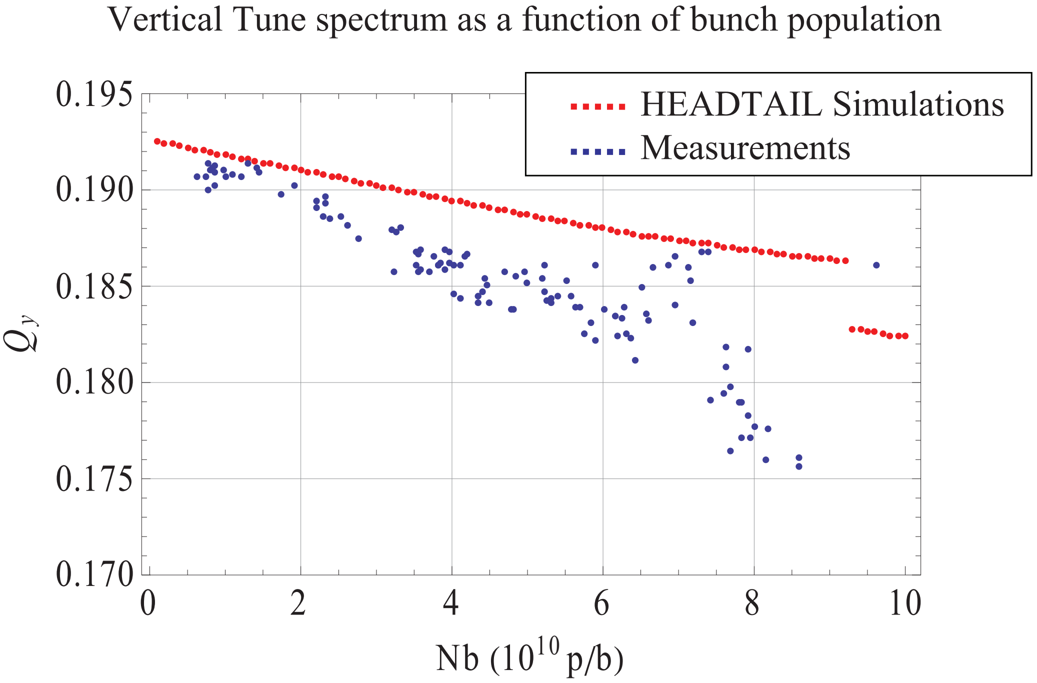

Figure 6.30: Comparison of bunch main spectral line vs. bunch population for SPS measurements in 2007 (blue dots) and *HEADTAIL* simulations for the 20 2006 SPS kickers computed with the Zotter/Métral model (red dots). The simulated tune data was normalized by the ratio of the experimental to simulated bunch length data to be able to compare the tune slopes.

spectral line seems to be subject to the same tune step when the instability threshold is met, both in the experiment and the simulation. The tune slope with intensity and the instability threshold differ between experiment and simulations. This is expected as this coarse impedance model only takes into account the SPS kickers. The observables that can be obtained from these measurements are summarized in Tab. 6.3. All these observations are not yet proofs, but these accumulated similitudes with a TMCI are giving more weight to the hypothesis that this fast vertical SPS instability is a TMCI. In addition to these

Observable	Measurements
Horizontal effective impedance Z_x^{eff}	-2.6 MΩ/m
Vertical effective impedance Z_y^{eff}	20.3 MΩ/m
Horizontal instability threshold $N_{b,x}^{th}$	not observed
Modes involved in horizontal instability	N/A
First vertical instability threshold $N_{b,y}^{th\ (1)}$	6 10^{10} p/b
Modes involved in first vertical Instability	0 and ?
Intermediate stable region	6 to 6.3 10^{10}
Second vertical instability threshold $N_{b,y}^{th\ (2)}$	7.6 10^{10} p/b
Modes involved in second vertical Instability	-1 and -2 and ?
Damping of coherent oscillations	yes
Chromaticity threshold for damping instability at 1.2 10^{11} p/b	0.42

Table 6.3: Summary of beam dynamics observables measured at injection in the SPS. The effective impedances are estimated with the Sacherer formula for the mode 0 assuming a Gaussian bunch [46].

measurements at injection, other types of measurements in the SPS have been used to gain access to transverse impedance observables:

- The growth/decay rate of the coherent transverse oscillations as a function of chromaticity enables to scan different ranges of frequencies of the dipolar impedance contributions. An example of such a measurement in the SPS was presented in Ref. [146].

- The measurement of the phase advance at each of the 202 SPS BPMs enable to reconstruct the average phase advance along the machine for several single bunch populations. An impedance source at a given location should perturb the expected phase advance at this location, and that perturbation should increase with intensity. Comparing the measured phase advance along the machine for various bunch intensities with the expected phase advance extracted from *MADX* should allow localizing significant impedance sources. An algorithm for reconstruction was described in Ref. [147] and results of measurements as well as comparisons with *HEADTAIL* simulations are reported in [148].

- The transverse impedance of the SPS can also be studied by injecting a single long bunch into the SPS, and observing its debunching without RF. Longer bunches allow for higher frequency resolution of the longitudinal and transverse bunch spectra acquired with strip line couplers connected to a fast data acquisition. It also gives access to the frequency content of the transverse impedance. Results from measurements with short and long bunches in the SPS performed in 2008 were compared with simulations in Ref. [149].

In addition to including the impedance contribution of more SPS elements into the SPS impedance model, it will be important to study in detail more realistic macroparticle simulations accounting for direct space charge, chromaticity, detuning with amplitude and the injection of a longitudinal and transverse bunch distributions similar to the longitudinal and transverse bunch distributions injected from the PS. These simulations should improve our understanding of the outcome of measurements with the SPS beam, and enable a more efficient tuning of the machine and beam parameters during the measurement sessions.

Chapter 7

Conclusions

This thesis work brought new contributions to the theory, simulation and measurement of the beam coupling impedance and its effect on the beam dynamics applied mainly to the case of the CERN SPS but also the crucial issue of the LHC collimator impedance.

New RF bench measurements of the impedance at low frequency of the LHC collimators validated the transverse impedance theory developed by B. Zotter and E. Métral, which predicts a vanishing real part of the transverse impedance when the frequency tends to 0.

A new formula for the longitudinal impedance of an infinitely long cylindrical beam pipe made of an arbitrary number of layers of homogeneous materials of any type in all ranges of frequencies for any bunch velocity was presented and implemented.

A new expression for the horizontal and vertical quadrupolar impedances of simple models of kickers was derived in the frame of Tsutsui's formalism. The successful benchmark of both the theoretical transverse dipolar impedance contributions computed by H. Tsutsui and these new theoretical transverse quadrupolar impedance contributions with 3D *CST Particle Studio* EM simulations for the parameters of the SPS kickers enables us to be more confident with (1) the new theoretical quadrupolar expressions derived in this manuscript, (2) the time domain *CST Particle Studio* simulations of simple geometries made of ferrite, and (3) the procedure to obtain the dipolar and quadrupolar contributions of the beam impedance in time domain simulations. Compared to contributions classically obtained from the circular beam pipe transformed into a flat chamber with the Yokoya factors, the quadrupolar wake contributions for the SPS kickers are much larger. This larger quadrupolar wake contribution leads to different beam dynamics observables simulated with *HEADTAIL*; in particular a positive horizontal coherent tune shift, a strong damping of the transverse coherent oscillations, and a higher intensity threshold. *CST Particle Studio* simulations of the SPS BPMs impedance with more complicated geometries were also performed and successfully benchmarked with dedicated RF bench measurements. An upgrade of the *ZBASE* impedance database is ongoing and allowed to add these transverse wake contributions of the SPS kickers and BPMs to the theoretical wake calculations of the beam pipe and produce the total transverse dipolar and quadrupolar wakes for the current SPS impedance model.

A successful benchmark was performed between *MOSES* mode coupling formalism and the macroparticle simulation code *HEADTAIL* in predicting a Transverse Mode Coupling Instability between azimuthal modes -2 and -3. The code was modified to take independent transverse dipolar and quadrupolar wakes as inputs of macroparticle simulations and the results for the implemented SPS impedance model was presented and compared with dedicated measurements of the fast instability at injection in the SPS machine. Unavoidable measurement noise prevented us from observing clearly the small sidebands of interest before the onset of the instability, and mode coupling was not observed in the measurements. However, the many similitudes observed between features of the *HEADTAIL* simulations predicting a TMCI at injection in the SPS and the measurements performed with the SPS beam give more weight to the hypothesis that the fast instability limiting the single bunch current at injection in the SPS is indeed a TMCI.

Further comparison of the coherent tune shifts and instability thresholds confirm that the SPS model consisting of the SPS beam pipe, kickers and BPMs presented in this work is still missing a contribution amounting to 30% to 40% of the total SPS impedance. Electromagnetic simulation and bench measurement campaigns will therefore be performed in the near future to understand which components can be responsible for this remaining impedance contribution. Additional suspected components (e.g. pumping ports, RF cavities, instrumentation) but also a bad matching of the external circuits for the kickers and BPMs are currently studied and will be imported into *ZBASE*.

Finally, this work presented the general framework of *ZBASE*, applying all steps from the impedance calculation, simulation or measurement of single elements to the integration of all contributions into a global model accounting for all elements, and finally to comparison between macroparticle simulations using this global impedance model and beam measurements. This general framework is in place and will now be implemented to all accelerators at CERN in order to be able to improve the performance of the CERN LHC complex for particle physics experiments.

Appendix A

Glossary

A.1 Units

The International System (SI) of Units has defined seven base units, which are used to define all other SI units [150].

- m : Meter (SI unit of distance),
- kg : Kilogram (SI unit of mass),
- s : Second (SI unit of time),
- A : Ampere (SI unit of intensity),
- K : Kelvin (SI unit of temperature),
- mol : Mole (SI unit of quantity of substance),
- cd : Candela (SI unit of luminous intensity),

All the following units can be therefore obtained as a combination of these base units.

- J : Joule (SI unit of energy) [J] = [kg.m^{2}.s^{-2}],
- W : Watt (SI unit of power) [W] = [kg.m^{2}.s^{-3}],
- F : Farad (SI unit of capacitance) [F] = [s^{4}.A^{2}.m^{-2}.kg^{-1}],
- V : Volt (SI unit of voltage) [V] = [m^{2}.kg.s^{-3}.A^{-1}],
- C : Coulomb (SI unit of charge) [C] = [A.s],
- H : Henry (SI unit of inductance) [H] = [m^{2}.kg^{2}.s^{-2}.A^{-2}],
- T : Tesla (SI unit for magnetic field strength) [T] = [kg.A^{-1}.s^{-2}],
- °C : Degree Celsius (alternate unit for temperature) $[°C] = [K - 273.15]$,
- eV : Electron-Volt (alternate unit of energy) 1 eV = 1.6 10^{-19} J,
- eV/c : eV over c (alternate unit of momentum) 1 eV/c=5.34 10^{-28} kg.m.s^{-1},
- eV/c^2 : eV over c^2 (alternate unit of mass) 1 eV/c^2=1.78 10^{-36} kg,
- b : barn (common unit of cross section) 1 b =10^{-}28 m^{2},
- fb^{-}1 : inverse femtobarn (count of particle collision events over a given period of time),

A.2 Physical Constants

- c : speed of light $c = 3.000\ 10^8$ m/s,
- m_e : electron rest mass $m_e = 511$ keV$/c^2$,
- m_p : proton rest mass $m_p = 0.938$ MeV$/c^2$,
- e : proton charge $e = 1.60\ 10^{-19}$ C,
- ε_0 : vacuum permittivity $\varepsilon_0 = 8.85\ 10^{-12}$ F/m,
- μ_0 : vacuum permeability $\mu_0 = 4\pi 10^{-7}$ H/m,
- Z_0 : vacuum impedance $Z_0 = \mu_0 c = \frac{1}{\varepsilon_0 c}$ in Ω.

A.3 Physical Quantities

A.3.1 Particle Coordinates in Phase Space

- x : horizontal position in m,
- y : vertical position in m,
- x' : horizontal angle in rad,
- y' : vertical angle in rad,
- s : curvilinear longitudinal position along the design orbit in m,
- θ : angular position in rad,
- ϕ : phase of the particle with respect to the phase of the RF cavity ϕ_{RF}.

A.3.2 Single Particle Dynamics and Machine Parameters

- α_{cp} : momentum compaction factor,
- $\alpha_{x,y}$: optics parameter defined from the derivative of the beta function,
- β : particle relativistic velocity factor $\beta = v/c$ (no unit),
- $\beta_(x, y)$: horizontal (resp. vertical in m.rad) beta function in m,
- $D_{x,y}$: horizontal (resp. vertical) dispersion in m,
- E_t : particle total energy in eV,
- $\mathcal{E}$: particle total energy in eV (notation for Section 3.2.2),
- $\varepsilon_{x,y}$: horizontal and vertical r.m.s. bunch emittances in πm.rad,
- $\varepsilon^{95\%}_{x,y}$: horizontal and vertical phase space ellipse that contains 95% of the ellipse trajectories of all particles in πm.rad,
- $\varepsilon^{N}_{x,y}$: horizontal and vertical normalized emittance in πm.rad,

- ε_z : longitudinal bunch emittance in m.rad,
- f_{rev} : revolution frequency of the particle in Hz,
- F : Lorentz force on the particle in N,
- ϕ_{RF} : phase of the RF voltage in rad,
- g: cavity gap in m,
- γ : particle mass relativistic factor $\gamma = (1 - \beta^2)^{-1/2}$ (no unit),
- γ_t : relativistic factor at transition (no unit),
- $\gamma_{x,y}$: optics parameter defined from the beta function and its derivative in 1/m,
- h: harmonic number (no unit),
- η : slip factor (no unit),
- I_b : bunch current in A ($I_b = N_b e f_{rev}$),
- $\kappa_{x,y}$: horizontal (resp. vertical) wavenumber in 1/m,
- L: orbit length in m ,
- $\mathcal{L}$: luminosity commonly expressed in cgs units (cm$^-$2.s$^-$1) or (b.s$^-$1),
- N_b : bunch population in particles per bunch (p/b),
- ω_0 : revolution angular frequency in rad.s^{-1},
- ω_β : betatron angular frequency in rad.s^{-1},
- ω_s: synchrotron angular frequency in rad.s^{-1} ,
- p : particle momentum, for the particle in eV/c,
- Q_s: synchrotron tune (no unit),
- $Q_{x,y}$: horizontal (resp. vertical) tune (no unit),
- R_0: radius of the design orbit in m,
- σ_t : r.m.s. longitudinal bunch “length” in s,
- $\sigma_{x,y,z}$: r.m.s. horizontal (resp. vertical, longitudinal) bunch sizes in m,
- ρ : radius of curvature of the particle in m,
- T: transit time factor (no unit),
- v : particle velocity in m/s (in general $v \approx v_s$),
- v_s : longitudinal particle velocity in m/s ,
- V: RF voltage in V,
- $\hat{V}$: effective RF voltage ($\hat{V} = TV$) in V,
- $\xi_{x,y}$: horizontal (resp. vertical) chromaticity,
- $\psi_{x,y}$: horizontal (resp. vertical) phase advance in rad.

A.3.3 Electromagnetic Quantities

- $\vec{B}$: magnetic field (also called magnetic induction or magnetic flux density) (in T),
- $\vec{D}$: electric displacement field ($\vec{D} = \varepsilon\vec{E}$) in C/m^2,
- δ : skin depth in m.
- $\vec{E}$: electric field in V/m,
- ε : real permittivity of a material in F/m,
- ε_c : complex permittivity of a material ($\varepsilon_c = \varepsilon + \sigma/(j\omega)$ no unit) in F/m,
- $\hat{\varepsilon}_r$: real relative permittivity of a material ($\varepsilon = \varepsilon_0\hat{\varepsilon}_r$ no unit),
- ε_r : relative complex permittivity of a material ($\varepsilon_r = \varepsilon_r/\varepsilon_0 = \varepsilon_r' - j\varepsilon_r''$ no unit),
- $\vec{H}$: magnetic field strength, also called magnetic field intensity or magnetizing field, ($\vec{B} = \mu\vec{H}$) in A/m,
- μ : permeability of a material in H/m,
- μ_r : relative complex permeability of a material ($\mu_r = \mu/\mu_0 = \mu_r' - j\mu_r''$),
- μ_i : initial permeability of a material,
- ρ : resistivity of a material in Ω.m,
- ρ_{DC} : DC resistivity of a material in Ω.m,
- σ : conductivity of a material in Ω^{-1}.m^{-1},
- τ : electron relaxation time of a material in s,
- τ_μ : magnetic relaxation time of a material,

A.3.4 Beam Coupling Impedance Quantities

- $X_{//}$ (or X_{long}): longitudinal quantity X, where $X = Z$ (in Ω), W or G (in V/C),
- $X_\perp$ (or X_{trans}): transverse quantity X, normalized to the beam or source displacement, where $X = Z$ (in Ω/m), W or G (in V/(Cm)),
- X^{dip} : dipolar contribution of quantity X,
- X^{quad} : quadrupolar contribution of quantity X,
- X^{tot} : total contribution of quantity X (in a linear approximation $X^{tot} = X^{dip} + X^{quad}$),
- f_{res} : Resonator frequency (longitudinal or transverse) in Hz,
- G : wake function in V/C or V/(Cm),
- J : source beam current density,
- L : device length in m,
- ρ : source beam charge density,

- Q (in the context of impedance calculation): source beam total charge in C,
- Q (in the context of resonator impedance model) : resonator quality factor (no unit),
- R_s : resonator shunt impedance (longitudinal in Ω and transverse in Ω/m),
- W : wake potential in V/C or V/(Cm),
- Z : beam coupling impedance in Ω or Ω/m.

A.3.5 Collective Effects Quantities

- D : transverse dipole displacement of the distribution,
- $\langle Iy \rangle$: dipole moment of the distribution,
- Ω : angular frequency shift to be found,
- ω_ξ : chromatic angular frequency shift,
- Ψ : distribution function,
- ρ : longitudinal charge distribution,
- $\tilde{\rho}$: Fourier Transform of the longitudinal charge distribution,
- τ (in the context of mode coupling formalism): quasi-time in s,
- τ (in the context of instabilities): coherent instability rise time in s,
- u : normalized transverse displacement.

A.4 Useful Definitions in the Context of this Manuscript

- Aperture: part of the phase space in which the particles should remain in order not to be lost against the surrounding beam pipe.
- Beam: ensemble of all accelerated particles traveling in the machine.
- Beam pipe: pipe in which the beam circulates (also called vacuum chamber).
- Beam position monitor: accelerator instrumentation that measures the position of the beam.
- Beta function: envelope around all transverse particle trajectories in an accelerator.
- Broadband resonator impedance model: theoretical impedance model that describes an impedance with a single resonance.
- Bucket: part of the longitudinal phase space in which the particles are grouped together by the RF cavities.
- Bunch: group of accelerated particles traveling together in distinct RF buckets. The beam is composed by the total number of bunches circulating at a given time in the machine.
- Chromaticity: relative change of tune generatad by a relative change of momentum.

- Closed orbit: trajectory of the particles that closes on itself after one turn. Due to errors, the closed orbit does not in general coincide with the design orbit.
- Coherent : attribute of the motion of the center-of-mass of the bunch of particles.
- Collimator: accelerator element consisting of jaws that interecept particles on unwanted trajectories.
- Design orbit: ideal trajectory of the particles in the machine.
- Dispersion: deviation trajectory of an off-momentum particle from the design orbit
- Emittance: area covered by the particle distribution in phase space
- Incoherent : attribute of the motion of individual particles within the bunch.
- Instability (coherent): growing coherent motion leading in general to particle losses against the beam pipe. Coherent instabilities can also be damped by several mechanisms before losses occur.
- Kick : integrated effect of an external force on a particle.
- Kicker: magnets that switch on just long enough to kick the particles off their trajectory (towards a beam line, a dump, a transfer line), or to excite coherent oscillations to measure the tune.
- Luminosity: rate of collision events that can be recorded within a particle detector.
- Macroparticle : group of particles modelled together as a single simulated particle in order to allow full beam simulations.
- Mode : harmonics of the frequency spectrum of the bunch coherent motion. For transverse single-bunch motion, there are two degrees of freedom and hence two sets of bunch coherent modes: the azimuthal modes differ in betatron frequency and the radial modes differ in amplitude in synchrotron phase space. The radial modes are clustered by azimuthal modes at low bunch currents and they separate as current increase and may couple.
- Momentum compaction factor: relative change of orbit circumference generated by a relative change of momentum.
- Orbit: physical trajectory of a particle in the machine.
- Phase advance: fraction of betatron oscillation performed between two points along the closed-orbit.
- Phase space (longitudinal): Coordinate system used to define both the particle longitudinal position z in the accelerator and its momentum deviation Δp.
- Phase space (transverse): Coordinate system used to define both the particle transverse position (x or y) in the accelerator and its transverse angle(x' and y').
- Quench: Brutal loss of superconductivity of a material resulting in a rapid rise in resistance, ohmic losses and temperature.
- Resistive-Wall impedance: impedance contribution due to the interaction of the particles with a resistive wall, from which the indirect space charge impedance is subtracted.

- Skin depth: average width of penetration of electromagnetic fields in a conductor.
- Slip factor: relative change of angular frequency generated by a relative change of momentum.
- Space charge impedance (direct): impedance contribution due to the interaction of the particles with themselves.
- Space charge impedance (indirect): impedance contribution due to the interaction of the particles with a perfect conducting wall.
- Synchrotron tune: number of synchrotron oscillations in the longitudinal plane performed per turn,
- Tune: number of betatron oscillations in the transverse plane performed per turn (also called betatron tune),
- Transition : particular situation for which the particle energy is such that the slip factor becomes zero.
- Wall impedance: impedance contribution due to the beam pipe wall, including both the indirect space charge impedance and the resistive wall impedance.
- Yokoya factors: form factors derived by Laslett for low frequency limit and extended to all frequencies by Yokoya. These form factors relate the impedance of a cylindrical geometry to the dipolar and quadrupolar impedance contributions of a flat chamber (see Tab. 5.1). The validity of the Yokoya factors is limited to the case of an ultrarelativistic beam in a longitudinally uniform beam pipe, and for which the skin depth is much smaller than the dimensions of the beam pipe and the thickness of the material.

A.5 Index of Acronyms

- BPH (BPV): Horizontal (Vertical) Beam Position Monitor.
- CERN: European Organization for Nuclear Research.
- CFC: Carbon Fiber Reinforced Graphite.
- CLIC: Compact Linear Collider.
- CTF3: CLIC test Facility.
- CNGS: CERN Neutrinos to Gran Sasso.
- CPU: Computer.
- DC: Direct Current; In this context DC refers to teh value of the quantity in the very low frequency limit.
- DFT (iDFT): Discrete Fourier Transform (inverse Discrete Fourier Transform).
- DUT: Device Under Test.
- EM: ElectroMagnetic.

- FFT: Fast Fourier Transform.
- GPIB: General Purpose Interface Bus.
- HGAP: Horizontal gap.
- IF (bandwidth): Intermediate Frequency.
- IP: Interaction Point.
- LAN: Local Area Network.
- LEIR: Low Energy Ion Ring.
- LEP: Large Electron Positron Collider.
- LHC: Large Hadron Collider.
- LINAC: Linear Accelerator.
- MKE: SPS Extraction Kicker Magnet.
- MKD: SPS Dump Kicker Magnet.
- MKP: SPS Injection Kicker Magnet.
- MKQ: SPS Tune Measurement Kicker Magnet.
- PEC: Perfect Conductor.
- PIM: Plug In Module.
- PS: Proton Synchrotron.
- PSB: Proton Synchrotron Booster.
- Re (Im): Real (Imaginary) part.
- RF: Radio Frequency.
- r.m.s.: Root Mean Square.
- SPS: Super Proton Synchrotron.
- TCS: LHC Secondary Collimator.
- TMCI: Transverse Mode Coupling Instability.
- VNA: Vector Network Analyzer.
- ZBASE: Impedance Database.
- 3D: 3 Dimensions.

Appendix B

Tables of Parameters

B.1 SPS Parameters at Injection

Parameter Name	Symbol	Value	Unit
Synchrotron tune	Q_s	$3.24\ 10^{-3}$	
Beam momentum	p	26	GeV/c
Revolution frequency	f_{rev}	43375.9	Hz
Momentum compaction factor	α_{cp}	$1.92\ 10^{-3}$	
Circumference length	L	6911	m
Lorentz factor	γ	27.7	
relativistic	β	0.9993	
Horizontal tune	Q_x	26.13	
Vertical tune	Q_y	26.18	m
average hor. beta function	$\langle\beta_x\rangle$	42.1	m
average vert. beta function	$\langle\beta_y\rangle$	42	m

Table B.1: SPS parameters for the LHC beam at injection.

B.2 SPS Kickers Parameters

Kicker name	s	β_x	β_y	a_x	a_y	L
MKQH.11653	524.6862	64.51628263	37.18936746	0.0575	0.01615	0.768
MKQV.11679	535.7712	33.88205276	70.08010989	0.051	0.028	1.133
MKDV.11731	550.619	25.67947335	88.27890912	0.0375	0.028	2.314
MKDV.11736	553.81	31.20930269	75.43638958	0.0415	0.028	2.314
MKDH.11751	556.021	35.78009206	67.27615428	0.048	0.028	1.28
MKDH.11754	557.92	40.18895848	60.74980054	0.048	0.028	1.28
MKDH.11757	559.819	45.04422676	54.66919838	0.0525	0.03	1.28
MKPA.11931	615.0954	26.32846707	85.78059522	0.05	0.0305	2.738
MKPA.11936	618.7174	32.83381238	71.58828026	0.05	0.0305	2.738
MKPC.11952	620.6964	37.06977126	64.51718449	0.05	0.0305	1.424
MKP.11955	624.3184	46.06987627	52.8262161	0.07	0.027	2.738
MKE.41631	3973.3482	91.97415903	24.04002731	0.07385	0.0175	1.658
MKE.41634	3975.6612	82.32638786	27.57688617	0.07385	0.0175	1.658
MKE.41637	3977.9742	73.3360295	31.77278931	0.0675	0.016	1.658
MKE.41651	3980.2872	65.00308396	36.62773673	0.0675	0.016	1.658
MKE.41654	3982.6002	57.32755122	42.14172842	0.07385	0.0175	1.658
MKE.61631	6277.1828	92.08511966	24.1173812	0.07385	0.0175	1.658
MKE.61634	6279.4958	82.42272904	27.70364897	0.07385	0.0175	1.658
MKE.61637	6281.8088	73.41858957	31.95318364	0.0675	0.016	1.658
MKE.61651	6284.1218	65.07270125	36.86598519	0.0675	0.016	1.658

Table B.2: Parameters for the SPS kickers in 2006: Kicker name, longitudinal coordinate along the accelerator s, beta functions at this location $\beta_x(s)$ and $\beta_y(s)$, horizontal aperture a_x, vertical aperture a_y and length of the ferrite L (in m). The thickness of the ferrite is assumed to be 6 cm for all kickers. It is important to note that all the kickers are designed to deflect the beam horizontally (i.e. the magnetic field is vertical and the ferrite blocks are aligned horizontally as in Fig. 5.15), apart from 3 vertical kickers (MKQV and MKDVs) which ferrite blocks are rotated by $\pi/2$ to produce a horizontal magnetic field. Extraction with *MADX* from the SPS aperture data. Magnetic length data obtained from Laurent Ducimetière (CERN/TE/ABT).

B.3 ***MOSES*** Calculation Parameters

Parameter Name	Symbol	Value	Unit
Beam momentum	p	26	GeV/c
Revolution frequency	f_{rev}	43375.9	Hz
Momentum compaction factor	α_{cp}	$1.92\ 10^{-3}$	
Betatron tune spread		0	
Synchrotron tune	Q_s	$3.24\ 10^{-3}$	
Average beta function	$\langle\beta_x\rangle = \langle\beta_y\rangle$	40	m
Linear chromaticity	$\xi_x = \xi_y$	0	
r.m.s. bunch length	σ_z	0.21	m
Resonator shunt impedance	R_s	10	MΩ/m
Resonator frequency	f_{res}	1	GHz
Resonator quality factor	Q	1	

Table B.3: SPS parameters for the LHC beam at injection used in *MOSES* calculations.

B.4 *HEADTAIL* Simulation Parameters

Parameter Name	Symbol	Value	Unit
Beam momentum	p	26	GeV/c
Revolution frequency	f_{rev}	43375.9	Hz
Momentum compaction factor	α_{cp}	$1.92\ 10^{-3}$	
Circumference length	L	6911	m
Lorentz factor	γ	27.7286	
Betatron tunes	Q_x / Q_y	26.185 / 26.13	
Synchrotron tune	Q_s	$3.24\ 10^{-3}$	
Average beta functions	$\langle\beta_x\rangle$ / $\langle\beta_y\rangle$	40 /40	m
Initial r.m.s. beam sizes	σ_x / σ_y	1.8 / 1.8	mm
Linear chromaticities	ξ_x / ξ_y	0 / 0	
Initial r.m.s. bunch length	σ_z	0.21	m
Initial r.m.s. longitudinal momentum spread	$\sigma_{\Delta p/p_0}$	$9.3\ 10^{-4}$	
Cavity harmonic number	h	4620	
Resonator shunt impedance	R_s	10	MΩ/m
Resonator frequency	f_{res}	1	GHz
Resonator quality factor	Q	1	
Initial kick amplitude		0.9	mm
Number of slices		500	
Number of macroparticles		10^6	
Longitudinal restoring force		linear	
Frozen wake field		yes	

Table B.4: SPS parameters for the LHC beam at injection used in *HEADTAIL* simulations.

B.5 *HEADTAIL* Simulation Parameters (Old Working Point)

Parameter Name	Symbol	Value	Unit
Beam momentum	p	26	GeV/c
Revolution frequency	f_{rev}	43375.9	Hz
Momentum compaction factor	α_{cp}	$1.92\ 10^{-3}$	
Circumference length	L	6911	m
Lorentz factor	γ	27.7286	
Betatron tunes	Q_x / Q_y	26.13 / 26.18	
Synchrotron tune	Q_s	$4.19\ 10^{-3}$	
Average beta functions	$\langle\beta_x\rangle$ / $\langle\beta_y\rangle$	42.1 /42	m
Normalized r.m.s. transverse emittances	$\varepsilon_{N,x}$ / $\varepsilon_{N,y}$	2.8 / 2.8	μm
Linear chromaticities	ξ_x / ξ_y	0 / 0	
Initial r.m.s. bunch length	σ_z	0.150	m
Initial r.m.s. longitudinal momentum spread	$\sigma_{\Delta p/p_0}$	$9.2\ 10^{-4}$	
Cavity harmonic number	h	4620	
Initial kick amplitude		0.9	mm
Number of slices		500	
Number of macroparticles		10^6	
Longitudinal restoring force		linear	
Frozen wake field		no	

Table B.5: SPS parameters for the LHC beam at injection used in *HEADTAIL* simulations for the working point used before 2006.

B.6 LHC Beam Parameters in the SPS at Injection for TMCI Measurement

Parameter Name	Symbol	Value	Unit
Beam momentum	p	26	GeV/c
Revolution frequency	f_{rev}	43375.9	Hz
Momentum compaction factor	α_{cp}	$1.92\ 10^{-3}$	
Circumference length	L	6911	m
Lorentz factor	γ	27.7286	
Betatron tunes	Q_x / Q_y	26.185 / 26.13	
Average beta functions	$\langle\beta_x\rangle$ / $\langle\beta_y\rangle$	42 /42	m
RF Voltage at injection	V_{RF}	1	MV
Initial r.m.s. beam sizes	σ_x / σ_y	1 / 1	mm
Linear chromaticities	ξ_x / ξ_y	≈0.05 / 0.05	
Initial r.m.s. bunch length	σ_t	0.5	ns
Initial longitudinal emittance	ε_l	0.15 eV.s	
Cavity harmonic number	h	4620	

Table B.6: SPS parameters for the LHC beam at injection for TMCI measurements.

B.7 LHC Beam Parameters in the SPS for Tune Shift Measurements

Parameter Name	Symbol	Value	Unit
Beam momentum	p	26	GeV/c
Revolution frequency	f_{rev}	43375.9	Hz
Momentum compaction factor	α_{cp}	$1.92\ 10^{-3}$	
Circumference length	L	6911	m
Lorentz factor	γ	27.7286	
Betatron tunes	Q_x / Q_y	26.185 / 26.13	
Average beta functions	$\langle\beta_x\rangle$ / $\langle\beta_y\rangle$	42 /42	m
RF Voltage at injection	V_{RF}	3	MV
Initial r.m.s. beam sizes	σ_x / σ_y	2 / 1	mm
Linear chromaticities	ξ_x / ξ_y	≈0.05 / 0.05	
Initial r.m.s. bunch length	σ_t	0.5 - 0.6	ns
Initial longitudinal emittance	ε_l	0.35 eV.s	
Cavity harmonic number	h	4620	

Table B.7: SPS parameters for the LHC beam during flat bottom for tune shift measurements.

Appendix C

Additional HEADTAIL Simulations

C.1 HEADTAIL and MOSES with Chromaticity

In Section 6.2.2, the mode spectra and instability thresholds simulated with *HEADTAIL* were successfully benchmarked to *MOSES* mode coupling analytical calculations for a round chamber transverse impedance modeled as a broadband resonator (see Eq. 6.27). In this paragraph, *HEADTAIL* simulations and *MOSES* calculations are performed accounting for a non zero chromaticity. Apart from chromaticity, the same parameters from Tab. B.4 were used. The mode spectra calculated with *MOSES* and simulated with *HEADTAIL* are compared for increasing chromaticities in Fig. C.1.

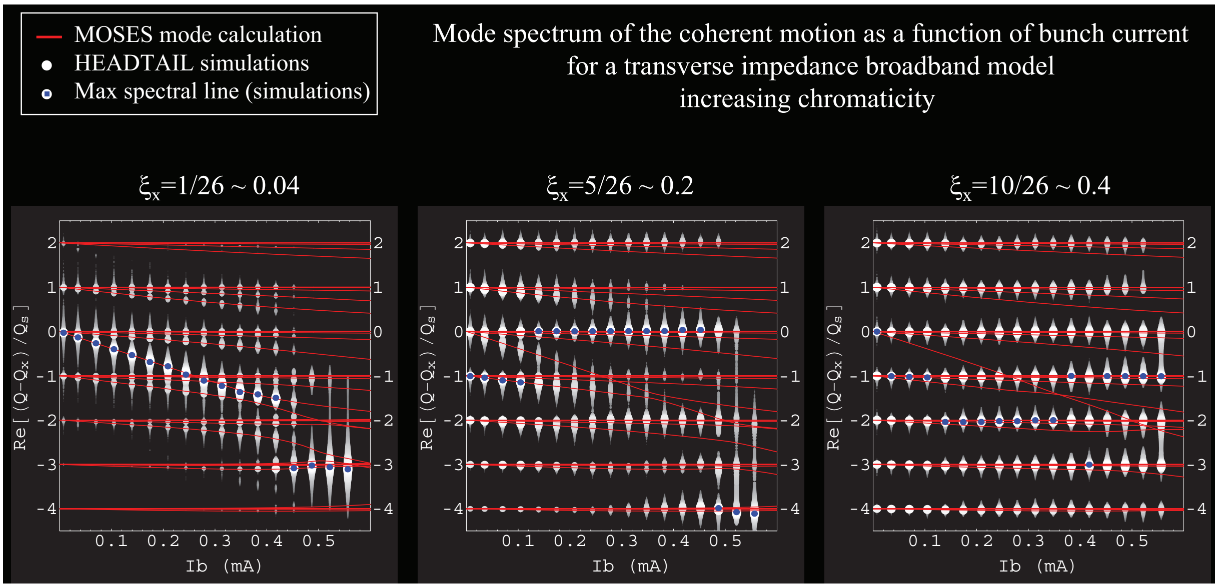

Figure C.1: *HEADTAIL* simulated mode spectra as a function of bunch population for a bunch interacting with the impedance of a round chamber modeled as a broadband with increasing horizontal chromaticity (for $\xi_x = 0.04$ (left), $\xi_x = 0.2$ (center) and $\xi_x = 0.4$ (right)). Simulated mode spectra are displayed using white dots, whose size and brightness are both non-linear functions of their spectral amplitude (bigger brighter dots have a higher amplitude than smaller darker dots). For each bunch population, the main spectral line is indicated by a blue spot.

The simulated growth rates are presented in Fig. C.2. In this case, the growth rates obtained with *MOSES* are not easy to interpret since many modes have significant positive and negative contributions. As they can not be directly related to the mode spectra, they are not presented here.

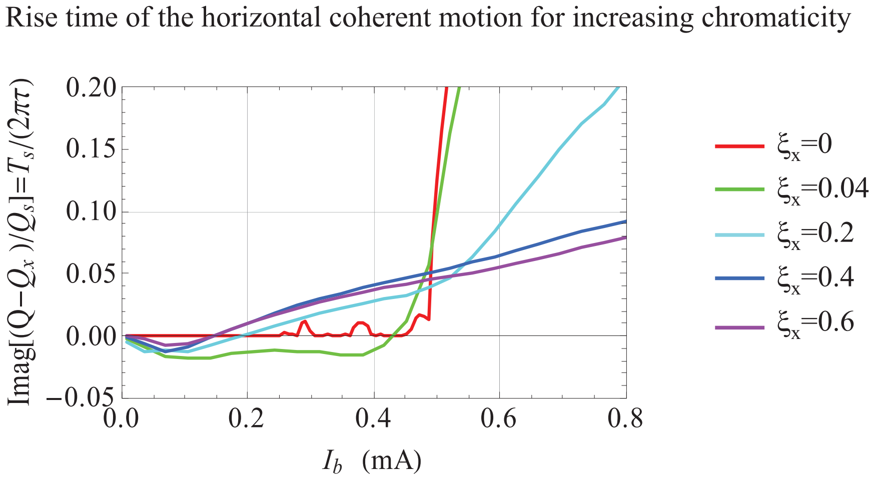

Figure C.2: *HEADTAIL* simulated instability rise time as a function of bunch population for a bunch interacting with the impedance of a round chamber modeled as a broadband with increasing horizontal chromaticity (for $\xi_x = 0$ (red), $\xi_x = 0.04$ (blue), $\xi_x = 0.2$ (green), $\xi_x = 0.4$ (purple) and $\xi_x = 0.6$ (yellow)).

When the horizontal chromaticity is increased to $\xi_x = 0.04$ (left figure in Fig. C.1), the mode spectra remain similar to those observed for zero chromaticity in Fig. 6.8. The evolution of the simulated modes with increasing bunch population is following closely the evolution predicted by *MOSES*. This evolution is particularly visible for azimuthal modes 1 (3 radial modes), 0 (3 radial modes), -1 (2 radial modes), -2 (2 radial modes) and -3 (2 radial modes). In contrast with the situation for which $\xi_x = 0$, azimuthal mode -3 becomes very strong and an instability occurs at bunch current $I_b = 0.45$ mA in simulations while *MOSES* predicts that coupling between azimuthal modes -2 and -3 should happen at higher bunch current $I_b = 0.6$ mA. In fact, the mode -2 responsible for the mode coupling in *MOSES* is observed to be rather far from the mode -3 when the instability occurs for $I_b = 0.45$ mA. One explanation to this phenomenon is that mode coupling does not take place in simulations in this case. Another explanation is that the tune spread induced by chromaticity leads to an enlargment of the lines predicted by *MOSES* into bands of finite width. These thicker bands could then overlap at lower bunch intensities than the crossing between the center of the bands. The coherent instability rise time in Fig. C.2 for $\xi_x = 0.04$ is negative before the onset of the instability and reveals a strong damping of the coherent oscillations created by the incoherent tune spread.

When the chromaticity is increased to $\xi_x = 0.2$ (center figure in Fig. C.1), the coupling between the transverse and longitudinal planes through chromaticity becomes of the same order than the coupling induced by the impedance. The mode spectra become dominated by the synchrotron side bands generated by the decoherence/recoherence process induced by chromaticity that can be observed in Fig. C.3). The tune (mode 0) is still observed shifting down with bunch current, as well as radial modes of azimuthal modes -1 and 1, but the radial modes of azimuthal mode -2 can only be guessed by an asymmetric enlargement of the spectral line. No clear coupling can be observed. In addition, the evolution of the rise time with bunch population is not as brutal as for the previous cases of $\xi_x = 0$ or 0.04 observed in Fig. C.2, and the onset of the instability occurs much earlier (below I_b=0.2 mA). These observations also hold for $\xi_x = 0.4$ (right figure in Fig. C.1), for which the tune is completely shadowed by the chromaticity decoherence/recoherence peaks. All these observations lead to the conclusion that increasing the chromaticity leads to a slower instability that replaces the TMCI.

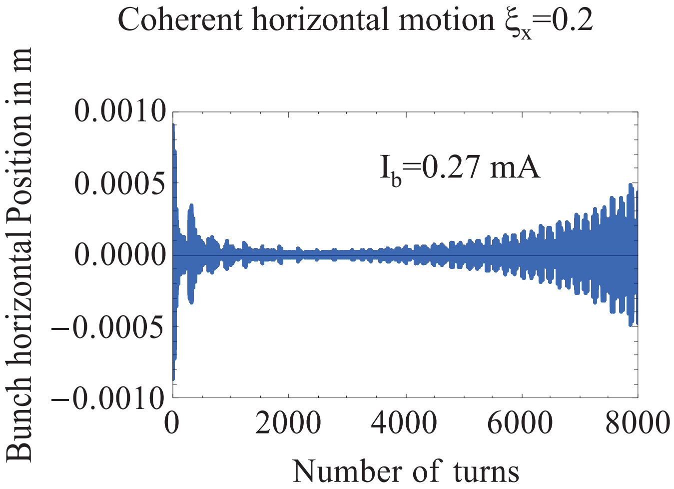

Figure C.3: Example of horizontal coherent motion simulated with *HEADTAIL* for bunch population $N_b = 4\ 10^{11}$ p/b and horizontal chromaticity $\xi_x = 0.2$. The simulated bunch interacts with the impedance of a round chamber modeled as a broadband.

C.2 HEADTAIL Simulations in the Longitudinal Plane

HEADTAIL Simulations with a modeled longitudinal resonator impedance were performed to assess whether the longitudinal microwave intensity threshold could be observed. The longitudinal broadband resonator impedance $Z_{//}(f)$ is defined as [35]

$$Z_{//}(f) = \frac{R_s}{1 + jQ\left(\frac{f}{f_{res}} - \frac{f_{res}}{f}\right)}, \tag{C.1}$$

where f is the frequency, and we chose $R_s = 10\ \Omega$ as longitudinal resonator shunt impedance, $f_{res} = 1$ GHz as resonator frequency and $Q = 1$ as resonator quality factor. No transverse impedance was modeled, and the other parameters were taken from Tab. B.4. We applied the same *SUSSIX* frequency analysis to the HEADTAIL simulations outputs as for the transverse plane and the evolution of the longitudinal coherent frequency shifts vs. intensity is presented in Fig. C.4 (left). No clear mode coupling as in the transverse plane is observed, which may be due to the fact that the frequency signals are largely dominated by modes 0 and 1.

The r.m.s. bunch length vs. intensity is plotted in Fig. C.4 (top right), where two regimes can be distinguished. The first (almost) linear regime corresponds to potential-well bunch lengthening. The second is the regime of microwave instability. The intensity threshold between the two regimes is then observed to be $N_b^{th} \approx 1.35\ 10^{11}$ p/b. Comparisons of this simulated bunch length evolution vs. intensity with analytical formulae were performed in Ref. [151]. The evolution of

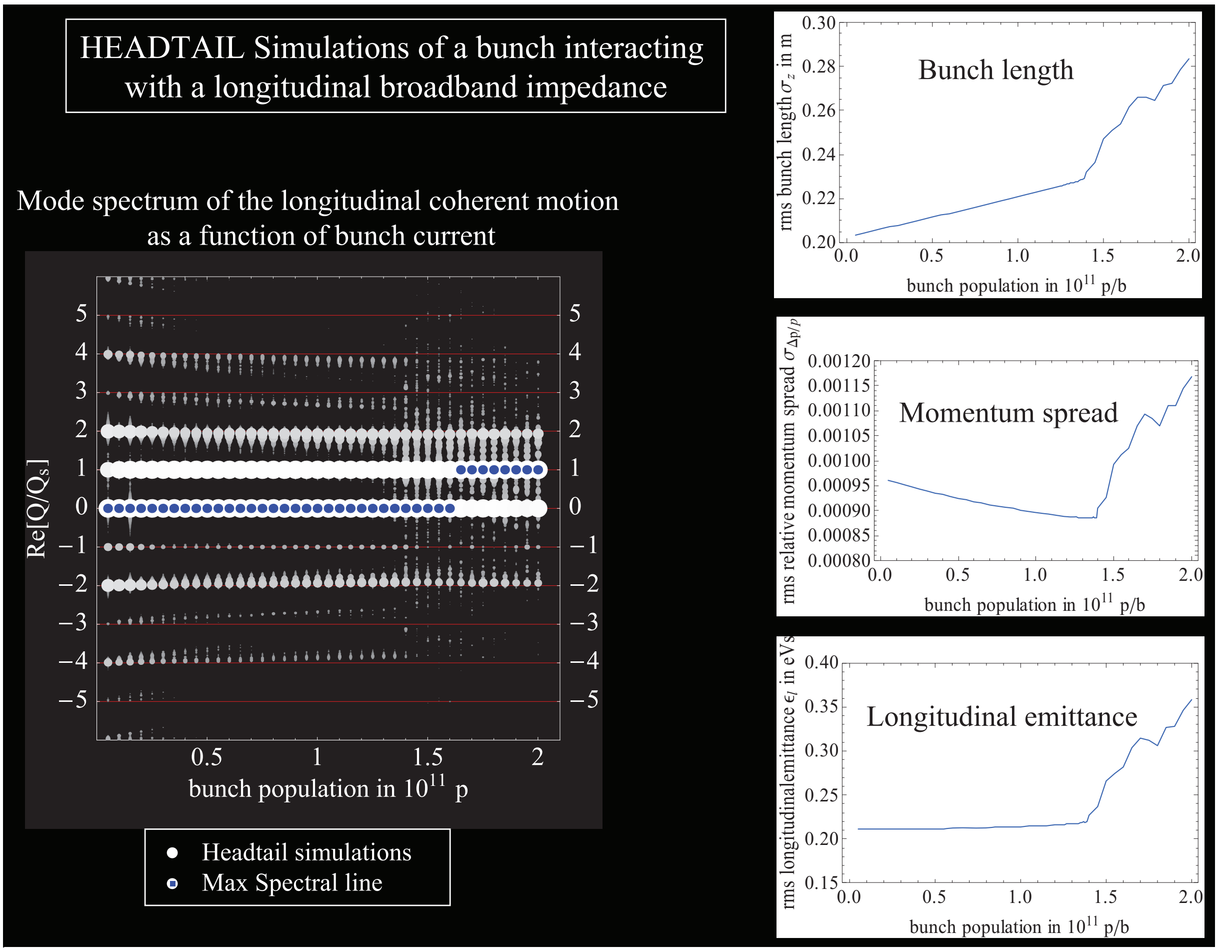

Figure C.4: *HEADTAIL* Simulations of a bunch interacting with a longitudinal broadband impedance: Mode spectrum as a function of bunch population (left) with simulated mode spectra displayed using white dots, whose size and brightness are both non-linear functions of their spectral amplitude (bigger brighter dots have a higher amplitude than smaller darker dots, and the main spectral line is indicated by a blue spot for each bunch population; simulated r.m.s. bunch length as a function of bunch population (top right), simulated r.m.s. momentum spread as a function of bunch population (middle right) and simulated r.m.s. momentum spread as a function of bunch population (bottom right).

both momentum spread and longitudinal emittance vs. intensity obtained from *HEADTAIL* are also shown on the middle right and bottom right of Fig. C.4.

Appendix D

List of Contributions to other Topics

Here is a list of significant contributions to other topics not directly related to the main subject of the PhD thesis :

(a) Beam-based measurements in SPS with prototype collimators [103],

(b) Localization of impedance sources in the SPS using intensity dependent optics [148],

(c) *HEADTAIL* simulations of the Head-tail instability in the the CERN PS [152],

(d) Instability studies at transition in the PS, including modification of the *HEADTAIL* code to take particle acceleration into account [153],

(e) Impedance studies for the collimators of the CLIC Beam Delivery System [154],

(f) Measurement of the dependence of Electron-Cloud instability on beam energy in the SPS [155],

(g) Transmission microwave measurements of the Electron-Cloud in carbon coated SPS magnets [156],

(h) 3D EM simulations and beam measurements of beam instrumentation (SPS BPM, Head-tail Monitor and Exponential Coupler [157]),

(i) 3D thermomechanical simulations and measurements of the mechanical resistance of PS bellows to a horizontal stroke [158],

(j) 3D simulation studies of magnetic shielding for a cryostat of the ASACUSA experiment (to be published).

Appendix E

List of Publications

Nota: This list only contains the contributions published during the course of the PhD thesis on a subject related to the subject of the PhD thesis.

In Refereed Journals

- F. Roncarolo, F. Caspers, T. Kroyer, E. Métral, N. Mounet, B. Salvant, and B. Zotter. *Comparison between laboratory measurements, simulations, and analytical pre- dictions of the transverse wall impedance at low frequencies.* Phys. Rev. ST-AB, 12, 2009.
- G. Rumolo, G. Arduini, E. Métral, E. Shaposhnikova, E. Benedetto, R. Calaga, G. Papotti, and B. Salvant. *Dependence of the electron-cloud instability on the beam energy.* Phys. Rev. Let., 100, 2008.

In Proceedings of Conferences or Workshops

2009

- G. Arduini, R. Calaga, E. Métral, G. Papotti, D. Quatraro, G. Rumolo, B. Salvant, and R. Tomás. *Transverse Impedance Localization using (Intensity) Dependent Optics.* Proc. PAC'09 Vancouver, BC, Canada, 2009.
- S. Aumon, W. Bartmann, S. Gilardoni, E. Métral, G. Rumolo, B. Salvant, and R. Steerenberg. *Beam Instabilities studies at transition crossing in the CERN Proton Synchrotron.* Proc. PAC'09, Vancouver, BC, Canada, 2009.
- M.J. Barnes, F. Caspers, T. Kroyer, E. Métral, F. Roncarolo, and B. Salvant. *Measurement of the Longitudinal and Transverse Impedance of Kicker Magnets using the Coaxial Wire Method.* Proc. PAC'09, Vancouver, BC, Canada, 2009.
- R. de Maria, J.D. Fox, W. Höfle, G. Kotzian, G. Rumolo, B. Salvant, and U.Wehrle. *Performance of Exponential Coupler in the SPS with LHC Type Beam for Transverse Broadband Instability Analysis.* Proc. DIPAC'09, Basel, Switzerland, 2009.
- E. Métral, F. Caspers, A. Grudiev, T. Kroyer, B. Salvant, F. Roncarolo, and B. Zotter. *Impedance Studies for the Phase 2 LHC Collimators.* Proc. PAC'09 Vancouver, BC, Canada, 2009.
- D. Quatraro, G. Rumolo, and B. Salvant. *Recent Developments for the HEADTAIL Code: Updating and Benchmarks.* Proc. PAC'09 Vancouver, BC, Canada, 2009.

- B. Salvant, G. Arduini, C. Boccard, R. Calaga, F. Caspers, A. Grudiev, R. Jones, E. Métral, F. Roncarolo, G. Rumolo, B. Spataro, C. Zannini, D. Alesini, and M. Migliorati. *Coupling Impedance of the CERN SPS Beam Position Monitors.* Proc. PAC'09 Vancouver, BC, Canada, 2009.
- B. Salvant, G. Arduini, H. Burkhardt, R. Calaga, H. Damerau, W. Höfle, R. de Maria, E. Métral, G. Papotti, G. Rumolo, R. Tomás, and S. White. *Analysis of the Transverse SPS Beam Coupling Impedance with Short and Long Bunches.* Proc. PAC'09 Vancouver, BC, Canada, 2009.
- B. Salvant, H. Medina, and E. Métral. *An Update of ZBASE, the CERN Impedance Database.* Proc. PAC'09 Vancouver, BC, Canada, 2009.

2008

- E. Métral, G. Arduini, T. Bohl, H. Burkhardt, R. Calaga, F. Caspers, H. Damerau, T. Kroyer, H. Medina, G. Rumolo, B. Salvant, M. Schokker, E. Shaposhnikova, B. Spataro, and J. Tuckmantel. *CERN SPS Impedance in 2007.* Proc. EPAC'08 Genoa, Italy, 2008.
- F. Roncarolo, F. Caspers, T. Kroyer, E. Métral, and B. Salvant. *Comparison between Laboratory Measurements, Simulations and Analytical Predictions of the Resistive Wall Transverse Beam Impedance at low frequencies.* Proc. EPAC'08, Genoa, Italy, 2008.
- F. Roncarolo, F. Caspers, T. Kroyer, E. Métral, and B. Salvant. *Measurement of the Transverse Resistive Wall Impedance of a LHC Graphite Collimator at Low Frequency.* Proc. HB'08, Nashville, TN, USA, 2008.
- G. Rumolo, G. Arduini, E. Benedetto, R. Calaga, E. Métral, G. Papotti, B. Salvant and E. Shaposhnikova. *Experimental Study of the Electron Cloud Instability at the CERN SPS.* Proc. EPAC'08, Genoa, Italy, 2008.
- B. Salvant, G. Arduini, R. Calaga, E. Métral, G. Papotti, G. Rumolo, R. Steinhagen and R. Tomás. *Transverse Mode-Coupling Instability in the CERN SPS : Comparing MOSES Analytical Calculations and HEADTAIL Simulations with experiments in the SPS.* Proc. EPAC'08, Genoa, Italy, 2008.
- B. Salvant, G. Arduini, R. Calaga, E. Métral, G. Papotti, G. Rumolo, R. Steinhagen and R. Tomás. *Transverse Mode-Coupling Instability in the CERN SPS: Comparing HEADTAIL Simulations with Beam Measurements.* Proc. HB'08, Nashville, TN, USA, 2008.
- B. Salvant, F. Caspers, T. Kroyer, E. Métral, and F. Roncarolo. *Bench Measurements of the Low Frequency Transverse Impedance of the CERN LHC Beam Vacuum Interconnects with RF Contacts.* Proc. EPAC'08, Genoa, Italy, 2008.

2007

- G. Arduini, T. Bohl, H. Burkhardt, E. Métral, G. Rumolo, and B. Salvant. *Fast Vertical Single-bunch Instability at Injection in the CERN SPS : An Update.* Proc. PAC'07, Albuquerque, NM, USA, 2007.
- E. Métral, G. Arduini, R. Assmann, A. Boccardi, C. Bracco, , T. Bohl, F. Caspers, M. Gasior, O. R. Jones, K. K. Kasinski, T. Kroyer, S. Redaelli, G. Robert-Demolaize, F. Roncarolo, G. Rumolo, B. Salvant, R. Steinhagen, T. Weiler, and F. Zimmermann. *Transverse Impedance of LHC Collimators.* Proc. PAC'07, Albuquerque, NM, USA, 2007.

- E. Métral, G. Arduini, T. Bohl, H. Burkhardt, R. Calaga, F. Caspers, H. Damerau, E. Gaxiola, T. Kroyer, H. Medina, G. Rumolo, B. Salvant, E. Shaposhnikova, M. Schokker, B. Spataro, and J. Tuckmantel. *SPS Impedance.* Proc. BEAM'07, CARE-HHH-APD Workshop on Finalizing the Roadmap for the Upgrade of the CERN and GSI Accelerator Complex, CERN, Geneva, Switzerland, 2007.

- E. Métral, G. Rumolo, B. Salvant, and R. Steerenberg. *Simulation study of the horizontal head-tail instability observed at injection of the CERN Proton Synchrotron.* Proc. PAC'07, Albuquerque, NM, USA, 2007.

- E. Métral, B. Salvant, and B. Zotter. *Resistive-Wall Impedance of an Infinitely Long Multi-Layer Cylindrical Beam Pipe.* Proc. of PAC'07, Albuquerque, NM, USA, 2007.

- G. Rumolo, G. Arduini, E. Métral, E. Shaposhnikova, E. Benedetto, R. Calaga, G. Papotti, B. Salvant. *Experimental studies on the SPS electron cloud.* Proc. BEAM'07, CARE-HHH-APD Workshop on Finalizing the Roadmap for the Upgrade of the CERN and GSI Accelerator Complex, CERN, Geneva, Switzerland, 2007.

- B. Salvant, E. Métral, G. Rumolo, and R. Tomás. *Transverse mode coupling instabil- ity in the SPS: HEADTAIL simulation and MOSES calculations.* Proc. BEAM'07, CARE-HHH-APD Workshop on Finalizing the Roadmap for the Upgrade of the CERN and GSI Accelerator Complex, CERN, Geneva, Switzerland, 2007.

Websites Created and Managed

- *RF impedance measurement webpage* (renamed *LHC impedance webpage* and now managed by N. Mounet) `http://cern.ch/rf-impedance-measurement`

- *SPS impedance webpage* `http://cern.ch/sps-impedance`

Bibliography

[1] Cern official website. `http://www.cern.ch`.

[2] P. Collier and O. Brüning. Building a behemoth. *Nature*, 448:285–289, 2007.

[3] The LHC Study Group. *Design Study of the Large Hadron Collider (LHC): A Multiparticle Collider in the LEP Tunnel.* CERN 91-03, 1991.

[4] Steven Weinberg. The making of the standard model. *European Physical Journal C*, 34:5, 2004. `doi:10.1140/epjc/s2004-01761-1`.

[5] John Ellis. Beyond the standard model with the LHC. *Nature*, 448:297–301, 2007. `http://dx.doi.org/10.1038/nature06079`.

[6] *LHC Design Report, Vol. I, II and III.* CERN-2004-003, 2004.

[7] W. Herr and B. Muratori. *Concept of luminosity.* CERN report 2006-002, 2006. CERN Accelerator School: Intermediate Course on Accelerator Physics, Zeuthen, Germany, 15 - 26 Sep 2003.

[8] Elias Métral and Giovanni Rumolo. *USPAS Course on Collective Effects.* US Particle Accelerator School, June 2009. `http://uspas.fnal.gov/materials/09UNM/CollectiveEffects.html`.

[9] R. Garoby. *Main Accelerator Science Challenges: the Injectors.* Academic training lecture: Scenarios and Technological Challenges for a LHC Luminosity Upgrade, CERN indico event 55045, 2009.

[10] W. Sweet. Europe's supercollider project. *IEEE Spectrum*, page 47, October 1994.

[11] C. Seife. Physics tries to leave the tunnel. *Science*, 302:36–38, October 2003.

[12] K. Grim. High-energy physics beyond $e = mc^2$. *Symmetry Breaking*, February 2009. `http://www.symmetrymagazine.org/breaking/2009/02/13/high-energy-physics-beyond-emc2/`.

[13] J. Faure et al. Controlled injection and acceleration of electrons in plasma wakefields by colliding laser pulses. *Nature*, 444:737–739, 2006.

[14] J. Faure et al. Energy doubling of 42 GeV electrons in a metre-scale plasma wakefield accelerator. *Nature*, 445:741–744, 2007.

[15] A. Blondel et al. *Physics opportunities with future proton accelerators at CERN.* CERN-PH-TH/2006-175, 2006. `http://arxiv.org/pdf/hep-ph/0609102`.

[16] O. Brüning. *LHC Challenges and Upgrade Options*, volume 110. Journal of Physics: Conference Series - 112002, 2008.

[17] L. Rossi. *LHC luminosity upgrade: Magnet Technology.* Academic training lecture: Scenarios and Technological Challenges for a LHC Luminosity Upgrade, CERN indico event 55044, 2009.

[18] L. Evans. *Upgrade scenario for the LHC complex.* Academic training lecture: Scenarios and Technological Challenges for a LHC Luminosity Upgrade, CERN indico event 55041, 2009.

[19] E. Shaposhnikova. *SPS Challenges.* Proc. BEAM'07, CARE-HHH-APD Workshop on Finalizing the Roadmap for the Upgrade of the CERN and GSI Accelerator Complex, CERN, Geneva, Switzerland, June 2009.

[20] J. Wenninger. *Status of LHC Commissioning.* Proceedings of PAC'09, Vancouver, Canada, 2009.

[21] F. Zimmermann. *LHC Upgrade Scenarios.* Proceedings of PAC'07, Albuquerque, New Mexico, USA, 2007.

[22] E. Shaposhnikova. *Intensity upgrade for CERN-LHC injectors.* Proceedings of HB'2008, Nashville, Tennessee, USA, 2008.

[23] Madx manual. `http://mad.web.cern.ch/mad/`.

[24] J. Rossbach and P. Schmüser. *Basic Course on Accelerator Optics*, volume 1. CERN report 94-01, 1994. CERN Accelerator School: Fifth General Accelerator Physics Course, University of Jyväskylä, Finland, 7-18 September 1992.

[25] B. Holzer. *Introduction to Transverse Beam Optics.* CERN Accelerator School: Introduction to Accelerator Physics, Zakopane, Poland, 1-13 October 2006, 2006.

[26] S.Y. Lee. *Accelerator Physics.* World Scientific, 2 edition, 2004.

[27] O. Brüning. *Linear Imperfections and Resonances.* CERN Accelerator School: Introduction to Accelerator Physics, Zakopane, Poland, 1-13 October 2006, 2006.

[28] C. Prior. *Electromagnetism.* CERN Accelerator School: Introduction to Accelerator Physics, Zakopane, Poland, 1-13 October 2006, 2006.

[29] J.D. Jackson. *Classical Electrodynamics.* Wiley, 3rd edition, 1999.

[30] H. Wiedemann. *Particle Accelerator Physics.* Springer, 3 edition, 2007.

[31] J. Le Duff. *Longitudinal Dynamics.* CERN Accelerator School: Introduction to Accelerator Physics, Zakopane, Poland, 1-13 October 2006, 2006.

[32] W. Bartmann, M. Benedikt, C. Carli, B. Goddard, S. Hancock, J.M. Jowett, and Y. Papaphilippou. Optics considerations for the PS2. *Proceedings of PAC07, Albuquerque, New Mexico, USA*, 2007.

[33] A. W. Chao. *Physics of Collective Beams Instabilities in High Energy Accelerators*. Wiley, 1993.

[34] K.Y. Ng. *Physics of Intensity Dependent Beam Instabilities*. World Scientific, 2006.

[35] B. Zotter and S. Kheifets. *Impedances and Wakes in High-Energy Particle Accelerators*. World Scientific, 1997.

[36] T. Weiland and R. Wanzenberg. *Wake Fields and Impedances*. DESY M-91-06, May 1991.

[37] CST Computer Simulation Technology AG.

[38] W. Bruns. *GdfidL : A Finite Difference Program with Reduced Memory and CPU Usage*. Proc. PAC'97, Vancouver, BC, Canada, 1997. `http://www.gdfidl.de/`.

[39] A. Hofmann. *Tune Shifts from Self-Fields and Images*. CERN Accelerator School: Fifth General Accelerator Physics Course - University of Jyväskylä, Finland, September 1992, 1992.

[40] J. Gareyte. *Impedances: Measurements and Calculations for Non-symmetric Structures*. CERN-SL-2002-028 (AP), 2002.

[41] A. Koschik. *Simulation of Transverse Multi-Bunch Instabilities of Proton Beams in LHC*. PhD thesis, 2004.

[42] G. Rumolo and F. Zimmermann. *Practical user guide for HEADTAIL*. SL-Note-2002-036-AP, 2002.

[43] K. Schindl. *Space Charge*. CERN report 2006-002, 2006. CERN Accelerator School: Intermediate Course on Accelerator Physics, Zeuthen, Germany, 15 - 26 Sep 2003.

[44] S. Heifets, A. Wagner, and B. Zotter. *Generalised Impedances and Wakes in Asymmetric Structures*. SLAC/AP 110, 1998.

[45] D. Möhl. *On Landau Damping of Dipole Modes by Non-Linear Space Charge and Octupoles*. CERN/PS 95-08 (DI), 1995.

[46] F. Sacherer. *Theoretical Aspects of the behaviour of Beams in Accelerator and Storage Rings*. CERN 77-13, 1977.

[47] O. Brüning. *ZBASE User's Guide Version 1.1 : an Impedance Data Base Program*. CERN-SL-96-069-AP, 1996.

[48] H. Medina and E. Métral. *ZBASE3 : la nouvelle base de données de l'Impédance des Accélérateurs du CERN*. Mémoire de Master 2, September 2007. `http://sps-impedance.web.cern.ch/sps-impedance/documents/Rapport%20Cern%20MEDINA%20Hubert_Elias.pdf`.

[49] B. Salvant, H. Medina, and E. Métral. *An Update of ZBASE, the CERN Impedance Database.* Proc. of PAC'09, Vancouver, BC, Canada, 2009.

[50] O. Henry and O. Napoly. *The resistive-pipe wake potentials for short bunches.* DPhN/STAS/91-R08, 10 edition, December 1991. CLIC Note 142.

[51] B. Zotter. *New Results on the Impedance of Resistive Metal Walls of Finite Thickness.* CERN-AB-2005-043, 2005.

[52] A. Burov and V. Lebedev. *Transverse Resistive Wall Impedance for Multi-Layer Round Chamber.* Proc. EPAC'02, Paris, France, 2002.

[53] E. Métral. *Transverse resistive-Wall impedance from very low to very high frequencies.* CERN-AB-2005-084, 2005.

[54] M. Ivanyan and V. Tsakanov. *Longitudinal impedance of two-layer tube*, volume 7. Phys. Rev. ST-AB, 2004. 114402.

[55] M. Ivanyan and A.V. Tsakanian. *Transverse impedance of two-layer tube.* proc. PAC'05, Knoxville, Tennessee, USA, 2005.

[56] R.L. Gluckstern. *Analytic Methods for Calculating Coupling Impedances.* CERN-2000-011, 2000.

[57] M. Ivanyan and A.V. Tsakanian. *Analytical presentation of resistive impedance for the laminated vacuum chamber*, volume 9. Phys. Rev. ST-AB, 2006. 034404.

[58] M. Ivanyan, E. Laziev, V. Tsakanov, A. Vardanyan, S. Heifets, and A. Tsakanian. *Multilayer tube impedance and external radiation*, volume 11. Phys. Rev. ST-AB, 2008. 084001.

[59] N. Wang and Q. Qin. *Resistive-wall impedance of two-layer tube*, volume 10. Phys. Rev. ST-AB, 2007. 111003.

[60] E. Métral, B. Salvant, and B. Zotter. *Resistive-Wall Impedance of an Infinitely long Multi-Layer Cylindrical Beam Pipe.* Proc. of PAC'07, Albuquerque, NM, USA, June 2007.

[61] H. Hahn. *Matrix Solution of Coupling Impedance in Multi-Layer Circular Cylindrical Structures.* Proc. of PAC'09, Vancouver, BC, Canada, 2009.

[62] F. Roncarolo, F. Caspers, T. Kroyer, E. Métral, N. Mounet, B. Salvant, and B. Zotter. Comparison between laboratory measurements, simulations, and analytical predictions of the transverse wall impedance at low frequencies. *Phys. Rev. ST-AB*, 12(084401), 2009.

[63] N. Mounet and E. Métral. *Electromagnetic fields created by a macroparticle in an infinitely long and axisymmetric multilayer beam pipe.* CERN BE note, to be published, 2009.

[64] M. Abramowitz and I. A. Stegun. *Handbook of Mathematical Functions With Formulas, Graphs, and Mathematical Tables.* United States Department of Commerce, National Bureau of Standards, 10 edition, December 1972.

[65] E. Métral. *News on the transverse wall impedance at low frequencies.* CERN/GSI beam dynamics and collective effects collaboration meeting, Feb. 18/19, 2009, GSI Darmsadt, Germany, 2009. `http://www-linux.gsi.de/~boine/CERN-GSI-2009/metral.pdf`.

[66] N.W. Ashcroft and N.D. Mermin. *Physique des Solides.* EDP Sciences, 2002.

[67] K. Yokoya. *Resistive Wall Impedance of Beam Pipes of General Cross Section.* Number 41. Part. Acc., 1993.

[68] B. Salvant, O. Aberle, F. Caspers, A. Grudiev, E. Métral, and N. Mounet. *TDI impedance and power loss.* CERN Internal talk, 2009. `http://lhc-impedance.web.cern.ch/lhc-impedance/TDI/PowerLossComputation/TDI%20impedance%20and%20power%20loss2.ppt`.

[69] R.W. Assmann. *Collimation and Machine Protection.* Academic training lecture: Scenarios and Technological Challenges for a LHC Luminosity Upgrade, CERN indico event 55045, 2009.

[70] E. Métral, G. Arduini, T. Bohl, H. Burkhardt, R. Calaga, F. Caspers, H. Damerau, T. Kroyer, H. Medina, G. Rumolo, B. Salvant, M. Schokker, E. Shaposhnikova, B. Spataro, and J. Tuckmantel. *CERN SPS Impedance in 2007.* Proc. EPAC'08 Genoa, Italy, 2008.

[71] P.E. Faugeras, C.G. Harrison, M. Mayer, and G.H. Schröder. *A Laminated-Iron Fast Pulsed Magnet.* CERN-SPS/ABT/77-16, 1977.

[72] L. Vos. *Longitudinal impedance from ferrite.* CERN-SL-2000-010 AP, 2000.

[73] E. Métral, G. Arduini, E. Benedetto, H. Burkhardt, G. Rumolo, and E. Shaposhnikova. *Transverse Mode-Coupling Instability in the CERN Super Proton Synchrotron.* talk at 33rd ICFA Advanced Beam Dynamics Workshop : High Intensity High Brightness Hadron Beams, Bensheim, Germany, 18 - 22 Oct 2004, 2004. `http://ab-abp-rlc.web.cern.ch/ab-abp-rlc/Meetings/2004/2004.11.26/TMCIInTheCERNSPS.pdf`.

[74] T. Kroyer, F. Caspers, and E. Gaxiola. *Longitudinal and Transverse Wire Measurements for the Evaluation of Impedance Reduction Measures on the MKE Extraction Kickers.* CERN AB-Note-2007-028, 2007.

[75] W. H. Press, B. P. Flannery, S. A. Teukolsky, and W. T. Vetterlin. *Numerical Recipes in C.* Cambridge University Press, 2 edition, 1992.

[76] E. Métral and B. Salvant. *Update on the SPS kickers.* Presented at the CERN Accelerator Performance Committee, April 2007. `http://sps-impedance.web.cern.ch/sps-impedance/documents/UpdateOfSPSKickers_APC_27-04-07.pdf`.

[77] E. Métral, F. Caspers, M. Giovannozzi, A. Grudiev, T. Kroyer, and L. Sermeus. *Kicker Impedance Measurements For The Future Multiturn Extraction Of The Cern Proton Synchrotron.* Proc. EPAC'06, Edinburgh, Scotland, 2006.

[78] E. Métral. *SPS Impedance Budget Follow-up.* Presented at the CERN SPS Impedance Meeting, 18/07/2008, July 2008. `http://sps-impedance.web.cern.ch/sps-impedance/documents/SPSImpedanceBudget_FollowUp_18-07-08.pdf`.

[79] H. Tsutsui. *Some Simplified Models of Ferrite Kicker Magnet for Calculation of Longitudinal Coupling Impedance.* CERN-SL-2000-004 AP, 2000.

[80] H. Tsutsui. *Transverse Coupling Impedance of a Simplified Ferrite Kicker Magnet Model.* LHC Project Note 234, 2000.

[81] F. Caspers, A. Mostacci, and H. Tsutsui. *Impedance Evaluation of the SPS MKE Kicker with Transition Pieces between Tank and Kicker Module.* CERN-SL-2000-071 (AP), 2000.

[82] M.J. Barnes, F. Caspers, T. Kroyer, E. Métral, F. Roncarolo, and B. Salvant. *Measurement of the longitudinal and transverse impedance of kicker magnets using the coaxial wire method.* Proc. PAC'09, Vancouver, BC, Canada, 2009.

[83] R.E. Collin. *Field Theory of Guided Waves.* IEEE press, 2 edition, 1990.

[84] L. Xiao, W. Gai, and X. Sun. *Field analysis of a dielectric-loaded rectangular waveguide in accelerating structure*, volume 65. Phys. Rev. E, 2001.

[85] B. Salvant, G. Arduini, C. Boccard, R. Calaga, F. Caspers, A. Grudiev, R. Jones, E. Métral, F. Roncarolo, G. Rumolo, B. Spataro, C. Zannini, D. Alesini, and M. Migliorati. *Coupling Impedance of the CERN SPS Beam Position Monitors.* Proc. PAC'09 Vancouver, BC, Canada, 2009.

[86] C. Zannini. *Master's thesis report.* To be published, 2009.

[87] C. Zannini, E. Métral, G. Rumolo, and B. Salvant. *Simulations of the SPS kickers with CST Particle Studio.* talk at the SPS impedance meeting, August 2009. `http://sps-impedance.web.cern.ch/sps-impedance/documents/Kickers_sim2.pptx`.

[88] The MAFIA collaboration. *MAFIA User Guide.* DESY, LANL, KFA, June 1987.

[89] Anticorodal 110 - en aw-6082 (alsi1mgmn).

[90] W. Hofle. *Active feedback for curing the transverse resistive wall instability in the SPS.* Proc. of 10th Workshop on LEP-SPS Performance, Chamonix, France, 17 - 21 Jan 2000, 2000.

[91] Y.H. Chin. *User's Guide for New ABCI Version 6.1 (Azimuthal Beam Cavity Interaction).* CERN SL/92-49 (AP), 1992.

[92] B. Salvant. *Trying to understand the routine that Bruno is using to get the impedance from the wake.* SPS impedance meetings, November 2008. `http://sps-impedance.web.cern.ch/sps-impedance/documents/BrunoYongHoWakeFFTc.ppt`.

[93] E. Métral. *Procedures for frequency and time domain EM Simulations in asymmetric structures.* in CERN SPS impedance meetings minutes, November 2008. `http://sps-impedance.web.cern.ch/sps-impedance/documents/ProceduresForFrequencyAndTimeDomainEMSimulationsInAsymmetricStructures_EM.pdf`.

[94] F. Caspers. *in Handbook of Accelerator Physics and Engineering.* A. Chao and M. Tigner (editors), World Scientific, 1998.

[95] B. Salvant, G. Arduini, C. Boccard, R. Calaga, F. Caspers, A. Grudiev, E. Métral, F. Roncarolo, G. Rumolo, B. Spataro, and C. Zannini. *Simulations and RF Measurements of SPS Beam Position Monitors (BPV and BPH).* SPS impedance meeting, March 2009. `http://sps-impedance.web.cern.ch/sps-impedance/documents/SPS%20BPM%20simulations%207march09.ppt`.

[96] V.G. Vaccaro. *Coupling Impedance Measurements.* INFN/TC-94/023, 1994.

[97] E. Gaxiola, J. Bertin, F. Caspers, L. Ducimetire, and T. Kroyer. *Experience with Kicker Beam Coupling Reduction Techniques.* Proc. PAC'05, Knoxville, USA, 2005.

[98] E. Gaxiola, F. Caspers, L. Ducimetire, P. Faure, T. Kroyer, B. Versolatto, and E. Vossenberg. *The SPS Fast Extraction Kicker System in LSS6.* Proc. PAC'06, Edinburgh, Scotland, UK, 2006.

[99] L. Evans. Challenges of the lhc: the accelerator challenge. *Eur. Phys. J.*, C 34:5760, 2004.

[100] J. Laslett, K. Neil, and A. Sessler. Transverse resistive instabilities of intense coasting beams in particle accelerators. *Rev. Sci. Instrum.*, 36:436, 1965.

[101] A. Koschik, F. Caspers, E. Métral, L. Vos, and B. Zotter. *Transverse Resistive Wall Impedance and Wake Function with "Inductive Bypass".* Proc. EPAC'04, Lucerne, Switzerland, 2004.

[102] H. Burkhardt, G. Arduini, R. Assmann, F. Caspers, M. Gasior, A. Grudiev, R. Jones, T. Kroyer, E. Métral, S. Redaelli, G. Robert-Demolaize, F. Roncarolo, D. Schulte, R. Steinhagen, J. Wenninger, and F. Zimmermann. *Measurements of the LHC Collimator Impedance with Beam in the SPS.* Proc. PAC'07, Albuquerque, NM, USA, 2007.

[103] E. Métral, G. Arduini, R. Assmann, A. Boccardi, C. Bracco, , T. Bohl, F. Caspers, M. Gasior, O. R. Jones, K. K. Kasinski, T. Kroyer, S. Redaelli, G. Robert-Demolaize, F. Roncarolo, G. Rumolo, B. Salvant, R. Steinhagen, T. Weiler, and F. Zimmermann. *Transverse Impedance of LHC Collimators.* Proc. PAC'07, Albuquerque, NM, USA, 2007.

[104] T. Kroyer. *Simulation of the low-frequency collimator impedance.* CERN-AB-Note-2008-017, 2008.

[105] F. Roncarolo, F. Caspers, T. Kroyer, E. Métral, and B. Salvant. *Comparison between Laboratory Measurements, Simulations and Analytical Predictions of the Resistive Wall Transverse Beam Impedance at low frequencies.* Proc. EPAC'08, Genoa, Italy, 2008.

[106] G. Nassibian and F. Sacherer. Methods for measuring transverse coupling impedances in circular accelerators. *Nucl. Instrum. Methods*, 159:21, 1979.

[107] F. Caspers, U. Iriso-Ariz, and A. Mostacci. *Bench Measurements of Low Frequency Transverse Impedance.* Proc. PAC'03, Portland, Oregon, 2003.

[108] R.S. Popović. *Hall effect devices.* IoP Publishing Ltd, 2004.

[109] E. Métral, F. Caspers, A. Grudiev, T. Kroyer, B. Salvant, F. Roncarolo, and B. Zotter. *Impedance Studies for the Phase 2 LHC Collimators.* Proc. PAC'09 Vancouver, BC, Canada, 2009.

[110] R. Veness, J.C. Brunet, O. Gröbner, P. Lepeule, C. Reymermier, G. Schneider, B. Skoczen, V. Kleimenok, and I. Nikitine. *Beam Vacuum Interconnects for the LHC Cold Arcs.* Proc. PAC'99, New York, NY, USA, 1999.

[111] S. Calatroni, F. Caspers, K. Couturier, N. Hilleret, J.R. Knaster, P. Lepeule, M. Taborelli, R. Veness, and L. Vos. *Design aspects of the RF contacts for the LHC beam vacuum interconnects.* Proc. PAC'01, Chicago, IL, USA, 2001.

[112] B. Salvant, F. Caspers, T. Kroyer, E. Métral, and F. Roncarolo. *Bench measurements of the Low Frequency Transverse Impedance of the CERN LHC Beam Vacuum Interconnects with RF Contacts.* Proc. EPAC'08, Genoa, Italy, 2008.

[113] F. Caspers and E. Métral. *Review of Impedance Issues and First Ideas for Phase 2.* CERN Phase 2 Specification and Implementation meeting, February 2008.

[114] Y. H. Chin. *User's guide for new MOSES Version 2.0.* CERN/LEP-TH/88-05, 1988.

[115] G. Besnier, D. Brandt, and B. Zotter. *The Transverse Mode Coupling Instability in Large Storage Rings.* CERN/LEP-TH/84-11, 1984.

[116] A.W. Chao. *Transverse Instability excited by R.F. Deflecting Modes for PEP.* SLAC/PEP-Note-321, November 1979.

[117] Y.H. Chin and K. Satoh. Transverse mode coupling in a bunched beam. *IEEE Transactions on Nuclear Science*, 30(4):2566–2568, Aug. 1983.

[118] Y. H. Chin. *Transverse Mode Coupling Instability in the SPS.* CERN/SPS/85-2, 1985.

[119] J. L. Laclare. *Bunched Beam Instabilities.* CERN Accelerator School: Advanced Accelerator Physics - The Queen's College, Oxford, England, September 1985, 1987.

[120] F. Ruggiero. *Transverse Mode Coupling Instability due to Localized Sources.* CERN/LEP-TH/84-21, 1984.

[121] F. Sacherer. *Methods for Computing Bunched-Beams Instabilities.* CERN/SI-BR/72-5, 1972.

[122] G. Stupakov. *Classical Mechanics and Electromagnetism in Particle Accelerators.* US Particle Accelerator School: Nashville, Tennessee, US, June 2007, 2007.

[123] M. Sands. *The Head-tail effect: an instability mechanism in storage rings.* SLAC-TN-69-8, 1969.

[124] D. Brandt, J.P. Delahaye, and A. Hofmann. *Transverse Mode-Coupling Instability in the CERN Super Proton Synchrotron.* LEP Note 595, 1987.

[125] Y. H. Chin. *Hamiltonian Formulation for Transverse Bunched Beam Instabilities in the Presence of Betatron Tune Spread.* CERN-SPS-85-9-DI-MST, 1985.

[126] E. Métral, G. Arduini, E. Benedetto, H. Burkhardt, G. Rumolo, and E. Shaposhnikova. *Transverse Mode-Coupling Instability in the CERN Super Proton Synchrotron.* Proc. HB2004, 33rd ICFA Advanced Beam Dynamics Workshop : High Intensity High Brightness Hadron Beams, Bensheim, Germany, 2004.

[127] G. Rumolo and F. Zimmermann. *Electron Cloud Simulations: Beam Instabilities and Wake Fields.* Proc. Mini-Workshop on Electron-Cloud Simulations for Proton and Positron Beams, CERN Geneva, 2002.

[128] D. Quatraro, G. Rumolo, and B. Salvant. *Recent developments for the HEADTAIL code: updating and benchmarks.* Proc. PAC'09 Vancouver, BC, Canada, 2009.

[129] G. Rumolo, G. Arduini, E. Benedetto, E. Métral, D. Quatraro, B. Salvant, D. Schulte, R. Tomás, and F. Zimmermann. *Recent developments of the HEADTAIL code.* Talk at the CERN/GSI beam dynamics and collective effects collaboration meeting, Feb 2009. `http://www-linux.gsi.de/~boine/CERN-GSI-2009/rumolo.pptx`.

[130] B. Salvant, E. Métral, G. Rumolo, and R. Tomás. *Transverse mode coupling instability in the SPS: HEADTAIL simulation and MOSES calculations.* Proc. BEAM'07, CARE-HHH-APD Workshop on Finalizing the Roadmap for the Upgrade of the CERN and GSI Accelerator Complex, CERN, Geneva, Switzerland, 2007.

[131] G. Arduini, E. Benedetto, H. Burkhardt, E.Métral, and G. Rumolo. *Observation of a Fast Single-Bunch Transverse Instability on Protons in the SPS.* Proc. EPAC'04, Lucerne, Switzerland, 2004.

[132] E. Métral, G. Arduini, T. Bohl, H. Burkhardt, G. Rumolo, and B. Spataro. *Transverse Mode-Coupling Instability in the CERN Super Proton Synchrotron.* Proc. EPAC'06 Edinburgh, Scotland, UK, 2006.

[133] R. Cappi, E. Métral, and G. Métral. *Beam Break-up Instability in the CERN PS near Transition.* Proc. EPAC'00, Vienna, Austria, 2000.

[134] E. Métral and G. Rumolo. *Simulation Study on the Beneficial Effect of Linear Coupling for the Transverse Mode-coupling Instability in the CERN Super Proton Synchrotron.* Proc. EPAC'06 Edinburgh, Scotland, UK, 2006.

[135] R. Bartolini and F. Schmidt. *Computer Code for Frequency Analysis of Non-Linear Betatron Motion.* CERN SL-Note-98-017-AP, 1998.

[136] R. Bartolini and F. Schmidt. Normal form via tracking or beam data. *Part. Accel., 59*, pages 93–106, 1998.

[137] J. Laskar. Frequency analysis for multi-dimensional systems. global dynamics and diffusion. *Physica D:Nonlinear Phenomena*, 67:257–281, 1993.

[138] J. Laslett. *On intensity limitations imposed by transverse space-charge effects in circular particle accelerators.* Proc. Summer Study on Storage Rings, Accelerators and Instrumentation at Super High Energies, BNL Report No. 7534, 1963.

[139] A. Burov and V. Danilov. Suppression of transverse bunch instabilities by asymmetries in the chamber geometry. *Phys. Rev. Lett.*, 82:2286, 1999.

[140] E. Métral. *Effect of Bunch Length, Chromaticity, and Linear Coupling on the Transverse Mode-Coupling Instability due to the Electron Cloud.* Proc. ECLOUD02 Workshop, CERN, Geneva, April 2002.

[141] G. Guignard. *The general theory of all sum and difference resonances in a three-dimensional magnetic field in a synchrotron.* CERN-76-06, 1976.

[142] G. Arduini, T. Bohl, H. Burkhardt, E. Métral, G. Rumolo, and B. Salvant. *Fast Vertical Single-bunch Instability at Injection in the CERN SPS : An Update.* Proc. PAC'07, Albuquerque, NM, USA, 2007.

[143] M. Gasior and R. Jones. *High Sensitivity Tune Measurement by Direct Diode Detection.* Proc. DIPAC'05, Lyon, France, 2005.

[144] R. Jones and H. Schmickler. *The measurement of Q' and Q" in the CERN SPS by head-tail phase shift analysis.* Proc. DIPAC'01, Grenoble, France, 2001.

[145] R. Jones and H. Schmickler. *The High Frequency Longitudinal and Transverse Pick-ups used in the SPS.* CERN SPS/ARF/78-17, 2001.

[146] H. Burkhardt. *SPS transverse impedance measurements.* Presentation at the Accelerator Performance Committee, 17/08/2007, 2007.

[147] G. Arduini, C. Carli, and F. Zimmermann. *Localizing Impedance Sources from Betatron-phase Beating in the CERN SPS.* Proc. EPAC'04 Lucerne, Switzerland, 2004.

[148] G. Arduini, R. Calaga, E. Métral, G. Papotti, D. Quatraro, G. Rumolo, B. Salvant, and R. Tomás. *Transverse Impedance Localization using Dependent Optics.* Proc. PAC'09 Vancouver, BC, Canada, 2009.

[149] B. Salvant, G. Arduini, H. Burkhardt, R. Calaga, H. Damerau, W. Höfle, R. de Maria, E. Métral, G. Papotti, G. Rumolo, R. Tomás, and S. White. *Analysis of the Transverse SPS Beam Coupling Impedance with Short and Long Bunches.* Proc. PAC'09 Vancouver, BC, Canada, 2009.

[150] A. Thompson and B. N. Taylor. *Guide for the Use of the International System of Units (SI)*, volume 811. NIST Special publication, 2008.

[151] E. Métral, G. Arduini, T. Bohl, H. Burkhardt, R. Calaga, F. Caspers, H. Damerau, E. Gaxiola, T. Kroyer, H. Medina, G. Rumolo, B. Salvant, E. Shaposhnikova, M. Schokker, B. Spataro, and J. Tuckmantel. *SPS Impedance.* Proc. BEAM'07, CARE-HHH-APD Workshop on Finalizing the Roadmap for the Upgrade of the CERN and GSI Accelerator Complex, CERN, Geneva, Switzerland, 2007.

[152] E. Métral, G. Rumolo, B. Salvant, and R. Steerenberg. *Simulation study of the horizontal head-tail instability observed at injection of the CERN Proton Synchrotron.* Proc. PAC'07, Albuquerque, NM, USA, 2007.

[153] S. Aumon, W. Bartmann, S. Gilardoni, E. Métral, G. Rumolo, B. Salvant, and R. Steerenberg. *Beam Instabilities studies at transition crossing in the CERN Proton Synchrotron.* Proc. PAC'09, Vancouver, BC, Canada, 2009.

[154] B. Salvant, E. Métral, A. Grudiev, G. Rumolo, and R. Tomàs. *Dielectric Collimators for the CLIC Beam Delivery System? First ideas from studies for the LHC collimators.* presented at the ILC-CLIC LET Beam Dynamics Workshop, CERN, Geneva, Switzerland, 2009. `http://indico.cern.ch/getFile.py/access?contribId=32&sessionId=6&resId=0&materialId=slides&confId=56133`.

[155] G. Rumolo, G. Arduini, E. Métral, E. Shaposhnikova, E. Benedetto, R. Calaga, G. Papotti, and B. Salvant. Dependence of the electron-cloud instability on the beam energy. *Physical Review Letters*, 100(14):144801, 2008.

[156] F. Caspers, S. Federmann, E. Mahner, B. Salvant, and D. Seebacher. *Diagnostic of Coating Results: Microwave Measurements.* Anti e-Cloud Coatings Workshop - AEC'09, CERN, Geneva, Swizerland, 2009.

[157] R. de Maria, J.D. Fox, W. Höfle, G. Kotzian, G. Rumolo, B. Salvant, and U. Wehrle. *Performance of Exponential Coupler in the SPS with LHC Type Beam for Transverse Broadband Instability Analysis.* Proc. DIPAC'09, Basel, Switzerland, 2009.

[158] B. Salvant, D. Allard, R. Brown, and G. Villiger. *Assessing the mechanical resistance of PS bellows to a horizontal stroke.* presented at the CERN-ABP/LIS meeting, November 2007. `http://ab-dep-abp.web.cern.ch/ab-dep-abp/LIS/Minutes/2007/20071126/PS_Bellows/PS%20bellows2.ppt`.

BENOIT SALVANT

French nationality
Born April, 17th 1978 (31)

Quai du Cheval Blanc 7
CH-1227 Geneva
Switzerland

Office : +41 22 76 71 333
Mobile: +33 6 16 950 788
Benoit.Salvant@espci.org

Doctoral student, manager of research projects

EDUCATION

2006 -2009 **EPFL Lausanne - CERN Geneva** *Switzerland*
Doctoral student in Accelerator Physics. Performed theoretical, computational and experimental studies to improve the performance of the CERN particle accelerator complex.

2002 - 2003 **Imperial College London** *UK*
International Diploma in Electrical Engineering and Management (grade A). UNITECH degree.

1998 - 2002 **ESPCI Paris** (Ecole Supérieure de Physique et Chimie Industrielles - ParisTech) *France*
Diplôme d'ingénieur (MSc in General Engineering) within the Paris Institute of Technology.

1996 - 1998 Baccalauréat S Mention Très Bien, followed by "classes prépas" at Ecole S^te^ Geneviève, Versailles (PCSI, PC*). *France*

WORK EXPERIENCE

2004 - 2006 **Michelin** - **Project Manager** in Materials and Process R&D, Clermont-Fd *France*
2.5 years
In charge of a research project to understand and improve tire performance (1 M€ budget with collaborators in Europe and the US). In charge of applied research studies in Physics, Chemistry, and Thermo-mechanics of charged elastomeric materials. Management of technicians and students. In charge of collaborations with suppliers and research institutes in the UK, France and Germany.

2003 - 2004 **DaimlerChrysler AG** - Research student in Combustion Engines, Stuttgart *Germany*
7 months
Applied Neural Networks to a diesel engine sensor system (2 patents granted). In charge of measurements on a Mercedes-Benz diesel engine testbench. Management of 3 technicians.

2001 **University of California, Berkeley** - Research student in Accelerator Physics, LBNL *USA*
6 months
Performed magnetic measurements and provided support for the ALS machine commissioning. In charge of analyzing and minimizing the resulting drop in X-ray beam quality for end-users.

2001 **CEA** (Commissariat à l'Energie Atomique) - Research student in Materials *France*
5 months
Modeled mechanical properties of polyimides macromolecules using Molecular Dynamics.

2000 **Bayer AG** - Research student in Pharmaceutical biochemistry, Leverkusen *Germany*
5 months
Synthesized new pharmaceutically active core structures by solid-phase combinatorial biochemistry.

LANGUAGES AND TECHNICAL SKILLS

French	Mother tongue.
English	Fluent (6 month in California, 1 year in London).TOEIC: 965/1000: Higher Professional Level (2002).
German	Fluent (two 6-month-internships in Germany in 2001 and 2004, frequent use for professional matters).
Spanish	Average level (Imperial College London Spanish course - grade A).
Italian	Average level.
Computing	Proficient at word, database, and image processing, as well as design of professional web pages. Programming languages Matlab, Mathematica, C and Fortran on Windows and UNIX platforms. Thorough experience of computer modeling, neural networks, finite element analysis, and commercial simulation software in various fields of application.

EXTRA-CURRICULAR ACTIVITIES

Junior Entreprise	Managed projects performed by ESPCI students for private companies (customer relations and accounting).
Associations	President of the ESPCI sports club. President of the high school student union. Geneva Canton volunteer.
Sports	Practice of handball at highest national level, along with athletics and volleyball at regional level since 1994.
Leisure	Regular practice of tennis, ski, sailing (dinghy, catamaran, windsurfing), and guitar.

PERSONAL WEB PAGE : HTTP://WWW.BENOIT.SALVANT.ESPCI.ORG/